# SPATIOTEMPORAL CONTROL OF CHEMICAL REACTION NETWORKS USING DROPLET MICROFLUIDICS


Submitted in accordance with the requirements
for the Ph.D. degree

**Ph.D. Student**

Maheen Rana

**Supervisor**

Professor Annette Taylor

JANUARY 18, 2024

## Declaration

I, the author, confirm that the Thesis is my own work. I am aware of the University's Guidance on the Use of Unfair Means (www.sheffield.ac.uk/ssid/unfair-means). This work has not previously been presented for an award at this, or any other, university.

Parts of this thesis appear in the following publication:

M. Rana, R. Ahmad and A. F. Taylor, Lab on a Chip, 2023,
DOI: 10.1039/D3LC00711A.

# Acknowledgements

I am very grateful for the funding from the European Union's Horizon 2020 research and innovation programme under Marie Skłodowska-Curie Grant Agreement No. 812868. This generous support has been crucial to the completion of this research project.

I would like to thank my dear supervisor Professor Annette Taylor for her tireless support, guidance, and encouragement. Her expertise and mentorship, especially around urea-urease reaction kinetics and modelling, have been instrumental in shaping the direction and quality of this research. She has always encouraged me to take the lead and find the solutions, and empowered me to explore new ideas and approaches independently. Her confidence in my abilities was a huge source of assurance, as she never called my abilities into question and ensured me that it was okay to experience failures and setbacks. I am incredibly thankful for her involvement and encouragement, which have had a significant influence on my academic and personal development. I wish to express my heartfelt thanks to my best friend, Ludovica Luongo. As part of Professor Taylor's group, she has been there for me through thick and thin, and has made my challenging life as a PhD student both easier and more purposeful. In times of doubt and hardships, Ludovica was a source of comfort, listening to me and believing firmly in my ability to reach my potential. Her friendship was a priceless gift that made the journey not only rewarding academically, but also very enriching on a personal level. I would also like to thank Anna, Federica, and Vittoria for their friendship. Their support, especially as "girls in science and research", was a source of energy that helped me to accomplish this journey.

I am profoundly indebted to my lovely and nurturing parents Ghazala and Rana Tehseen, whose firm belief in my potential has served as the foundation for my path to academic achievement. They were my pillars who always gave me unquestioning love and encouragement in all my endeavours. My parents' continuous motivation and environment of encouragement have made me the strong and independent person I am today. Since a young age, they have instilled in me the belief that I can achieve anything I set my mind to, and this belief has guided me through the challenges of this PhD venture. I would also like to thank my wonderful brothers (Massub and Muntasib) and the whole family for their love and encouragement.

Finally, I would also like to express my heartfelt appreciation to my loving husband, Dr. Raheel Ahmad, whose companionship and encouragement has been the rock of my life during this life-changing journey. His devotion to our relationship and his faith in my abilities have been the fuel behind my success, both professionally and personally. His sense of encouragement to pursue my dreams and his readiness to stand by my side in every venture has been nothing short of remarkable. Beyond the academic world, he was my rock, giving me love, care and comfort in times of exhaustion and stress.

# Abstract

A number of cellular organisms, such as yeast, bacteria and slime moulds, exhibit dynamic behaviour, in particular switching and rhythms that are controlled by feedback mechanisms in enzyme-catalysed reactions. The mechanisms of these processes are well understood, and recently there has been a focus on generating similar reactions in synthetic biocatalytic systems to establish bioinspired analogues for applications in materials and medicine. In this context, compartmentalisation of biochemical reactions within synthetic cell models such as micelles, vesicles, and W/O/W-based double emulsions is attracting growing attention for applications in the field of therapeutics. In this respect, it is necessary to adopt easier-to-use stimuli-responsive (react to pH, temperature or light) biochemical reactions, to apply artificial cell models to the biomedical context, and regulate artificial cell communication in a spatiotemporal controlled way. As a first step, it is crucial to control the output of a chemical reaction that maybe exploited for applications in the field of programmable materials and biomedicine. Droplet emulsion and synthetic vesicle systems have been widely employed as bioinspired micro- or nanoreactors for production of materials such as hydrogels and ceramic particles. They also provide test platform for biomimetic cell like behaviour.

To address this, we have developed and fine-tuned a platform with synthetic bottom-up chemistry that has enabled us to systematically and thoroughly investigate the effects of entrapment on a feedback-driven enzymatic reaction. As a result of this process, we have revealed a system that is more intricate than originally thought. Firstly, taking advantage from pressure driven droplet microfluidics, we developed a system of enzyme-encapsulated (urea-urease) double emulsion (W/O/W) droplets to obtain a localised pH pulse, with a controllable induction time to program material properties. The urease-catalysed hydrolysis of urea (urea-urea reaction), has a feedback through the production of the base ($NH_3$). This leads to a change from an acidic to a basic pH after an induction time ($T_{ind}$), resulting in an environment with auto-changing pH conditions. Reaction was initiated by addition of urea and a pulse in base (ammonia) was observed in the droplets after a time lag of the order of minutes. The pH-time profile can be manipulated by the diffusion timescale of urea and ammonia through the oil layer, resulting in localised pH changes not accessible in bulk solutions.

Secondly, we performed a computational investigation of the nonlinear reaction chemistry (urea-urease) within the designed platform of the W/O/W-based reactor. A radially distributed reaction diffusion model is presented for a layered sphere mimicking a double emulsion. Here we have combined the experiments with simulations (shell-core model) to demonstrate the influence of urea transport triggered by the shell, the core and the external solution surrounding the cell model (μ-reactor) on the induction time/period ($T_{ind}$) of urea-urease reaction.

Third, inspired from natural cellular systems (e.g. bacterial quorum sensing), we focus on the use of urea-urease reaction confined to double emulsions to investigate chemical communications. We observed a system that resulted in a system of microreactors acting as individual units with distinct induction periods ($T_{ind}$) for the first time. We show that in contrast to other systems, the release of ammonia can accelerate the reaction in all the droplets but there is no evident synchronisation of activity characterised by a wide distribution of induction times across the population of micro-reactors. However, the investigation of behaviour of population/group of μ-reactors as a function of substrate urea concentration and the density of μ-reactors highlights the possibility of transitions to collective behaviours.

Finally, we aimed to use the double emulsion template for potential biomedical and therapeutic applications using the autocatalytic urea-urease reaction. We used the platform to produce thiol-acrylate gels in the form of double emulsion loaded gel films and spherical microcapsules for potential drug delivery applications. In addition, we employed the encapsulated double emulsion platform of the enzyme urease to study the inhibition of the enzyme itself; which is important in the development of anti-microbials for ureolytic bacteria.

By building this platform, we have not only learned how to control the kinetic output of the reaction (urea-urease), but have also demonstrated its potential in future applications.

# List of Abbreviations

| | |
|---|---|
| PEG | Poly(ethylene glycol) |
| BZ | Belousov-Zhabotinskii |
| W/O | Water-in-oil |
| W/O/W | Water-in-oil-in-water |
| GUVs | Giant Unilamellar Vesicles |
| POPC | 1-palmitoyl-2-oleoyl-*sn*-glycero-3-phosphocholine |
| ODEs | Ordinary differential equations |
| TEMDA | Tetramethylethylenediamine |
| Pyranine | 8-hydroxypyrene-1,3,6-trisulfonic acid |
| PVA | Poly(vinyl alcohol) |
| PAM | Poly(acrylamide) |
| PHEMA | Poly(2-hydroxyethyl methacrylate) |
| PEGDA | Poly(ethylene glycol) diacrylate |
| EPS | Extracellular polymeric substance |
| MO | Mineral oil |
| SPAN-80 | Sorbitan monooleate |
| MF | Middle flow |
| IS | Inner solution |

| | |
|---|---|
| OS | Outer solution |
| ES | External solution |
| PF127 | PLuronic F-127 |
| AA/HA | Acetic acid |
| PDMS | Polydimethylsiloxane |
| $P_{IS}$ | Pressure for the inner solution channel |
| $P_{MF}$ | Pressure for the outer solution channel |
| $P_{IS}$ | Pressure for the middle flow channel |
| F458/F405 | Fluorescence intensity at 485/ Fluorescence intensity at 405 |
| $I_{ex}$ | Exicitation intensity |
| $I_{em}$ | Emission intensity |
| $T_{ind}$ | Induction time |
| $pH_{ss}$ | Stady state pH |
| $pH_{max}$ | Maximum pH |
| $pH_{app}$ | Apparent pH |
| $pH_{O}$ | Outside pH |
| S/C | Shell/Core |
| UU | Urea-urease |
| µ-reactor | Micro reactor |
| MM | Michaelis-Menten |

| | |
|---|---|
| pKa | Acid dissociation constant |
| $K_M$ | Michaelis constant |
| $K_{es1}$ and $K_{es2}$ | Acid protonation equilibria |
| $K_S$ | Substrate inhibition factor |
| $K_P$ | Product inhibition factor |
| L | Inner aqueous core |
| BL | Shell layer |
| L2 | Outer external solution (ES) layer |
| $\mathbf{f(C_i)}$ | Reaction term |
| $\boldsymbol{Di}$ | Diffusion coefficient |
| $\mathbf{C_i}$ | Chemical specie |
| NDFs | Numerical differentiation formulae |
| AbsTol | Absolute tolerance |
| $P_i$ | Permeability coefficients |
| $\mathbf{ki}$ | Partition coefficients |
| PDE | Partial differential equations |
| SA | Self-assembly |
| RD | Reaction-diffusion |
| ETTMP | Ethoxylated trimethylolpropane tri(3-mercaptopropionate) (THIOCURE® ETTMP 1300) |
| M.W. | Molecular weight |

| | |
|---|---|
| EVs | Extracellular vesicles |
| MPSS | Methylprednisolone sodium succinate |
| APIs | Active pharmaceutical ingredients |
| EDTA | Ethylenediaminetetraacetic acid |
| ATP | Adenosine triphosphate |

## Contents

# 1 Introduction and Background

## Contents:

## 1.1 Cell compartmentalisation: A spatiotemporal perspective

Cells that are the fundamental units of nature are extremely complicated systems and are extraordinary microreactors. Compartmentalisation and spatial arrangement are among the primary approaches in living cells that provide spatial and temporal properties for biological pathways. In particular, the membrane-bound organelles of eukaryotic cells exhibit substantial compartmentalisation, as shown in **Figure 1.1**. Organelles such as the mitochondria, golgi apparatus, nucleus, vesicles, endoplasmic reticulum, and lysosomes all serve distinct purposes and offer specialized environments for diverse cellular functions. Collectively, these organelles sustain diverse environments that enable specific biochemical reactions to proceed without disruption. For example, vesicles (membrane-bound sacs) are engaged in the delivery and transportation of different molecules within and among various cellular compartments. Compartmentalisation also facilitates effective movement of molecules and ions between organelles, thereby assisting important cellular processes such as signal transduction, metabolism, and cell communication.

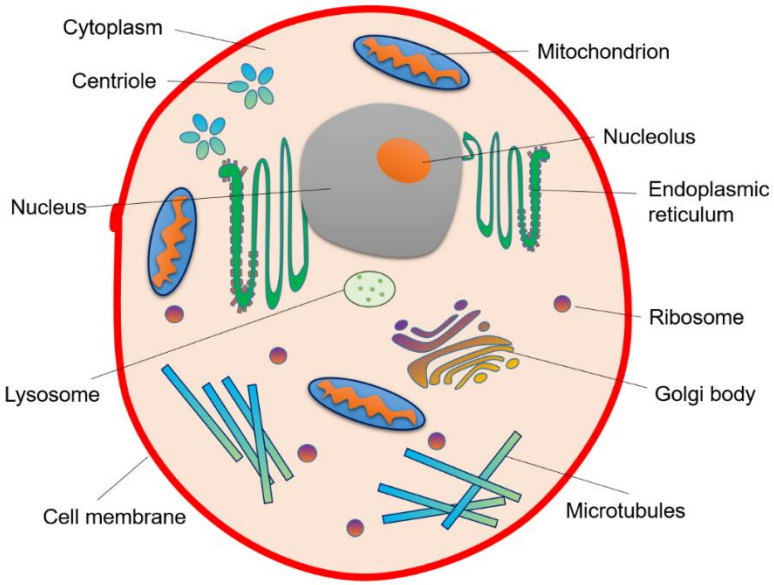


***Figure 1.1 A schematic illustration of a typical eukaryotic cell****, adapted from*[1]*, Copyright © 2020 Springer Nature Switzerland AG.*

### 1.1.1 Cell Membrane

A common feature of all living cells, although multicellular organisms have different structures and functions, is the presence of a cell membrane also known as the plasma membrane. This important membrane wraps around the cell, providing protection and regulating the movement of materials to and from the cell.

The cell membrane is a rather flexible structure consisting of two layers of phospholipids and is called a 'bilayer'. Also embedded in the membrane are cholesterol and various other proteins that give the membrane its functionality. An individual molecule of phospholipid possesses a phosphate group at one terminal end, termed the 'head', and has two adjacent fatty acid chains, which form the 'tails' of the lipid (**Figure 1.2**). The bilayer configuration results from the orientation of these individual phospholipids, with the lipid tails of two opposing layers facing each other at the interface between the two, while the lipid heads on one side face the cell interior and the other layer of heads face the cell exterior (**Figure 1.2**).

The phosphate groups are negatively charged and therefore make the lipid head polar and hydrophilic (water-loving). This makes the head attracted to the aqueous environment of the cell interior and exterior. In contrast, the tails of lipids are uncharged (nonpolar) and hydrophobic (water-repellent). Thus, the presence of both hydrophilic and hydrophobic regions is what makes phospholipids amphipathic molecules.

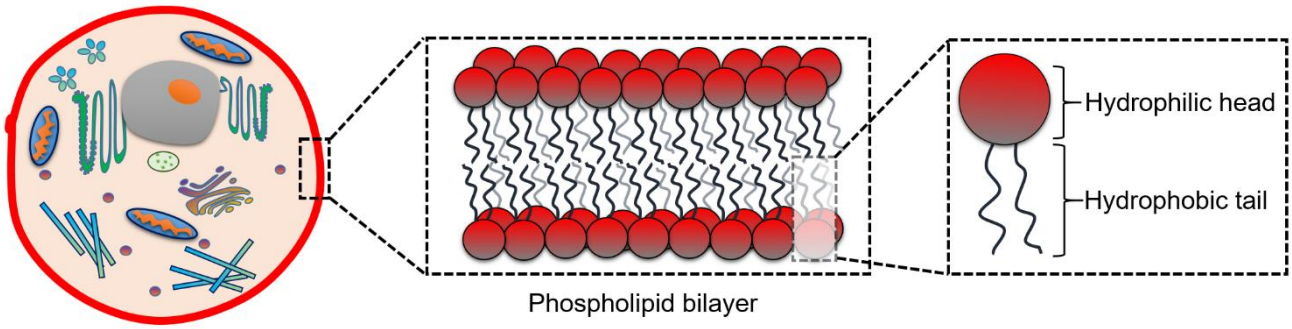


***Figure 1.2 Structure of phospholipid and bilayer,*** *A phospholipid molecule consists of a 'head' hydrophilic polar phosphate and a 'tail' nonpolar hydrophobic lipid. The phospholipid bilayer is comprised of two neighbouring layers of phospholipids that are placed from the tail to the tail. The hydrophobic tails are interconnected and form the inner part of the membrane. The polar heads come into contact with the fluids both within and external to the cell (from two opposite sides)*[2].

### 1.1.2 Transport Across the Cell Membrane

The cell membrane offers initial level of protection by enclosing the cell interior as well as allowing the transport of nutrients to the cell and removal of toxic substances from within the cell. The composition of the lipid bilayer forms a fairly densely packed structure with a hydrophobic interior. This configuration makes the membrane selectively permeable[2,3], i.e. only certain substances can pass through it, shown in **Figure 1.3**. In cell, for example, relatively small and nonpolar molecules such as oxygen, other lipids, and carbon dioxide gases, and alcohol can move easily through the bilayer (by simple diffusion).

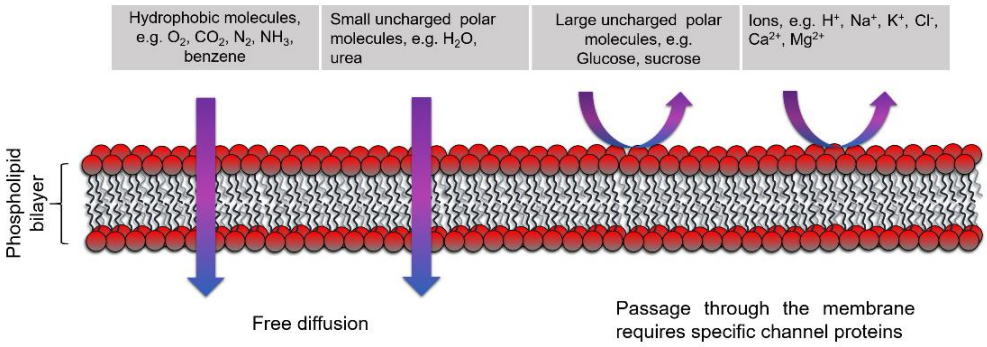


***Figure 1.3 Transport of molecules through the phospholipid bilayer**, indicated by the permeability of the lipid bilayer. The membrane represents a hurdle to the diffusion of large polar molecules and all charged molecules[2].*

On the other hand, water-soluble substances such as amino acids, glucose, and electrolytes rely on help to pass across the membrane since they are rejected by the hydrophobic tails of the phospholipid bilayer. Substances that traverse the barrier use either of two approaches, which are defined based on the need, or lack of need, for energy. Passive transport involves the movement of substances through the membrane with no cellular energy being expended (by diffusion). In active transport, on the other hand, substances are moved across the membrane with the help of adenosine triphosphate (ATP).

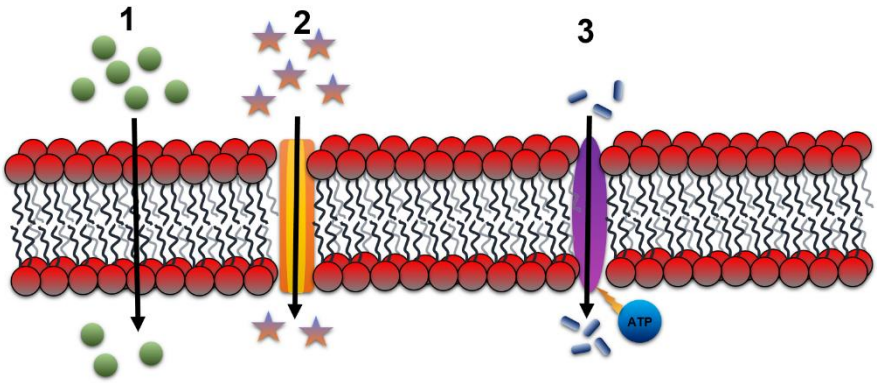


***Figure 1.4 Transport mechanisms across the cell lipid bilayer****: passive vs active passage 1. Simple diffusion of small hydrophobic molecules (e.g. $O_2$, $CO_2$, $N_2$, $NH_3$), 2. Facilitated diffusion via protein channels, 3. Active transport using ATP energy for large polar molecules and charged ions*[2].

In passive transport, simple diffusion (see **Figure 1.4**(1)), small molecules such as $O_2$ and $CO_2$ cross the lipid membrane and enter an aqueous solution on the other side of the membrane, the rate of diffusion being proportional to the concentration gradient across the membrane. Osmosis is the process by which water molecules pass through the lipid bilayer membrane, passing through the region based on the difference in solute concentration on the two sides of the bilayer. When the solute concentration is the same on both sides of the lipid bilayer, the net transfer of water is zero and is referred to as isotonic. Facilitated diffusion (labelled (2) in the **Figure 1.4**), on the other hand, is caused by specific permeases embedded in the membrane. Just like simple diffusion, facilitated diffusion involves the movement of specific molecules along the concentration gradient with the help of specific channel/carrier proteins. These proteins allow hydrophilic passage through the hydrophobic lipid bilayer. Active transport (labelled (3) in the **Figure 1.4**) requires additional energy to move certain molecules (such as amino acids, glucose, and ions) against the concentration difference (from an area with high concentration to an area with low concentration). In this case, the channel proteins require energy in the form of ATP to move the molecules through the bilayer.

## 1.2 Enzymes: An Overview

Cells contains many different enzymes and enzymatic reactions play an important role in regulating and carrying out most life processes. Enzymes provide support for many different important processes within the body and accelerate (catalyse) chemical reactions in cells. More precisely, they reduce the barrier required to initiate the desired reaction. They perform this by binding to another substance called a substrate. For example, based on the functions there are oxidoreductases, transferases, hydrolases, kinases, phosphatases, isomerases, ligases, polymerases, proteases, and lyases. Glycolysis is a primal metabolic pathway that occurs in the cytoplasm of cells. In this process, glucose is converted into two molecules, pyruvate and energy. The enzymes which are involved include hexokinase, phosphofructokinase, and pyruvate kinase[4'5'6].

### 1.2.1 Catalytic Activity of Enzymes

There are two basic features of enzymes that are common to all other catalysts. One, they accelerate the speed of chemical reactions while not being used up or permanently altered in the reaction itself. Second, they accelerate the rate of reaction without disturbing the chemical equilibrium among the reactants and the products.

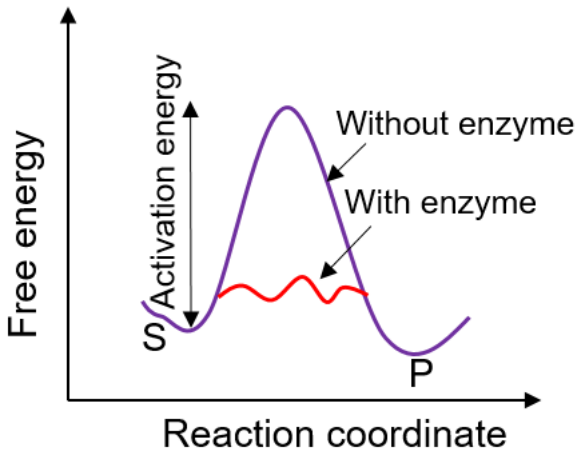


***Figure 1.5 Energy diagrams for uncatalysed (purple) and catalysed (red) reactions***. *Adapted from[7], Copyright © 2000, Geoffrey M Cooper.*

These fundamentals of enzymatic catalysis are exemplified in the example here, where the substrate [S] is changed into a product P ([P]) by the action from an enzyme. However, in the lack of an enzyme, the reaction can be represented as follows:

$$S \rightleftharpoons P \qquad (1.1)$$

***Equation 1.1*** *Reversible reaction in which the substrate [S] is converted into the product [P].*

The chemical equilibrium between S and P is governed by the principles of thermodynamics and is given by the relationship between the rates of the forward and reverse reactions, S→P and P→S respectively. The addition of the enzyme accelerates the transformation of S into P, but the balance between S and P stays unchanged. Hence, the enzyme must expedite both the forward and the reverse reactions to the same extent. The following equation shows an example of an enzyme catalysed reaction.

$$S \overset{E}{\rightleftharpoons} P \qquad (1.2)$$

***Equation 1.2*** *Reversible enzymatic reaction in which the substrate [S] is converted into the product [P].*

The enzyme concentration remains unaltered throughout the reaction. The activity of an enzyme changes the energy barriers associated with the reaction progression from S to P. Without enzymatic catalysis, in fact, the vast majority of biochemical reactions are sufficiently slow that they just could not proceed under the mild temperature and pressure conditions compatible with life, **Figure 1.5** shows an illustrative comparison between the enzymatically catalysed and the uncatalysed reaction course as well as comparative energy barriers for both. The reaction equilibrium is governed by the final energy states of the substrate [S] and the product [P] and is not changed by the introduction of an enzyme catalyst. However, regardless of the presence of an enzyme, the substrate has to have to pass through the transition state (a high energy state) by overcoming the activation energy (the energy required to reach the transition state) which is considered as a barrier to the progression of the reaction. The presence of enzymes, however, reduces the activation energy and hence increases the rate of the reaction.

Enzymes impart their catalytic activity by enabling the formation of an enzyme-substrate complex (ES) by substrate binding. The binding (ES) happens at a distinct site of the enzyme, called the active site, where the substrate performs a series of

chemical changes that eventually lead to the conversion of the product (P). However, the enzyme (E) remains unchanged during the conversion. The reaction of the substrate (S) to product (P) catalysed by the enzyme can be described as follows and as presented by Leonor Michaelis and Maude Menten in 1913[8,9]:

$$E+S \underset{k_{-1}}{\overset{k_1}{\rightleftharpoons}} ES \xrightarrow{k_{cat}} E+P \qquad (1.3)$$

***Equation 1.3*** *Reaction mechanism for enzymatic reactions.*

It is further given by the following equation:

$$\frac{d[P]}{dt} = \frac{k_{cat}[E]_0[S]}{[S]+K_M} \qquad (1.4)$$

***Equation 1.4*** *Michaelis Menten rate equation for enzyme kinetics.*

Where, $k_1$ *is the forward rate constant,* $k_{-1}$ *is the reverse rate constant, and* $k_{cat}$ *is the catalytic rate constant (first order),* $E_0$ is the total enzyme concentration and $V_M = k_{cat}[E]_0$ (maximal velocity of the reaction), $K_M$ is referred to as the Michaelis constant, defined as the substrate concentration at the half maximum rate point.

### 1.2.2 Mechanisms of Enzymatic Catalysis

Active sites are distinct slits or ridges on the enzyme surface, generally formed by amino acids from various folded protein polypeptide chain regions that come collectively in the enzyme's tertiary structure. The enzyme provides a template/platform on which the reactants are combined and directed in the right way to facilitate the transition state formation in which they interact. The most simplistic example of enzyme-substrate interaction is the lock-and-key type[7] (as illustrated in **Figure 1.6**), in the case of which the substrate precisely fits into the active centre. In other cases, however, the substrate has to go through conformation changes to resemble the transition state, known as ‘induced fit model’.

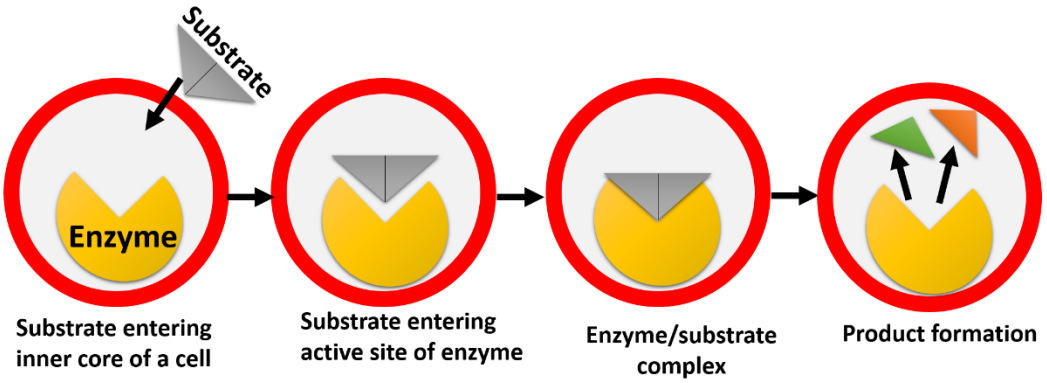


***Figure 1.6 Enzyme-substrate interaction model**. In the lock-and-key model, the substrate matches exactly with the 'active site' of the enzyme. The enzyme offers a template on which the substrates are placed in the proper position and alignment to interact with each other. Here the red outer line (circle) indicates the lipid bilayer.*

## 1.3 Approaches for Compartmentalisation

Various approaches have been made to mimic natural cells either by the top-down approach of genome editing[10] or more recently through the bottom-up approach, where units of cells are put together to construct a life-like cell[11]. Contemporary research provides somewhat insight into biochemical pathways and individual constituents of a cell, however, communication between different factors of a cell has still been an interesting research question[11]. Scientists in the fields of synthetic biology, systems chemistry, systems engineering, and supramolecular catalysis have developed self-assembled soft matter frameworks that imitate these natural catalytic compartmental structures. Underlying this research are three motivations. One, compartmentalisation results in the formation of a closed space for the catalytic species, thereby addressing incompatibility issues and improving the efficiency and selectivity of the catalyst. Second, (nano)micro-compartments are being engineered with the goal of building micro-environments that better mimic cellular architecture. These biomimetic platforms will be exploited to improve our understanding of understanding cellular processes. Finally, design rules (inspired from nature) are used to build biomolecular entities with exceptional functionality, which are then employed as artificial cells or semi-synthetic cell-like structures with potential applications in drug delivery[12,13]. Compartmentalisation has a number of advantages. To begin with, it enables catalyst stabilization and thus extends the operating window.

Compartmentalisation also creates a confined space in which the catalyst may be more reactive compared to the surrounding medium, and/or in which the reaction settings are favourable for specific reaction types, resulting in greater selectivity of the reaction. In addition, the concentrated microenvironment can also induce substrate specificity[12].

### 1.3.1 Creating Membrane Boundaries

Biological membranes[14–16] are an important field of research for creating compartmentalised entities and gaining insight into cellular dynamics, and represent key objectives for medical and biotechnological implementations. Over the years, various membrane models have been used to compartmentalise and effectively coordinate comprehend their specific interactions with other molecules and/or triggers to[17–19] better understand the dynamics. Of the many straightforward model frameworks, various sized vesicles, in particular giant unilamellar vesicles (GUVs), and supported bilayers are given preferential consideration over some others [20].

Bottom-up approaches are extensively employed to develop cell-like compartmentalised entities built on vesicles through the in vitro construction of biomimetic materials. Liposomes (lipid vesicles) are nano/micro-sized vesicles composed of a lipid bilayer enveloping an aqueous nucleus (core), which are perfectly well adapted for the transport, isolation, localization, and preservation of molecules [21,22]. The vesicles are structurally developed from cholesterol and phospholipids[21,23,24].

The lipids that are used most frequently are phospholipids (particularly for the investigation of signal transmission and transport phenomenon), especially the neutrally charged phosphatidylcholine and the negative charged phosphatidylserine, phosphatidic acid, and phosphatidylethanolamine, all of which have a varying chain combination of fatty acids in the hydrophobic domain of the molecule. For cationic liposomes, stearylamine are used. The charge and the nature of fatty acid (presence of double bonds in the chain) give the bilayer its properties (phase behaviour and elasticity) [25]. For example, the presence of both DPPC (1,2-dipalmitoyl-*sn*-glycero-3-phosphocholine) and DPhPC (1,2-diphytanoyl-*sn*-glycero-3- phosphocholine) in the membrane creates domains within it[26]. **Table 1.1** gives a classification of the biomimetic materials used for the construction of synthetic bilayers.

***Table 1.1*** *Biomimetic materials (inspired by nature) for the self-assembly of vesicles, Taken from[27].*

| **Biomimetic materials** | **Features** |
|---|---|
| Phospholipid materials | Less stability<br>Good permeability<br>High lateral mobility<br>Limited chemical versatility |
| Hybrid materials | Composite phospholipid/polymer materials<br>Phase segregation<br>Domain cleavage |
| Block copolymer materials | Increased stability<br>Less lateral mobility<br>limited permeability<br>increased chemical versatility |
| Native materials extracted from the cell membrane | Monitored permeability (membrane proteins)<br>Functional properties (ion channels) |

Lipid vesicles were first prepared by Bangham and coworkers in the 1960s[28,13]. However, most of these vesicles consisted of hundreds of concentric lipid bilayers (as shown in the **Figure 1.7**) and are therefore now called multilamellar vesicles (MLVs). The limitations associated with the MLVs accelerated research towards more homogeneous synthesis schemes. It was determined that small unilamellar vesicles (SUVs) with dimensions between 25 nm and 100 nm can be produced by sonication of MLVs[29]. Large unilamellar vesicles (LUVs) with diameters varying from 100 nm to 1 µm were first prepared in the mid-1970s[30]. In addition, other methods for the preparation of vesicles involving dispersion of natural or synthetic phospholipids in aqueous solutions includes reverse evaporation (from organic solvent)[31,32], detergent dilution (or dialysis)[33,34,35], and pressure filtration[36]. Other preparative techniques includes induced shearing[37,38] and spontaneous formation of vesicles based on the aqueous mixtures of oppositely charged amphiphiles[39–41]. The commonly used preparation method is extrusion using polycarbonate filters[42].

Therefore, vesicles can be characterised by the size, lamellarity, and homogeneity of the lipid membrane[28], as shown in the **Figure 1.7**. Unilamellar vesicles consisting of a single bilayer and can be classified based on nomenclature into small unilamellar vesicles (SUVs) with a size of ~10-100 nm, large unilamellar vesicles (LUVs) with a size of ~100-1000 nm, and giant unilamellar vesicles (GUVs) with a size of > 1 μm. In addition, due to lamellarity, there are multilamellar vesicles (MLVs) with an onion-like shape and oligovesicular vesicles (OVVs), where a larger vesicle contains a number of smaller vesicles[20].

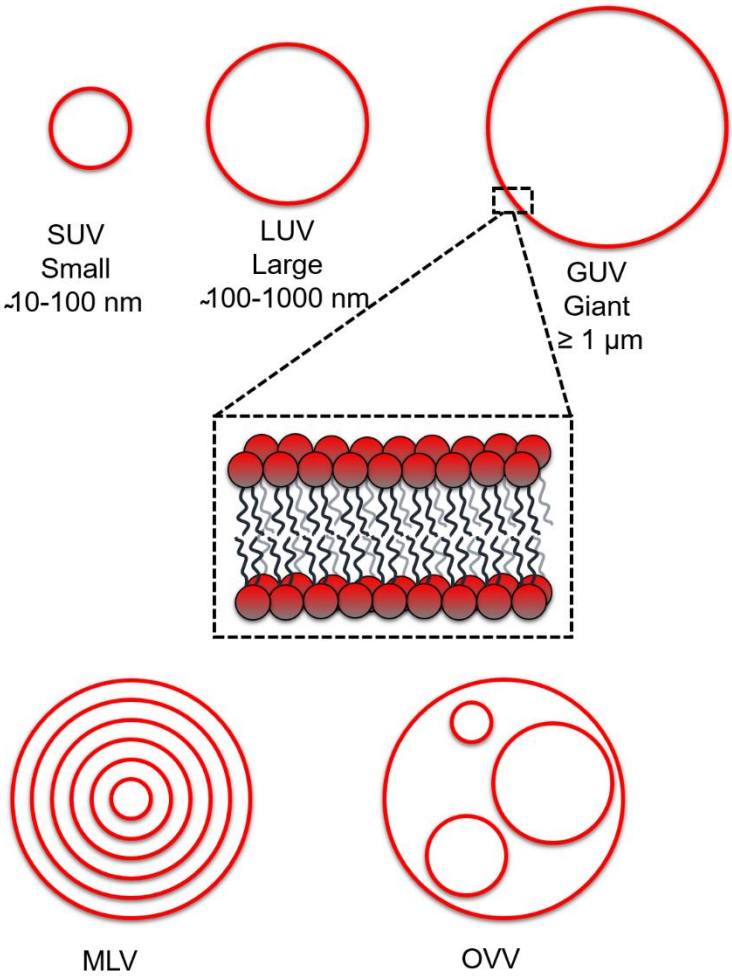


***Figure 1.7 Schematic illustration of different vesicles structures*** *with respect to the size, number of bilayers, and shape, where SUV = small unilamellar vesicle (~10-100 nm), LUV = large unilamellar vesicle (~100-1000 nm), GUV= giant unilamellar vesicle (> 1 μm), MLV = multilamellar vesicle, OVV = oligovesicular vesicle. Adapted from* [20,43].

### 1.3.2 Giant Unilamellar Vesicles (GUVs)

Giant unilamellar vesicles (GUVs) have a characteristic spherical shape and feature a spacious inner water core with the size similar to a natural cell. Due to their relatively large size, which allows direct observation with a light microscope, these GUVs occupy an important role in research and analysis. They act as useful templates for cell membranes and provide well-controlled environments for the study of different biological processes. In addition, GUVs are readily suitable for bioanalytical applications and enable understanding of the behaviour and specific interactions of biomolecules[19].

One of the earliest techniques for the production of GUVs is the controlled hydration of a thin dry lipid film by Reeves and Dowben[44], where the lipids were dissolved in organic solvent first and then subsequently removed by drying the film by passing nitrogen gas through the container. Next, the aqueous solution is added and the lipid film is set to swell which eventually leads to the synthesis of GUVs. The other names for this method are gentle hydration method, spontaneous swelling, and natural swelling[45] (as shown in **Figure 1.8** , method 1 a). Angelova and Dimitrov made further changes to the technique by using externally imposed electric fields to affect the hydration of lipids which were precipitated out of an organic solution upon a conductive glass top surface (glass coated with indium tin oxide (ITO)) or upon platinum wires. This method is termed the electroformation or electroswelling technique (method 1 b)[46,47,48]. Hydration of lipid films (spontaneous swelling) and electroformation processes generally do not permit effective entrapment of either large water-soluble molecules (e.g., enzymes) or charged molecules as they are formed, since the molecules to be entrapped need to migrate underneath the extreme layer of the deposited lipid film in some way, this is challenging given the slow interlayer mobility of large or charged molecules.

To overcome this limitation, GUVs are prepared by emulsion transfer method[49,50] (method 2), using water/oil/water (W/O/W) emulsions, particularly by microfluidic droplet techniques[51–53] (method 3), by the fusion of small vesicles[54,55] (method 4, which is inherently complicated since it requires opening existing enclosed bilayers to

an energetically adverse state and merging of many small vesicles to create a giant vesicle). Other bulk methods are presented in **Figure 1.8** as shown below[56–61,62,63].

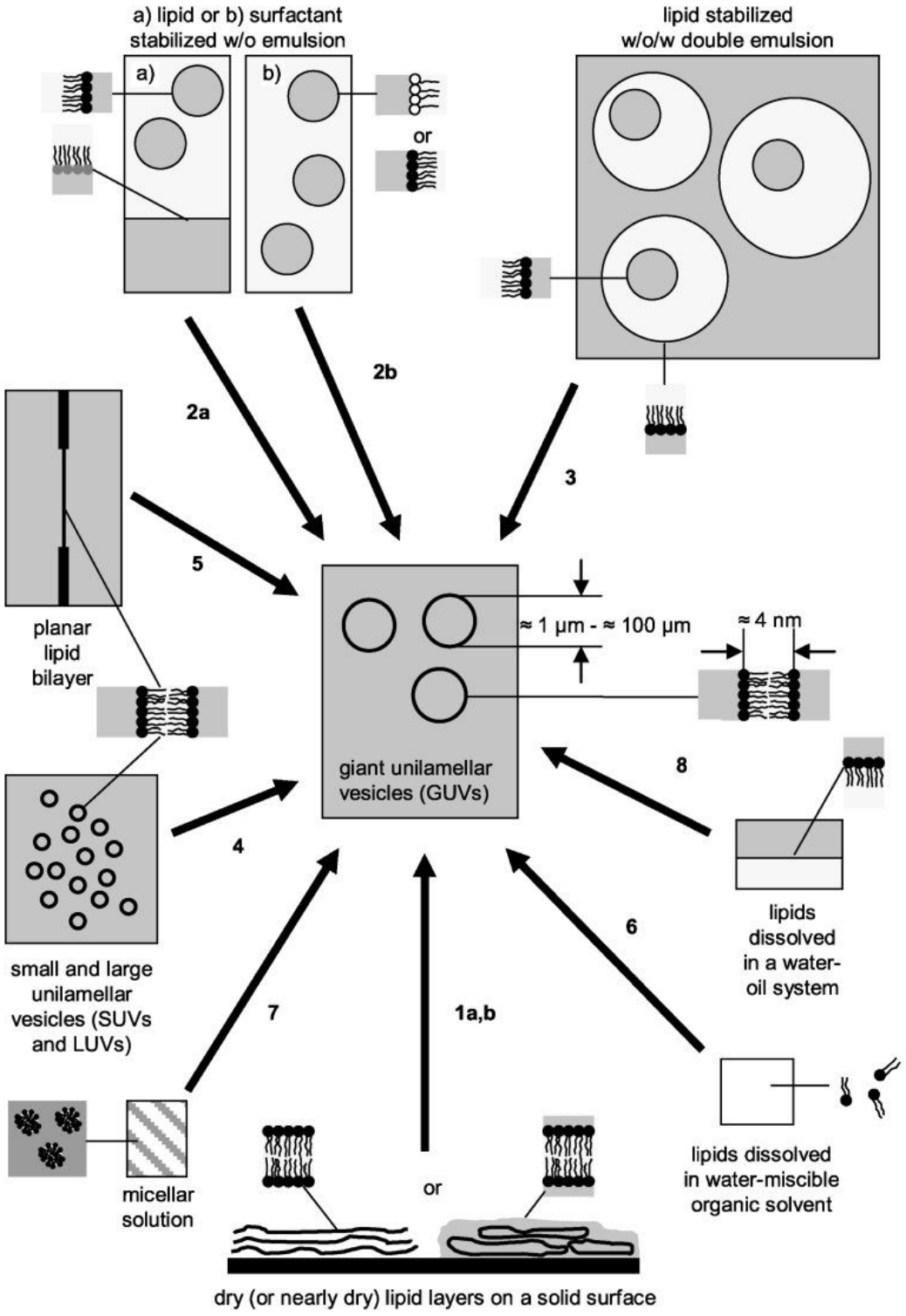


***Figure 1.8 Simplified schematic illustration of the key concepts of the main methods for the generation of giant unilamellar vesicles (GUVs).*** *Method 1: Controlled film hydration deposited from organus solvent, where hydration is performed under uninterrupted settings (method 1 a, spontaneous swelling (gentle hydration)) or. Electric field is applied (method 1 b, electroformation). Method 2: Transformation of a lipid-stabilised emulsions to GUVs using w/o emulsions (method 2 a: lipid stabilised*

*and method 2 b: surfactant stabilised). Method 3: Conversion of a lipid-stabilised w/o/w double emulsions into GUVS. Method 4: Giant vesicles generated by the fusion of small or large unilamellar vesicles. Method 5: GUVs produced by jet blowing on an originally flat lipid bilayer placed between two aqueous solutions. Method 6: GUVs derived from lipids dissolved in a water-miscible organic solvent. Method 7: Giant vesicles synthesied from a micellar lipid solution. Method 8: GUVs made from bilayer-creating lipids that are originally present in a two-phase system (w/o). Reproduced with permission from*[64]*, Copyright ©2010 WILEY-VCH Verlag GmbH & Co. KGaA, Weinheim.*

Emulsion transfer methods are usually preferred to study biochemical reactions or, in other words, to use compartmentalise units as micro/bioreactors[27]. This approach takes advantage of the innate features of giant vesicles, which are micron-sized aqueous droplets enclosed by a layer of amphiphilic material in a main aqueous solution. To produce a bilayer structure with a confined volume, water-in-oil droplets are initially generated, and then converted into vesicles by a process termed "droplet transfer/ phase transfer"[65]. In addition, the microfluidic methods are also based on the droplet template to generate double emulsions driven lipid vesicles. A comparison of the most frquently employed vesicle generation stratergies are presented in **Table 1.2**.

***Table 1.2*** *Advantages and disadvantages of different methods for the construction of giant vesicles*

| **Method** | **Advantages** | **Disadvantages** |
|---|---|---|
| Gentle hydration /natural swelling method[23] | Easy operation | Reduced synthesis rate<br>Reduced encapsulation efficiency<br>Irregular vesicle size |
| Electro-formation method[66,67] | Easy procedure<br>Easy for vesicle immobilization | Restriction to buffers with low ion concentrations<br>Restriction of construction materials (e.g. charged lipids) |
| Droplet/Phase transfer method[68,49,69] | Improved vesicle stability<br>Regular vesicle shape<br>Asymmetric vesicle composition leaflet<br>Adjustable protein alignment | Difficult operation<br>Non-uniform vesicle size |
| Microfluidic method[70–73] | Regular vesicle shape<br>Consistent vesicle size<br>Asymmetric vesicle composition leaflet<br>Adjustable protein alignment | Limited vesicle size (dependent on the size of microfluidic channel) |

In addition to GUVs, water-in-oil (W/O) droplets, and water-in-oil-in-water (W/O/W) double emulsions with interfacial layers constituting self-organised amphiphiles have been recognised as valuable simulators of cellular structures, permitting the examination of the compartmentalisation influence similar to the spatiotemporal controllability of a living cell[74]. Conventional methods for compartmentalisation such as droplet transfer technique results in low yields, polydispersity, less efficient encapsulation of biomolecules, and often fails to scale-up the technology and therefore microfluidic technologies are considered.

## 1.4 Microfluidics

Microfluidics involves the science and technology of integrated channel systems at the microscale level of tens to hundreds of micrometres, that allow small volumes of fluid (typically $10^{-9}$ to $10^{-18}$ litres) to flow in specific patterns that are manipulated and controlled in a highly systematic manner[75,76]. In 1990, Manz et. al. demonstrated, based on the fundamental theories of diffusion and hydrodynamics (that faster separations and transports are proportional to shorter length scales), a device for liquid chromatography in which the lengthwise contraction in the device can improve chromatographic separations, accelerate electrophoretic separations, and decrease transport times of reagents, in theory[77]. This multichannel device incorporated sample preparation, transport, detection and signal evaluation and hence was given the term *μ*TAS. The emergence of microfluidics thus traces back a number of decades, when it was driven by the need for miniaturisation in biochemical analysis[78,79]. The notion of 'lab-on-a-chip' or micrometre total analysis systems (microTASs/*μ*TASs) has since progressively become established[80]. The lab-on-a-chip techniques were since then applied to various fields such as chemical[81,82], medical[83], physical[77], biological[84,85], and engineering fields[86].

### 1.4.1 Fabrication Materials of Microfluidic Devices

The material for a microfluidic chip is selected on the basis of the properties required for the device and the intended use. Initial design of microfluidic devices utilised silicon as a substrate, using methods that are similar to those employed for semiconductor manufacturing[87]. For its optical transparency and chemical compatibility, glass is another preferred material[88], which is fabricated using photolithographic processes (as explained later) and subsequently etched to form the channel[89].

In addition, thermoplastics such as polycarbonate (PC), polyethylene terephthalate (PET), PMMA (poly(methyl methacrylate)), polyvinyl chloride (PVC), and polystyrene may be used with moulding processes to produce devices. However, their use is accompanied by some disadvantages. The moulds required for this procedure are usually metallic or silicone, which renders it difficult to perform multiple modifications to the device design during the prototyping stage (though mass fabrication becomes simpler). Also, such plastics are incompatible with the majority of organic solvents and are impermeable to gases, making them inadequate for prolonged cell culture

applications requiring gas transfer. Thermoplastic adhesion can be challenging, but can be obtained by techniques such as glue-based adhesion or mechanical clipping of channels to a manifold[90].

The most commonly used materials are soft polymer elastomers, which are made of interlinked polymer chains and give elastic characteristics when stressed mechanically[91]. The foremost preferred of such materials is polydimethylsiloxane (PDMS). PDMS is inexpensive and simple to synthesize, and therefore it is used in many microfluidics settings[88,91,92,93,94]. It is a liquid polymer that cures between 40 and 70 ºC and is moulded by the impression process, where templates can be copied with nanometer spatial resolution[88]. **Table 1.3** provides a comparison of various materials commonly used in the manufacture of microfluidic devices[95].

***Table 1.3*** *A comparative study of typical materials used in the manufacture of microfluidic devices*[95].

| **Property** | **Silicon/glass** | **Soft polymer** | **Paper** | **Thermoplastics** |
|---|---|---|---|---|
| Fabrication method | photolithography | casting | photolithography and/or printing | thermomoulding |
| Young's modulus (GPa) | 130-180/50-90 | ~0.0005 | 0.0003-0.0025 | 1.4-4.1 |
| Thermostability | very high | medium | medium | medium to high |
| Solvent compatibility | very high | low | medium | medium to high |
| Multilayer ability | hard | easy | easy | easy |
| Minimum channel size | <100 nm | <1 μm | ~200 μm | ~100 nm |
| Optical transparency | no/high | high | low | medium to high |
| Hydrophobicity | hydrophilic | hydrophobic | amphiphilic | hydrophobic |

#### *1.4.1.1 Microfluidic Flow*

Fluid flow in microfluidic devices is laminar, which is characterised by low Reynolds number, and arises when the viscous forces outweigh the inertial forces in a system[95,96,97,98]. Continuous flow systems have taken advantage of this characteristic to build many novel microscale settings[99]. The Reynolds number which gives the ratio between the inertial forces and the viscous forces in a flow can be calculated, as given below:

$$Re = \frac{\rho u D_H}{\mu} \qquad (1.5)$$

***Equation 1.5*** *Expression for Reynolds number, which is a ratio of the inertial forces to viscous forces in a flow.*

Where, $\rho$= density (kg/m$^3$), u= average fluid velocity (m/s), $D_H$= hydraulic diameter of the channel (m), and $\mu$= fluid viscosity (kg/m.s).

Here, $D_H = \frac{4A}{P}$, showing the dependence on the channel area and its wetted perimeter[96].

### 1.4.2 Droplet Microfluidics

A subset of microfluidics is droplet microfluidics, in which dispersed droplets are generated and manipulated by immiscible multiphase flows in microchannels[100]. Droplet microfluidics differentiates from continuous flow devices because it is used to create homogeneous, discrete fluid volumes within a second immiscible fluid[101]. Droplets that are monodisperse in the nanometre to micrometre diameter range can be generated at speeds of up to MHz[102–104]. The field of droplet microfluidics has changed fundamentally due to two distinct but complementary goals: the development of microscale flow reactors to investigate micro-total analysis systems (μTAS) and the generation of complicated droplet-based particles to drive materials research[105].

### *1.4.2.1 Microfabrication*

Soft lithography is the predominant technique in microfluidics that enables the fabrication of microstructures. In this process, an inverted mould is created by irradiating a mask with UV light, which cures a light-sensitive epoxy resist underneath. The uncured photoresist is then removed by etching, creating a mould. This mould is used to make a stamp from polydimethylsiloxane (PDMS), as shown in **Figure 1.9.** PDMS is then plasma bonded to other substrates (mainly glass) to create channels for fluid flow.

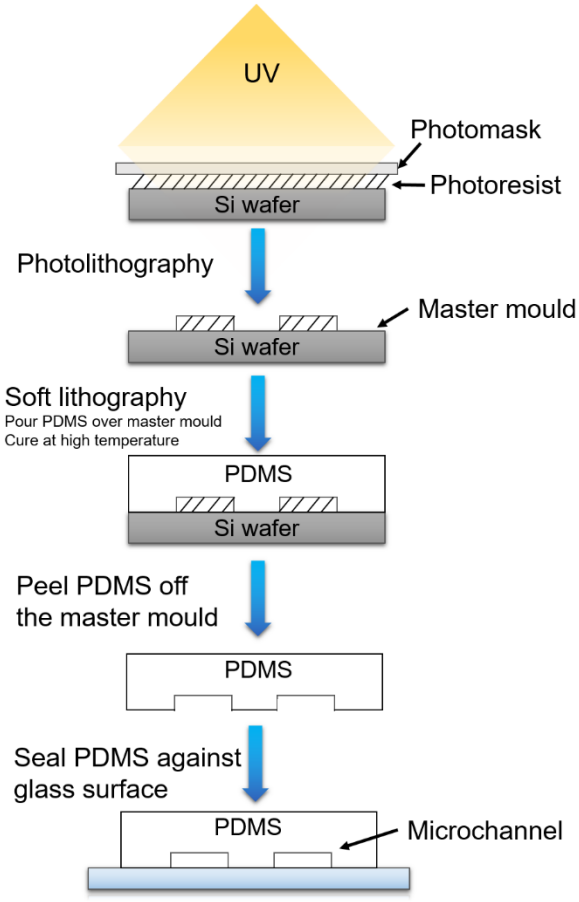


***Figure 1.9 A schematic for replica moulding for microfluidic systems**. Channels are designed on Auto CAD. A commercial printer takes the CAD file to generate high resolution transparency (~5000 dpi) which is used as a photomask to generate master mould through UV aligners. A master is made up of a positive or negative photoresist on a silicone (Si) wafer which then acts as a mould for PDMS curing. The PDMS is then peeled off the Si wafer and sealed to glass slide using plasma bonding. Adapted from*[106].

The PDMS used in soft lithography is usually available in two ingredients, one base and one curing agent. Both parts combined (usually in a 10:1 (v/v) base: curing agent ratio) forms the liquid prepolymer, to be casted onto the master mould and cures it.

The liquid PDMS prepolymer adapts to the form of the master and mimics the configuration with high accuracy. The inherent reduced surface free energy and flexibility of PDMS enable it to be detached from the master mould with no damage both to the master and itself [107,108].

### *1.4.2.2 Geometries for Droplet Generation*

There are a number of different designs for droplet synthesis. However, the three most important geometries for droplet generation in microfluidics are coaxial, cross flow (T-junction) and flow focusing, which are shown in **Figure 1.10.**

In coaxial geometry, also known as co-flow, the inner fluid (dispersed phase) and the outer fluid (continuous phase) flow in the common direction in concentric channels. This configuration is usually shown as in **Figure 1.10** (A). The experimental devices employing the coaxial shape are usually fabricated by fitting a relatively small round innternal glass capillary tube into a relatively bigger square capillary tube[109,110,111]. In order to guarantee that the fluid flow around the tip is approximately axially symmetrical, the inner capillary tube is made tapered at the tip. Later, the researchers devised coaxial channels made of PDMS (polydimethylsiloxane) for rapid prototyping[112].

In the T- junction design, the inlet channel carrying the dispersed phase intersects at right angles with the inlet channel carrying the continuous phase[113–116], as shown in (**Figure 1.10** (B)).The shear forces induced by the continuous phase and the pressure gradient drive the disperse phase to expand into the primary inlet/main channel until the expansion is so small that break-up occurs. The size of a droplet is regulated by relative flow rates, relative fluid viscosity, and channel dimensions[101].

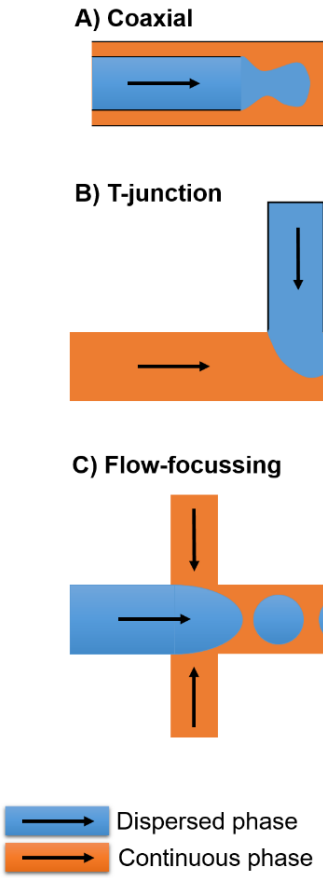


***Figure 1.10 The three most frequently used geometries for droplet synthesis**, (A) Coaxial, (B) T-junction, and (C) Flow focussing. Orange colour indicates continuous phase and blue shows dispersed phase, aerrows gives the direction of flow. Adapted from* [97].

There are many variants of microfluidic devices for flow-focusing configuration. Common to almost all of these devices is the consistent design characteristic of a junction of two channels that create a cross. The dispersed phase passes through the middle channel, while the continuous phase flows through the two side channels. The fluids join at the junction where droplets or jets of dispersed phase are formed while the fluids flow into the central channel. Flow-focusing design creates nearly extensible streams at the junction, for instance by hydrodynamic focusing or by narrowing the width (or opening) of the channel at the junction.

In the flow-focusing design, the dispersed and continuous phases are constrained through a restricted space in the microfluidic device[117–121]. The design utilises symmetrical shear of the continuous phase onto the dispersed phase, which allows for more regulated and stabilised droplet formations.

The droplet size decreases as the flow rate of the continuous phase increases[121], and as shown in **Figure 1.11** (A), increasing the continuous phase flow rate (oil flow rate, Qo) also increases the frequency of droplet formation. The droplet size gets smaller with higher Qo and larger with higher Qw, which is attributed to the preservation of the mass flow of the water phase[119]. **Figure 1.11** (B) confirms that more oil (Qo) leads to smaller droplets, while **Figure 1.11** (C) shows that production of larger droplets takes more time and will decrease with higher water flow (Qw).

Many modifications of the fundamental design of the flow focusing have been constructed to suit the needs of even more sophisticated applications[122]. Flow focusing techniques have been applied to produce multifunctional particles[123], microbubbles[121], double emulsions[124], and ionic fluid emulsions[125].

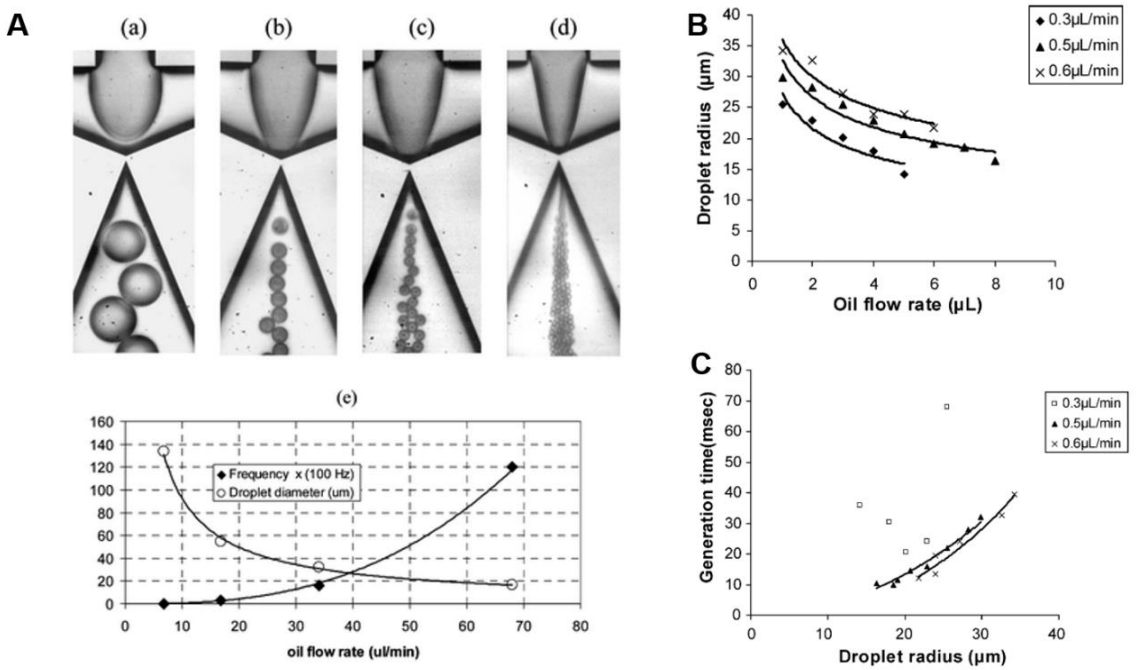


***Figure 1.11 Effect of flow rates on droplet sizes**, A) Generation of water-in-silicone oil droplets utilising a flow focusing device at increasing oil flow rates and a fixed water flow rate; the graph below indicates reducing droplet size and rising frequency of formation as the oil flow rate increases, taken from[121] Copyright © The Royal Society of Chemistry 2006 , B) The droplet size reduces as the oil flow rate (Qo) increases, and C) The time it takes to produce a single droplet increases with increasing droplet size and decreases with increasing water flow rate (Qw), taken from [119], Copyright © 2005 Published by Elsevier B.V.*

The fluid behaviour in droplet microfluidics can be characterised by non-dimensional numbers derived from the flow conditions, the geometric parameters, and the fluid properties[97,126]. These non-dimensional numbers provide information about the relative significance of the various forces involved. The Reynolds number (Re), as described in 1.4.1.1, is the first important dimensionless number, which compares inertial forces with viscous forces. At characteristic flow rates in droplet microfluidics, Re number is frequently quite small, which means that the inertial forces are negligible. The predominant forces in droplet generation are the extension and distortion of the interface due to local shear stresses and the resistance to distortion induced by the capillary pressure. The capillary number (Ca) is a further significant dimensionless number that relates the strength of viscous forces to the forces of interfacial tension. Ca number assists in predicting droplet size and dimensions. In droplet microfluidics, the interfacial tension and viscous forces are the primary forces involved. The last is the Weber number (We), which compares the inertial forces with the interfacial tension. At high flow velocities, inertial effects become significant and can lead to the crossover of discrete droplets into steady jets. The three dimensionless numbers, along with the respective forces, are the major considerations in droplet microfluidics. But under certain conditions, other forces such as gravity, buoyancy and elastic effects can make it relevant. These complementary forces can be described by appropriate dimensionless numbers.

### 1.4.3 Double-Emulsion Droplets

Multi-stage emulsification is another way of refining droplet geometry to create double or multiple emulsion droplets if desired. In this type of hierarchical system, smaller droplets are contained within the larger droplets, making a multi-layered or nested configuration that is common in both encapsulation and release applications. The nested droplet feature enables accurate manipulation and monitoring of the enclosed materials, thereby facilitating a broad range of uses in materials science, chemistry and biology. Double emulsions can be formed by using the three basic droplet-generating assemblies in sequence.

A dual-stage T-junction device was developed for this aim[127]. In the initial stage, droplets of water-in-oil (W/O) emulsion were created in a hydrophobic T-branch located upstream; in the second stage, the droplets were enveloped by a different aqueous phase flowing through a hydrophilic T-branch downstream, resulting in water-in-oil-in-water (W/O/W) double emulsions, as shown in **Figure 1.12** (A). In an effort to develop a one-step mechanism for the production of double emulsions, Weitz et al[128] developed a capillary-based device that combined the co-flow and flow-focusing configurations. This setup paved the way for the formation of double emulsions through the simultaneous convergence of three phases at a single point. The inner liquid and the immiscible middle liquid were coaxial with each other, whereas the outer liquid, which is immiscible with the middle liquid, was directed in the opposite direction. By allowing all three liquid phases to flow through a tapered orifice, hydrodynamic focusing was achieved, resulting in the synthesis of double emulsions in a single-stage process. **Figure 1.12** (B) and (C) illustrates this approach.

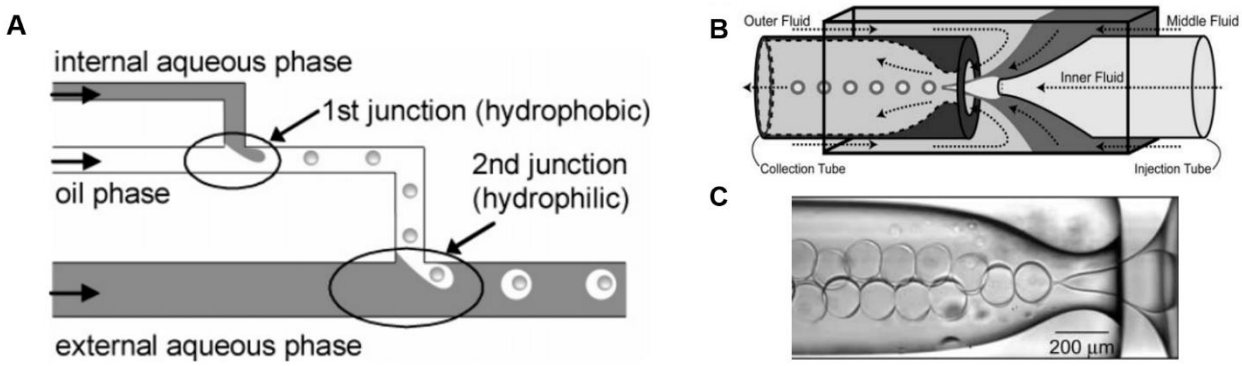


***Figure 1.12 Microfluidic fabrication of double emulsions**. A) Basic concept for preparing double emulsions (W/ O/W) using T-junction microchannels. Taken from[127], Copyright © 2004 American Chemical Society. B) Microcapillary device for the fabrication of double emulsions from coaxial nozzles. Schematic representation of the coaxial microcapillary fluidic device. The design requires the outer fluid to be immiscible with the middle fluid and the middle to be immiscible with the inner fluid. C) Steady-state drop formation mechanisms that result in monodisperse double emulsions with a single internal droplet, Taken from [128], Copyright © 2005 American Association for the Advancement of Science.*

In this context, the technique of double emulsions is used in particular for the generation of vesicle-based compartmentalised units[129,130,131]. Huck and co-workers, for example, reported a microfluidic approach for the rapid and efficient production of droplets with monodisperse coacervates[132], as shown in **Figure 1.13**. By exploiting

the versatility and controllability of microfluidics, they were able to obtain giant vesicles with a hierarchical conformation that can be employed as a template for mimicking protocells. A range of droplet-based microfluidic schemes have subsequently been used for liposome production[133,134]. Most of these have highlighted the feasibility of producing liposomes laden with biologically active bio compounds (like DNA and enzymes)

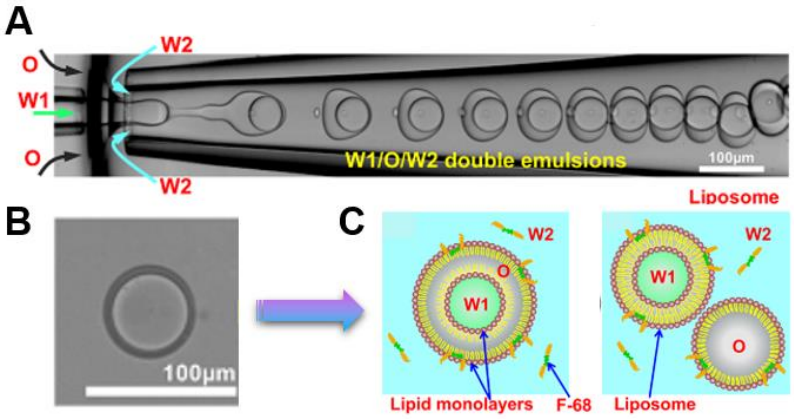


***Figure 1.13 Liposome-based monodisperse double emulsions*** *A) Fabrication of W1/O/W2 double emulsions in a device based on microcapillaries. B) Confocal image of the formed W1/O/W2 double emulsion, C) Illustration of the surfactant-assisted assembly of liposomes which is dewetting off the double emulsion droplets*, *Reproduced from*[132], *Copyright © 2016 American Chemical Society.*

### 1.4.4 Applications of Microfluidic Droplets

In addition to the key advantages of compartmentalisation, high-throughput production, and monodispersity, the ability to perform a variety of functional actions with droplets (e.g. reagent mixing, sampling, droplet partitioning, dilution, fusion, and sorting) has broadened the range of potential applications for droplet-based microfluidic solutions[101,135,136].

Droplet-based microfluidic techniques have been used to conduct a variety of biological and chemical experiments[126]. Among these are protein crystallization investigations[137], DNA amplification[138], high throughput biochemical assays[78,139,140], cell-based enzymatic assays[137], the generation of microspheres[141] and core–shell configured structures[127,128,142–144] and the tailored production of monodisperse nanomaterials, **Figure 1.14** shows few of the examples here. In addition,

pharmaceuticals, green fuels and high-grade biomaterials such as antibodies and proteins have also been made in droplet-based micro/nano reactors[101,135,145]

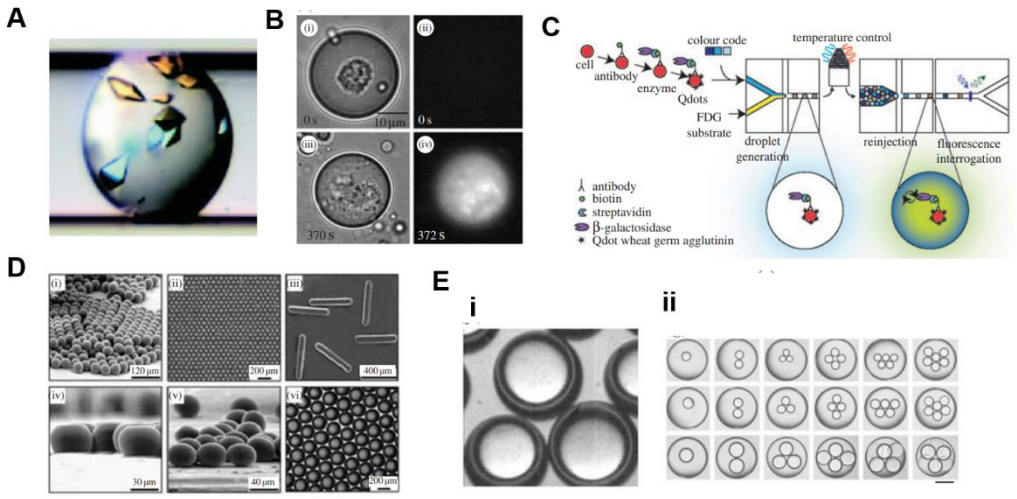


***Figure 1.14 Applying droplet-based microfluidics in chemistry and biology*** *(A) Photograph of protein crystals that formed in a microdroplet following chaotic mixing[137]. (B) A cell-based enzymatic assay contained in a droplet with a single cell. Following photolysis, the intracellular enzyme is liberated into the droplet and then reacts with a substrate to generate a fluorescent product[146,135]. (C) A droplet-based microfluidic system for high-throughput cell sorting using enzymatic amplification[147]. (D) Optical microscopic images of polyTPGDA particles(i –iv) and agarose discs (vi) prepared in droplet-based microfluidic reactors[141]. (E) Core–shell structures fabricated from double emulsions(i), generated using glass capillaries[128] and multiple emulsions(ii) generated using scalable microcapillary devices, scale bar is 200 μm[144]. Adapted from[131], Copyright* © 2016 *The Royal Society.*

## 1.5 Enzymatic Reactions in Synthetic Compartmentalised Units

A compartmentalised chemical reaction network addresses the challenge in the generation of synthetic bio-like constructs. This network, a collection of molecules, possesses enough complexity to mimic properties of living organisms. Reactions can take place in synthetic vesicles, which are cell mimics composed of a water core surrounding by a polymer/lipid layer. Concentrated localisation of reaction components is likely to speed up reaction rate, which allows selective permeability of reaction components and controlled material transport and maintains out-of-equilibrium systems.

Szostak et al., suggested a replicating vesicle with replicator molecules and catalysts that works inside the vesicles allowing fast evolutionary mechanism and optimization of the system, as shown in **Figure 1.15** [148,149]

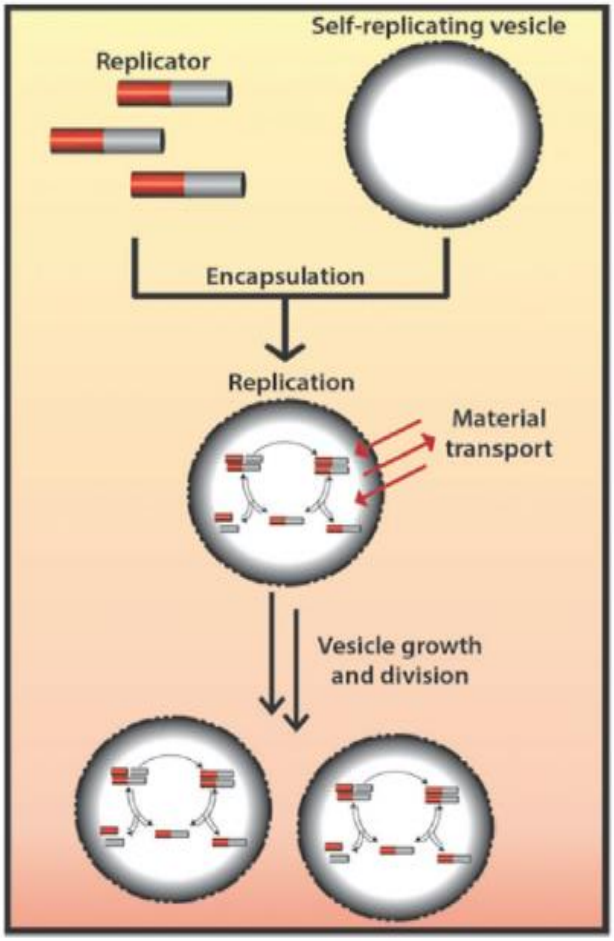


***Figure 1.15 Self replication of vesicles****. Single network for autonomously developed replicators (RNA) and self-replicating membrane vesicles. Reproduced from* [148]*, Copyright ©The Royal Society of Chemistry 2017.*

One important study is performed by Petrikovics et al. in which a nanoreactor was formed *in vitro* with the unilamellar vesicles of nanometer range encapsulating phosphotriesterase enzymes as shown in **Figure 1.16**[150]. This nanoreactor system was injected into the bloodstreams and organophosphorus compounds were hydrolysed by the enzymes inside the vesicles into nontoxic components[151]. In another study, phospholipid vesicles (100 nm size) were used to encapsulate glucose oxidase and catalase to convert D-glucose into glucono-δ-lactone which was then hydrolysed non-enzymatically to gluconic acid, as shown in **Figure 1.16**[150]. OmpF, a channel protein, was used to facilitate the transport of D-glucose from bulk to inside the vesicle.

The second enzyme catalase was used to retain the activity of oxidase, by degrading $H_2O_2$, which tends to deactivate owing to the presence of byproduct ($H_2O_2$) inside vesicles[152]. These encapsulated enzymes work as nanoreactors for the oxidation of D-glucose to gluconic acid which is an advantageous food additive and raw material for the making of medicines and polymers (biodegradable).

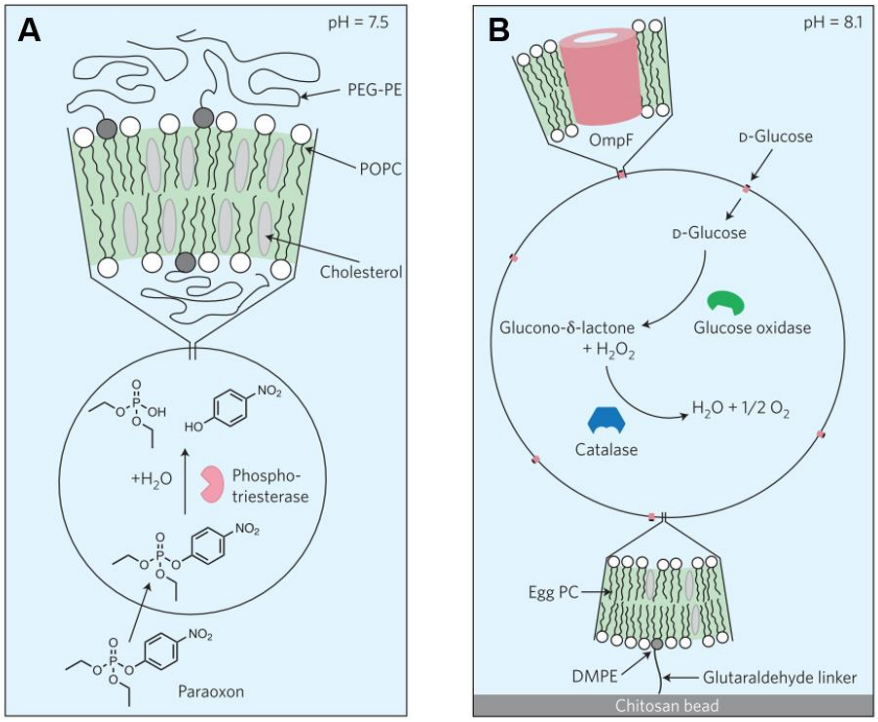


***Figure 1.16 Enzymatic reactions in vesicles*** *A) Enzymatic hydrolysis of paraoxon into non-toxic diethylphosphate and p-nitrophenol inside a unilamellar vesicle of diameter 100 nm*[151]*. B) Enzymatic nanoreactor (phospholipid based unilamellar vesicles with a size of about 100 nm) for the conversion of D-glucose into glucono-δ-lactone*[152]*.Taken from* [150]*, Copyright © 2016 Macmillan Publishers Limited.*

One important advantage of enzyme encapsulation is its ability to selectively control the confinement of enzymes. For example, to avoid systemic immunological reactions (chills, skin rashes, fever), L-Asparaginase (L-ASP), an efficient chemotherapeutic agent, was successfully encapsulated in vesicles. Encapsulated L-Asp showed considerably enhanced antitumor affects as compared to free and unencapsulated L-Asp in tumorized mice because of the controlled localization of tumor sites[153].

## 1.6 Feedback-driven Processes and Spatiotemporal Control in Compartmentalised Biochemical Reactions

Controlling the output of a chemical reaction has been considered essential to alter molecular networks and for synthetic material formation for biological applications. Predicting the spatial and temporal characteristics of a chemical reaction provides basics for multiple applications, such as a controlled molecular network for polymer synthesis and the formation of autonomous life-like materials. Two methods, passive and active, had been employed to regulate the temporal and spatial behaviour of a reaction. The passive methods depend on the built-in nature of systems to anticipate the time and region of a chemical reaction. On the other hand, the active methods benefit from the external stimulant such a light to initiate the reaction and achieve spatial control[154].

The phenomenon where the output of the system affects the system behaviour is known as a feedback driven process. The spatial and temporal regulation of chemical signals in living systems often relies on feedback behaviours. Feedback process has found applications in biological practices such as signal amplification, bistable switches, and rhythms. Mechanical ways, for example, gel volume hysteresis with pH and chemical ways, for instance, autocatalysis is used to set up feedback-driven processes. The notion that positive and negative feedbacks can induce an interaction between intricate chemical reactions and physical events to bring about a distinct function within a chemical system is what has drawn the field such a great deal of interest in recent years[148].

A chemical clock method is one way to achieve temporal control through reaction kinetics, which includes a programmable and changeable reaction time between mixing and final output of the reaction. These chemical clocks mainly depend on a sudden change in property such as pH after an amendable amount of time, which also indicates the formation of a product after an adjustable time or delay.

A chemical clock can be achieved by autocatalysis (positive feedback)[155], whereby one of the reaction products itself serves as a catalyst for the reaction:

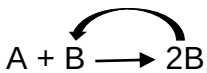


(1.6)

***Equation 1.6*** *General expression for positive feedback autocatalysis.*

In this case, "B" is a product and its formation leads to a faster production of "B", resulting in autocatalysis and a positive feedback loop.

A chemical clock can also be achieved by removal of an inhibitor species, B (substrate-depletion clock):

$$A \longrightarrow C$$

$$B + C \longrightarrow P \qquad (1.7)$$

***Equation 1.7*** *General expression for substrate-depletion clock reaction.*

When substrate "B" is present, the clock species "C" is used up quickly in the second reaction. It is only when substrate "B" is completely consumed or depleted that species "C" can increase in quantity, resulting in a colour change. An example of this clock reaction is the sulphite-iodate reaction or iodine clock reaction, also known as the Landolt reaction[155–157].

Positive feedback or autocatalysis signifies that the reaction is catalysed by its products, implying that the reaction rate rises with the formation of the products. Whereas, negative feedback serves to remove the autocatalyst[158]. Clock reactions have been used to drive time delayed polymerisation. For example, pH clocks can be used to produce base which then catalyzes the polymerisation, as an example, Pojman and coworkers used the clock reaction of formaldehyde-sulfite which showed a fast increase in pH after an adjustable interval of time to trigger the polymerisation of pH sensitive hydrogel (thiol-acrylate)[159].

One important feature of a coupled chemical reaction network with feedback is oscillations. The Belousov–Zhabotinsky reaction[160] provided a basis for many chemical oscillators. The design scheme for oscillations involves an activator (positive feedback), an inhibitor (negative feedback), and to maintain the system far from equilibrium, the reactions are performed in flow reactors. This network shows four diverse behaviours in flow conditions, oscillations, presence of high and low steady states, and bistability[148]. The BZ reaction was used for the temporal control of polymerisation, by coupling the radical reactions that take place with a free radical polymerisation[153].

pH oscillators have also been coupled with nanoparticle (NP) formation, NP propagation fronts, and surface phenomena (nano-particle based surface coatings: deposition and removal). For example, Lagzi et al. tested gold (Au) and silver (Ag) NPs and observed controlled rhythmic aggregation of NPs using methylene-glycol-sulfite-gluconolactone (MGSG) oscillator having a pH range from 6.8 - 9[161].

In another approach to achieve spatial control in structures is based on Alan Turing's theoretical concept of activator-inhibitor reaction-diffusion to obtain spatiotemporal structures[162]. These are called Turing structures in which an inhibitor's diffusion coefficient should be higher than the activator's diffusion coefficients to achieve activation locally and inhibition laterally in the interfacial polymerisation. Tan et al., developed a scheme, as shown in **Figure 1.17**[163], based on reaction of Schotten-Baumann, which is an irreversible and interfacial polymerisation of two monomers (multifunctional) at the interface location of two-phase heterogeneous system of liquids,[164,165] and by achieving a diffusion-driven instability and generated nanoscale Turing structures (spotted and striped) using an activator piperazine (PZ) and an inhibitor trimesoyl chloride (TMC). With the contact of the aqueous solution of activator and organic solution of an inhibitor, the reaction starts at the porous surface of support polysulfone (PSU). When some amount of PVA macromolecule is added to the aqueous phase, solution viscosity increases and the diffusion coefficients of the activator decreases. After the diffusion-driven instability was formed, the Turing structures were made[166].

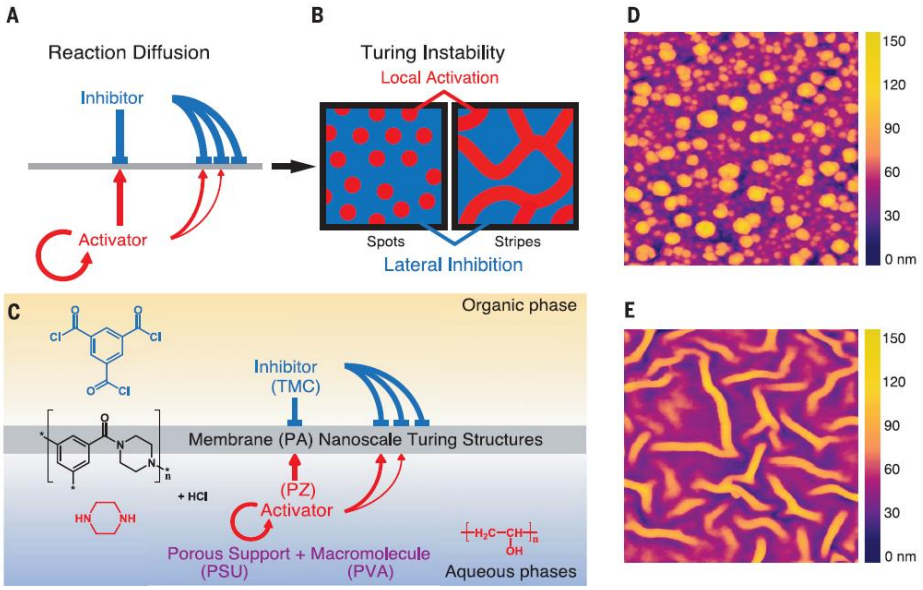


***Figure 1.17 Turing Patterns*** *(A) Representation of activator and inhibitor in a process of reaction-diffusion. Two competitive kinetic pathways red (activator) and blue (inhibitor) define Turing structures. (B) Turing structures are mostly in the form of spots or stripes and are spatially formed by activation (locally) and inhibition (laterally). (C) An illustration of interfacial polymerisation for Turing structures. Top; organic phase dissolving inhibitor (TMC), Bottom; aqueous phase dissolving an activator (PZ) and PVA the macromolecule. PSU is the porous support for the membrane (PA) with a Turing system. (D and E) Bright orange regions relate to the nanoscale Turing-type structures. Topographic images of AFM for the membranes of PA (Turing-structured). Reproduced from* [163]*, Copyright © 2018 American Association for the Advancement of Science.*

There are only a few enzyme-catalysed reactions that exhibit feedback behaviours in vitro[167–169]. However, due to its widespread occurrence in nature, one example that has been investigated widely is the urea-urease reaction. In addition, the urea-urease enzyme-catalysed reaction is a good candidate for biocompatible material applications.

### 1.6.1 Urea-Urease Reaction

The enzyme urease hydrolyses urea to give ammonia and carbon dioxide as given in the following equation:

$$CO(NH_2)_2 + H_2O \xrightarrow{urease} 2NH_3 + CO_2 \qquad (1.8)$$

***Equation 1.8*** *Urease hydrolyses urea to give ammonia and carbon dioxide.*

This reaction has applications in many biological systems such as bacteria in the stomach (*H. Pylori* and *P. Mirabilis*) use urease to hydrolyse urea in order to give ammonia which raises the pH and hence save it from the acidic environment.

#### *1.6.1.1 Reaction Mechanism*

Enzyme urease is Ni-containing metalloenzyme with a high molecular weight (typically ~ 550 kDa). The structure of the urease varies depending on the origin from which it is isolated, but the active site usually includes a pair of nickel atoms ($Ni_1$ and $Ni_2$), one carbamylated lysine, one aspartate residue, and four histidines. Furthermore, a hydroxide ion links the two Ni atoms, which together with three additional terminal water molecules form a tetrahedral structure, H-bonded water cluster in the active site[170,171].

The urease catalysed urea hydrolysis has been an interesting question and subject of debate[172,173],however, from the urease inhibition studies there seems to be an agreement[174–177]. Urea is thought to bind to the first nickel atom ($Ni_1$) via the carbonyl oxygen by replacing water in the active site (Figure 18 A), which increases the electrophilicity of the urea carbon and enhances its susceptibility to nucleophilic attack (Figure 18 B). The urea then attaches to the second nickel atom ($Ni_2$) using either of its amino nitrogen atoms and forms a bidentate bond with the urease (**Figure 1.18** C), which eventually aids the nucleophilic attack of the water on the carbonyl carbon. Ultimately, a tetrahedral intermediate is then generated (**Figure 1.18** D), from which $NH_3$ and carbamate are released (**Figure 1.18** E)[178].

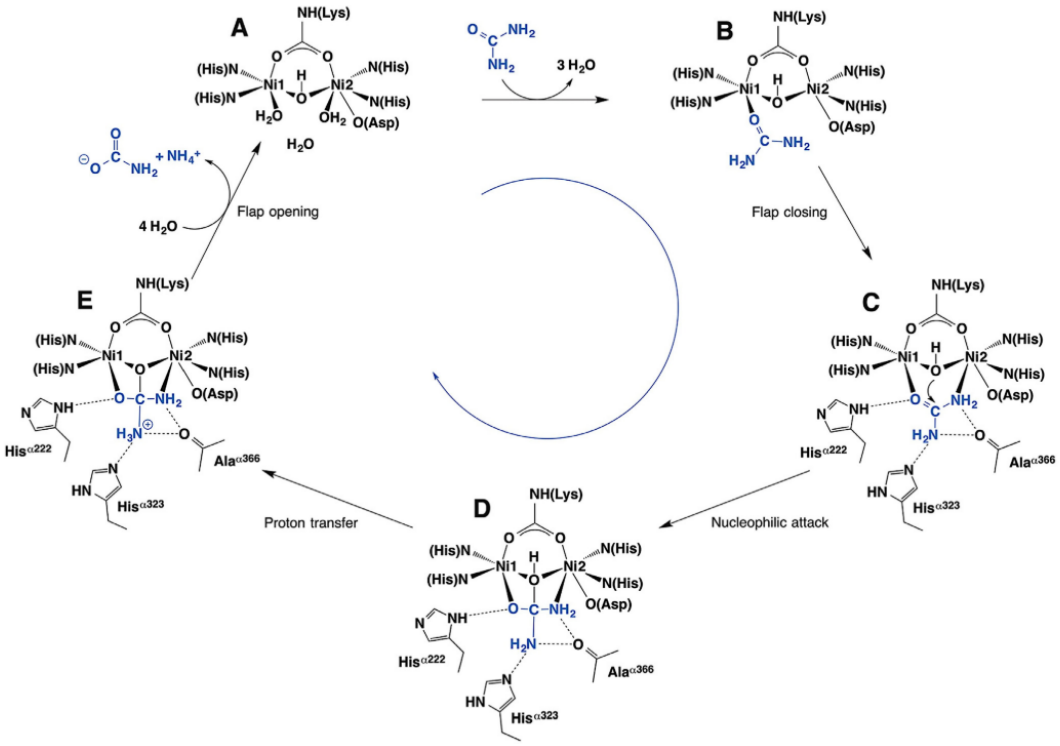


***Figure 1.18 Catalytic reaction mechanism of urease**, taken from[178], Copyright ©2018 Production and hosting by Elsevier B.V.*

Furthermore, as discussed above, the urease catalysed urea hydrolysis (urea-urease reaction) follows the Michaelis-Menten type kinetic model[170,179]:

$$EH + U \rightleftharpoons EHU$$

$$EHU \rightleftharpoons P + EH \qquad (1.9)$$

***Equation 1.9** Mechanism of urease catalysed urea hydrolysis reaction.*

Here EH is the active protonated form of the enzyme, U is the urea substrate, EHU is the enzyme-substrate complex and P is products ($2NH_3$ and $CO_2$). By applying the steady-state approximation to EHU and using $E_0 = E + EHU$, wherein $E_0$ = the total enzyme concentration, we obtain the Michaelis-Menten expression for the velocity, where $V_{max}$ is the maximum velocity and $K_M$ is the Michaelis constant:

$$V = \frac{V_{max}[U]}{[U]+K_M} \qquad (1.10)$$

***Equation 1.10** Michaelis-Menten rate expression for enzyme kinetics, as applied to the urea-urea reaction.*

The hydrolysis of urea is significantly increased by the presence of the enzyme due to its high urease activity and the stability intrinsic to urea. The reaction rate of urea hydrolysis in the presence of the enzyme is $10^{14}$ fold higher when compared to the non-catalysed system[180].Urease activity is related closely to pH. The majority of ureases have a Michaelis constant ($K_M$) in the range of 1-4 mM, which indicates the substrate concentration where the reaction rate attains half of the maximum rate ($V_{max}$) for the reaction[180–182]. Notably, the $K_M$ values show little fluctuations with changes in pH[180–182]. However, on the other hand, the $V_{max}$ in itself, and subsequently the turnover rate ($k_{cat}$), which is a measure of the amount of substrate molecules transformed into a product per enzyme in a given unit of time at complete saturation, is greatly impacted by the pH. To articulate this rate, reference is made to Appendix 7.1[183].

$$V = \frac{V_{\max} U}{\left(K_M + U\left(1 + \frac{U}{K_S}\right)\right)\left(1 + \frac{[NH_4^+]}{K_P}\right)\left(1 + \frac{K_{es2}}{H^+} + \frac{H^+}{K_{es1}}\right)} \qquad (1.11)$$

***Equation 1.11*** *Rate expression for urease catalysed urea hydrolysis reaction.*

Where, the $V_{max}$ is the maximum rate, $K_M$ is the Michaelis constant, $U$ is the substrate urea concentration, and $K_{es2}$ and $K_{es1}$ are protonation equilibria of the substrate-enzyme complex. Additionally, substrate and product inhibition terms are also included here. The equilibrium constant for uncompetitive substrate inhibition is given by $K_S$ and equilibrium constant for non-competitive product inhibition is denoted by $K_p$. **Table 1.4** gives the typical values of enzyme constants for urea-urease reaction.

***Table 1.4*** *Enzyme constants for the rate of hydrolysis of urea by urease, from*[179]

| **Enzyme constants** | **$K_M$** | **$K_{es1}$** | **$K_{es2}$** | **$K_S$** | **$K_P$** |
|---|---|---|---|---|---|
| | $3 \times 10^{-3}$ M | $5 \times 10^{-6}$ M | $2 \times 10^{-9}$ M | 3 | 0.002 |

This correlation, in which fluctuations in pH modify the conformation of the protein binding site, is reflected in the rate at which the enzyme is able to catalyze the reaction, which ultimately leads to the bell-shaped rate-pH curve (characteristic of feedback), and shown in **Figure 1.19.** The urease-mediated transformation of urea into a weak

base exhibits a peak rate at pH 7[170]. As a result, when the initial pH is lowered by the addition of acid, the reaction subsequently accelerates as it proceeds.

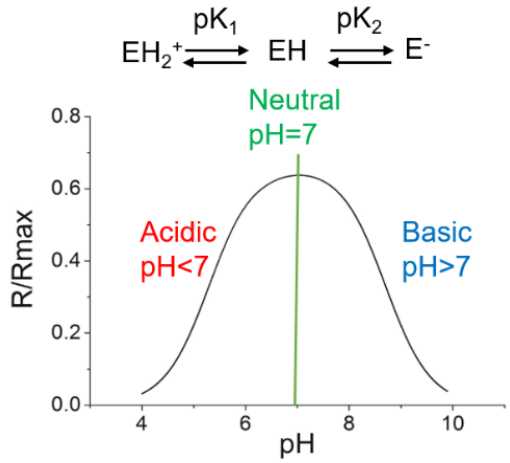


***Figure 1.19 A general representation of rate dependence with respect to pH**. Enzyme-catalysed rate R relative to maximum rate Rmax as a function of pH. Reproduced from [184,185], Copyright © 2021 The Authors. Published by American Chemical Society.*

### 1.6.2 pH Induction/Clock Reaction of Urea-Urease

The urease catalysed urea hydrolysis reaction results in the production of ammonia and carbon dioxide, and hence results in the increase in the pH (due to the formation of hydroxide ions associated with $NH_3$).

$$NH_3 + H_2O \rightleftharpoons NH_4^+ + OH^- \qquad (1.12)$$

***Equation 1.12** Ammonia/ammonium equilibria derived from urea-urease reaction.*

At a low initial pH (pH≤4), there is a slow increase in pH, followed by a rapid/sharp increase in pH (pH~7) and a further rather slow increase to a high pH (pH~9). This increase in pH gives a sigmoidal shaped pH-time profile and is generally referred to as a 'pH clock', where pH changes from a low to high state after a lag time. Clock reactions have two characteristic features: first, the delay time between the mixing of the reactive components and the start of the reaction, also known as the induction time (or clock time), and second, the maximum reaction rate observed at a non-zero time.

This dependence of enzyme urease on pH gives autocatalytic characteristics and the feedback-driven behaviour has shown to exhibit complex behaviours (such as oscillations and bistability).

Taylor and co-workers used a theoretical model derived from previous work in which they identified a suitable range of parameters for which oscillatory behaviour and bistability could be demonstrated, in addition to clock behaviour, in a compartmentalised urease system which is immersed in a substrate solution (urea) or in an open reactor[186]. In addition, pH clocks have also been observed experimentally for specific conditions of the enzyme urease, acids and the substrate urea, e.g. in batch and flow reactors[187], alginate beads[188], and hydrogel beads[189]. **Figure 1.20** gives a typical urea-urease clock behaviour in a closed reactor (A)[190], and the effect of changing initial concentration of urea, urease, and acid on the clock/induction time (B,C, and D)[191].

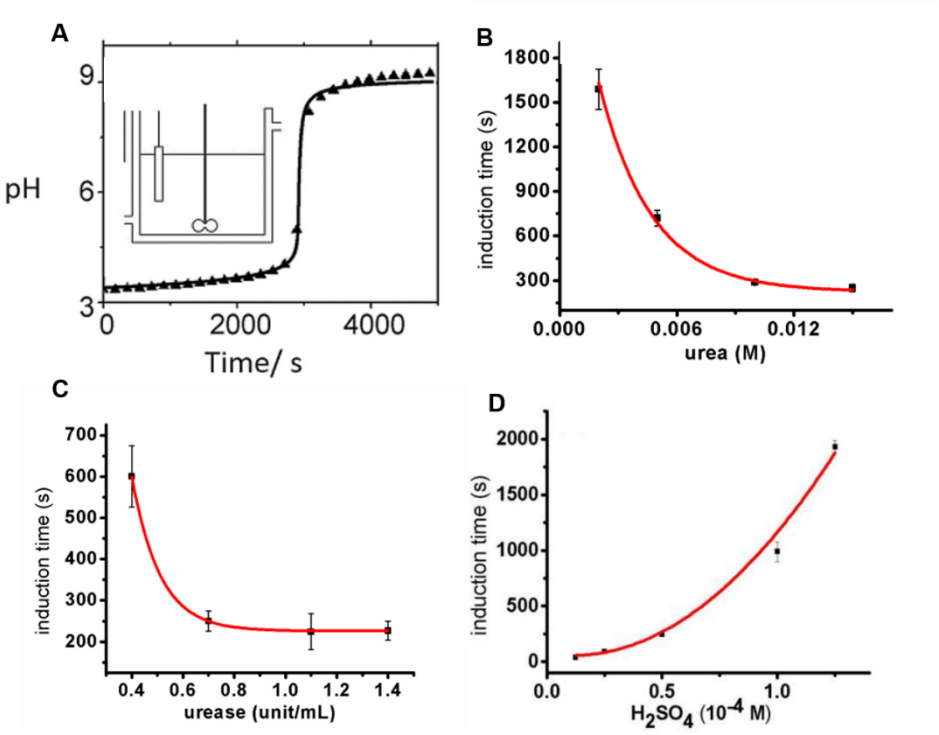


***Figure 1.20 Clock behaviour in urea-urease reaction**. A) Change in pH in a closed reactor for the urea-urease reaction[190], Copyright © 2018 Wiley-VCH Verlag GmbH & Co. KGaA, Weinheim. Clock/Induction time changes as a function of B) urea concentration, C) urease concentration, and D) sulphuric acid concentration [191] Copyright © 2012 The Authors, University of Leeds, School of Chemistry.*

Hu et al. have recognised that the urea-urease reaction rate-pH curve is used to set-up the feedback driven process.[187] After thousands of seconds, a pH switch was observed from acidic to basic (low to high) inside a closed reactor. Hysteresis and bistability was observed when the reaction was performed in open conditions (flow reactor). The reaction was used to understand and develop pH-dependent feedback loop with the production of the base.

Urea-urease reaction with intrinsic nonlinear pH ramp has also been used to analyze changes to proteins. Chang et al. exhibited an analytical method to observe the modifications in protein structure with pH alterations caused by the autocatalytic urea-urease reaction[192]. The urea-urease clock reaction caused pH switch (acidic to basic) which triggered protein refolding and hence was examined in real time using mass spectroscopy.

### 1.6.3 Coupling Urea-Urease Reaction with pH-Responsive Materials

The urea-urea reaction system, which has been recognised for years and researched mainly for applications in analytical chemistry[193], has now received attention for its pH-dependent properties by coupling the reaction with pH-sensitive materials[194,195]. In this regards, in the search for autonomous materials, Bon and co-workers showed the fabrication of fibres (as shown in **Figure 1.21**[196]) and beads (soft hydrogel objects) using microfluidic technology[196]. These hydrogel objects exhibited independently programmed time delay in their behaviours to a common environmental stimulus. The urea-urease reaction was incorporated in the system to introduce an environment of self-changing pH which triggers the gel fibre disintegration or a change in colour in the case of gel beads. The spatio-temporal responses of these hydrogels have significant importance in creating biologically inspired materials.

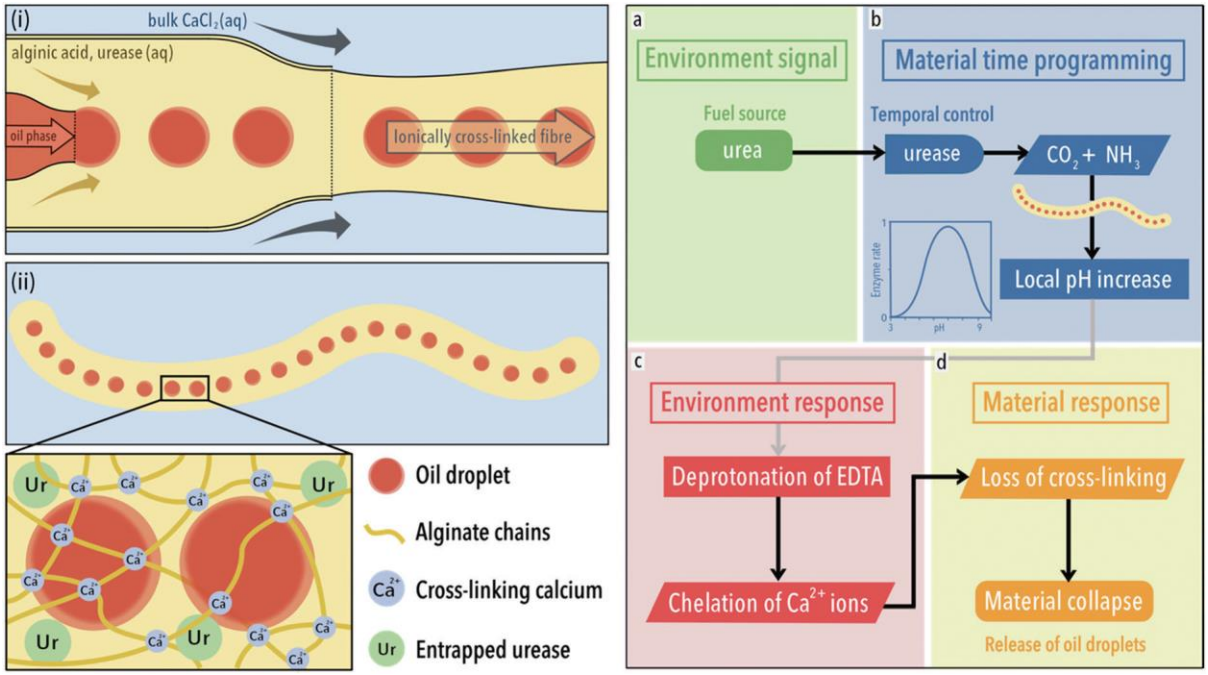


***Figure 1.21 Fabrication and response of hydrogel fibres using microfluidic synthesis.*** *(i) Formation of fibres of sodium alginate with calcium ion cross-linking. A fluid stream, containing 1 wt% sodium alginate solution and oil droplets, interacted with a bulk solution of 0.1 mol $dm^{-3}$ of calcium ions and resulted in the formation of the cross-linked (with calcium) gel fibre. (ii), (iii) The gel structure containing oil droplets, enzyme urease, and cross-linking calcium ions. (a) Exhibiting programmed response, the gel fibre network transforms urea to ammonia due to the incorporation of urease in its structural network. (b) A local increase in the pH occurs after a defined period of time. (c) (d) After the local increase of pH in fibre, the partially protonated EDTA, found in the low pH bulk environment, gets deprotonated and chelated $Ca^{2+}$ ions. This follows in a destruction of cross-linking and the freeing of oil droplets eventually leading to material collapse. Taken from [196], Copyright © The Royal Society of Chemistry 2017.*

Furthermore, Bon and co-workers demonstrated that these soft hydrogels can be functionalized and programmed to react non-uniformly across their entire structures upon the exposure to an external fuel source (urea). As shown in Figure 1.22[197], they created triggerable active zones at specific sites of a soft hydrogel object by non-uniform dispersal of the enzymes (urease). A local increase in the pH occurs at these active zones with the fuel supply (urea) due to the formation of ammonia and causes the changes in the structure of the hydrogel [197].

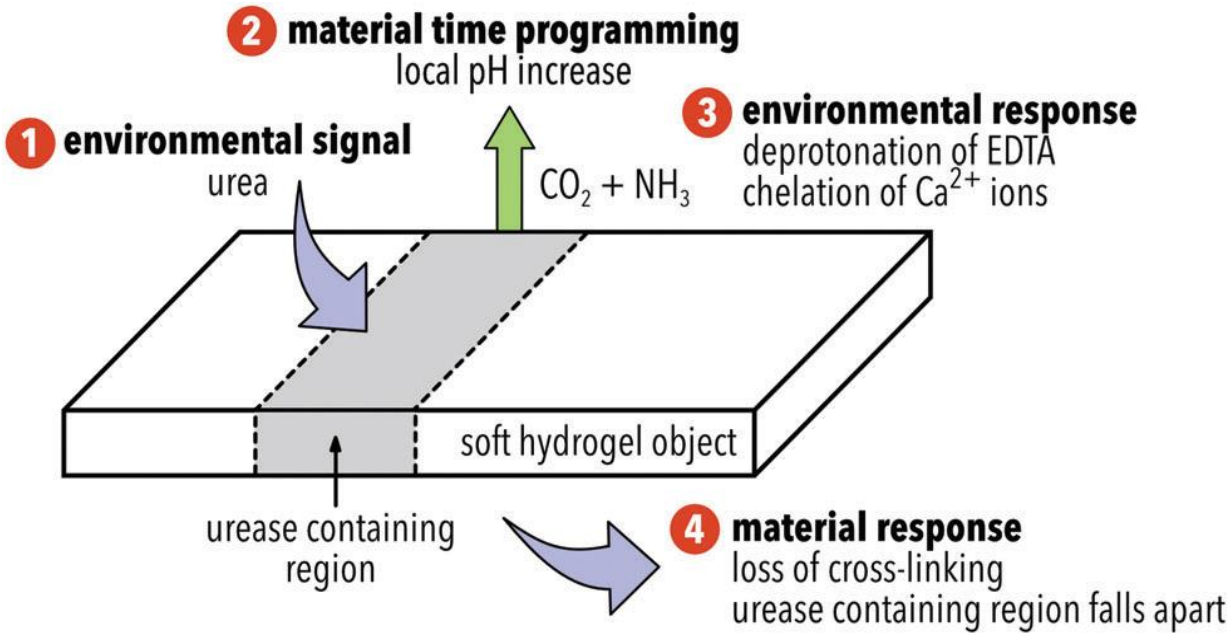


***Figure 1.22 An illustration depicting the response of hydrogel material (ionically cross-linked)**. (1) Active zone of the semi-permeable soft material that transform urea (a fuel source) to ammonia due to the distribution of urease in selectively active zones of its structure (2) after a determined time period, material raises the pH at the sites of urea region (3) Partially protonated ethylenediaminetetraacetic acid (EDTA) in the low pH (3.50) surrounding environment becomes locally deprotonated with the increase of pH due to urea and results in the chelation of calcium ions from the hydrogel (4) With the loss of ionic cross-linking, disruption and of the structure occrs at the sites of the urease distribution regions. Taken from [197], Copyright © The Royal Society of Chemistry 2017.*

Jee et al. have introduced a technique under mild environments for polymerisation fronts and gelation for the applications of gelation-on-demand[198]. They used the product of an autocatalytic reaction (aqueous phase) to trigger the gelation of thiol-acrylate (hydrogel) instead of changing the intrinsic rate in polymerisation. To make an aqueous phase (one-pot), they used monomers of ethoxylated trimethylolpropane tri (3-mercaptopropionate) (Thiocure ETTMP 1300) and poly(ethylene glycol) diacrylate (PEGDA 700), and the basic/high pH state of urea-urease system was employed to start base-catalysed polymerisation reaction. Taylor and co-workers developed a scheme that enables a system inherent pH switch of urea-urease hydrolysis reaction to control gelation and degradation of polyethylene glycol diacrylate (PEGDA) after an induction time. Gelation was monitored and regulated by the initial concentrations and the reaction was set locally by a base, which brings about polymerisation and turned the reaction mixture to a gel. **Figure 1.23**[198] illustrates the reaction and polymerisation of PEGDA.

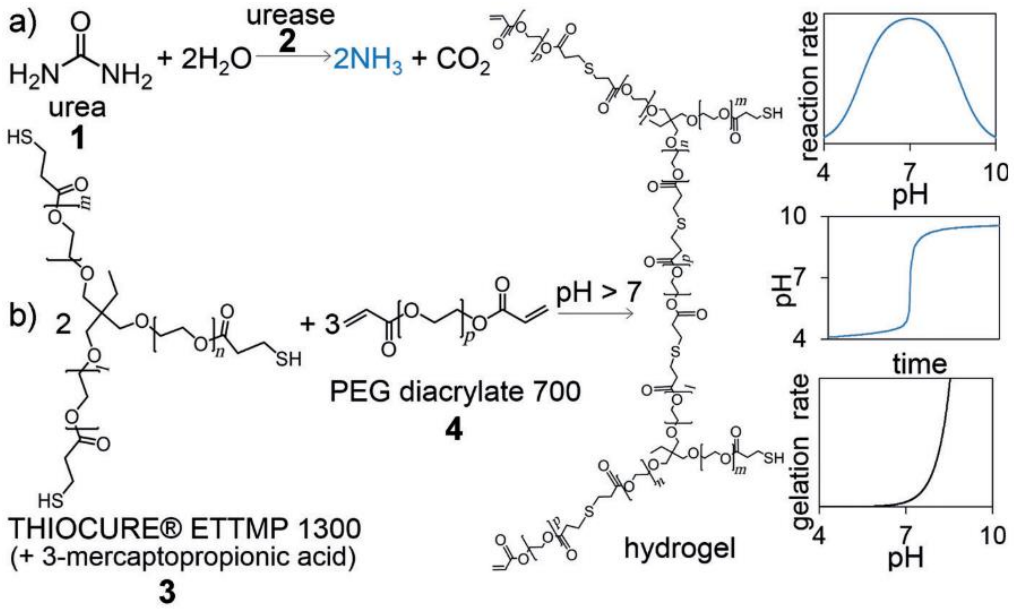


***Figure 1.23 Thiol acrylate gelation via urea-urease reaction****. a) (1,2) Urea-urease reaction, b) (3,4) Base catalysed PEG diacrylate polymerisation. Graphs indicate the reaction rate of the urea-urease system, pH vs time plot, and the dependency of gelation on pH. Taken from* [198]*, Copyright © 2016 The Authors. Published by Wiley-VCH VerlagGmbH &Co. KGaA, Weinheim.*

Urease has also been encapsulated in nano and microvesicles and the synchronisation of activity observed across a population[199]. In addition, urease was encapsulated in polymerosomes, for feedback control of the substrate[200]. Recently, the reaction was performed in pH sensitive vesicles for the observation of self-division of vesicles[201]. One disadvantage in these systems is the fast permeation of ammonia through the vesicle wall which leads to an increase in pH in the external solution, and limits the potential for more complex behaviour. However, such studies have demonstrated many important bioinspired features are possible with compartmentalisation of urease.

## 1.7 Overview and Aims of Research

A number of cellular organisms, such as yeast, bacteria and slime moulds, exhibit dynamic behaviour, in particular switching and rhythms that are controlled by feedback in enzyme-catalysed reactions. The mechanisms of these processes are well understood, and recently there has been a focus on generating similar reactions in synthetic biocatalytic systems to establish bioinspired analogues for applications in materials and medicine. In this thesis, we bring together these scientifically highly interesting disciplines and work towards an ultimate goal of combining state-of-the-art

microfluidic technology with nonlinear enzyme kinetics to generate new bionspired systems for applications.

Droplet emulsion and synthetic vesicle systems are indeed widely used as micro- or nanoreactors for the production of materials such as hydrogels and ceramic particles and as test platforms for biomimetic cell-like behaviour. However, constructing a system from a bottom-up perspective through a monodisperse compartmentalisation of the feedback-driven enzymatic reaction (urea-urease) in a microreactor and studying the associated behaviour will allow us to better control the system dynamics and is a step towards using this technology for material and therapeutic applications as well as to understand some insight into the complex cellular behaviours. The key research aims are further divided into four sections, as given below:

(1) Taking advantage from pressure driven droplet microfluidics, to develop a system of enzyme-encapsulated (urea-urease) double emulsion (W/O/W) droplets to obtain a localised pH pulse, with a controllable induction time to program material properties, such as formation of inorganic particles. This is addressed in chapter2.

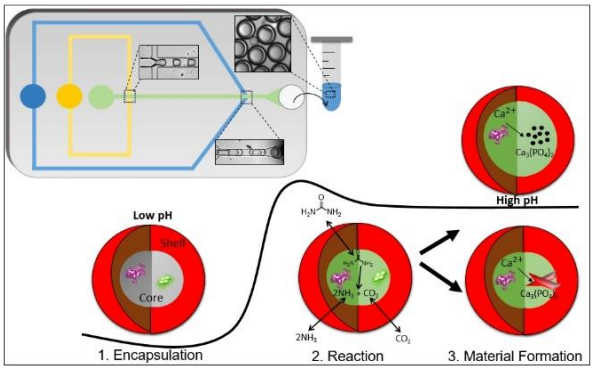


***Figure 1.24 Microfluidic production of W/O/W double emulsion droplets*** *with encapsulated enzyme. The pH time profile and material formation are controlled by both the reaction and droplet properties.*

(2) Computational investigation of the nonlinear reaction chemistry within the designed platform of the W/O/W-based reactor. A radially distributed reaction-diffusion model is presented for a layered sphere mimicking a double emulsion. Here we have combined the experiments with simulations (shell-core model) to demonstrate the influence of urea transport triggered by the shell, the core and

the external solution surrounding the cell model (μ-reactor) on the induction time/period ($T_{ind}$) of urea-urease reaction. This is given in chapter 3.

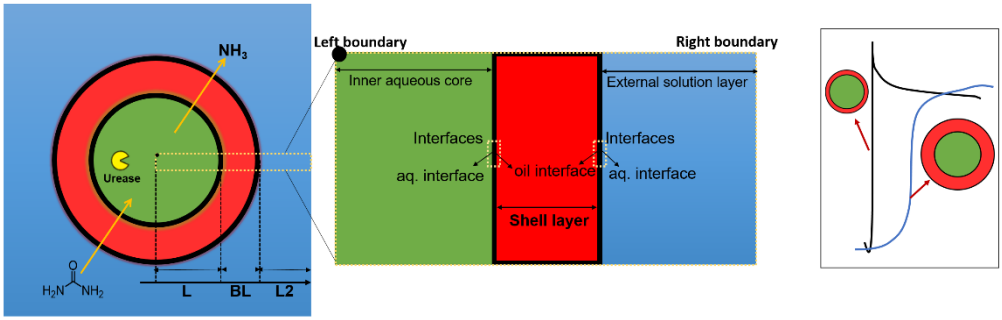


***Figure 1.25 The shell-core model****. Schematic representation of the cross-section of the radially symmetric one-layer sphere (shell-core model) on the right side and predictive behaviours on the left side.*

(3) To build a unique system inspired by the natural reaction-diffusion process observed in quorum sensing of bacteria. The system is based on enzyme-encapsulated microfluidic double emulsion (W/O/W) droplets that serve as microreactors to mimic synthetic cell models. In particular, we will focus on the urease-catalysed hydrolysis of urea (urea-urea reaction, UU), which has a feedback through the production of the base ($NH_3$). This leads to a change from an acidic to a basic pH after an induction time ($T_{ind}$), resulting in an environment with auto-changing pH conditions. The main objective here is to study chemical communication in microfluidic double emulsions. By monitoring the interactions in this system, we hope to determine how variations in substrate concentration and microreactor population size impact chemical communication through the $NH_3$ signal. The findings of this research will highlight the potential of this pH-triggered double emulsion platform for the development of tunable and on-demand communicative behaviours for material applications. This is addressed in chapter 4.

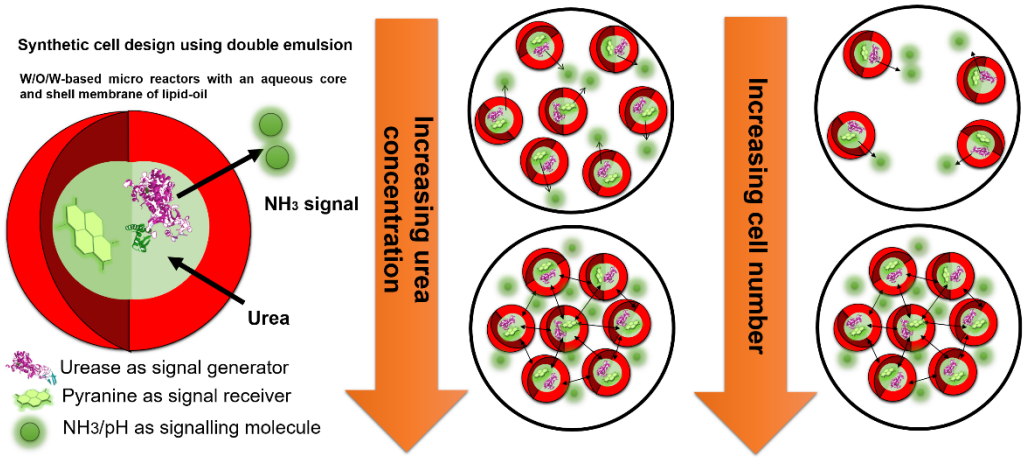


***Figure 1.26 Schematic representation of the proposed chemical communication between W/O/W double emulsions based µ-reactors.*** *The µ-reactors are loaded with urease enzyme that processes urea from the environment to produce ammonia, and gives green fluorescent output. Increasing substrate concentration and the cell (µ-reactor) number, a high amount of signalling molecules is produced ($NH_3$), which triggers population wide response.*

(4) As compartmentalised double emulsion droplet systems are frequently used in both science, for cell models, and industry; they have many potential applications. Here, we explore how to use the microfluidic enzyme immobilisation technique for encapsulated urea-urease emulsions to enable their use in medical testing, biosensors and drug delivery devices. We have used the urea-urease reaction as a potential initiator of supramolecular pH-dependent gelation. These droplets can be employed as templates for the fabrication of structured materials – gels with droplets embedded - and structured gel microparticles with core-shell configurations. We also used the double emulsion platform as a means to study urease inhibition, which has important applications for the prevention of infections caused by ureolytic bacteria. This is addressed in chapter 5.

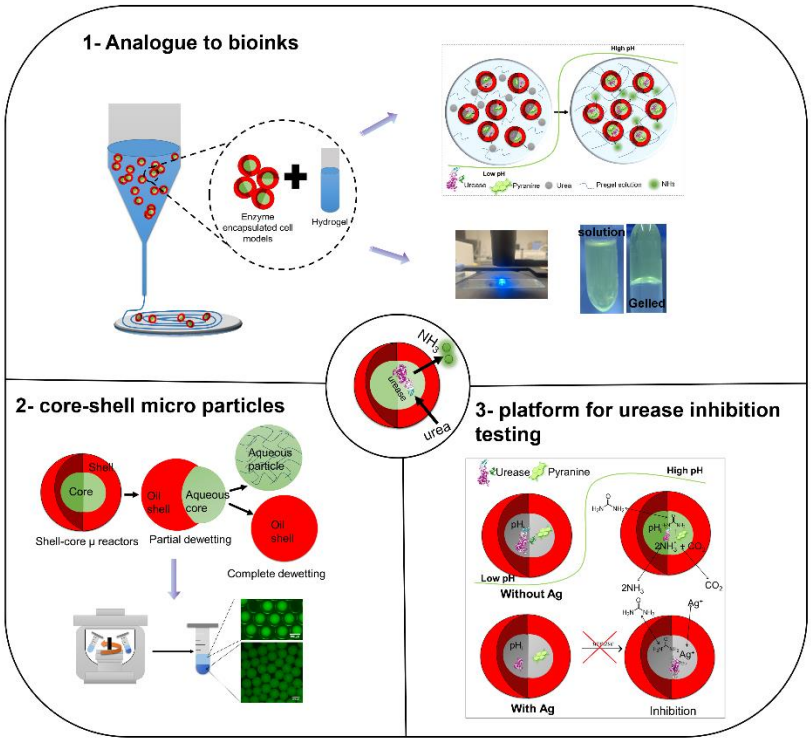


***Figure 1.27 Applications of microfluidic double emulsions****. Schematic illustration of different approaches used in the study to utilise microfluidic enzyme immobilisation technique and platform for material and testing applications*

Through these research objectives, we were able to uncover a system that is more complex than initially expected. This underlying complexity, in terms of the dynamics of the system, resulted from the diffusion mechanism through the surfactant stabilised shell-core membrane and the combination of a urea-urea reaction confined to microfluidic droplets. Nevertheless, by assembling a platform that enables a comprehensive investigation of the parameter space (chapter 2) combined with theoretical modelling (chapter 3), we have acquired not only control over the kinetic results, but also gained a more holistic view of the behaviour of the system in its complete form. This better understanding has allowed us to broaden our scope and extend the practicality of our microfluidic system, e.g. in terms of chemical communication (chapter 4) and potential material applications (chapter 5).

## 1.8 Outline of the Thesis

This thesis is presented in the form of a portfolio consisting of a series of four related papers, all of which contribute to the overall research objectives outlined in section 1.7. The following chapters are stand-alone manuscripts, one of which has already

been published (Chapter 2), while the other chapters are ready for submission and are presented in final paper form. Chapter 2 and the subsequent chapters (3, 4 and 5) form a coherent framework for the entire thesis.

In chapter 2 (published), we developed a system of enzyme-encapsulated (urea-urease) double emulsion (W/O/W) droplets to obtain a localised pH pulse, with a controllable induction time to program material properties. Then, in chapter 3, we performed a computational study of the nonlinear reaction chemistry (urea-urease) within the designed platform of the W/O/W-based reactor and compared it with experimental findings. Chapter 4 focuses on the use of the urea-urea reaction, which is confined to double emulsions, to study chemical communication. In chapter 5, we aimed to use the double emulsion template for potential biomedical and therapeutic applications using the autocatalytic urea-urease reaction.

The experimental methods, including on-chip W/O/W double emulsion generation, microfluidic reservoir solution preparation, reaction observation, imaging and analysis are described first in Chapter 2 and then in Chapters 3, 4 and 5, as they are separate works (presented as stand-alone papers). However, the solution concentrations for the preparation of the microfluidic reservoir solutions, i.e. the inner solution (IS), the outer solution (OS) and the external solution (ES), may vary slightly in the different chapters/papers. In chapters 2, 3 and 4, mostly exactly the same components are used in IS, OS and ES, with different concentrations, while in chapter 5 additional components are added to IS, OS and ES. For example, the addition of different acids (acetic acid and HCl), $AgNO_3$ and hydrogel solutions.

# 2 A Microfluidic Double Emulsion Platform for Spatiotemporal Control of pH and Particle Synthesis

*This chapter has been published:*

***M. Rana, R. Ahmad and A. F. Taylor, Lab on a Chip, 2023,***

***DOI:10.1039/D3LC00711A.***

## Contents:

## 2.1 Introduction

Droplet emulsion and synthetic vesicle systems have been widely employed as bioinspired micro- or nanoreactors for production of materials such as hydrogels, protein crystals and ceramic particles[126,202,203,204,205,206]. They also provide a test platform for biomimetic cell-like behaviour, including motion, division and communication[207,208,209,210,201,64,211,212,213,214]. One of the most important parameters for controlling chemical processes in cells or droplets is the pH[215,216]. For initiating particle synthesis, changes in pH have been mainly achieved by passive diffusion of acidic or basic species into the droplets, for example ammonia and tetramethylethylenediamine (TEMDA)[217,218]. With larger molecules, these processes can be slow and result in an internal gradient in pH. Concentrated solutions result in faster transport but also potential for droplet-particle deformation[218]. Changes in pH have also been achieved under relatively mild conditions in vesicles with encapsulated enzymes[219,220]. Generally these reactions are accompanied by changes in the pH in the external solution as a result of the fast transport of weak acids or bases out of the compartment, requiring additional methods for internal regulation of the pH[199]. Other methods of pH control in micro-reactors involve external intervention, such as electrochemical stimulation[221,222].

Herein, we controlled the pH-time profile in microdroplets by exploitation of the properties of a water-oil-water (W/O/W) double emulsion with the enzyme urease encapsulated in the aqueous core. This enzyme catalyses the hydrolysis of urea to form ammonia and carbon dioxide and is widely found in plant seeds and cellular systems such as bacteria[223]. The reaction can display feedback driven by base production and a switch from acid to base with pH ~ 9 after an induction period (or clock time)[187]. Urease has been compartmentalised in liposomes, polymerosomes, hydrogels etc. and the reaction triggered by addition of urea for bioinspired material applications[224,225,226,227,228,229,230,231]. Encapsulating urease in W/O/W double emulsions resulted in a localised pulse in ammonia with a tuneable steady state in pH, balanced by the rate of diffusion of urea in and ammonia out of the droplet. W/O/W emulsions are frequently used as templates for liposome formation by removal of the oil[232,233,234], however the oil shell can be used to control the diffusion time of neutral species and hence the pH change, in contrast to earlier work with phospholipid membranes or polymer shells.

The double emulsion droplets were prepared using microfluidics for easy manipulation of droplet size and the shell to core ratio[233,235,236]. Droplet-based microfluidics provides a method for encapsulation of species resulting in higher encapsulation efficiencies compared to other methods with the added advantages of monodispersity, reproducibility, and high throughput[237,150]. Microdroplets can give better control over conditions for synthesis of particles and crystals compared to bulk solutions[238,239] and the reactive double emulsions with urease can be used to fine-tune the pH for material applications. The reaction is fast compared to internal mixing thus ensuring a uniform pH change in 100 µm droplets and the pH-time profile can be manipulated by parameters such as oil shell thickness.

Urease plays an important role in biomineralisation, driving calcium carbonate formation both in natural environments and for engineering applications[240,241,242,243]. Calcium phosphate particles have important uses in the medical and food industry[244,245], and the urease reaction may provide a benign route for particle formation, however in the presence of phosphates typically a mixture of calcium phosphate and calcite are formed[244,246]. Here, the urease double emulsion droplets were used for selection of either brushite microplatelets which form at pH ~ 6, or particles of hydroxyapatite at higher pH ~7, depending on oil shell to core ratio. No calcite was obtained as the steady state pH was maintained below 8. Thus the pH-pulse in the double emulsions was tuned for the selection of one polymorph when typically multiple are formed in bulk solution. This general approach may be used with other acid or base producing enzyme reactions to provide spatiotemporal control of pH for material formation under mild conditions.

## 2.2 Experimental Section

### 2.2.1 Chemicals

The following stock solutions were prepared in distilled, deionized water: urea (66612, Sigma) [urea] = 0.6 M, acetic acid (100% glacial acetic acid, Sigma-Aldrich) [$CH_3COOH$] = 0.05 M, urease (type III Jack bean U1500-20KU, typically 25920 units/g solid, Sigma-Aldrich) [urease] = 350 Units/mL (U/mL), 8-hydroxypyrene-1,3,6-trisulfonic acid (pyranine, cat no. L11252.14, Alfa Aesar) [pyr] = 0.2 mM, glucose (G5400, D-(+)-Glucose, minimum 99% GC, Sigma-Aldrich) [Glucose] = 1 M, sucrose ($\geq 99.5\%$ GC, Sigma-Aldrich) [Sucrose] = 1 M, Pluronic F-127 (Sigma-Aldrich) [PF-

127] = 2%, glycerol (87%, Sigma-Aldrich) [glycerol] = 20%, polyvinylalcohol (P8136, 87-90% hydrolysed, avg. M.W. 30,000-70,000, Sigma-Aldrich) [PVA] = 1%, calcium chloride (CAS. 10035-04-8, Sigma-Aldrich) [$CaCl_2$. $2H_2O$] = 0.3 M. The 1-Palmitoyl-2-oleoyl-sn-glycero-3-phosphocholine (P516, Anatrace) [POPC] = 6.5 mM, was prepared in mineral oil (light oil, M5904, density 0.84 g/mL at 25℃, Sigma-Aldrich), sorbitan monooleate (Span-80, 85548, viscosity 1000-2000 mPa.s at 20 ℃), nile red (Sigma-Aldrich).

Urease type III (25920 U/g) solution was prepared by addition of the powder to water to give a certain U/mL. To determine the concentration of enzyme, urease was fluorescently labelled using AnaTag™ HiLyte™ Fluor 488 Microscale Protein Labeling Kit (see supplementary information for further information). A 350 U/mL stock solution contained 1.04 ± 0.02 µM enzyme. The concentration of free orthophosphate in urease type III (25920 U/g) solution was determined using a phosphate assay kit (MAK308, Sigma-Aldrich). A solution of 0.02 U/mL had total concentration of $[phosphate]_T$ = 32 ± 4 µM.

### 2.2.2 Preparation of Microfluidic Reservoir Solutions

The lipid-oil solution (middle flow reservoir in the microchannel, MF) contained 6.5 mM POPC dissolved by sonication in mineral oil (MO) and 2% Span-80 for three hours at room temperature using an ultrasonic bath (FB15051, Fisherbrand). Phospholipids enhance W/O/W emulsion stability[247]. The inner solution (IS) reservoir contained sucrose (0.2 M), pyranine (50 µM), urease (50 U/ mL), acetic acid (1 mM), and pluronic F-127 (0.28%), unless otherwise stated. Calcium chloride (0.1 M and 0.15 M) was also added to the IS for the experiments involving mineral precipitation. The outer solution (OS) reservoir contained glucose (0.2 M), glycerol (20%), pluronic F-127 (0.28%), acetic acid (1 mM). Sucrose and glucose were added to the IS, OS and external solution (next section) to reduce osmotic imbalance during the enzyme reaction. Pluronic F-127 was used to act as a surfactant to avoid coalescence and to increase the stability of the double emulsions[248]. Glycerol was incorporated in the OS to increase the viscosity of the aqueous phase to enhance the shearing of the oil by the continuous phase. To visualise the enzyme in the droplets urease/pyranine in the inner solution were replaced with HiLyte™ Fluor 488 labelled-urease from a stock solution

of 350 U/ mL (1.04 ± 0.02 µM). The enzyme-dye was diluted to 50 U/ mL (0.14 µM) in the inner solution and loaded into the emulsion droplets.

### 2.2.3 On-chip Generation of W/O/W Double Emulsions

We used a flow-focusing device with two droplet formation junctions to synthesize the double emulsion (see section 7.2 of Appendix and **Figure 7.1**, **Figure 7.2**, and **Figure 7.3**). The design of the PDMS-microfluidic device was based on the work of Teh et al[233]. The polydimethylsiloxane (PDMS) microchannel was fabricated using conventional soft lithography[249,250](**Figure 7.1**). The first junction of the channel has a hydrophobic surface to allow the formation of W/O (water in oil) droplet while the second junction is hydrophilic (PVA coated, **Figure 7.2**) to preferentially make O/W (oil in water) droplet, thus forming W/O/W double emulsions at the end of the microfluidic device[251,252]. A pressure-driven pump (OB1 MK3+, Elveflow, Paris, France) was used to transport both the aqueous inner and outer solutions (IS and OS) and the lipid-oil middle fluid (MF) at a persistent flow and a 2 mL Eppendorf tube was used as a collection vial for the double emulsions (**Figure 7.3**).

The channel geometry and inlet flow rates of the solutions can be changed to control the size of the emulsion droplets; we manipulated the pressure flows of the IS, MF, and OS to obtain the desired size and the shell/core ratio. In a typical experiment, W/O droplets at the first junction were obtained with the IS at $P_{IS}$ = 36 mbar and the MF at $P_{MF}$ = 69 mbar, or, the flow pressures were varied with a fixed ratio of ($P_{MF}/P_{IS}$)~2, and the double emulsions were obtained by adding OS at $P_{OS}$ = 19 mbar. Larger droplets were obtained by varying the pressures and changing the ratio $P_{MF}/P_{IS}$, and thicker oil shells were obtained by increasing $P_{MF}/P_{IS}$.

### 2.2.4 Reaction Observation, Imaging, and Analysis

For the reaction, the double emulsions were mixed with an equal volume of an external solution (ES) containing acetic acid (1 or 2 mM), glucose (0.2 M), and urea (0.04 – 0.07 M) and 1 µL of mixed solution was immediately injected into a reaction chamber. We used either CoverWell™ perfusion chambers (800 – 900 µm diameter and 1200 µm depth) or assembled our own chambers from double-sided tape (source) with a circular hole (1000 µm diameter x 200 µm depth), and sealed with a coverslip (section 7.2.4 of Appendix and **Figure 7.4**).

We used pyranine as a fluoroprobe to observe the increase in pH due to the formation of ammonia inside the microreactors. For determination of the apparent pH in the droplets, a calibration curve of pH vs ratio of fluorescence intensities F458/F405 was used (**Figure 7.5**). Ratiometric measurements of fluorescence intensity were obtained with a Leica TCS SP8 confocal microscope using the 405 nm and 458 nm laser consequetively for excitation and the emission wavelength range of 485 – 555 nm. The reaction was also monitored using an inverted fluorescence microscope (Etaluma LS560). In the microscopic experiments, care was taken to minimise the effects of photobleaching of pyranine. The protocol involved taking images at intervals to avoid prolonged exposure to the excitation source. Pyranine bleaching was generally observed during longer imaging sessions (more than one hour). The reactions studied were designed to be completed within a time frame of approximately 15 minutes or less to avoid problems associated with photobleaching of pyranine. For the urease-driven precipitation, the calcium phosphate and calcium carbonate crystals were characterized using a Senterra II Raman confocal microscope (Bruker) with an excitation wavelength of 532 nm, and power of 25 mW (see Appendix 7.2.12).

Analysis of images was achieved with a combination of ImageJ and MATLAB (Version R2020a). MATLAB code was developed to track individual emulsions in the case of droplet motion and the size of the shell and aqueous core were determined from the brightfield images (**Figure 7.6**). The intensity in time was obtained from the average intensity of a droplet in fluorescence images (**Figure 7.6**) and the induction time was determined as the time to maximum rate of change of fluorescence intensity. The apparent area associated with formation of calcium phosphate crystals was determined using ImageJ (see Appendix 7.2.13, **Figure 7.13**).

## 2.3 Results and Discussions

### 2.3.1 Production of Urease-encapsulated W/O/W Double Emulsions

The microfluidic device had three inlets for the inner solution (IS) phase, the lipid-oil (MF) phase, and the outer solution (OS) phase (**Figure 2.1** A). Two successive flow-focusing (droplet formation) junctions were included on the chip. The IS (sucrose, urease, acetic acid, PF127, and pyranine) was sheared with the MF (POPC, mineral oil (MO), and SPAN-80) into monodispersed droplets at the first droplet forming junction to form a single W/O emulsion (**Figure 2.1** B). The single droplets were then

sheared in the second flow-focusing junction with the 'OS' (glucose, glycerol, acetic acid, and PF127), thus resulting in the formation of W/O/W double emulsions (**Figure 2.1** C). The double emulsions were collected from the outlet Eppendorf tube and mixed with external solution (ES) off-chip to initiate the reaction (**Figure 2.1** D).

The distribution of species in the lipid-oil shell and inner aqueous core of the emulsion droplets can be observed in the confocal images shown in **Figure 2.1** E. Nile red (0.01%) was added to the middle fluid to locate and visualize lipids in the oil layer (**Figure 2.1** Ei) and the pH dependent fluoresent probe pyranine was visible in the aqueous core ($l_{ex}$ = 405, $l_{em}$ = 490 – 500 nm, **Figure 2.1** Eii). In separate experiments, the HiLyte™ Fluor 488 labelled-urease of concentration 50 U/mL (0.14 µM) was also observed to be uniformally distributed in the aqueous core of the droplets (lex = 488, lem = **Figure 2.1** Eiii). Both pyranine and the enzyme were confined to the aqueous core, as determined by superposition of the fluorescent and brightfield images.

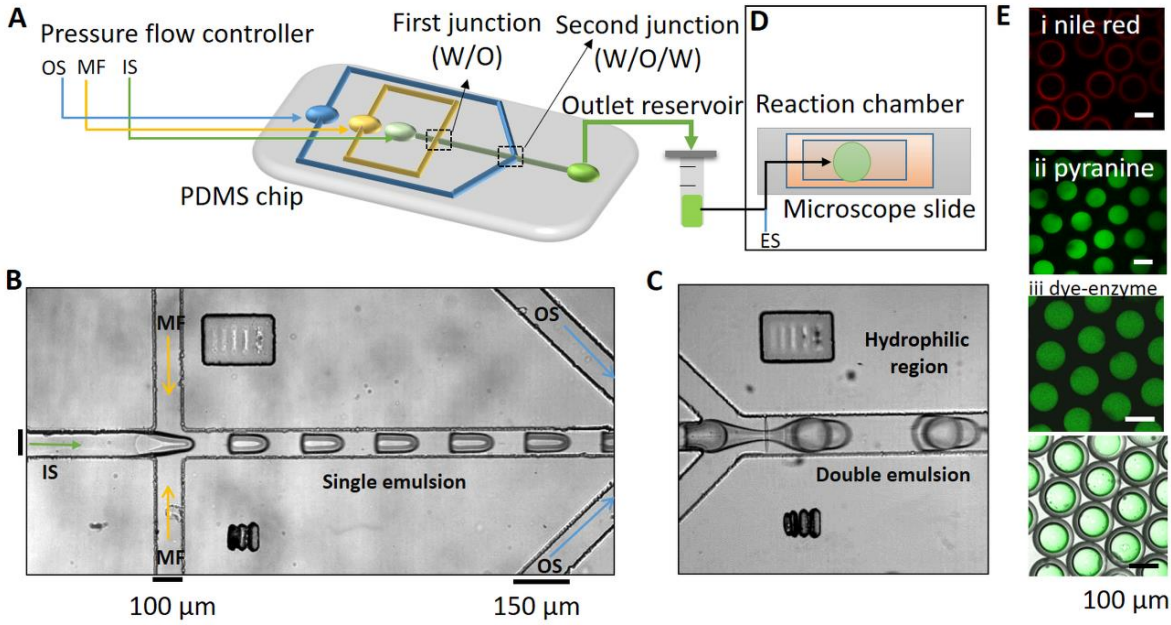


***Figure 2.1 Synthesis of urease-encapsulated water-oil-water double emulsions**. (A) Schematic representation of the microfluidic device with three inlets comprising outer solution (OS) middle fluid (MF) and inner solution (IS), and two flow focussing junctions (first (W/O) and second (W/O/W) junction). (B) and (C) Microscope images of single droplets and double emulsions on-chip, captured using phase-contrast microscopy (Leica DMi8, 10x magnification): (B) Water in oil (W/O) droplets are formed when the IS (urease, sucrose, acetic acid, PF127, pyranine) is sheared by the MF (POPC, mineral oil, span-80) at the first junction, (D) which then enters the second junction where droplets are sheared by the OS (glucose, glycerol, PF127, acetic acid). (D) Off-chip imaging of reaction after mixing of the double emulsions with external solution (ES) containing urea. (E) Confocal images of the double emulsions*

*with (i) nile red localized lipids in the MF and (ii) fluoroprobe pyranine in the IS and (iii) HiLyte™ Fluor 488 labelled-urease in the IS (upper) and superposition of fluorescence image and brightfield image (lower).*

### 2.3.2 A pH Pulse in Urease-encapsulated W/O/W Double Emulsions

The urease reaction has been well studied in batch reactors, and the rate depends on the initial concentration of urea, enzyme and acid[187]. With relatively high concentrations of enzyme, the pH increases rapidly to pH 7, then more slowly to pH ~ 9; the enzyme has a bell-shaped rate-pH curve with a maximum at pH 7 (**Figure 2.2** A and **Figure 7.7**).

In the double emulsion droplets, there was a pulse in pH characterized by a lag time, or induction time $T_{ind}$, before the sudden increase to a maximum pH ($pH_{max}$ ~ 8) and then a slow decrease to a steady state pH, $pH_{ss}$ ~ 7 (**Figure 2.2** B). The apparent pH (calculated from a calibration plot, **Figure 7.5**) depends on the transport rate of species between the droplet and external solution, as well as reaction rate. We assume here that transport involves diffusion of urea and ammonia through the oil; however, it may be facilitated by surfactant and other mechanisms such as formation of reverse micelles may play a role[253].

A series of images of the reaction in a double emulsion droplet and intensity in time are shown in **Figure 2.2** C. Initially droplets were at low pH (low intensity). Urea was transported across the oil layer from the solution and was hydrolysed in the aqueous core of the droplet, forming ammonia. There was a rapid increase in the fluorescence, followed by a slight decrease to a steady state in which the rate of reaction in the droplet matched the rate of loss of ammonia to the external solution. The fluorescence intensity increased uniformly across the whole droplet (**Figure 2.2** D), indicating fast internal mixing relative to the reaction timescale.

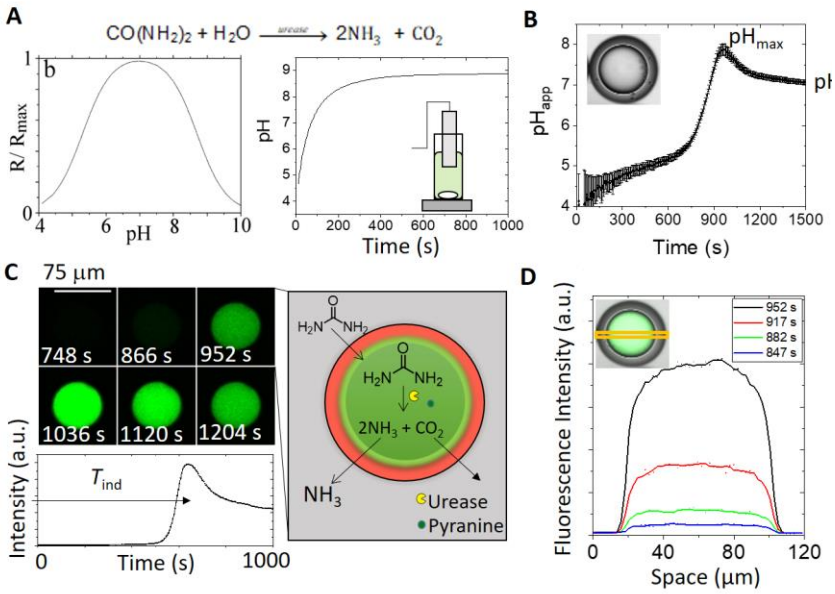


***Figure 2.2 Comparison of typical pH time profiles in a batch reactor (2.8 ml) and in a urease-encapsulated double emulsion microreactor*** *with concentrations [urea] = 0.07 M, [acetic acid] = 2 mM; [urease] = 50 U/ mL, [pyranine] = 50 µM, [phosphate]$_T$ = 80 mM. (A) Rate-pH curve for urease (plotted from relationship with experimentally-determined parameters, see 7.2.8) and pH in time in a batch reactor (B) Apparent pH in time in a double-emulsion droplet (from confocal images and calibration curve, Fig. S4); the induction time $T_{ind}$ = time to max rate of change of fluorescence; maximum pH = $pH_{max}$, and steady state pH = $pH_{ss}$. (C) Series of images obtained using confocal microscopy showing increase in fluorescence ($\lambda_{ex}$ = 458 nm) in a droplet in time with pH-dependent fluoroprobe pyranine. Schematic illustration of process: urea permeates through the oil layer and is locally hydrolysed by urease producing ammonia and carbon dioxide. (D) Average fluorescence intensity across the centre of the droplet (area indicted on inset image) at different times.*

### 2.3.3 Control of pH-time Profile in the W/O/W Double Emulsions

The characteristic features of the pH time profile, $T_{ind}$ and $pH_{ss}$, can be controlled by manipulation of the transport rates of urea and ammonia between the double emulsion droplet and external solution. In a typical experiment, 50 – 100 double emulsions were spatially distributed in the reaction chamber and the fluorescence in a group of droplets is shown in the series of images in **Figure 2.3** A. In contrast to earlier work with liposomes or polymerosomes, each microreactor behaved virtually independently and a distribution of induction times was obtained[199]. The oil shell provided a barrier between the core and external solution such that diffusion of ammonia was greatly reduced and there was a slow increase in pH in the external solution (**Figure 7.8**); the induction time depended on the layer depth (**Figure 2.3** B). Localised pH changes

have only otherwise been achieved with photosynthetic membrane proteins or by external buffering[254].

The average induction time across a population was controlled by the bulk concentration of urea and decreased with an increase in urea concentration (**Figure 2.3** C). It is unlikely that there is a variation in enzyme concentration in different droplets, but the distribution of induction times within a population may result from structural variations between droplets. In some experiments, motion of the inner core was observed to contribute to the induction time, as illustrated in **Figure 2.3** D; the reaction occurs first in droplet 1 after the core moved, followed by droplet 2 and finally droplet 3 with no core motion. The thinner shell during droplet motion resulted in faster increase of urea in the droplet and therefore accelerated the reaction. We also note that some droplets were unstable, particularly in experiments with lower PF-127 concentration or thinner shells, and both partial dewetting and bursting was observed (**Figure 7.9**). Reaction was faster in partially dewetted droplets (**Figure 7.10**).

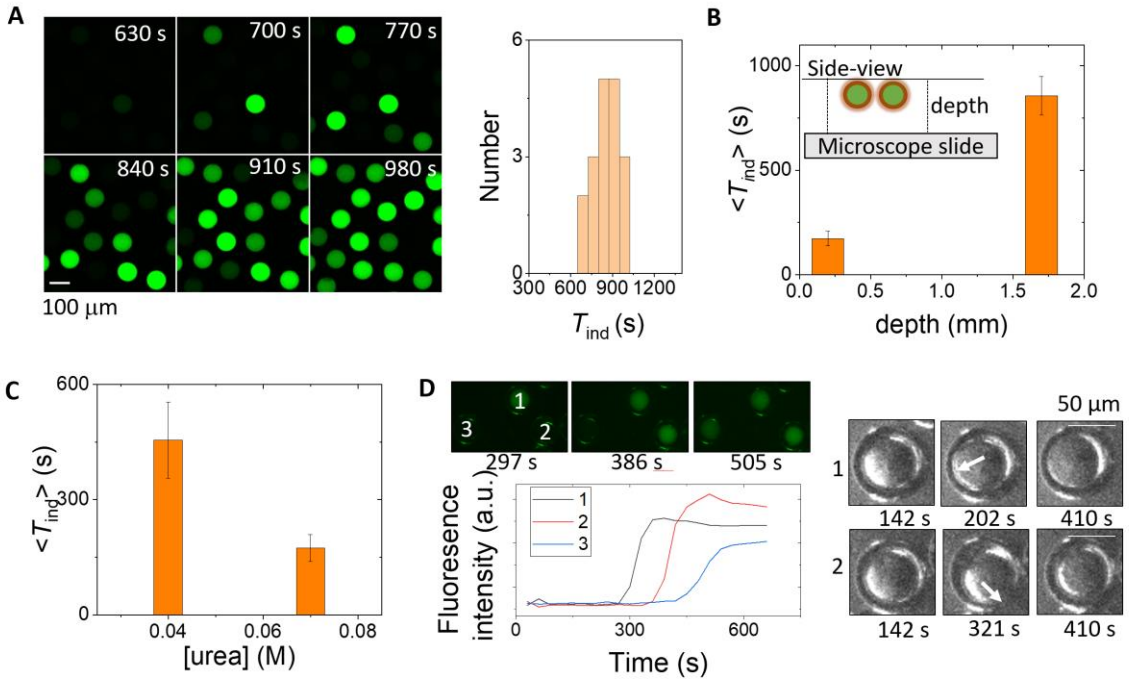


***Figure 2.3 Factors affecting the induction time in the droplets**. (A) Fluoresence images of 20 droplets in time and corresponding distribution of induction times in reaction layer depth 1700 µm (concentrations: [urea] = 0.07 M, [pyranine] = 50 µM, [AA] = 2 mM, and [urease] = 50 Units/mL). (B) Average induction time as a function of solution depth (C) Average induction time with urea (concentrations) in reaction chamber of depth 200 µM. Standard deviations from 20 droplets. (D)*

*Fluorescence images of reaction in 3 droplets (conc, layer depth) and right shows brightfield images with inner motion of aqueous droplet in 1 and 2 resulting in thinning of oil layer before reaction occurs.*

A non-monotic change in pH is difficult to achieve in the urease reaction and usually involves coupling the process with additional reactions or external processes such as light-driven proton production; here we used the emulsion properties to control of the pH-time profile in the droplets. The rate of change of pH in the droplets depended on factors including oil shell thickness relative to core size. In general, an increase in the pressure ratio $P_{MF}/P_{IS}$ results in an increase in S/C, with smaller core and thicker shells (**Figure 2.4** A). By manipulation of both the internal pressure $P_{IS}$ and $P_{MF}$, samples could be obtained with larger core size at fixed S/C. The clock time increased with increasing shell/core (**Figure 2.4** A,B) and the maximum rate of change of pH decreased (**Figure 2.4** C) as a result of the longer time taken for urea to cross the oil layer. Unlike in bulk solutions, the reaction can approach a steady state in pH with values below or above 7, and $pH_{ss}$ increased with increasing S/C as the ammonia transport out of the droplet was reduced in emulsions with thicker shells (**Figure 2.4** D).

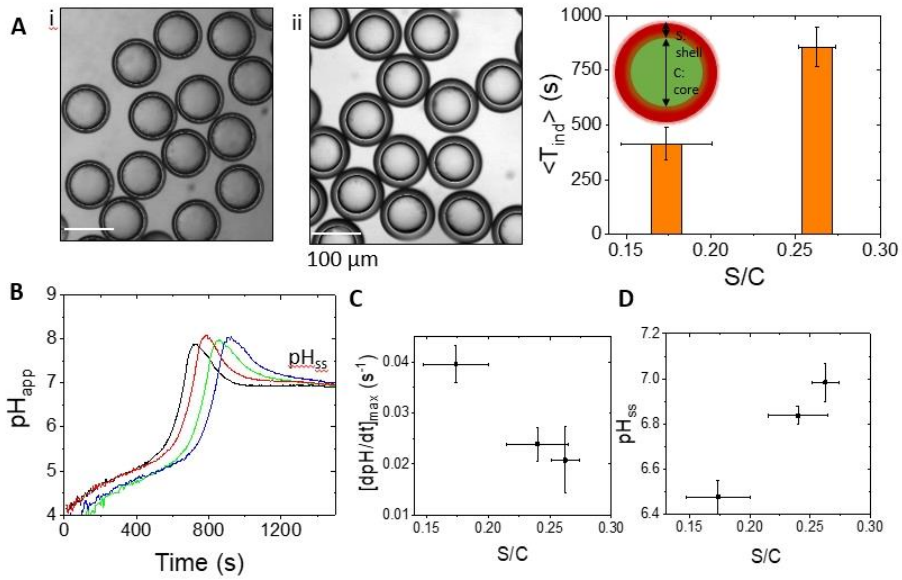


***Figure 2.4 . Control of the pH-time profile with different shell/core (S/C) ratio in the urease µ-reactors double emulsion*** *in reaction chamber of depth 1 mm. (A) droplets produced with different S/C (0.15 and 0.27) and corresponding average induction times. (B) Apparent pH in time in four droplets with S/C = 0.27. (C) Average rate of rate of pH and (D) Steady state pH as a function of S/C. Plots show average and standard devation from 20 droplets. The concentrations were [urea] = 0.07 M, [pyranine] = 50 µM, [AA] = 2 mM, and [urease] = 50 U/ mL, $[phosphate]_T$ = 80 mM.*

### 2.3.4 Double Emulsion Platform for pH Regulated Production of Minerals

The urease reaction is involved in biomineralisation, such as formation of calcite and struvite in bacterial colonies, and has been exploited for environmentally benign production of minerals in various applications[240,255,256,257]. Urease-aided calcium carbonate has been more thoroughly investigated than calcium phosphate precipitation, however, inorganic phosphates have wide ranging uses in the medical and food industries, including in bone and dental implants, and as drug delivery carriers[258,259]. These precipitates have multiple polymorphs and morphologies that depend sensitively on the conditions of synthesis including the solution pH[260]. Typically, amorphous calcium phosphate (ACP) is observed as a precursor to hydroxyapatite (HAP, $Ca_{10}(PO_4)_6OH_2$) at high pH or brushite (dicalcium phosphate dihydrate DCPD, $CaHPO_4.2H_2O$) at lower pH[261,262]. Methods for production of calcium phosphates include batch, stirred crystalizers, sol–gel synthesis and double emulsions[217,263]. Concentrated ammonium solutions have been frequently used to raise the pH resulting in spherical HAP particles composed of needle-like nanoparticles[217,264]. The urease loaded water-oil-water (W/O/W) double emulsion may be used to regulate phosphate precipitation in the droplets, with control of the internal pH achieved by changes in droplet properties.

In batch, stirred solutions with urease in sodium phosphate and calcium chloride, a mixture of precipitates was obtained (**Figure 2.5** A); amorphous calcium phosphate or weakly crystalline hydroxyapatite particles of size ~100 nm and micrometer-sized calcite dumbells, identified using Raman spectroscopy (see **Figure 7.11**)[246]. The increase in pH from the net production of ammonia shifts the dihydrogen phosphate and carbon dioxide equilibria to phosphate and carbonate ions respectively, driving the increase in supersaturation and formation of precipitate:

$$CO(NH_2)_2 + 2H_2O \xrightarrow{urease} 2NH_3 + CO_2 \qquad (2.1\ i)$$

$$H_2PO_4^- \rightleftharpoons HPO_4^{2-} + H^+ \rightleftharpoons PO_4^{3-} + H^+ \qquad (2.1\ ii)$$

$$CO_2 + H_2O \rightleftharpoons HCO_3^- + H^+ \rightleftharpoons CO_3^{2-} + H^+ \qquad (2.1\ iii)$$

$$5Ca^{2+} + 6PO_4^{3-} + 2OH^- \rightarrow Ca_{10}(PO_4)_6OH_2\ (s) \qquad (2.1\ iv)$$

$$Ca^{2+} + CO_3^{2-} \rightarrow CaCO_3\ (s) \qquad (2.1\ v)$$

***Equation 2.1*** *Reactions involve in batch stirred solution with urease in sodium phosphate and calcium chloride resulting in mixture of precipitates.*

In the double emulsions, we coencapsulated urease with sodium phosphate and calcium chloride and mixed the droplets with the external solution of urea in acid as described in the previous section. There was an induction period before the rapid appearance of preciptates in the droplets and the crystal polymorph depended on the shell to core ratio (**Figure 2.5** B). In droplets with thick shells, spherical hydroxyapatite particles of ~ 500 nm formed whereas with thinner shells, typically brushite microplatelets of ~ 50 µm were obtained, as confirmed by Raman spectroscopy (**Figure 7.12**):

$$Ca^{2+} + HPO_4^{2-} \rightleftharpoons CaHPO_4.H_2O \qquad (2.2)$$

***Equation 2.2*** *Chemical reaction for the formation of brushite microplatelets in double emulsions.*

The apparent area occupied by the precipates increased faster with brushite than with HAP (**Figure 2.5** C) and the growth rate of the crystals was of the order of 0.1 µm $s^{-1}$ (**Figure 7.13**). Brushite was not previously observed in experiments with urease-driven mineralisation since it is typically stable under slightly acidic conditions. In contrast to other experiments, the pH reaches a steady state in the W/O/W droplets controlled by the production rate of ammonia by reaction and loss rate to the external solution and thus steady state pH values lower than 7 can be attained.

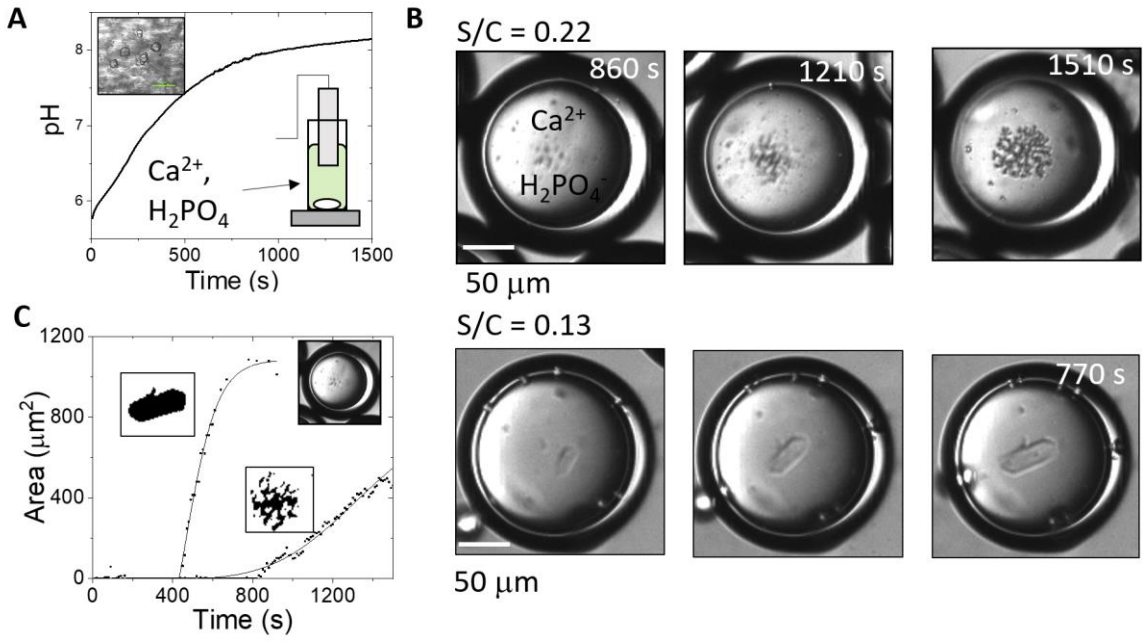


***Figure 2.5 Urease-driven biomineralisation****; comparison of reaction in bulk and in double emulsion droplets. Concentrations were: [urea] = 0.15 M, [AA] = 1 mM, [urease] = 50 Units/mL, and [$CaCl_2$] = 0.17 M (A) bulk solutions resulting in a mixture of phosphates and calcite with the increasing pH (B) Calcium phosphate precipitation in the W/O/W microreactors of different shell thickness: with S/C (C) area occupied by precipitates in time in the droplets.*

In individual droplets, typically only one polymorph formed under these conditions. In a population of droplets, the probability of a particular polymorph depended on the average ratio of shell to core and hence the steady state pH (we note that it was not possible to determine the pH in these experiments as the high calcium ion concentration quenches pyranine fluorescence). With thin shells, the pH in droplets approached $pH_{ss}$ < 7 in experiments without calcium and brushite dominated with calcium added, whereas with thicker shells the $pH_{ss}$ > 7 without calcium thus favouring formation of hydroxyapatite (**Figure 2.6**). With higher concentrations of calcium, multiple platetets could be observed in some droplets (**Figure 2.6** A and **Figure 7.14**). There was no evidence of calcite forming in any droplets under these conditions, unlike in bulk solutions, as the $pH_{ss}$ was maintained ~7[246,264].

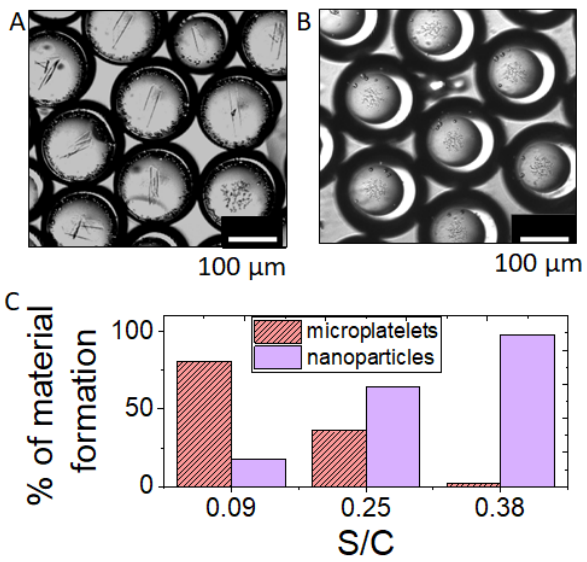


***Figure 2.6 Precipitation of either calcium phosphate platets (brushite) or particles (hydroxyapatite) as a function of average shell to core ratio (S/C) in the double emulsion droplets***. *Images of (A) platelets with S/C = 0.09 ± 0.03 (B) particles with S/C = 0.38 ± 0.02. (C) % of either platelets or nanoparticles in the droplets as a function of S/C. Concentrations were: [urea] = 0.15 M, [AA] = 1 mM, [urease] = 50 U/ mL, [phosphate]$_T$ = 80 mM and [$CaCl_2$] = 0.15 M.*

## 2.4 Conclusion

In this paper, taking advantage from pressure-driven droplet microfluidics, we developed a system of enzyme-encapsulated double emulsion (W/O/W) droplets to obtain a localised pH pulse, with a controllable induction time and steady state in pH. Urease-encapsulated double emulsion droplets of ~ 100 – 200 µm with a mineral oil shell thickness of 10 – 40 µm were prepared using a flow focussing device and the reaction was initiated off-chip by addition of droplets to a solution of urea. The pH increased uniformly and rapidly across the droplets after a time lag controlled by the diffusion of urea and then decreased to a steady state value either above or below pH 7, regulated by the rate of transport of ammonia out of the droplet. A distribution of induction times was obtained in the droplets thus demonstrating their potential to act as individual (µ)micro-reactors, whereas in other encapsulated urease systems the fast diffusion of ammonia resulted in increase in the pH in the surrounding solution[199].

We demonstrated that this approach has potential applications in regulating pH changes for pH programmable material synthesis in confined environments. The steady state pH can be manipulated by varying shell thickness of double emulsions, and here we triggered phosphate precipitation and showed that the polymorph that

formed within the core of microfluidic double emulsions depended on the shell thickness, and hence the steady state pH. This demonstrated that compartmentalisation of the urease reaction may be exploited for selecting polymorphs through internal pH regulation, in contrast to bulk solutions where the pH continued to increase resulting in a mixture of precipitates.

In conclusion, compartmentalisation of the urea-urease reaction in double emulsions generates new potential in the development of biocompatible feedback for pH-triggered processes and bioinspired applications in materials science. In the future, the microfluidic-based double emulsion platform could be used for fine tuning material properties, such as pH-triggered organic polymer-phosphate particles for medical applications[265].

# 3 A Modelling Approach to Predict the Influence of Shell-core Reactor Configuration on the Induction Time of Urea-urease Reaction

*Simulation-Experimental Comparative Analysis*

## Contents:

## 3.1 Introduction

The approaches to compartmentalisation of biological entities and biochemical reactions are important considerations for applying the concept of biological cells to artificial systems and open up exciting possibilities in the field of therapeutics. In this context, there has been a growing interest in layered spheres consisting of an inner cavity (core) and an outer diffusion-barrier layer[266], such as lipid-based vesicles[183] and emulsion droplets[267]; they have been employed as carriers of biomolecules for applications related to drug delivery and as micro-reactors to host various enzyme-catalysed biochemical reactions[150,268,269], mainly due to their stability and non-toxicity. In addition, these cell models are used in the field of synthetic biology to investigate various cellular traits (e.g. metabolism, division, and communication)[270].

Motivated by the efficiency of lipid-based micro-reactors for enzyme-catalysed reactions[271,272,273], we proposed microfluidic-based W/O/W double emulsion model[74,274] consisting of an inner aqueous cavity/core and an outer lipid-oil layer as it allows better control of system dynamics, higher encapsulation efficiency[275,126,276], and membrane permeability to certain chemical signals compared to synthetic vesicles[270,277]. In addition, confinement within the multiple layers of double emulsions diminishes the rapid degradation of reactive components which is an important consideration to employ these as artificial cell models for drug delivery systems.

There are various enzyme catalysis reactions, amongst which the urease-catalysed (pH-dependent) hydrolysis of urea (UU) has proven to be a great candidate to exploit in applications, such as base-induced material formation and therapeutics[198,186,187,271]. Compartmentalisation of urease has proven useful for numerous therapeutic applications. For example, Wolfe and Chang in 1987 used orally administered microcapsules containing urease and zirconium phosphate as a means of removing urea from the gastrointestinal tract[278]. Another interesting application of compartmentalisation is the development of systems for timed drug delivery. In this context, the interaction between urease and urea and the increase in pH triggered by urea could be used to induce specific responses, similar to a study by Giannos et al. in 1995[279]. The researchers investigated the approach of coupling pH oscillators with membrane diffusion to obtain controlled drug release. In a model system, a pH-oscillating medium incorporating benzoic acid was placed adjacent to a lipophilic

ethylene-vinyl acetate copolymer membrane. The underpinning assumption was that pH variations in the range of pH 2 to 7 would lead to intermittent diffusion of benzoic acid (uncharged) through the lipophilic membrane. A related approach could be adopted to urease-encapsulated systems, in which urea would induce pH changes that would in turn result in controlled drug release from the encapsulated droplets. Such an approach reveals the inherent potential to develop sophisticated systems that react to specific triggers and opens up possibilities for the creation of novel therapeutic applications by compartmentalisation.

Here, we studied the local production and permeation of the base from the inner core and through the diffusion-barrier lipid-oil layer into an external environment. Hydrolysis of urea by the enzyme urease results in the production of a weak base, ammonia, and occurs in numerous cellular systems; for example, the Helicobacter Pylori uses it to raise the pH to protect itself from the severe acidic environment of the stomach[280]. The overall stoichiometry of the reaction is given below (1). The urea-urease reaction follows the kinetics of Michaelis-Menten[281,282,283,187,186,284] and has a bell-shaped rate-pH curve with maximum at pH 7 and exhibits a change in pH due to the production of ammonia, also known as a 'pH clock' with an 'induction time, $T_{ind}$', which is the time elapsed between the start of concentration mixing and the observation of formation of the product[271]. In the case of the urea-urease reaction, the induction time is the amount of time it takes for the urease enzyme to catalyse sufficient breakdown of urea into ammonia and carbon dioxide. The reaction is initially slow because the enzyme is in an inactive form at low pH (see appendix 7.1.1). The UU reaction is a feed-back driven reaction due to the pH-dependence of the reaction rate.

$$CO(NH_2)_2 + H_2O \xrightarrow{urease} 2NH_3 + CO_2 \qquad (3.1)$$

***Equation 3.1*** *Urease catalysed urea hydrolysis reaction.*

In our previous experiments, we designed a microfluidic platform of W/O/W double emulsions to immobilize the enzyme urease (water soluble) in the core of the reactor in contact with an external aqueous solution (ES) containing urea through a lipid (POPC) oil layer to form W/O/W-based micro(μ) reactors. In short, the substrate urea from the external solution (ES) enters the core of the μ-reactor through the lipid-oil membrane, where the enzyme urease selectively detects the substrate and converts

it to $NH_3$ and $CO_2$. The neutral products behave as membrane-permeable signalling molecules. To observe the reaction using optical microscopy fitted with a fluorescence unit, we encapsulated pyranine (fluorescent probe) in the core of the μ-reactors. Pyranine (8-hydroxy-1,3,6-pyrenetrisulfonate) is a useful fluorescent probe due to its strong dependence of emission on pH in the range of 6 - 10[213] and the added advantage of its impermeability[285] through lipid-oil membrane. We have observed remarkable control over temporal behaviour of urea-urease (UU) reaction in individual μ-reactors, with discrete clock times occurring within the μ-reactors for the first time. This platform of microfluidic double emulsions can provide control over the output signal of the reaction by varying the μ-reactor configuration (shell/core, shell, and core size) using pressure-driven flows (chapter 2).

To be able to control chemical signalling and integrate it in various biomedical applications, as a first step, it is important to understand the factors influencing the output signal of a chemical reaction. In this context, the focus of this paper is modelling reaction and diffusion in a composite medium of finite length consisting of three layers (see **Figure 3.2**), mimicking the experimental W/O/W-based μ-reactors. Each layer is homogeneous, isotropic and has a constant diffusivity. This reaction-diffusion model is used to confirm the relationship between μ-reactor configuration and induction time of the urea-urease reaction. Although modelling approaches have already been taken to understand chemical release from concentric spheres for applications in the field of drug delivery[286], there is limited research devoted to investigate the non-linear reaction chemistry within these core-shell μ-reactors. Here, we have modelled a layered sphere encapsulating the urease enzyme, immersed in a finite medium of an external solution containing the substrate urea, and compared the numerical trends with our experimental results. Our goal was to create a simple model that gives an insight into the role of the core-shell μ-reactor configuration on the reaction dynamics to compare it with experimental trends that can potentially be used for biomaterials and medical applications.

## 3.2 Synthesis of W/O/W-based Model Micro(μ)-reactors Using Pressure-driven Droplet Microfluidics

We used a flow-focusing device with three inlets, two droplet formation junctions, and an outlet to synthesize double emulsions. Polydimethylsiloxane (PDMS)

microchannels were fabricated using conventional soft lithography[249,287]. There were three microfluidic inlet solutions, namely inner solution (IS), outer solution (OS), and middle flow (MF). The IS contained sucrose (0.2 M), pyranine (60 µM), urease, acetic acid, and pluronic F-127 (0.28%). The concentrations of urease and acetic acid were varied for different runs. The outer solution (OS) reservoir holds glucose (0.2 M), glycerol (20%), pluronic F-127 (0.28%), and acetic acid. The lipid solution (middle flow reservoir in the microchannel, MF) contained 6.5 mM POPC in mineral oil (MO) and 2% SPAN-80. A pressure-driven pump (OB1 MkIII+, Elveflow, Paris, France) was used to transport both the aqueous solutions (IS and OS) and the lipid-oil phase (MF) through the microfluidic chip by tuning the three pressure inlets ($P_{IS}$, $P_{OS}$, $P_{MF}$) connected to the pressure device. Water-in-oil droplets (W/O) were formed at the first junction of the flow-focusing device by running the IS and the MF at fixed flowrates of $P_{IS}$ and $P_{MF}$, the flow pressures were varied with a fixed ratio of $(P_{MF}/P_{IS})\sim 2$. The double emulsions were obtained at the second junction by shearing the W/O droplets made at the first junction with the OS at a fixed pressure flow of $P_{OS}$. The full details of the methods are in the Appendix section 7.2.1, 7.2.2, and 7.2.3.

## 3.3 Experimental

We selected W/O/W double emulsions synthesized through pressure-driven microfluidics as model micro µ-reactors. The synthesised emulsions encapsulate enzyme urease, acetic acid, and pyranine. The double emulsions were collected from the outlet Eppendorf tube and were mixed with an equal volume of an external solution (ES) containing urea, acetic acid, and glucose (0.2 M), in a separate mixing tube. Acetic acid was added to maintain a lower pH and glucose was added to prevent the osmotic imbalance between droplets and ES. The reaction was observed using an epifluorescent microscope or confocal imaging and a glass slide with an observation chamber (appendix 7).

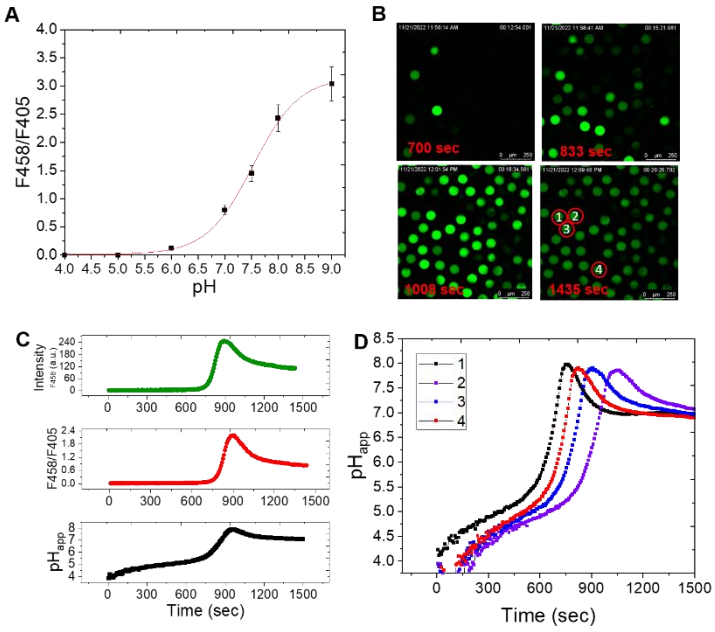


***Figure 3.1 Typical pH-time profile in the W/O/W double emulsions and determination of pH using a calibration curve****. (A) Ratio of fluorescence intensity, 458 nm/405 nm, vs pH in reacted solution of urea-urease reaction with pyranine and fitted equation (line): y=a+(b-a)/(1+10$^{c-x}$), where a = 0.0129 ± 0.03899, b = 3.155 ± 0.07021, and c = 7.5256 ± 0.03947 obtained from data fitting (B) Confocal images in time for the urease pH induction reaction in W/O/W based µ-reactors with 1 mM acetic acid, 50 units/mL of urease and 0.07 M urea (C) The average increase in fluorescence intensity of pyranine at 458 nm, the increase in avg. intensity ratio (F458/F405), and corresponding pH in time plot obtained from curve fitting (D) pH-time plot for the four selected W/O/W droplets in B.*

We have used pyranine as a fluoroprobe to detect the change in pH due to the formation of ammonia in µ-reactors (emulsions), which shows a fluorescent green colour as the pH increases. A calibration procedure (known as ratiometric imaging) was performed to relate the fluorescence intensity of pyranine with the pH of the solution[285]. The fluorescence intensity was measured by exciting the pyranine probe with two different wavelengths, 405 nm and 458 nm. The 405 nm wavelength primarily activates the protonated form of pyranine (pyrOH), while the 458 nm wavelength activates the deprotonated form of the indicator (pyrO$^-$). The pH of reacted solutions of the urea-urease reaction were adjusted with acid or base to obtain a range of pH solutions to plot a pH calibration curve (as shown in **Figure 3.1** A). We used the following equation: 'y=a+(b-a)/(1+10^c-x))' to fit the data obtained from pyranine's pH calibration using OriginPro's Nonlinear Curve Fit tool. Here, x is pH, y is fluorescence intensity, a, b and c are the parameters to be fitted. The fitting equation is from theoretical considerations of the equilibria discussed in detail elsewhere[288] and in

Appendix section 7.2.5). **Figure 3.1** B shows a sequence of images of the W/O/W double emulsions exhibiting urea hydrolysis reaction after an induction period, represented by an increase in fluorescence in an individual μ-reactor due to the formation of product ammonia. A matlab code was developed to extract the fluorescence data from figures (**Figure 3.1** B) and then correlate it with the pH using the calibration curve (**Figure 3.1** A). **Figure 3.1** C shows the correlation of the pyranine fluorescence intensity values with the apparent pH within the μ-reactor, **Figure 3.1** D gives the resultant pH-time profile of the four selected μ-reactors. Here, we defined the induction time as the time to the maximum rate of change of fluorescence intensity. The primary objective of this study is to compare the trend of induction time obtained with experimental parameters in our system with the results of our model simulation.

## 3.4 Model

The model is based on the experiments in which urease encapsulated W/O/W droplets are placed in an external solution (ES) containing urea and acetic acid in an observation chamber. In the present model we have considered an individual urease-loaded W/O/W droplet in contact with the external solution (ES) via oil layer. The model consisted of inner core and an outer shell with different permeability coefficients of reactive components surrounded by a finite medium of ES. The following reaction steps were taken into account (where HA corresponds to acetic acid):

| | | |
|---|---|---|
| $CO(NH_2)_2 + H_2O \xrightarrow{urease} 2NH_3 + CO_2$ | | (3.1 i) |
| $NH_4^+ \rightleftharpoons NH_3 + H^+$ | pKa = 9.25 | (3.1 ii) |
| $CO_2 + H_2O \rightleftharpoons H^+ + HCO_3^-$ | pKa = 6.35 | (3.1 iii) |
| $HCO_3^- \rightleftharpoons H^+ + CO_3^{2-}$ | pKa = 10.25 | (3.1 iv) |
| $H_2O \rightleftharpoons H^+ + OH^-$ | pKa=14 | (3.1 v) |
| $HA \rightleftharpoons H^+ + A^-$ | | (3.1 vi) |

***Equation 3.2*** *(i) The overall urea-urease reaction, and (ii-vi) a series of accompanying reaction equilibria involved in the urea-urease kinetic model. This also determines the pH value of the system.*

The rate of the enzyme catalysed reaction is of the Michaelis-Menten type[183,186,271] and incorporates pH dependence resulting from the active protonated form of substrate-enzyme complex ($K_{es2}$) and inactive biprotontated complex form ($K_{es1}$), as follows:

$$V = \frac{k_E E \quad U}{(K_M + U*(1+\frac{U}{Ks}))(1+\frac{NH4^+}{Kp})\left(1+\frac{K_{es2}}{H^+}+\frac{H^+}{K_{es1}}\right)} \qquad (3.3)$$

***Equation 3.3*** *The rate of the enzyme catalysed reaction (Michaelis-Menten)*

where E is the enzyme urease concentration in U/ml, U = [urea], $K_M$ is the Michaelis constant, $K_{es2}$ and $K_{es1}$ are protonation equilibria. $K_S$ is the substrate (urea) inhibition and $K_P$ is the product (ammonium) inhibition factors for noncompetitive reactions. The enzyme parameters were within the ranges quoted in the literature[271,289], with values chosen to best agree with experimental results: $k_E = 3.5 \times 10^{-6}$ ml M unit $^{-1}$ $s^{-1}$; $K_M$ = 0.003 M; $K_{ES1} = 5 \times 10^{-6}$ M; $K_{ES2} = 2 \times 10^{-9}$ M; $K_S$ = 3 M; $K_P$ = 0.002 M;

The following rate constants for the reversible reactions (3.1 ii–vi) were taken from the literature [290] :

$$k_2 = 24s^{-1}; k_{-2} = 4.3\times10^{10} M^{-1}s^{-1}; k_3 = 0.037s^{-1}; k_{-3} = 7.9\times10^4 M^{-1}s^{-1}; k_4 = 2.8s^{-1};$$
$$k_{-4} = 5\times10^{10} M^{-1}s^{-1}; k_5 = 1\times10^{-3} Ms^{-1}; k_{-5} = 1\times10^{11} M^{-1}s^{-1}; k_6 = 1\times10^9 s^{-1}; k_{-6} = 1\times10^{11} M^{-1}s^{-1}$$

Models based on diffusion from concentric spheres have been used for drug delivery, for example in the earlier work of Carr et al. where they have assumed diffusion flux continuity at all the interfaces of multi-layer sphere[286,291,292]. The novelty of our system is that we incorporated reaction rather than just diffusion and added permeability and partition coefficients of different reaction components (urea, ammonia, and carbon dioxide) to the model. We used a finite difference scheme for a radially symmetric, layered sphere with a variable diffusivity, and solved equations numerically[293]. A Matlab code was written for ten variables ($H_2O$ is a constant) using PDEs resulted from the reactions (1-6), and these were urea, ammonia, ammonium, $H^+, OH^-, CO_2, HCO_3^-, CO_3^{2-}, HA$ (acetic acid), and $A^-$ (see Appendix 7.3) in three different sections, namely the inner aqueous core (L), the shell layer (BL), and the

outer external solution (ES) layer (L2), for the four interfaces between these layers (two aqueous and two oil interfaces) and for the two boundaries (left and right), as shown in **Figure 3.2**. The resultant reaction-diffusion equation of the $i^{th}$ variable ($C_i$) takes the following form:

$$\frac{\partial \mathrm{Ci}}{\partial \mathrm{t}} = \mathrm{f}(\mathrm{C_i}) + \frac{Di}{r^2} \cdot \frac{\partial}{\partial r}\left(r^2 \frac{\partial C_i}{\partial r}\right) \qquad (3.4)$$

***Equation 3.4*** *The partial differential equation associated with the radially symmetric sphere for the reaction-diffusion of the $i^{th}$ variable ($C_i$).*

Where $\mathrm{f}(\mathrm{C_i})$ is the reaction term and $Di$ is the diffusion coefficient of $\mathrm{C_i}$ along the radial coordinate ($r$). The partial differential equations associated with the radially distributed system were solved using a central finite difference discretization method for space and a stiff ODE solver, in this case MATLAB's ode15solver. The solver is built on the backward difference algorithm, using the numerical differentiation formulae (NDFs) [294,295]. The spatial resolution was set as 0.001 mm and the total length of the domain was defined as T=L*N+BL*N+N*L2, where L= length scale of the inner aqueous core, BL= length scale of the shell layer, L2= length scale of the external solution layer, and N= 10 (number of the variables). The absolute tolerance (AbsTol) was set as $1\mathrm{x}10^{-11}$ in the 'options structure' in MATLAB for ode15solver. The diffusion coefficients were taken as $D_U = 1x10^{-3}$ mm$^2$ s$^{-1}$; $D_H = 2x10^{-3}$ mm$^2$ s$^{-1}$; $D_{OH} = 1x10^{-3}$ mm$^2$ s$^{-1}$; $D_{NH_3} = 1x10^{-3}$ mm$^2$ s$^{-1}$; $D_{NH_4^+} = 1x10^{-3}$ mm$^2$ s$^{-1}$; $D_{CO_2} = 1x10^{-3}$ mm$^2$ s$^{-1}$; $D_{HCO_3^-} = 1x10^{-3}$ mm$^2$ s$^{-1}$; $D_{co_3^{2-}} = 1x10^{-3}$ mm$^2$ s$^{-1}$; $D_{HA} = 1x10^{-3}$ mm$^2$ s$^{-1}$; $D_{A^-} = 1x10^{-3}$ mm$^2$ s$^{-1}$ for the aqueous phases and $D_{UO} = 1x10^{-3}$/20 mm$^2$ s$^{-1}$; $D_{NH_3O} = 1x10^{-3}$/20 mm$^2$ s$^{-1}$; $D_{CO_2O} = 1x10^{-3}$/20 mm$^2$ s$^{-1}$; $D_{HAO} = 1x10^{-3}$/20 mm$^2$ s$^{-1}$ for the oil layer, assuming the diffusivity is constant in each layer.

The boundary conditions at the aqueous oil interface involved the permeabilities and partition coefficients of the species. The permeability coefficients (P) of reactive components through the shell membranes were estimated to be $P_{CO_2} \geq P_{NH_3}$ ($\mathrm{P_N}$) > $P_{Urea}$ ($P_U$), in line with work using phospholipid membranes[199], and these were respectively $P_{CO_2}$ = 0.1 mm s$^{-1}$, $P_N$ = 0.1 mm s$^{-1}$, $P_U$=5 x $10^{-6}$ mm s$^{-1}$, and $P_{\mathrm{HA}}$ = 0.0001 mm s$^{-1}$ for acid. We have assumed that the permeability of all ions ($NH_4^+$, $H^+$, $HCO_3^-$, $CO_3^{2-}$ , $OH^-$) through the shell membrane is negligible. The partition coefficients (K),

which are defined as a degree of the solubility of the substance in lipid-oil, were set as $K$=0.01, $K_N$=1, $K_{CO_2}$ =1, and $K_{HA}$ =0.1, respectively. We were unable to find literature values for partition coefficients in mineral oil, so here we use reasonable estimates based on octanol[296].

The initial conditions were defined as U = 0 M, H = OH = 1 x $10^{-7}$ M at the aqueous core layer, U = H = OH = 0 in the shell layer, and U = 0.04 M, H = 1 x $10^{-5}$ M, OH = Kw/H in the external solution layer, unless otherwise stated. Symmetric conditions were employed at the left boundary and no flux boundary conditions were employed at the right. The Appendix section 7.3 contains the Matlab script files for the code.

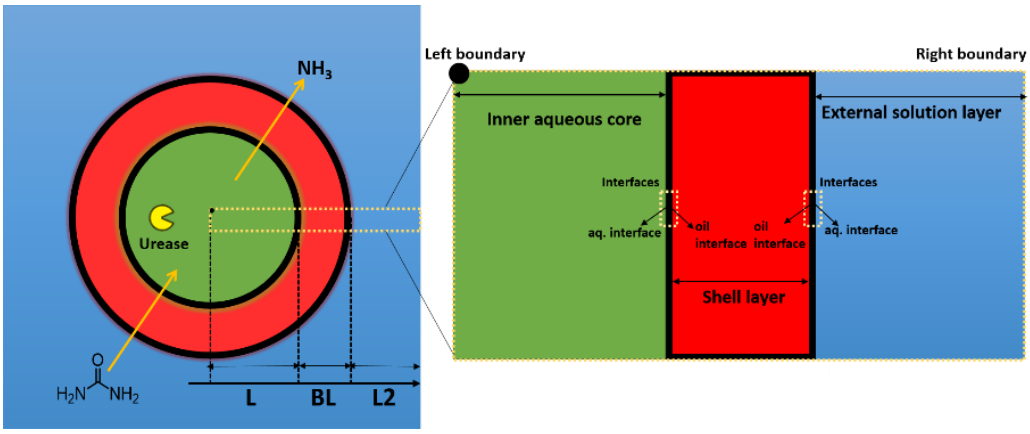


***Figure 3.2 Schematic representation of the cross-section of the radially symmetric one-layer sphere (shell-core model)****, comprising an internal core of radius L (green coloured) and the shell layer of thickness BL (red coloured). This sphere together with the external medium of thickness L2, represents the shell-core model presented here. A close-up of the cross-section on the right reveals the four interfaces, including two aqueous interfaces and two oil interfaces, that exist between the two layers and an aqueous core of the sphere: the inner aqueous core, the shell layer, and the external solution layer.*

## 3.5 Results and Discussion:

## 3.6 Model for Shell-core Based Micro-reactor

We have studied the kinetics of the urea-urease reaction by considering a diffusion-barrier layered (concentric) sphere with a core of radius "L" encapsulating the urease enzyme and an outer layer consisting of a lipid-oil shell of thickness "BL" immersed in a finite external substrate medium (urea) with a length scale of "L2" starting from the outer layer, **Figure 3.2**. We assume a radially symmetric PDE model (Appendix section 7.3). The overall goal of this approach is to better understand and predict the

behaviour of the urea-urease reaction as it occurs in a multilayer system. The chosen layer-by-layer model of mass transfer through the shell and core provides reasonable match compared to the experiments and is useful both from a theoretical point of view and for applications such as establishing the desired conditions for achieving programmable material formation or drug release in a micro-reactor.

## 3.7 pH-time Profile and Effect of Urea Concentration

A pH clock reaction exhibits a maximum acid or base production rate at a non-zero reaction time, as such, after a certain time a kinetically driven change in pH is observed. This switching behaviour is often due to a feedback loop, that is, the rate acceleration due to base/acid catalysis by base/acid production[187]. The urea hydrolysis by enzyme urease shows a feedback-driven trend with the production of base (ammonia), resulting in a switch in pH from acidic to basic with the maximum rate at pH 7 and this depends on the concentrations of the reactants (urease, urea, and acetic acid). This change in pH to a value of 7 in urea-urease reaction is called 'induction time, $T_{ind}$'.

In experiments, the switch in pH was generally sharp. In general, there was an increase in induction time with the decrease in initial concentration of urea as expected (the enzyme rate is slower, but also transport rate is lower). In **Figure 3.3**, the effect of substrate urea concentration (0.04 M and 0.07 M) on the induction time is presented, while keeping the concentration of urease (50 units/mL) and acetic acid (1 mM) constant, for droplets with the same core/shell and core size. **Figure 3.3** A, shows the time series of the progression of the reaction with 0.04 M urea, **Figure 3.3** B displays the shift of $T_{ind}$ by changing the urea concentration from 0.04 M to 0.07 M. The model, illustrated in **Figure 3.3** C. was simulated to determine the effect of the substrate urea concentration on induction time and the period decreased from 190 secs to 110 secs, in good agreement with the experimental trend (**Figure 3.3** D)

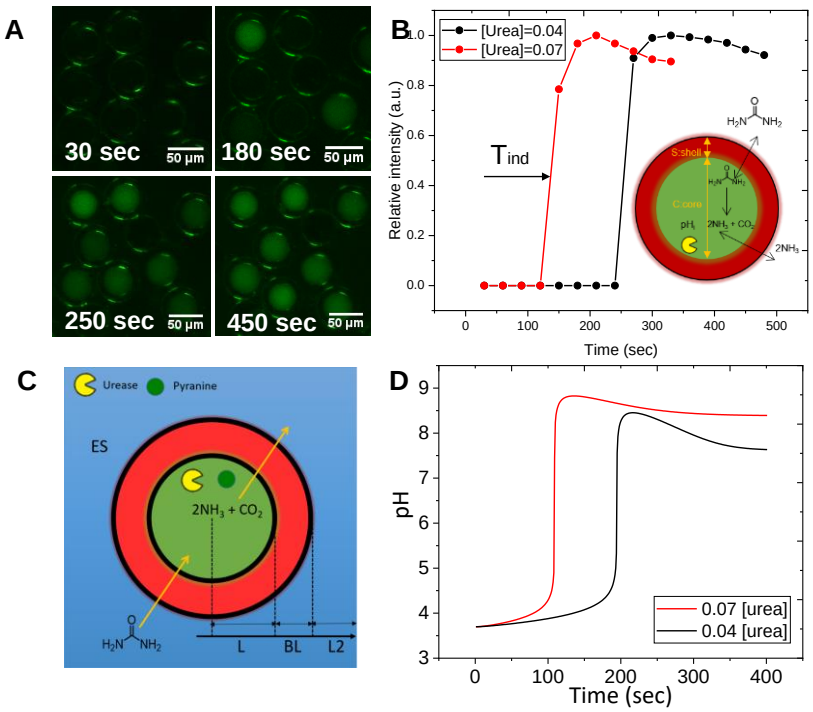


***Figure 3.3 Effect of changing urea concentration on urea-urease reaction in microfluidic W/O/W droplets*** *using urease (50 units/mL), acetic acid (1 mM), pyranine (50 µM), and urea (0.04 M and 0.07 M). (A) Epifluorescent microscopic images in time for [urea]=0.04 M (B) Average intensity(relative) in time for two different sample of µ-reactor population with varied urea concentration ([Urea]=0.04 M and 0.07 M) (C) An illustration of the shell-core mode for MATLAB simulations of an experimental µ-reactor, where L= radius of the inner aqueous core, BL= shell thickness, and L2= external solution layer (D) Effect of urea concentration on $T_{ind}$ of the urease induction reactions using the shell-core model, where Pu= 5 x $10^{-5}$ mm/s, Ku=0.001, L=50, BL=25, and L2=70, using [Urea]= 0.04 M and 0.07 M and [urease]= 50 units/mL for simulations.*

### 3.7.1 Tuning of pH-clocks by Varying the Shell/Core of µ-reactors

We observed a wide distribution of induction times for the W/O/W-based µ-reactors in experiments. The widely distributed induction periods highlighted that the trend of the pH-time profile depended on µ-reactor properties, unlike experiments with vesicles where a synchronous and homogeneous response was obtained. These discrete clock times may result from the different configuration (shell/core, shell, and core size) of µ-reactors within the same population due to the slight variations in the pressure flows associated with the microfluidic pump. Further, to investigate the relationship of µ-reactor configurations and the induction periods we tuned the pressure flows to obtain different shell/core sizes and compare them with the $T_{ind}$. Experimentally, this was achieved by changing the fixed ratio of $P_{MF}/P_{IS}$~2 to ~2.7, resulting in thicker shells of

double emulsions and correspondingly longer induction times. **Figure 3.4** (A, B and E) represents an experimental illustration of the effect of changing the shell/core (s/c) ratio on the pH induction periods, where increasing the average s/c from 0.1 to ~0.2 leads to an increase in $T_{ind}$. In general, reactors with a lower s/c (thinner shells) structure resulted in a sharp increase in pH, followed by a rapid decrease and then a gradual drop to a stable value and thus forming a pulse-like pH-time profile, as shown in **Figure 3.4** B for the s/c =0.11. Increasing the s/c ratio (thicker shells) resulted in a slower increase in pH (**Figure 3.4** B for s/c =0.18) and forms a more sigmoid pH-time profile compared to a decreased s/c (s/c =0.11). The faster increase in pH could be due to a faster transport of urea with thinner lipid-oil membranes, followed by a rapid conversion to ammonia, which quickly leaks out of the membrane and lowers the initial rise in pH. In contrast, thicker lipid-oil membranes reduce the transport of urea and lead to a more gradual increase in pH and usually resulting in a higher final value. **Figure 3.4** E compares the trend of increasing shell/core and $T_{ind}$ in a single population of µ-reactors. As the s/c ratio increases, the average $T_{ind}$ increases. We established through experiments that the µ-reactors could be produced using pressure-controlled microfluidic droplet techniques to tune induction periods on demand.

To get a clearer insight into the relationship between different µ-reactor configurations and the associated pH-time profile, the simulations were performed with the radially symmetric shell-core model. **Figure 3.4** (C, D, F and G) shows the simulation results that qualitatively compare the effect of s/c with the experiment. In simulations, this was controlled by changing 'BL'. A similar pH-time profile was obtained with the model. As such, the induction period ($T_{ind}$) within the µ-reactor decreases with lower s/c ratio with a comparable trend of a sharp increase to a higher pH (pH = 8.3) followed by a gradual decrease to a lower final pH (pH = 7.1) and thus forming a pulse-like pH-time profile, as shown in **Figure 3.4** C for s/c = 0.11. Whereas, increasing the s/c (s/c = 0.18) increases the $T_{ind}$ with a more gradual increase in pH resulting in a sigmoidal pH-time profile (**Figure 3.4** C for s/c = 0.18).

One possible explanation (discussed below) is that the pH-time profile was primarily controlled by urea transport, which in turn was influenced by shell thickness, as shown in **Figure 3.4** G, where there is a rapid increase at s/c=0.11 and then a decrease to a stable value, while urea transport is quite slow at s/c=0.18 compared to s/c=0.11. A

rapid and instantaneous increase and subsequent decrease in the internal pH, with thinner shells, resulted from a fast transfer of urea in to the core and the subsequent fast transfer of $NH_3$ into the external solution, which increased the external pH ($pH_O$) (as shown in **Figure 3.4** D for thinner shells, s/c = 0.11). For thicker shells, the reaction was more gradual due to the slow transfer of urea across the shell membrane, resulting in a slower build-up of ammonia within the core and a resultant slow release into the external solution. The increase in pHo for s/c = 0.18 is significantly lower relative to s/c = 0.11 (**Figure 3.4** D for s/c = 0.18). **Figure 3.4** F shows the similar influence of increasing s/c on $T_{ind}$ as observed in experiments (**Figure 3.4** E).

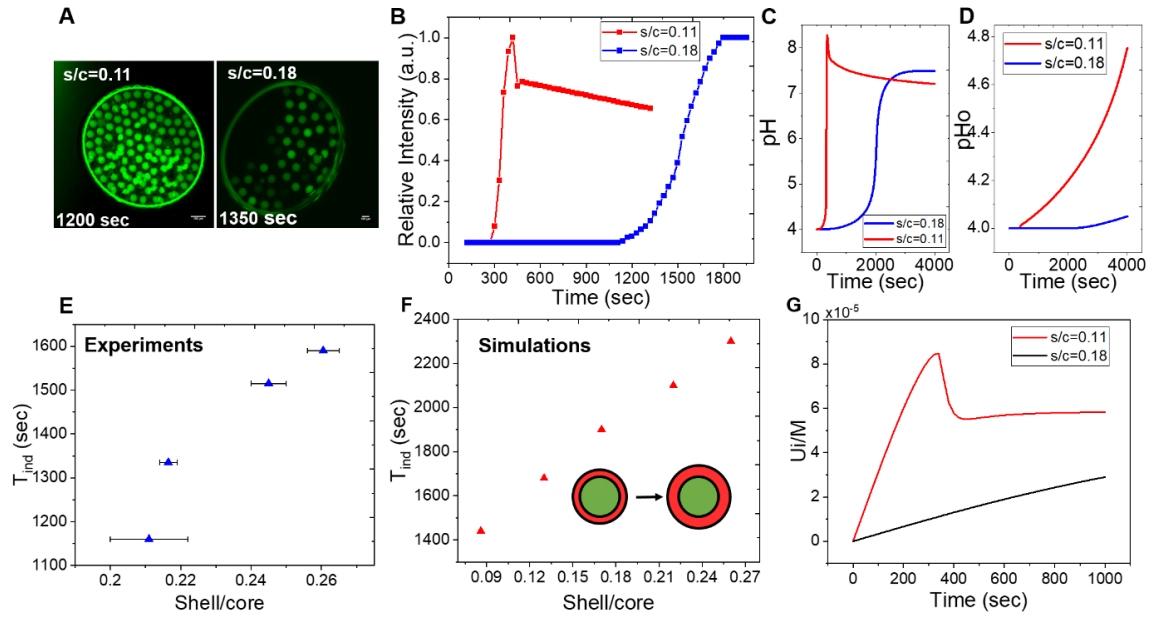


***Figure 3.4 Effect of changing shell/core ratio on pH-time profile and $T_{ind}$:*** *comparison of experiments and simulations (A) Microscopic images for different s/c (top: avg. 0.11 and bottom: avg. 0.18) sized µ-reactors, epifluorescent microscope (LS560 Microscope, green fluorescence, and brightfield, green filter: excitation 457-493 nm; emission 508-552 nm, etaluma), 10x magnification, and scale bar = 100 µm. (B) Intensity-time profile for s/c=0.11 and s/c=0.18, the reaction concentrations were: [urea] = 0.04 M, [pyranine] = 50 µM, [AA] = 1 mM, and [urease] = 50 Units/mL, (C) Simulations of shell-core model for pH-time reaction profiles for urea-urease reaction to compare the experimental trend (D) Simulations of outside pHo (pHo in the outer solution surrounding the shell-core model) vs time and the influence of changing s/c. (E) Experimental trend of induction time ($T_{ind}$) influenced by different s/c values from a single population of µ-reactors (F) Simulation result of the same influence of varied s/c on Tind using the shell-core model in MATLAB, (G) Plot of [urea] vs time exhibiting urea transport within the core of the droplet as a function of varied s/c (0.11 vs 0.18), here Pu= $5x10^{-6}$ mm/s and Ku=0.01.*

The pH-time profile in a reactor is primarily affected by the urea transfer rate (Pu). When the permeability coefficient of urea is high, the pH in the core and outer solution are similar (**Figure 3.5** A). However, when Pu is low, the pH in the core rapidly increases to a high value while the outside pH increases more slowly (**Figure 3.5** B). The induction period, the time it takes for the pH to change, increases as the permeability coefficient of urea decreases. Changing the partition coefficient of urea does not have a significant effect on the overall trend (**Figure 3.5** C), but it does affect the induction period (**Figure 3.5** D).

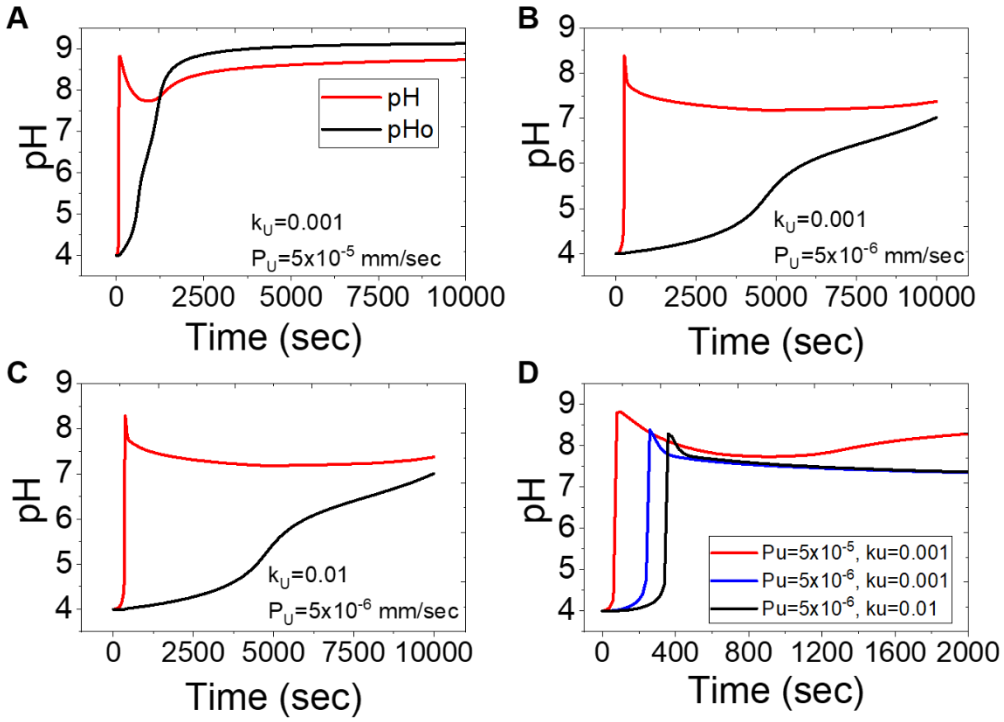


***Figure 3.5 Simulations of the pH-time profiles for urea-urease reaction in the shell-core model and the effect of changing permeability and partition coefficients of urea****, where L=20 µm , BL=7 µm, and L2=70 µm. . (A), (B) The impact of changing the permeability of urea on pH in time in the inside of core (pHi) and the outer solution (pHo), increasing the permeability (Pu= 5 x 10$^{-5}$ mm/s) results in similar pHi and pHo, whereas decreasing the permeability (Pu= 5 x 10$^{-6}$ mm/s) gives very slow or no increase in pHo. (C), (D) The pH-time profile influenced by the partition coefficient (ku) of urea, changing ku from 0.001 to 0.01 has a negligible effect on the trend of pH-time profile but shows a difference in $T_{ind}$ (D).*

The influence of changing shell size on the urea concentration inside the µ-reactor is shown in **Figure 3.6**. As expected, the model shows that as the shell becomes thinner, the transfer of urea within the core is faster and results in a rapid decrease in urea concentration, which leads to a pulse behaviour in the pH and ammonia concentration

profile. On the other hand, as the shell becomes thicker, the transfer of urea is slower, resulting in a smaller peak in the urea concentration profile, which leads to a slower formation of ammonia and slower transfer of ammonia into the outside solution, resulting in a sigmoidal trend in the pH and ammonia concentration profile.

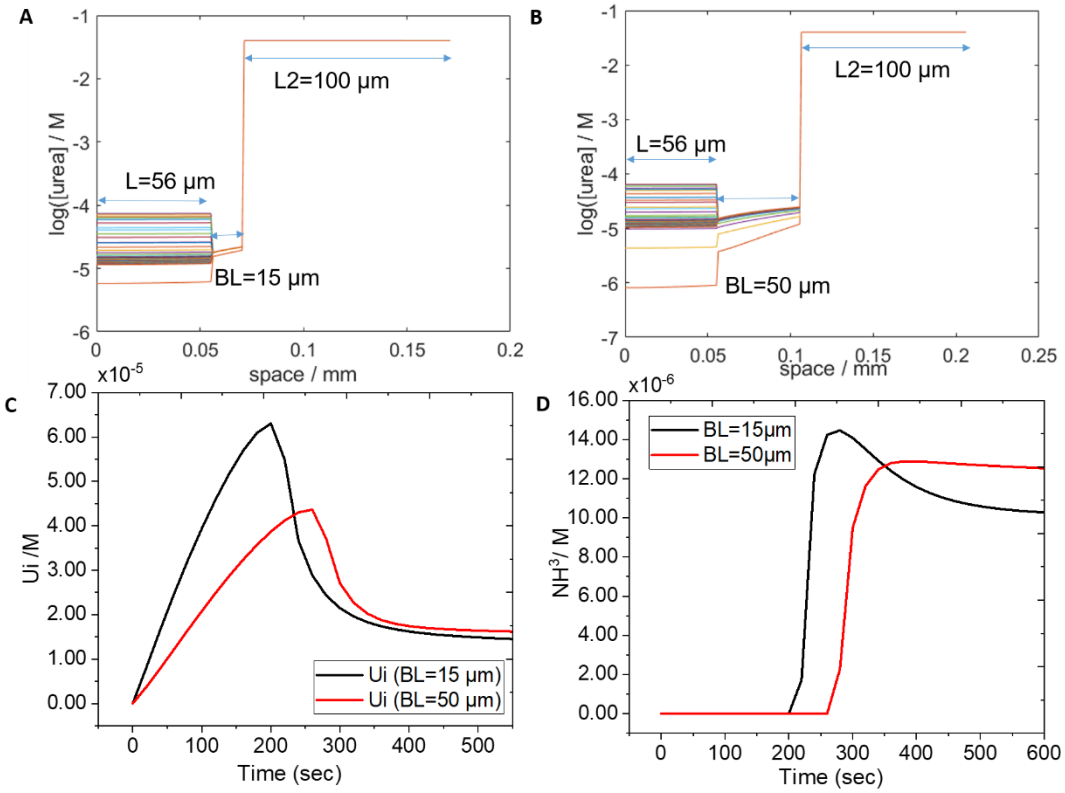


***Figure 3.6 Simulations of the shell-core model and influence of varied shell sizes on the urea transport****, where L=56 µm, L2=100 µm, and BL=15 µm and 50 µm. (A), (B) Represents the transport of urea in space from the external solution to the inner core of the shell-core model, where the coloured lines are at different time points. (C), (D) The effect of increased shell thickness (50 µm) on the urea and ammonia transport within the core, where with the 15 µm shell higher urea concentration peak is observed compared to 50 µm shell thickness which also corresponds to ammonia (concentration) peak in D, here Pu= 5x10$^{-5}$ mm/s and ku=0.001.*

### 3.7.2 Effect of Core Radius and External Solution on $T_{ind}$

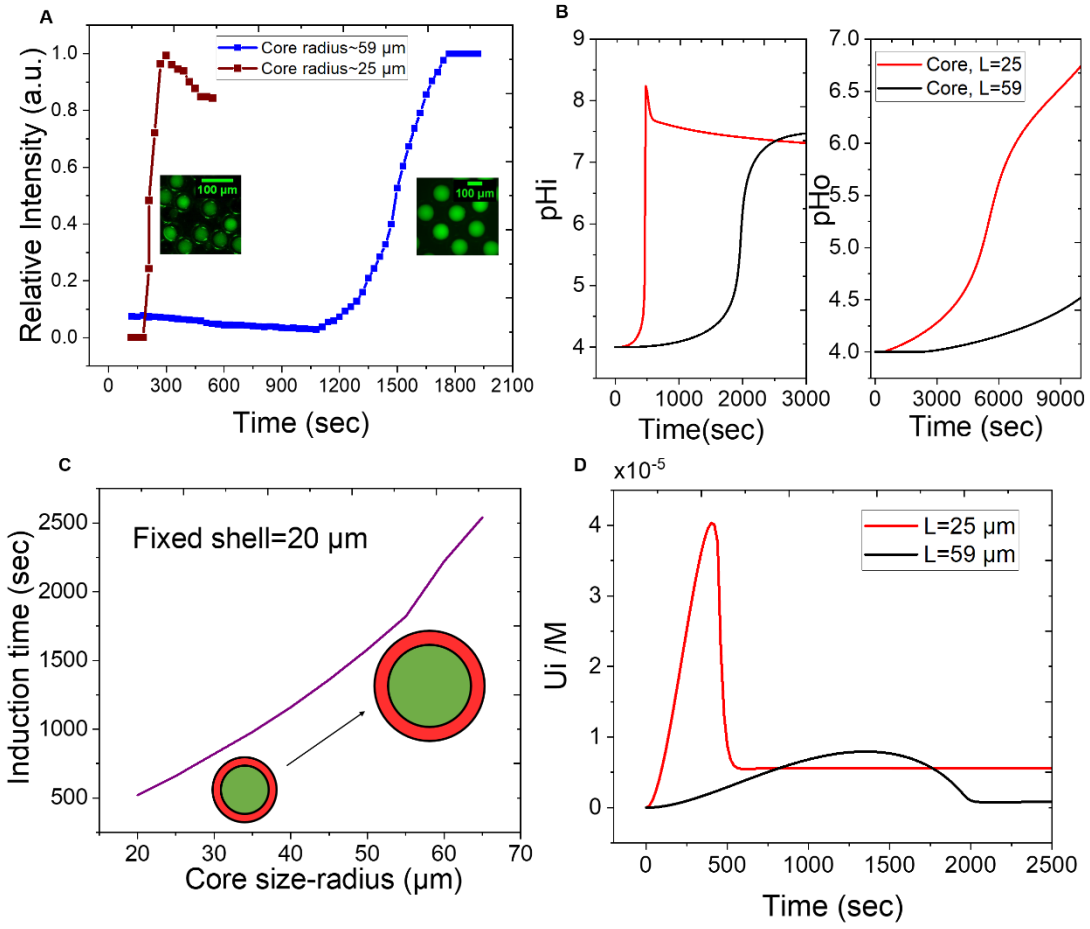


***Figure 3.7 The effect of µ-reactor core sizes on the pH-time profiles of urea-urease reaction and $T_{ind}$*** *(A) Experimental comparison of different µ-reactor core sizes on the trend of pH-time profiles, where the reaction concentrations were: [urea] = 0.04 M, [pyranine] = 50 µM, [AA] = 1 mM and [urease] = 50 units/mL, (B) Simulations of the shell-core model for comparison with experiments of the influence of different core sizes on internal pH and external pH (pHo) (C) The effect of increasing core sizes on $T_{ind}$ (D) Influence of core sizes on urea transport within the reactor core, here Pu= $5x10^{-6}$ mm/s and ku=0.01.*

Besides the shell sizes, the core sizes of the µ-reactors also showed a similar influence on the induction times and the pH-time profile; $T_{ind}$ increased with increasing core radius. **Figure 3.7** A shows two experiments with approximately the same s/c (~0.3) but different core sizes (radius ~59 µm and ~25 µm), where $T_{ind}$ was longer for the larger core reactor than for the smaller core reactor. The shell-core model also predicted a similar trend in induction times for different core sizes (**Figure 3.7** B and C). The smaller core gave a pH pulse profile, while the larger core gave a sigmoidal pH time profile (**Figure 3.7** B). The linear trend in **Figure 3.7** C was obtained by

varying the shell sizes while keeping the core size constant. The pH pulse profile observed in the smaller core reactor (**Figure 3.7** B) was likely due to a faster transfer of urea, which resulted in a more rapid increase in pH. In contrast, the sigmoidal pH time profile observed in the larger core reactor (**Figure 3.7** B) was a result of a slower increase of urea concentration inside the larger volume, leading to a slower and more gradual increase in pH over time (**Figure 3.7** D).

Furthermore, we also investigated the influence of the length scale of the external solution (L2) on the outer pHo in our simulations (**Figure 3.8**). Increasing the value of L2 increased the $T_{ind}$, which was attributed to not enough build-up of ammonia in the ES primarily due to the longer length of the external medium surrounding the micro reactor.

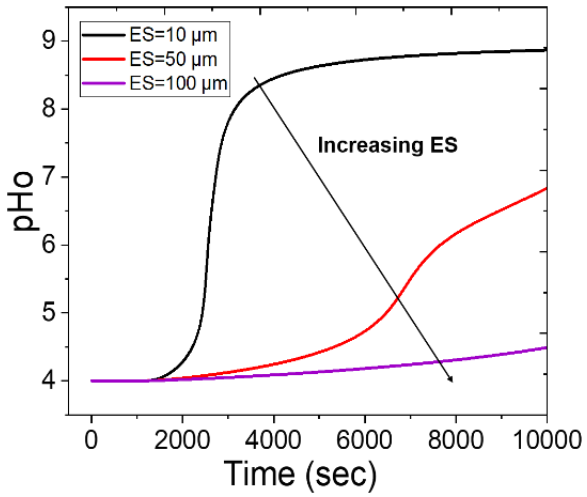


***Figure 3.8 The influence of the length scale of the external solution*** *(L2) on the outer pHo in simulations using the shell-core model. The arrow indicates the direction of increasing length scales for ES and consequently increased* $T_{ind}$.

## 3.8 Conclusion

In this work, we have simulated the kinetics of the urea-urea reaction by considering a diffusion-barrier, layered (concentric) sphere with a core encapsulating the urease enzyme and a layer consisting of a lipid-oil shell immersed in a finite external substrate medium (urea) and compared the numerical trends with our experimental results consisting of a microfluidic-assisted w/o/w double emulsion platform. We investigated the influence of the shell, shell/core, and core sizes of our W/O/W double emulsion micro-reactors on the induction time ($T_{ind}$) and pH-time profile of the urea-urease reaction. Our experimental results show that the induction time ($T_{ind}$) increased with

increasing core radius (or decreasing shell thickness), resulting in a pH pulse profile with a smaller core (or thinner shell) and a sigmoidal pH time profile with a larger core (or thicker shell). We also found that this trend was predicted by our shell-core model, which simulates the reaction-diffusion dynamics within the micro-reactor. The simulation results do not necessarily provide a quantitative comparison with the experimental results; instead, the focus is on a clear qualitative comparison of the influence of the various factors that contribute to a shift in $T_{ind}$, such as the urea transport controlled by the shell, s/c, and core size.

In summary, using the core-shell model, we have confirmed the influence of the μ-reactor configuration on the pH-time profile in addition to the influence associated with the reaction concentrations, and demonstrated relatively simple control of the $T_{ind}$ of the microfluidics-based μ-reactor platform. The size of the shell and core phases determinethe diffusion rate of the substrate urea. the W/O/W μ-reactors can be tuned using pressure flows to obtain programmable reaction times.

In addition, stimuli-triggered techniques, such as pH, temperature or light, often need external manipulation in order to apply synthetic cell models in a biomedical setting and to control communication in a spatially and temporally regulated fashion. Therefore, to fully exploit the potential of this μ-reactor platform for programmable material applications, it is important to understand how to control the output signal of the urea-urea reaction to achieve desired outcomes, such as inter-μ-reactor communication or collective behaviour. In this regard, the shell-core model qualitatively compares the transport of urea and ammonia for various configurations of μ-reactors resulting in different induction times and pH-time profiles and the W/O/W double emulsion provides a platform to better investigate more complex bioinspired processes such as biofilm formation in bacterial colonies[297,298] or to develop transient materials[299] exploiting pulse-like pH-time profiles[225,300,301].

# 4 Chemical Communication and Collective Effects in Urease Double Emulsion Systems

**Contents:**

## 4.1 Introduction

Coordinated clocks have huge significance, in the field of engineering and biology, due to the synchronisation of periodic activities between basic building components of large complex systems. In engineering, synchronisation was first detected by Huygens when he realized that two pendulum clocks oscillated in harmony when attached to a mutual support beam referred to as a coupling mechanism[302]. At a cellular level, in microorganisms, these coordinated behaviours are observed through biochemical signal communication. This chemical communication, at the sub-micron level, is described by the reaction and diffusion of a chemical signal molecule that can diffuse over a wide range of lengths and time[201]. Numerous interactive-communicating systems are based on the generation, transmission, and reception of signals (bio/chemical) between distinct microorganisms such as calcium wave dynamics and bacterial quorum sensing[303].

Two kinds of chemical communication have been recognised at a cellular level, involving active and passive transport. First, within a cell wall, bio/chemical communication is constrained to the nanometer range, and with trans-membrane proteins[207]. On the other hand, chemical reagents can spontaneously pass through biological membranes to an outer aqueous environment by diffusion[302,304]. These communicative routes have long been investigated in the field of bottom-up synthetic biology owing to the potential for complex behaviours.

In vitro study of such complex behaviour has directed the hunt towards straightforward and more controllable synthetic cell models. Towards this end, amphiphiles (notably phospholipids) capable of self-assembling into interfacial layers with void spheres have been found to be successful in simulating cellular behaviours to a certain extent. Since the membrane composition of phospholipid bilayers is similar to that of natural cells[305,64], lipid vesicles composed of self-assembled phospholipids (e.g. POPC, 1-palmitoyl-2-oleoyl-sn-glycero-3-phosphocholine) are of great interest in this context. In particular, giant unilamellar vesicles (GUVs) with the size range of 1-100 µm (comparable to most of the biological cells) have been opted as cell models[306,307]. In addition, water-in-oil (W/O) droplets, and water-in-oil-in-water (W/O/W) double emulsions with interfacial layers composed of self-assembled amphiphiles have been

demonstrated as valuable modulators of cellular structures, facilitating the investigation of the effects of compartmentalisation[308,309,310].

GUVs and emulsions are usually formulated by extrusion, either by hydration of dry lipid films or directly in bulk solution[311,312] and via electroformation [64]. More recently, some groups have adopted the bulk inverted emulsion technique (also known as the droplet transfer technique)[69,284,49,65] as this approach can be used to encapsulate diverse bio-macromolecules (such as cells, DNA, and enzymes) as well as microparticles. However, these methods lead to low yield, poor encapsulation, lack of monodispersity, and reproducibility. In contrast, droplet-based microfluidics technology[126] for the preparation of w/o/w double emulsions has been shown to be excellent for the controlled encapsulation of chemical reagents and other bio-molecules resulting in higher yields with the added advantage of monodispersity, exceptional reproducibility, and high throughput[52,232,313].

Further, in order to establish effective communication systems that display dynamic and cooperative behaviour, certain key criteria must be met. Firstly, the chemical reaction within the encapsulated system must have a non-linear mechanism that allows it to respond to outside stimuli while also generating chemical signals in a manner that can be regulated. The urea-urease reaction, in which urea is hydrolysed by the enzyme urease, satisfies these criteria and is therefore a suitable candidate for building reliable communication systems[198,186,187,271]. This reaction generates a chemical signal, $NH_3$, which shifts the pH of the system from acid to base after an induction time ($T_{ind}$), creating a feedback loop (because of the pH dependence of enzyme urease) that allows for the reaction to respond in a controllable way. The dynamic nature of the urea-urease reaction makes it an ideal candidate for building chemical communication systems, as it enables the transmission and reception of signal information through changes in pH. Secondly, the reaction should be compartmentalised in permeable membranes (as in model cells) to allow selective transport of reaction components and signal generation (reaction diffusion).

Recently, the collective behaviour of the urea-urease reaction[190] was primarily studied in giant unilamellar vesicles (GUVs), which showed that the fast transport of ammonia controlled the pH-time profile and synchronized the change in pH within the vesicles. In this context, synchronisation refers to a shift in behaviour (from low to high pH)

happening simultaneously in a heterogeneous group of vesicles. However, these studies have limitations in terms of the ability to control the reaction conditions due to lesser control over membrane permeability of $NH_3$ through the bilayer of GUVs[199]. Herein, inspired by imitation and insight of cooperative action in complex systems of living organisms, in this paper, we have developed a microfluidics-assisted W/O/W lipid stabilised double emulsions platform, which allows for greater control over the membrane permeability and diffusion of reaction components through oil-lipid layer and a more straightforward approach to studying the dynamics of acid and base changes in synthetic cell models.

We used W/O/W double emulsion template (encouraged by the work of The et al[314]), with an added advantage of pressure-driven fluid flows, using a flow-focusing microfluidic device. To begin with, control over the temporal behaviour of urea-urease (UU) reaction was observed in individual µ-reactors with a distribution of induction times ($T_{ind}$) for the first time (chapter 3). This pH-triggered double emulsions platform can be used to tune system dynamics by tailoring the middle oil-lipid layer to control the diffusion of reagents.

However, we also observed that the individual dynamics could be influenced by the other cells, or bursting cells, in a group, under some conditions. The urea-urease reaction within the core of µ-reactors results in the production of ammonia (base); this then diffuses out of the core and into the outer solution of the droplet and thus causing a rise in pH in the surrounding solution and eventually influencing the rate of urease catalysed urea hydrolysis (enzyme rate dependence on pH)[187] in the neighbouring µ-reactor droplets. This creates a cascade influence, where the production of ammonia in one droplet can trigger the production of ammonia in neighbouring droplets, leading to a synchronized and collective behaviour across a group of droplets. Additionally, the substrate urea concentration influences the overall ammonia production which in turn is responsible for collective behaviours within the population of µ-reactors. The concentration of urea was changed to observe the influence of overall ammonia production and the associated behaviour. When the concentration of urea is low, the reaction rate slows down and leads to a decrease in an overall ammonia production. This results in each emulsion droplet acting independently. On the other hand, high urea concentrations result in an increase in ammonia production with the faster rate of reaction which results in synchronous group behaviours in a population of µ-

reactors. This change in pH is detected by the pyranine indicator and serves as a means of transmitting information through the system, acting as a chemical communication. The concentration of urea plays a role in determining the overall production of ammonia which in turn defines the trends of the urea-urease reaction in the double emulsion system, leading to either separate or communicative behaviour.

In addition to the influence of the substrate urea concentration, the number of μ-reactors within the double emulsion system also has an impact on the behaviour of the urea-urease reaction within the μ-reactors. A higher number of μ-reactors leads to an increased reaction rate because of an increased overall production of ammonia resulting from different μ-reactors, which can result in a more pronounced increase in overall pH. This allows the double emulsion system to act as a chemical communication cell system, transmitting signal (ammonia) more effectively. The density dependent behaviour is reflective of certain micro-organisms, such as bacteria and yeasts where populations of micro-organisms undergo transitions to coordinated activity using extracellular signalling[315,283]. The tailored control of the urea-urease reaction in the double emulsion system allows for on-demand chemical communication, offering potential applications in engineering, materials science, and medicine through the integration of pH-stimulated processes, such as cell density-driven biofilm formation or biomineralisation, inspired by bacteria.

## 4.2 Experimental

### 4.2.1 Chemicals

The following stock solutions were prepared: urea (66612-1KG, M.W. 60.1, Sigma) [urea] = 0.6 M, acetic acid (100% glacial acetic acid, Sigma) [$CH_3COOH$] = 0.05 M, urease (type III Jack bean U1500-20KU, 25920 units/g solid, Sigma) [urease] = 400 Units/mL, 8-hydroxypyrene-1,3,6-trisulfonic acid (pyranine, cat no. L11252.14, M.W. 524.39, Alfa Aesar) [pyr] = 0.2mM, 1-Palmitoyl-2-oleoyl-sn-glycero-3-phosphocholine (P516-250mg, Anatrace) [POPC] = 6.5 mM in mineral oil (MO), mineral oil (molecular biology reagent: a mixture of liquid hydrocarbons, M5904-500mL, density 0.84 g/mL at 25℃, Sigma), sorbitan monooleate (SPAN-80, 85548-250 mL, viscosity 1000-2000 mPa.s at 20 ℃, M.W. 428.60, density 0.986 g/mL at 25 ℃), nilrot (nile red, M.W. 318.37, sigma), glucose (G5400-1Kg, D-(+)-Glucose, minimum 99% GC, molecular

biology tested, M.W. 180.16, Sigma) [Glucose] = 1M, sucrose (≥ 99.5% GC, molecular biology tested, M.W. 342.30, Sigma) [Sucrose] = 1 M, Pluronic F-127 (powder, suitable for cell culture ,sigma) [PF127]= 2%, glycerol (87%, Sigma) [glycerol] = 20%, poly vinyl alcohol (P8136-250G, 87-90% hydrolysed, avg. M.W. 30,000-70,000, Sigma) [PVA] = 1%.

The urease solution was made every day. The enzyme units, expressed in units/mL, were calculated using the urease activity printed on the packaging (25920 units/g, average) (1U corresponds to the release of 1.0 µmol ammonia from urea in one minute at pH 7 and 25℃). Pyranine is the fluorescent probe selected for observing the pH variations and Nile red is a dye used to localize the lipids. Distilled water was used to prepare the stock solutions. All the reagents were of analytical quality and were used without additional refining.

### 4.2.2 Synthesis of W/O/W Double Emulsions Using a Flow-focusing Droplet Microfluidic Technique

#### 4.2.1 Microfluidic Technique

We used a flow-focusing microchannel device with two droplet formation junctions to synthesize double emulsions (**Figure 4.1**). A pressure-driven pump (OB1 MkIII+, Elveflow, Paris, France) was used to transport solutions at a persistent flow. Three different solutions were prepared: inner aqueous solution to encapsulate enzyme and pyranine (IS), middle lipid-oil solution (MF), and outer aqueous solution (OS). The lipid solution (middle flow in the microchannel, MF) contains 6.5 mM POPC dissolved in mineral oil (MO) and 2% SPAN-80 by sonication for three hours at room temperature using an ultrasonic bath (FB15051, Fisherbrand). The inner solution (IS) contains sucrose (0.2 M), pyranine (60 µM), urease (50 Units/mL), acetic acid (1 Mm), and pluronic F-127 (0.28%). The concentration of urease and acetic acid was varied for a few experiments. The outer solution (OS) holds glucose (0.2 M), glycerol (20%), pluronic F-127 (0.28%), acetic acid (1 mM). Glycerol was incorporated in the OS to increase the viscosity of the aqueous phase to enhance the shearing of the oil by the continuous phase. Glycerol has also been revealed to interplay with lipid bilayers and help in the reduction of membrane flexibility and boost strength[316]. Pluronic F127 is

used in IS and OS as a surfactant to prevent coalescence and increase the stability of the double emulsions [317].

Water in oil droplets were formed at the first junction of the flow-focusing device by running the IS at $P_{IS}$ = 40 mbar and the MF at $P_{MF}$ = 85 mbar, however, the flow pressures were varied with a fixed ratio of $(P_{MF}/P_{IS}) \sim 2-3$. Double emulsions were obtained at the second junction by shearing the W/O droplets produced at the first junction with the OS at $P_{OS}$ = 25 mbar. A complete schematic representation of the droplet formation is given in **Figure 4.1**.

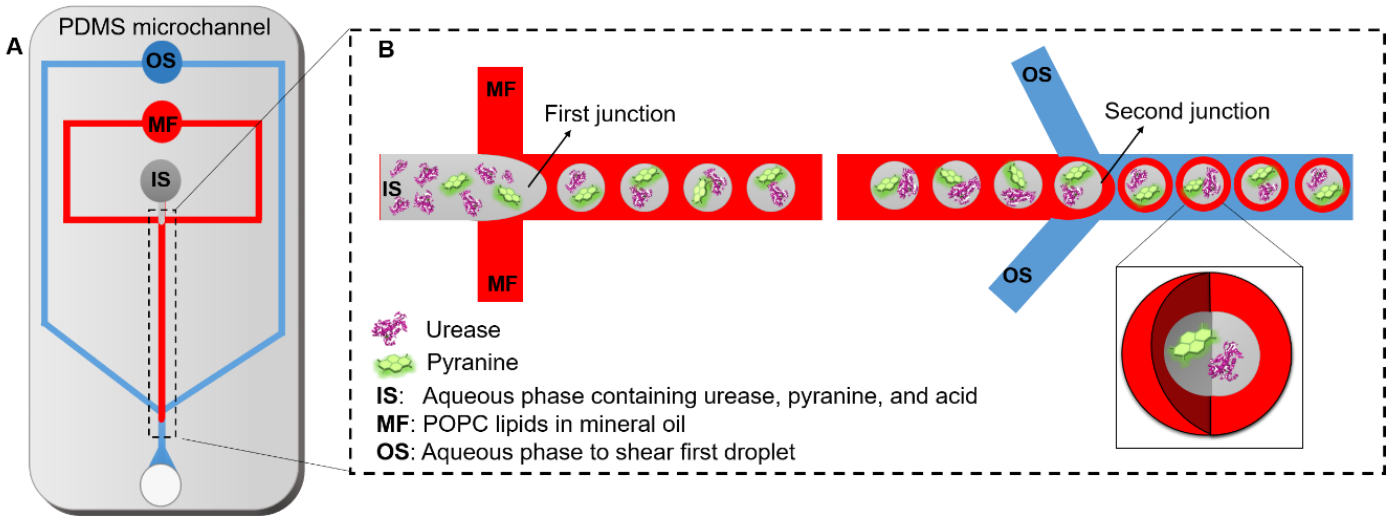


***Figure 4.1 The design of the platform consists of PDMS-formed channels.*** *There are two flow-focusing junctions arranged in sequence to create water-in-oil-in-water double emulsions. (A) Schematic representation of the microfluidic device exhibiting three inlets (OS, MF, and IS), two flow focussing junctions (first (w/o) and second (w/o/w) junction). (B) A close-up schematic of single and double emulsion synthesis. First, water in oil (w/o) droplets are formed when the inner aqueous solution (IS) containing enzyme urease, acetic acid, and pH indicator (pyranine) is sheared by the continuous phase comprising of POPC (6.5 mM) in minral oil and span-80 (2 %) at the first junction, which then enters the second junction where this stream of droplets is sheared by a flow consisted of an outer aqueous solution (OS) containing glucose (0.2 M), glycerol (20%), pluronic F-127 (0.28%), acetic acid and resulted in the synthesis of double emulsions at the outlet of the PDMS chip. The pressure flows for IS, MF, and OS were $P_{IS}$ = 40 mbar, $P_{MF}$ = 85 mbar, and $P_{OS}$ = 25 mbar, respectively, with a fixed ratio of $(P_{MF}/P_{IS}) \sim 2-3$*

### 4.2.2 Reaction Monitoring, Imaging, and Analysis

The W/O/W double emulsions were collected from the outlet Eppendorf tube. The collected double emulsions were mixed with an external solution (ES) containing acetic acid, glucose, and urea in a separate Eppendorf tube. The reaction was observed immediately infusing 1 µL of the mixed solution (containing double emulsions and ES) into a deep observation chamber (200 µm) assembled from clean and rinsed glass slide, coverslip, and double-sided tape. The protocol was run on the epifluorescent microscope (LS560 Microscope, green fluorescence, and brightfield, green filter: excitation 457-493 nm; emission 508-552 nm, etaluma). For, the effect of number of cells, a series of eight different experiments were performed under approximately similar lab and instrumental (microscopic) conditions, as such the number of emulsions were different in each experiment, this was executed by carefully pipetting the sample of emulsions mixed with the ES (containing urea, AA, and glucose). The protocol was run on the microscope with the fixed settings of gain = 3.750, illumination = 7.8 %, and exposure = 15.9 using 4x and 10x magnification to compare the induction times and average intensity.

The analysis of the time-lapse images was achieved with Matlab codes (Matlab R2019b) developed to track individual emulsions, the code was adapted based on the extent of droplet motion in an experiment. In short, the code is used to process a set of images by detecting circular droplets in each image. The position of the center of the detected circle is compared to the center of the circle detected in the prior image to track the dropletsin the images. The code also calculates the intensity of each circle/droplet in each frame and stores the data for later analysis, additionally specifying the ‘induction times($T_{ind}$)’ as the maximum rate of change of intensity (Matlab code for image tracking is given in the Appendix section 7.4).

## 4.3 Results

### 4.3.1 Enzyme Encapsulated µ-reactors as Platform to Tune Feedback-driven Induction Reactions of Urease Catalysed Hydrolysis of Urea

The microfluidics assisted µ-reactors-based platform was selected to investigate the pH-switch of urea-urease (UU) reaction. Due to better encapsulation of reaction components of the inner solution (IS) and higher yield[207], we synthesized W/O/W

double emulsions using the two-junctions flow-focusing microfluidic device. Subsequently, we encapsulated enzyme urease, acetic acid, and pyranine.

### 4.3.2 pH-induced Chemical Communication of Double Emulsions

The characteristic bell-shaped rate-pH curve of enzyme reactions linked to the formation of acid/base can lead to faster rate and a feedback-controlled response. In a base-forming reaction, if the initial pH is tuned by the introduction of acid so that the rate is first low, the rate speeds up with the formation of bases until it reaches the peak given by the bell-shaped rate-pH curve (as shown in **Figure 4.2** A). For example, the urea–urease (UU) reaction, widely studied [179,190], is urease (a nickel based enzyme) catalysed hydrolysis of urea, that yields ammonia and carbon dioxide. Since the reaction generates a base ($NH_3$), the reaction progresses, peaking at pH ~7 and dropping to ~zero at pH ~10. Base-catalysed feedback and a pH induction period are observed in this reaction by setting to a low initial pH. Here, pH “induction” refers to a reaction that displays a maximum rate of production of base ($NH_3$) at some nonzero extent of reaction. A kinetically induced change in pH is therefore monitored after a lag time, which is called the induction time ($T_{ind}$).

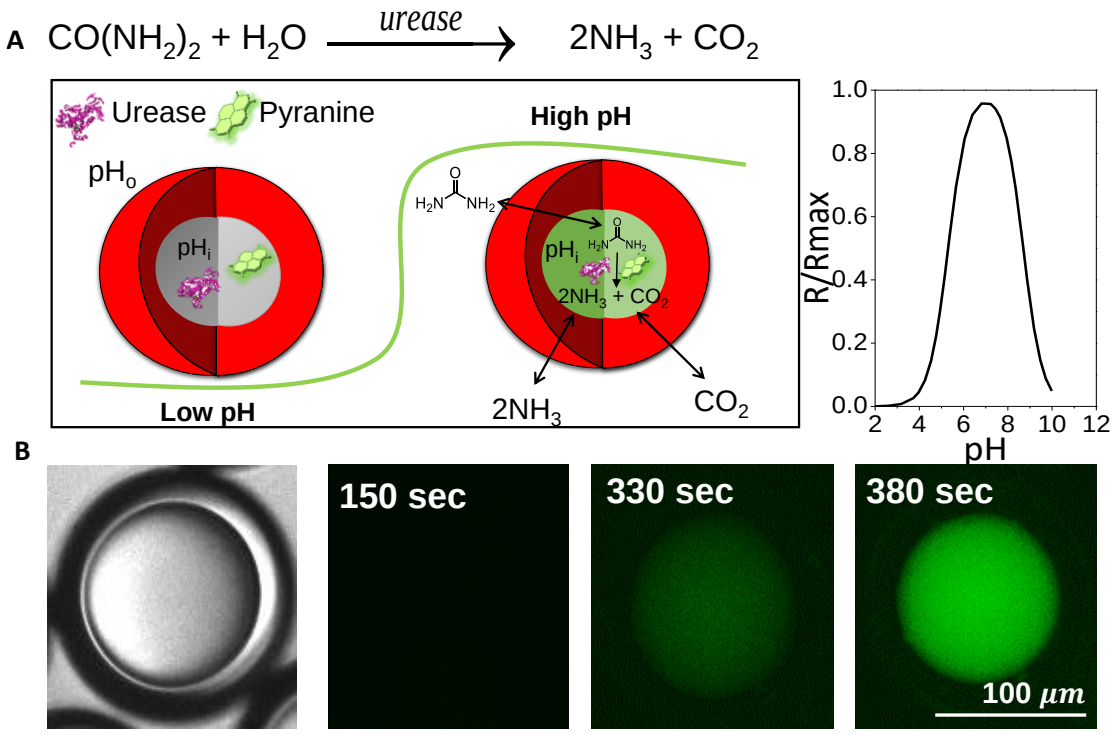


***Figure 4.2 Feedback-driven urease-catalysed urea hydrolysis reaction (UU) within W/O/W-based μ-reactors.*** *(A) A schematic illustration of reaction progression within water-oil-water (W/O/W) μ-reactors indicating no fluorescence at the start of the reaction (grey coloured core) with the corresponding low initial rate indicated by the stable low pH (green sigmodial curve) adjusted with the addition of acetic acid. There is an increased bright green fluorescence as urea in the external solution permeates through lipid-oil layer (red) into the core (green) of the μ-reactor and produces ammonia and carbon dioxide. The rate dependence of the UU reaction on pH; rate accelerates due to the formation of base ($NH_3$) until it reaches the maximum (~7) and then drops, given by the bell-shaped rate-pH curve, a so called feedback-driven process. (B) Fluorescence imaging of a single emulsion droplet mixed with external solution (ES) containing urea and acetic acid, and added to microscopic slide to observe urease catalysed hydrolysis of urea. The reaction concentrations were: [urea] = 0.04 M, [pyranine] = 50 μM, [AA] = 1.5 mM, and [urease] = 40 Units/mL, epifluorescent microscope (LS560 Microscope, green fluorescence, and brightfield, green filter: excitation 457-493 nm; emission 508-552 nm, etaluma), and scale bar = 100 μm*

The schematic presented here (**Figure 4.2** A) illustrates the urea-urease reaction occurring within a W/O/W double emulsion-based μ-reactor. The μ-reactor contains enzyme urease and pyranine within the core, which were added in the inner solution of microfluidic channels. We used pyranine as a fluoroprobe to measure the change in pH due to the formation of ammonia inside the μ-reactors (double emulsions). At low pH (adjusted using acetic acid), no pyranine is visible, however, as the urea (substrate) which is present in the outer aqueous phase of the double emulsion

diffuses through the oil-lipid layer into the inner aqueous core of the µ-reactor, the enzyme urease then catalysis the hydrolysis of urea, producing ammonia and carbon dioxide as the main products. The resultant base ($NH_3$) increased the pH in the inside of the µ-reactor after an induction period ($T_{ind}$) which is observed by the increase in green fluorescence of pyranine (**Figure 4.2** B). This scenario arises because of the presence of feedback: rate acceleration due to the base-catalysed production of base ($NH_3$), with the maximum rate of reaction at pH~7. The ammonia then diffuses out of the inner core of the aqueous droplets, through the oil-POPC membrane, and into the outer solution. The unique structure of this µ-reactor system enhances reaction control compared to traditional batch reactions.

**Figure 4.3** A, shows a finite population size of µ-reactors in an observation chamber (composed of 200 µm double sided tape on a glass slide and covered with a cover slip) under an epifluorescent microscope. The green color represents the reaction or the formation of product ammonia visualized through pyranine. The corresponding fluorescence intensity vs time plot (**Figure 4.3** B) for the selected µ-reactors is shown in Figure 3 A. We observed a wide distribution of induction times ($T_{ind}$) for the W/O/W-based µ-reactors. The widely distributed induction periods highlighted that the pH-time profile across the entire platform of µ-reactors is unique to each individual µ-reactor rather than a synchronous and homogeneous response. **Figure 4.3** C gives a distribution of induction times across the population of µ-reactors within the same experiment. **Figure 4.3** D shows the variation in fluorescence intensity in space (selected in **Figure 4.3** A, yellow line), indicating a reaction time lag between neighbouring µ-reactors, with peaks appearing at different locations and times along the selected length scale, suggesting that the reaction in one µ-reactor has negligible influence on the neighbouring reactors.

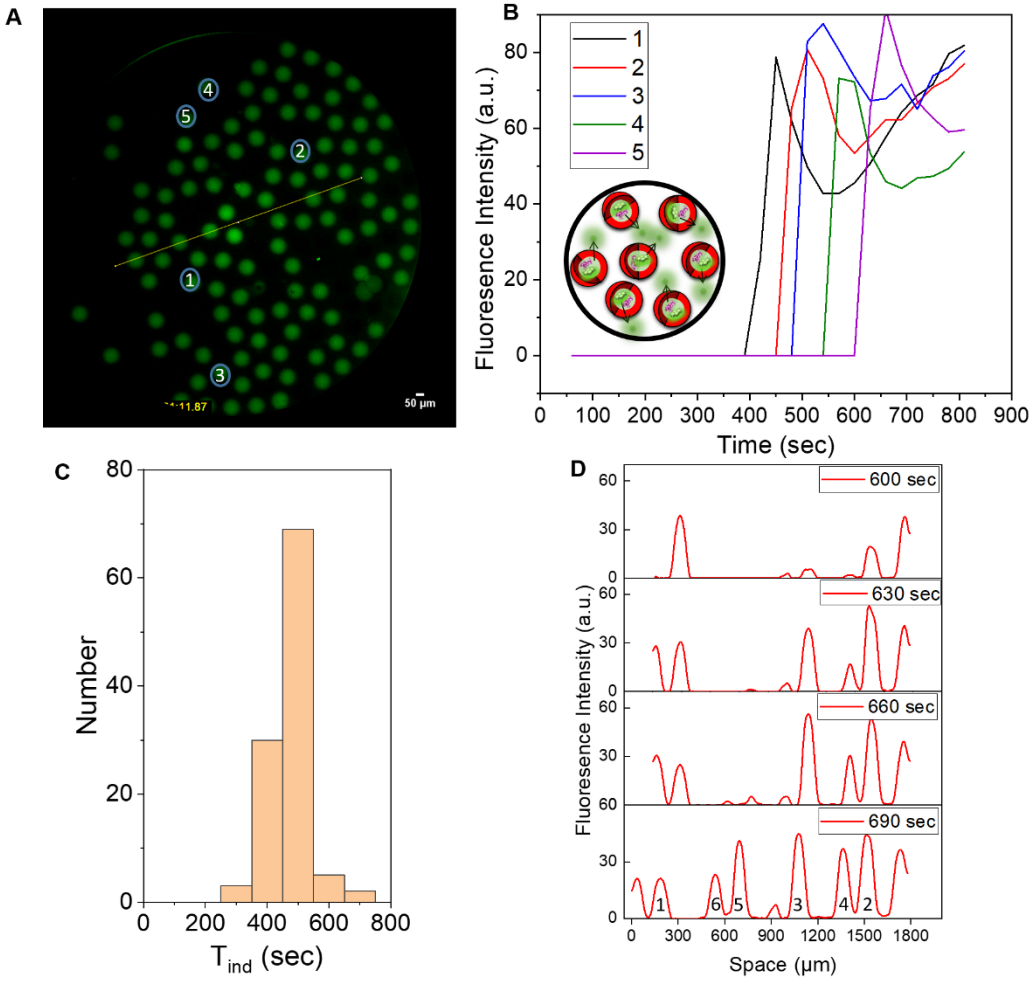


***Figure 4.3 Individual pH induction times in a population of W/O/W emulsions with core diameter~100 μm*** *(A) Fluorescence microscopic image of the sample of emulsions mixed with external solution (ES) and added to a microscopic slide to observe urease catalysed hydrolysis of urea. (B) Fluorescence intensity of the emulsions in time when added to an ES solution corresponding to the selected μ-reactor in A, showing a distribution of the induction times. (C) Plot of the induction time ($T_{ind}$) vs the number of μ-reactors indicating wide range in induction times in a population of μ-reactors. (D) Fluorescence intensity in space (for the selected yellow line in A) specifying a reaction time lag between neighbouring μ-reactors with peaks appearing at different points and time for the selected length scale. The numbering on the peaks indicates the order of the peaks appearing along the yellow selected line in A. The reaction concentrations were: [urea] = 0.04 M, [pyranine] = 50 μM, [AA] = 1.5 mM, and [urease] = 40 Units/mL, and scale bar = 50 μm.*

A transition to synchronisation (similar induction period) or wave behaviour was observed with the bursting of some μ-reactors which is caused by the instability of the double emulsions. **Figure 4.4** A shows an enlarged section in which some of the μ-reactors burst, leading to the escape of the core components (urease and pyranine)

and thus enabling the initiation of the reaction at the bursting site. The resulting product ammonia formed at this site influences the neighbouring µ-reactors through the external solution and leads to their synchronisation due to the feedback behaviour of the UU reaction. Wave behaviour was observed originating from droplet 1 next to two burst sites as shown in **Figure 4.4** B, which shows wave-like appearance of intensity peaks in one direction along the length of the selected yellow line. Additionally, **Figure 4.4** C shows a group behaviour between adjacent µ-reactors (selected yellow line) where all µ-reactors tend to respond synchronously due to the diffusive coupling of the ammonia signal (evident by a lower standard deviation of $T_{ind}$ in **Figure 4.4** D in droplets at the location of the burst sites compared to the separate, non-burst region). It is assumed that this collective behaviour arises through communication by means of chemical signals ($NH_3$) via an external solution. In this context, urease acts as the sender machinery, producing diffusive signaling molecules in response to the stimulus (substrate urea), the signaling molecule being ammonia ($NH_3$) which acts as a membrane-permeable molecule and raises the pH. Pyranine, on the other hand, acts as the receiver machinery, exhibiting a fluorescent output as a result of the communication process.

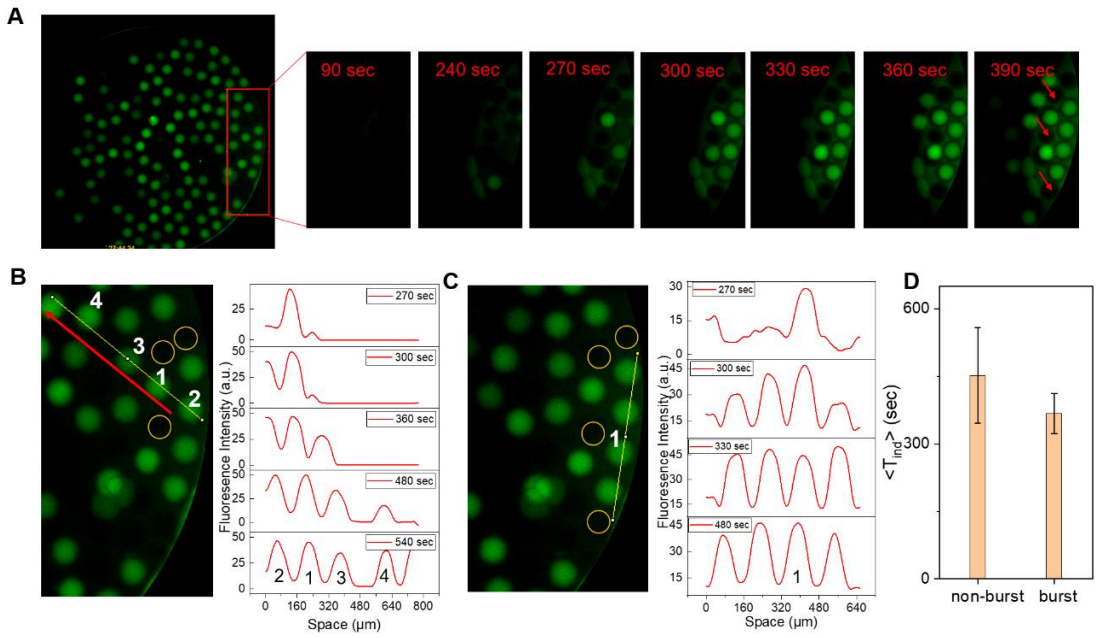


***Figure 4.4 Transition to synchronised behaviour and the influence of the µ-reactors bursting on induction times*** *(A) A zoomed-in section (red box) of figure 3 in which some of the µ-reactors burst (shown by red arrow), leading to the leaking of the core ingredients (enzyme urease and pH indicator pyranine) and thus enabling the initiation of the reaction at the bursting site. (B) Transition to wave behaviour of UU induction reactions (shown by red arrow pointing in the direction of wave, yellow circles*

*indicates the bursted emulsions) originating from the burst site, indicating wave-like appearance of intensity peaks, intensity vs space plot, in one direction along the length of the selected yellow line (C) Intensity-space plot indicating the group behaviour between adjacent µ-reactors (selected yellow line) where all µ-reactors tend to react synchronously after the initiation of the reaction in first µ-reactor (numbered 1) due to the increased diffusive coupling of the ammonia signal, here the yellow circles indicates the bursted emulsions (D) Comparison of the average induction reaction of the bursted region (red box in A) compared to the separated, non-burst region and standard deviation (error bars) in the induction times in the respective regions.*

Although in general, we observed wide distributions in induction times ($T_{ind}$) within the population of stable µ-reactors (**Figure 4.3**) there is an influence of substrate urea concentration on the average $T_{ind}$ within apopulation of µ-reactors. At high urea concentrations, the reaction kinetics are accelerated, leading to an increase in the rate of ammonia production and thus a subsequent shift in pH both inside and outside of the µ-reactor due to the diffusive coupling of the µ-reactors through ammonia signal.

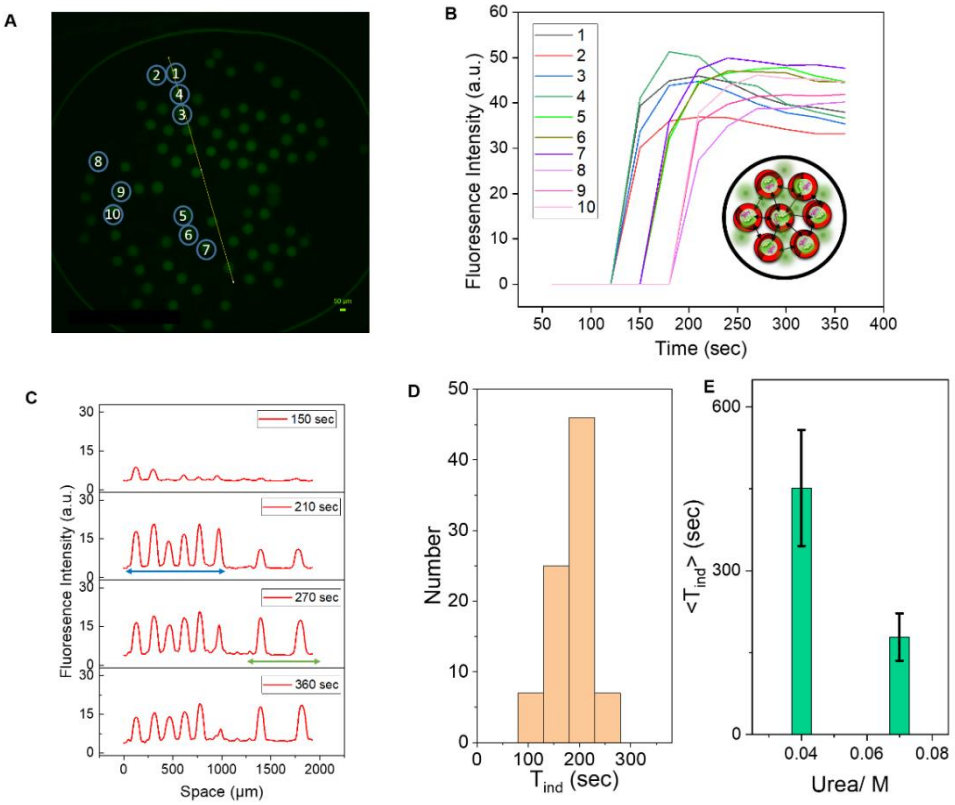


***Figure 4.5 Local chemical synchronisation and influence of urea concentration**. (A) Fluorescence microscopic image of the sample of emulsions mixed with external solution (ES) and added to microscopic slide to observe urease catalysed hydrolysis of urea with [urea] = 0.07 M. (B) Fluorescence intensity of the emulsions in time when added to an ES solution containing urea and acetic acid corresponding to the selected µ-reactors in A, showing a clustered group behaviour of intensity-time profiles and induction periods at different sites of the reaction chamber (C) Fluorescence intensity in*

*space (for the selected yellow line in A) indicating a synchronous appearance of peaks for the neighbouring µ-reactors for the selected length scale and showing a local synchronisation with six peaks (blue coloured arrow, upper part of the yellow line) appearing first at approximately the same time followed by the appearance of two peaks afterwards (green coloured arrow, lower region of the yellow line) (D) Plot of the induction time ($T_{ind}$) vs the number of µ-reactors signifying a range in induction reaction in a population of µ-reactors which exhibits local synchronisation (E) Comparison of the average induction reaction of the µ-reactor populations with different concentration of urea ([urea] = 0.04 M and 0.07 M) and standard deviation (error bars) in the induction times in the respective poplulations. The reaction concentrations were: [urea] = 0.04 M or 0.07 M, [pyranine] = 50 µM, [AA] = 1 mM, and [urease] = 50 Units/mL, and scale bar = 50 µm.*

**Figure 4.5** demonstrates the impact of increased urea concentration (0.07 M) on the behaviour of the neighbouring micro-reactors. The Intensity-Time plot in **Figure 4.5** B of the selected µ-reactors (illustrated in **Figure 4.5** A) reveals a similar trend and $T_{inds}$ among the neighbouring micro-reactors in groups 1 – 4; 5 – 7; 8 – 10. **Figure 4.5** C presents the intensity peaks plot in space (as indicated by the yellow line in **Figure 4.5** A), exhibiting a more collective behaviour where peaks occur at the same time along the space, in contrast to the discrete trend observed at a lower urea concentration (0.04 M, depicted in **Figure 4.3** D). The group behaviour is further emphasized by the small standard deviation in $T_{ind}$ for the higher urea concentration (0.07 M), as compared to the higher standard deviation in $T_{ind}$ for the lower urea concentration (0.04 M) shown in **Figure 4.5** E. However, this transition to synchronous behaviour, influenced by diffusive interactions of the ammonia signal through the common external solution medium, is local rather than global, as demonstrated by the lag time in the intensity time profile between different groups of µ-reactors within the same population (**Figure 4.5** B) as well as with the varied $T_{ind}$ vs. number plot in **Figure 4.5** D.

### 4.3.3 Chemical Communication as a Function of Number of µ-reactors

In addition to the influence of bursting and increased urea concentration, the group behaviour was also observed with an increase in the number of µ-reactors, indicating that the reaction dynamics within the double emulsion system can be influenced by multiple factors. In broader sense, this type of group behaviour can also be referred to as density-dependent behaviour, where the overall trend is influenced by the number of cells/µ-reactors involved, per unit volume of external solution. We have observed,

experimentally, the changing induction time ($T_{ind}$) of the reaction in response to the number of double emulsions as shown in **Figure 4.6**.

The more µ-reactors, the faster the induction time was observed. As presented in **Figure 4.6** B, the $T_{ind}$ for 82, 66, 26, and 19 emulsions were 180 sec, 420 sec, 570 sec, and 1020 sec, respectively, with no reaction in the case of 3 emulsions, and the trend was confirmed with a different set of the number of µ-reactors again, given in Appendix section 7.4.2 and **Figure 7.15**. The perceived correlation between the increased overall $T_{ind}$ and the number of emulsions (**Figure 4.6** C) might be explained by enhanced local communication due to ammonia signals with a high density of emulsions (closely packed). In other words, increased spatial proximity contributed to pronounced ammonia build-up and diffusion, thus, resulting in a faster change in overall reaction dynamics (faster induction time)[283]. Although the $T_{ind}$ decreases as the number of µ-reactors increases, there was still variation in induction times within the same population of µ-reactors (see standard deviations in **Figure 4.6** C).

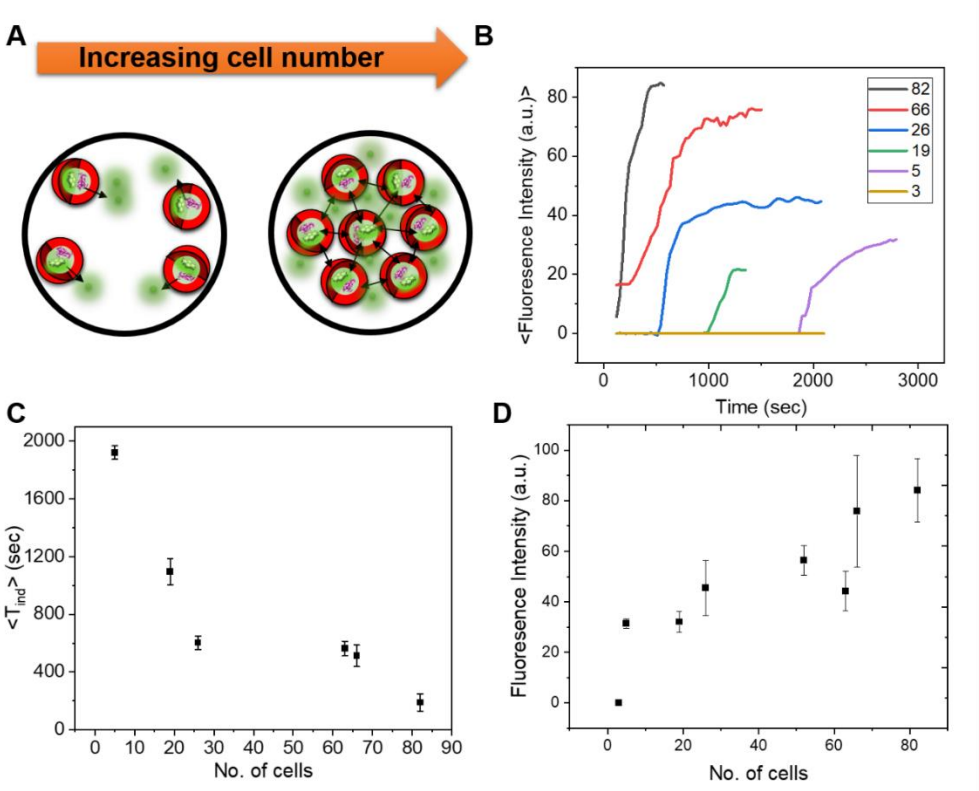


***Figure 4.6 Density-dependent behaviour of induction times*** *(A) Schematic representation of the influence of the number of emulsions on the induction time of the reaction (B) Intensity vs Time profile for comparing the avg. induction time for six setswith different number of emulsions (C) The trend of induction time vs no. of emulsions (cells) (D) A plot of the maximum intensity vs number of emulsions/cells. The reaction concentrations were: [urea] = 0.04 M, [pyranine] = 60 µM, [AA] = 1 mM,*

*and [urease] = 50 Units/mL. The protocol was run on the epifluorescent microscope (LS560 Microscope, green fluorescence, and brightfield, green filter: excitation 457-493 nm; emission 508-552 nm, etaluma) with the fixed settings of gain = 3.750, illumination = 7.8 %, and exposure = 15.9 using 4x and 10x magnification to compare the clock times and average intensity.*

As the experiments were performed in controlled conditions of microscopy, we plotted the number of emulsions/cells vs maximum fluorescence intensity (**Figure 4.6** D) and obtained a similar trend as in the case of number vs induction time.

## 4.4 Discussion and Conclusions

Different synthetic cell models have been used to investigate synchronised behaviours or chemical communication, such as emulsion microdroplets, catalytic particles, and vesicles[318–321]. In all these systems, the collective behaviour is believed to arise through communication by chemical signaling via the extracellular solution. The oscillations were mainly observed in the inorganic Belousov−Zhabotinsky (BZ) reaction, for example, using catalytic microparticles, in which catalyst for the reaction, $Fe(phen)^{2+}_3$ (ferroin) is immobilized on the cation exchange particles, placed in a catalyst-free BZ solution[320,322]. The system of porous catalytic particles and BZ reaction solution exhibits oscillations with the period depending on the catalyst loading, particle size, and the diffusion of products between the particles and BZ solution. In addition, a transition to synchronisation was observed when subjected to varied exchange/transfer rates (under different stirring rates) of catalytic particles and BZ solution. Different behaviours emerged at low and high transfer rates, highlight the importance of transport rate of signalling species which can play a critical role in determining the emergent behaviour of populations of chemical oscillators. While the principles of synchronisation and coupling elucidated in this study may have broader implications for understanding biological oscillators[323,324], for example in the suspensions of the cellular slime mold *Dictyostelium discoidium* and oscillatory behaviour in suspensions of yeast cells [325,326], the specific experimental setup using cation exchange resin particles may not fully capture the mechanisms of transport in biological systems.

However, the robustness of naturally occurring biochemical clocks is of significant importance given their important role in regulating biological processes. For this reason, researchers have explored the use of microdroplets or vesicles containing

DNA and RNA (an in vitro fluorescent transcriptional oscillator), as well as protein oscillators that are more biologically relevant[327,328], but with all reactive species confined within these structures. On the other hand, the enzyme urease encapsulated within the semi-permeable micro-compartments (vesicles and polymersomes) allows the diffusion of products: neutral acidic ($CO_2$) and basic products ($NH_3$), into the surrounding solution. For example, Che et al.,(2018)[200], used a pH feedback mechanism (urea-urease reaction) to control the "breathing" behaviour of the polymersomes, which allowed them to regulate the flow of molecules into and out of the vesicles. The polymersomes contained urease and HRP enzymes (model enzyme to detect the enzyme activity as a function of membrane permeability/addition (or blockage) of substrate for reaction), and their size and membrane permeability change in response to changes in pH triggered by the urease enzyme. The polymersomes switch between an "ON" and "OFF" state in response to the presence or absence of chemical fuel (urea). The authors suggest that the gradual increase in pH over time, due to the conversion of urea into ammonia, leads to the polymersomes returning to their initial contracted state and the enzyme catalysis spontaneously changing to "OFF" again. However, the pH-time profile of the solution and the intensity-time plot of the polymersomes indicate that the increase in pH is fairly identical inside and outside the polymersomes and that ammonia accumulates rapidly everywhere.

In another study, the collective behaviour of the urea-urea reaction in giant unilamellar vesicles (GUVs) was investigated, showing that the rapid transport of ammonia controls the pH-time profile and synchronises the pH change within the vesicles. In this context, synchronisation concerns a behavioural change (from a low to a high pH) that occurs simultaneously in a heterogeneous group of vesicles[199]. The results of these studies showed a more gradual increase in pH within the vesicles compared to aqueous-phase experiments, with the similar timing of the pH switch in each vesicle and a small standard deviation in each experiment, suggesting a synchronized switch in pH. However, these studies have limitations in terms of the ability to control reaction conditions, as the membrane permeability of $NH_3$ is less well controlled by the bilayer of GUVs[199] and in general achieve synchronisation due to quick build-up of ammonia (fast transport) in the surrounding solution which is responsible for synchronous/collective responses. Since methods for producing vesicles typically result in a distribution of sizes and enzyme content, however, a slight difference in pH

induction time in individual vesicles can be anticipated in the absence of a collective response[329,330].

It has also been suggested that the synchronisation or collective response is due to the influence of cell density. This is of great importance in nature because, for example, the increase of cell density in bacteria causes the formation of biofilm and bioluminescence which intend to protect the bacterial cells against antibodies.[315] In addition, microorganisms, dictyostelium discoideum as an example, exhibit synchronised chemical oscillations that are density-dependent[298,331]. In another article, Taylor and co-workers, investigated quorum sensing of enzyme microparticles which were diffusively coupled with each other, using the autocatalytic urea-urease reaction model. They aimed to obtain the dynamic response with changing group size of microparticles under the conditions of reaction-diffusion[283].

Here, we investigated the urease-urea reaction in a water-oil-water (W/O/W) double emulsion obtained using a microfluidic platform for encapsulation of urease. The autocatalytic feedback production of ammonia after an induction time ($T_{ind}$) in the reaction is the selected chemical signal. This reaction is used in many biological systems, e.g. bacteria in the stomach (*H. Pylori and P. Mirabilis*) use urease to hydrolyse urea to ammonia, which raises the pH and thus prevents problems with acid formation. Control of the pH-time profile in the ~100 µm droplets was achieved by manipulation of the oil shell to core ratio and hence diffusion timescale of substrate urea and product ammonia through the oil layer. This resulted in a system of microreactors acting as individual units with distinct induction periods ($T_{ind}$) for the first time. We showed that in contrast to other systems, the release of ammonia can accelerate the reaction in all the droplets but there is no evident synchronisation of activity as there was a wide distribution of induction times across the population of micro-reactors. The individual behaviour can be influenced by various parameters, highlighting the tune-on-demand potential of this double emulsion template using microfluidic techniques.

The investigation of behaviour of population/group of µ-reactors as a function of substrate urea concentration and the density of µ-reactors highlights that increasing the urea concentration and the number of µ-reactor triggers transitions to collective behaviours. This is attributed to the resulting increase in overall production and

diffusion of ammonia in the neighbouring μ-reactors. These experiments demonstrate the importance of diffusion vs reaction control (enzyme loading) in the investigation of collective effects driven by chemical communication in compartmentalised enzyme systems. This unique behaviour highlights the differences between the microfluidic reactors and the GUV host system used in previous studies and demonstrates the advantages of using microfluidic reactors for the study of complex biological systems and improved control over reaction dynamics.

The proposed platform of double emulsions based μ-reactors provides better control over diffusion controlled membrane permeability of urea and offers several potential applications and uses. This study can provide insight into the behaviour of chemical reactions in complex microenvironments, such as those found in living systems. It can also inform the design and development of new materials and devices for chemical sensing, actuation, and energy conversion, where multiple interacting agents are involved with the added advantage of enhanced control over reaction dynamics. For instance, the understanding of density-dependent behaviour in synthetic μ-reactors and local communication can be utilized to design new materials for drug delivery systems with the ability to spatially tune the system. Although, the system of microfluidic reactors exhibits a switch behaviour (low to high pH), however, modelling has shown the potential for autonomous (independent) oscillations in this system too, which would be interesting to explore in future work. Further, more experiments are planned to extend our findings of controlled communicative behaviours by integrating microfluidic-based double emulsion templates with hydrogel formation, such as pH-triggered chitosan gelation, for bioinspired film formation.

# 5 Exploitation of the Urease Double Emulsion Platform in Applications

**Contents:**

## 5.1 Introduction

Compartmentalised systems of double emulsion droplets are widely used in both science and industry as they can encapsulate multiple components simultaneously. These droplets can be used as templates for the fabrication of structured materials and microparticles with core-shell configuration[332,333]. In addition, two layer feature of the lipid and surfactant stabilised droplets can be exploited to investigate membrane permeability for various charged and neutral species[334]. Benefiting from the two-layer design of the double emulsion droplets and the adjustable features of the individual layers, there are applications in many fields including agriculture[335], food science[336,337], cosmetics[338], and biomedicine[339]. More importantly, the search for active, novel and smart materials/biomaterials is constantly increasing as the demand for substitute materials for complicated biomedical applications increases over time. In this context, a microfluidics droplet template[340] can not only enable the high throughput synthesis of materials but also provides enhanced spatial and temporal material properties. Nowadays several materials, such as polymers, hydrogels, metals, glasses, and ceramics, exhibit admirable bioactivity and biocompatibility and are being considered for applications as biomaterials. These materials are used in the fields of diagnostics and therapeutics because of their engineered properties which permit them to work together with biological systems for various biomedical applications. Amongst other materials, hydrogels are most commonly exploited as biomaterials owing to their versatility in physical structure and chemical nature.

Hydrogels are polymer-based water-rich materials featuring physical properties similar to those of the natural extracellular matrix. In the 1960s, Wichterle and Lim first suggested the use of glycol methacrylate-based hydrogels for biomedical purposes, exploiting their hydrophilicity, porosity, and biocompatibility to fabricate soft contact lenses[341]. Considerable advancement has been made since then in the synthesis and preparation of hydrogels from both natural and synthetic resources. Hydrogels from natural materials such as fibrin, collagen, chitosan, alginate, and agarose tend to have good biocompatibility and biodegradability[342]. Nevertheless, they may also have issues associated with immunogenicity, batch wise variations, and poor mechanical characteristics. These constraints can be addressed somewhat by using fully synthetic polymers including poly(acrylamide) (PAM), poly(vinyl alcohol) (PVA), poly(2-hydroxyethyl methacrylate) (PHEMA), and poly(ethylene glycol) (PEG). Synthetic

polymers allow for increased design versatility, greater ease of functionalization, and improved mechanical strength. These hydrogel materials has found numerous applications including drug delivery, cancer research, regenerative medicine, and cell therapy[343–345], yet they still lack the inherent biomolecular signatures and biodegradable ingredients that are found in natural biopolymers[346]. Due to this reason, the combination of the synthetic and natural hydrogel hybrid materials has also gained significant attention[347].

One important aspect is the immobilisation of biomolecules, especially enzymes, in hydrogels which is crucial (to ensure longevity, recovery, and re-use of enzymes)[348–351] for a variety of applications, involving sensing and synthesis through biocatalysis in flow reactors[352,353]. The enzyme entrapment within a hydrogel network generally requires the fabrication of hydrogel matrix in the presence of enzyme, which helps to lock the enzyme molecules within the hydrogel networks[340]. The approach is inspired by natural settings such as the immobilisation of bacterial cells in an extracellular matrix, where bacteria form a gluey film of extracellular polymeric substance (EPS) which assist them to bind to surfaces in colonies referred to as biofilms. The bacteria use an autocatalytic autoinducer signalling molecule to initiate biofilm formation above a certain threshold of group size, a phenomenon known as quorum sensing. Quorum sensing can be defined as the response of changes to cell number or cell density which in turn is responsible for the changes in overall behaviour [354,297]. In industry, biofilms are harmful in many cases and useful in many others, for example, in bacterial flow reactors, the biofilm protects the organisms from perturbations such as flows or aggressive chemicals and guarantees persistent bioactivity for continued chemical processing [355].

The synthesis of enzyme-hydrogel matrix involves careful consideration to prevent enzyme leaking and biomolecule degradation as the production techniques usually involves confined settings (such as microfluidics) and requires UV, initiators, and emulsion systems[356,357]. Scherman and co-workers used droplet microfluidic technique (T junction device) to investigated supramolecular polymer microcapsules, where they exploited the accumulation of colloidal particles at the interface which eventually decreases the interfacial energy and drive the polymerisation resulting in polymer shell at the water/oil interface[358]. The use of UV irradiation on surfaces is another interesting technique to drive self-assemble material formation. Doyle and

colleagues have verified this concept, for example, through the stereo-selective growth of $CaCO_3$ utilising photo-structured composite microstructures in a microfluidic channel. The composite incorporate poly(ethylene glycol) diacrylate (PEGDA) (photocurable monomer) and $CaCO_3$ nanoparticles that acts as seed crystals for $CaCO_3$ growth. The microfluidic setting improves mass exchange and allows preferential site-specific mineralisation on the composite microstructures [359]. Spatial control of hydrogel assembly under physiological environments is especially interesting for enzyme particle or surface coating and flow reactor applications, enabling the improvement of the biocatalytic process[22,361].

Inspired by nature, where biological processes combine reaction diffusion to coordinate and build spatio-temporal patterns, e.g. in morphogenesis[362] and cell movement[363]. These efficient nature-inspired strategies for building complex materials under the control of reaction-diffusion have led to the creation of various synthetic systems that use chemical gradients and mass transfer processes to produce materials. Zarket et al, inspired from natural onion layer by layer configuration with a developing bud at the centre and many water-based concentric layers surrounding it, created onion-like polymeric capsule structure using inside-out technique. In this approach, a reactant concentration gradient is formed in an oil droplet, which results in the formation of a shell. The generated shell is then progressively overlaid with additional layers of polymers to produce the onion-like structure[364]. Lovrak and colleagues, used the combination of self-assembly (SA) and reaction-diffusion (RD) scheme to generate concentric gradients leading to the formation of free-standing hydrogel structures. Diffusion in combination with pH triggers is a potential initiator for supramolecular pH-responsive self-assemblies, and the spatial and temporal variability of pH can be utilised to control hydrogel characteristics[365]. Acid diffusion, e.g. employing proton releasing materials, either agarose or poly(dimethylsiloxane) (PDMS) surfaces, creates 3D-structured gels and surfaces[366]. Similarly, gelation triggered by a low pH trigger can be used to generate multilayer structures with adjustable stiffness gradients[367–369]. On the other hand, the use of autocatalytic reactions offers the additional advantage of generating chemical gradients and thus diffusion patterns by an internal mechanism, as a means of in-situ release of trigger resulting in homogeneous hydrogel formation[225] (e.g. acid/base-catalysed autocatalytic processes)[370–372].

Here, we exploited our urease microfluidics double emulsion template to explore the potential for biomedical applications. Encouraged by natural cellular systems, for example bacterial biofilms, we used the enzyme urease encapsulated double emulsion template to produce hydrogels. The autocatalytic urea-urease reaction, where urease, catalyses formation of ammonia from urea, was encapsulated in the inner core solution and coupled with polymerisation of a water-soluble thiol (ETTMP) and polyethylene glycol diacrylate (PEGDA) to form uniform hydrogels throughout the sample. The dynamic pH switch of the urea-urea reaction is beneficial for the design of time-controlled polymerisation, which in a wider context could lead to the fabrication of new materials. We show how the urea-urea reaction can be used to design functional materials, such as double emulsion (μ-reactors) loaded biofilm inspired gel films and monodisperse spherical gel microparticles with increased longevity of immobilised enzyme molecules. These soft materials will potentially serve as biomaterials for drug delivery platforms or as biosensors; with added components for therapeutics or detection.

On the other hand, the enzyme urease, produced by bacteria, fungi, and yeasts catalyses the breakdown of urea to a nitrogen source which is important for the survival of these organisms. Urease, however, can also function as a virulence factor in various pathogenic bacteria, which makes it imperative for the growth of the host organism and the anchoring of the bacterial cells in the tissues. Its activity causes different consequences like the occurrence of urinary stones, hepatic coma, ammonia encephalopathy, pyelonephritis, and gastritis[373]. Among the most frequently studied bacterial ureases is that of H. pylori, a causative agent of gastric cancer, gastritis, and peptic ulcers[374]. Therefore, approaches based on the inhibition of urease are viewed as potentially effective in the prevention of diseases associated with urease-producing bacteria and as a tool to decrease the loss of nitrogen from urea used as fertilizer[375,376]. Here, we also exploited the double emulsions template to investigate the transport of silver (Ag) ions through lipid-surfactant stabilised oil shell of the μ-reactors to explore controlled urease inhibition, which could be useful for developing a platform of antimicrobial agents to target pathogenic bacteria.

## 5.2 Methodology

### 5.2.1 Chemicals

The following stock solutions were made:

0.6 M of urea (66612-1KG, M.W. 60.1, Sigma), 0.05 M of acetic acid (100% glacial acetic acid, Sigma), 400 Units/mL of urease (type III Jack bean U1500-20KU, 25920 units/g solid, Sigma), 0.2mM of pyranine (8-hydroxypyrene-1,3,6-trisulfonic acid, cat no. L11252.14, M.W. 524.39, Alfa Aesar), 6.5 mM of POPC in mineral oil (MO) (1-Palmitoyl-2-oleoyl-sn-glycero-3-phosphocholine (P516-250mg, Anatrace), 2 % SPAN-80 (Sorbitan monooleate, 85548-250 mL, viscosity 1000-2000 mPa.s at 20 ℃, M.W. 428.60, density 0.986 g/mL at 25 ℃), 1 M of glucose (G5400-1Kg, D-(+)-Glucose, minimum 99% GC, molecular biology tested, M.W. 180.16, Sigma), 1 M of sucrose (≥ 99.5% GC, molecular biology tested, M.W. 342.30, Sigma), 2% of Pluronic F-127 (powder,sigma), 20% glycerol (87%, Sigma), 1% PVA (poly vinyl alcohol, P8136-250G, 87-90% hydrolysed, avg. M.W. 30,000-70,000, Sigma), 0.01 mM of silver nitrate ($AgNO_3$, 0.1 N, Acros Organics), 0.0026 M of HCl (1M Honeywell). Poly(ethylene glycol) diacrylate (PEGDA, average $M_n$ = 700) was purchased from Sigma Aldrich. The tri-thiol: ethoxylated trimethylolpropane tri(3-mercaptopropionate) (THIOCURE® ETTMP 1300) was acquired from Bruno Bock Chemicals. All the stock solutions were prepared using distilled deionized water (Millipore 18.2 MΩ).

The urease stock solution was freshly prepared every day. The enzyme units, as expressed in units/ml, were worked out from the urease activity labelled on the packaging (25920 units/g, average) (1 U is equivalent to the emission of 1.0 µmol of ammonia from urea in one minute at pH 7 and 25 ℃).

### 5.2.2 Preparation of W/O/W Double Emulsions with Microfluidic Technology

As explained elsewhere, a flow-focusing microfluidic device was used to synthesize double emulsions. The PDMS-based microchannel consists of two droplet formation junctions, three inlets, and an outlet for collection of the prepared double emulsions. Three different solutions were prepared: inner aqueous solution to encapsulate enzyme and pyranine (IS), middle lipid-oil solution (MF), and outer aqueous solution (OS). The lipid solution (middle flow in the microchannel, MF) contains 6.5 mM POPC

dissolved in mineral oil (MO) and 2% SPAN-80 using ultrasonic bath (FB15051, Fisherbrand) until there was no visible POPC particles in the solution.

The recipes of the working fluids for the inner solution (IS) and outer solution (OS) were varied for different experimental investigations. There were two variations of the OS's consisting of different acids, acetic acid and HCl. The acetic acid based OS consists of 0.2 M glucose, 20% glycerol, 0.28% F127, and 1 mM of acetic acid (AA). The HCl based OS was made of 0.01 mM of HCl as a substitute for acetic acid to reduce the pH, whereas all the other components were identical.

Furthermore, three different inner solutions (IS) were prepared for varied experimental conditions. Two of the versions simply differ in the presence of the kind of acids (acetic acid and HCl) with all other compositions being kept constant. The acetic acid based IS was composed of 0.2 M sucrose, 90 μM pyranine, 50 units/mL of urease, 1 mM AA, and 0.28% F127. Similar to the OS, the HCl based IS consists of 0.01 mM HCl in replacement to the AA, whereas all the other components were kept constant. Additionally, 0.01 mM of silver nitrate ($AgNO_3$) was added to the ES to investigate $Ag^+$ ions membrane permeability for inhibition experiments. The third version of the IS contained 0.2 M sucrose, 90 μM pyranine, 150 units/mL of urease, 0.28% F127, 0.15 M of PEGDA, and 0.1 M of ETTMP for the thiol-acrylate gels.

Water in oil droplets were formed at the first junction of the flow-focusing device by running the IS at $P_{IS}$ = ~40 mbar and the MF at $P_{MF}$ = ~85 mbar, however, the flow pressures were varied with a fixed ratio of $(P_{MF}/P_{IS}) \sim 2-3$. Double emulsions were obtained at the second junction by shearing the W/O droplets produced at the first junction with the OS at $P_{OS}$ = ~25 mbar.

### 5.2.3 Urea-urease Reaction Monitoring

The W/O/W double emulsions were collected from the outlet Eppendorf tube. The collected double emulsions were mixed with an external solution (ES) in a separate Eppendorf tube containing acid, glucose, and urea. The reaction was observed immediately after infusing the mixed solution (containing double emulsions and ES) into a deep observation chamber of a 96 well plate. The protocol was run (if needed) on the epifluorescent microscope (LS560 Microscope, green fluorescence, and brightfield, green filter: excitation 457-493 nm; emission 508-552 nm, etaluma). The

ES added here also had different versions depending on the type of investigation in the experiments. Mainly it differs in the type of acid (AA or HCl), as explained for the IS and the OS. However, for the experiment with the gel films, it also contained 0.15 M PEGDA and 0.1 M ETTMP for the thiol-acrylate gels, together with urea and glucose. All experiments were performed at room temperature (~20 ± 1 °C).

### 5.2.4 Thiol-acrylate Double Emulsions Loaded Hydrogel Film and Particles

For the hydrogel film, a solution of double emulsions containing sucrose (0.2 M), pyranine (50 µM), urease (150 units/mL), and F127 (0.28%) in the IS (inner core of the double emulsions) was mixed with the ES of urea/ETTMP/PEGDA containing 0.2 M of glucose, 0.07 M of urea, 0.1 M of ETTMP, and 0.15 M of PEGDA in an Eppendorf tube and poured over an observation chamber of a 96 well plate. For the gel microparicles synthesis, the gel monomers (ETTMP and PEGDA) were added in the IS composition instead of the ES. As such, the IS contained sucrose (0.2 M), pyranine (50 µM), urease (150 units/mL), F127 (0.28%), ETTMP (0.1 M), and PEGDA (0.15 M) and the reaction was initiated after mixing an equal volume of double emulsions and ES containing urea and glucose. Solid gelled particles obtained at the end of the reaction were filtered and washed in 1 mM acetic acid solution using a spin-x micro centrifuge filter column in a centrifuge (Heraeus Pico 17, Thermo electron corporation) for 3 min at 1000xg. The remaining precipitant was collected from the bottom of the filter column and stored in a separate Eppendorf tube in a 1 mM AA solution in a refrigerator for the reusability tests.

For the reusability test with aqueous thiol acrylate particles, the stored aqueous core particles were suspended in an external solution (ES) of urea/glucose to re-initiate the reaction with the urease loaded in the hydrogel matrix of the microparticles. The reaction mixture was infused into an observation chamber consisting of a perfusion chamber (8-9 mm diameter x 0.6 mm depth, CoverWell ™ perfusion chamber) sealed against the slides. The reusability assay was performed over several days to record enzyme activity as a function of urea-urea reaction induction times over this period.

## 5.3 Results and Discussion

### 5.3.1 Thiol-acrylate Hydrogels: Bioinspired Gel Films and Microparticles

Poly(ethylene glycol) diacrylate (PEGDA) is hydrophilic, nontoxic, and a bio-inert material used especially for drug delivery and tissue engineering[377,378]. PEGDA requires a photoinitiator and UV irradiation to undergo rapid gelation[379], however, the use of many photoinitiators is classified as dangerous[380,381,382] for biological context (such as cell viability). Although PEGDA gels have excellent mechanical properties, pure PEGDA gels do not facilitate cell adhesion because the gel surface hinders the adsorption of adhesion proteins for example fibronectin; consequently, there is an insufficiency of cellular adhesion spots[383]. Additionally, the lack of spatiotemporal control over the gelation of pure PEGDA gels hampers the use of such hydrogels for biomedical applications. An alternative solution for PEGDA-based hydrogel fabrication is the Michael addition of a thiol to an acrylate, which can be carried out under mild settings and hardly affects biological functions (e.g. cell viability)[384]. In addition, by tuning the ratio of thiol to acrylate, the stiffness and stability of the hydrogel can be readily modified, allowing a higher level of controllability and reproducibility. The possibility to customise the chemistry of a synthetic hydrogel is a feature that most biological hydrogels are lacking[385,386].

The Michael addition of a thiol and an acrylate leads to the synthesis of a hydrogel by base catalysis at a physiological pH (~7.4). The synthesis formulation involves the reaction of a trithiol (ETTMP) with linear crosslinker PEGDA in the presence of a base (NaOH) to achieve a Michael addition, as shown in **Figure 5.1**. The hydrogel was synthesized by reacting a trithiol (ETTMP) with PEGDA (linear crosslinker) in the presence of a base (NaOH) to achieve a Michael addition (**Figure 5.1**). NaOH was employed to deprotonate a thiol group (-SH) to a thiolate ($-S^-$), which then enables the addition of an acrylate group[387,388]at a pH above 7.

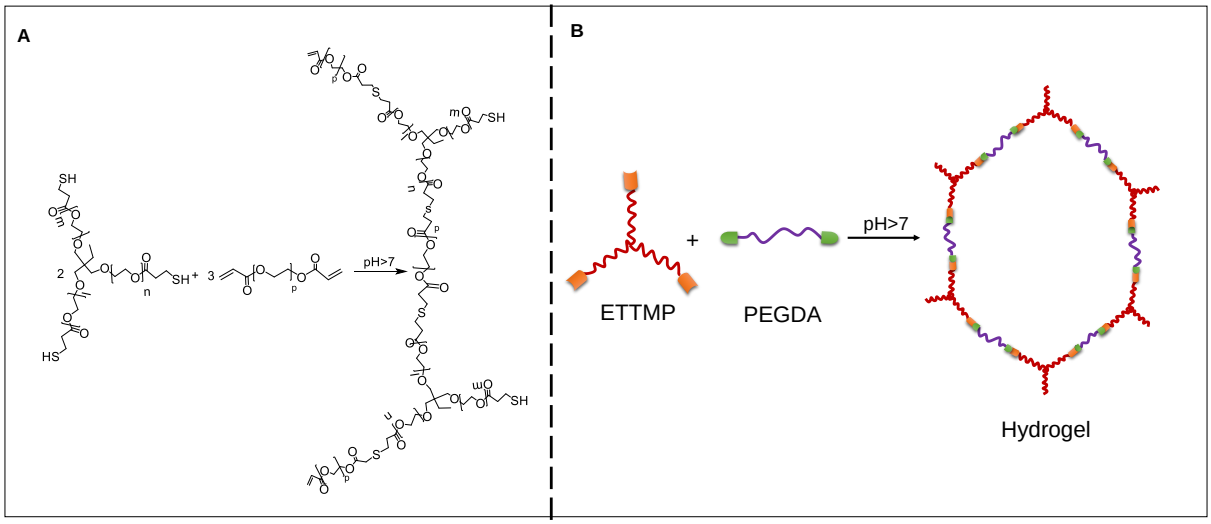


***Figure 5.1 The synthesis of thiol-acrylate hydrogels*** *(A) Michael's base-catalysed addition reaction for the synthesis of thiol-acrylate hydrogels (B)Schematic representation of the cross-linking of ETTMP (trithiol) and PEGDA (diacrylate) leading to the binding of the thiol to the acrylate when the reaction is stoichiometrically balanced.*

Originally, thiol-acrylate hydrogels were proposed as base-catalysed polymerisations for injectable formulations, and a 2:3 ratio of thiol and acrylate functional groups were combined to form a cross-linked network of hydrogels to obtain equimolar stoichiometric ratio[389]. The thiol-acrylate hydrogel synthesis was then adapted by exploiting an in-built pH switch (increase in pH after an induction period) of urea-urease reaction to activate the base-catalysed Michael addition reaction of trithiol to a polyethylene glycol diacrylate (PEGDA)[198].

The urea-urease reaction exhibits an accelerated rate on account of its bell-shaped pH curve related to the formation of a base. In case the initial pH is low (pH~3-4), there is a slow increase in pH followed by a rapid transformation to a high pH state (pH≥ 7.5) as the formation of ammonia leads to an increase in the production rate of ammonia due to the autocatalytic nature of the reaction. The switch to a high pH state inherent to the urea-urease reaction can be exploited to use as an ON/OFF state for thiol-acrylate hydrogel formation. Where, the ‘OFF’ state refers to the low pH with ‘no gel’ phase, whereas, the ‘ON’ state refers to the high pH with solid hydrogel phase. In other words, the high pH of the reaction can be used to trigger a base-catalysed thiol-

Michael addition reaction of the water-soluble monomers thiocure (ETTMP 1300) and PEGDA (Mn=700).

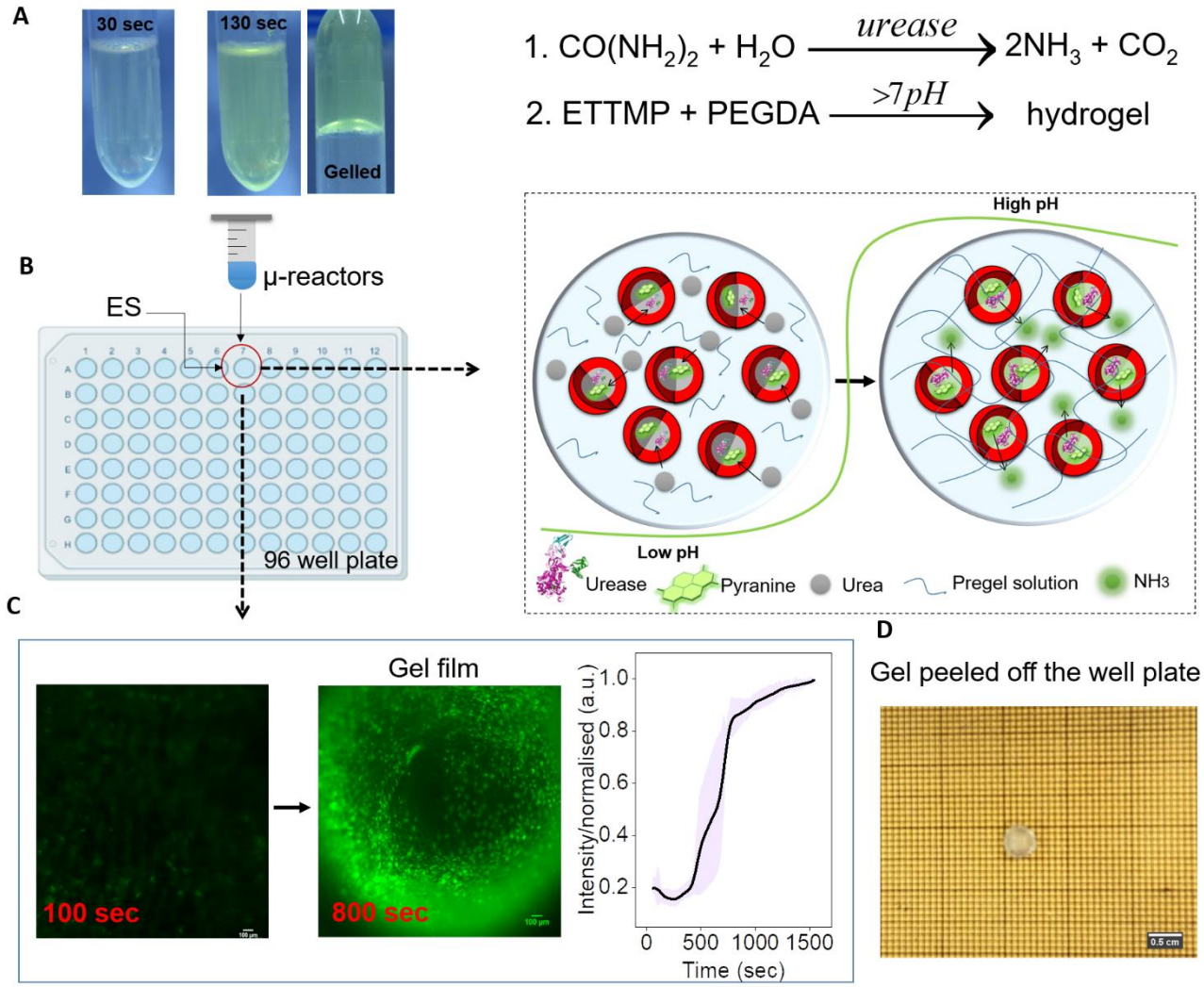


***Figure 5.2 Thiol acrylate gelation with urea-urea reaction*** *A) A test tube experiment showing pH-triggered gelation of THIOCURE ETTMP 1300 and polyethylene glycol diacrylate by a urea-urea reaction (left picture). The reaction of urea and urease (1) produces ammonia base (>pH 7) which, after an induction period, triggers the gelation of thiol acrylate (2). The reaction concentrations were: [urea] = 0.07 M, [pyranine] = 50 μm, [urease] = 100 units/mL, [ETTMP] = 0.1 M, and [PEGDA] = 0.15 M (B) Schematic representation of the experimental setup for the preparation of a thiol-acrylate gel film. The W/O/W μ-reactors encapsulating the enzyme urease, acetic acid, and pyranine (fluorescent indicator) were added to a solution of urea/ETTMP/PEGDA in a 96-well plate, the initial pH was about 4 due to the small amount of 3-mercaptopropionic acid (3-MPA) present in ETTMP and increased to over 7 after an induction period, the produced ammonia permeates into the outer aqueous solution of urea/ETTMP/PEGDA and triggers the gelation of thiol- acrylate (right image) (C) Fluorescence microscopy images of the UU reaction observation with the corresponding intensity-time plot (purple region shows the standard deviation in induction periods for different μ-reactors) and the formation of the thiol-acrylate gel film (embedded in μ-reactors), the reaction concentrations were: [urea] = 0.07 M,*

*[pyranine] = 50 µM, [urease] = 150 units/mL, [ETTMP] = 0.1 M and [PEGDA] = 0.15 M, scale = 100 µm (D) Thiol-acrylate hydrogel film (peeled from 96 well plate) on mm square paper, scale = 0.5 cm.*

The initial pH was about 4 when the urease solution was added to the solution of urea, ETTMP, and PEGDA, due to the small amount of 3-mercaptopropionic acid (3-MPA) groups contained in ETTMP, and then raised to above 7.5 after a tuneable (by changing the concentrations of urea, urease, or acid content) induction period of the urea-urease reaction which drives the gelation of the thiol-acrylate, as shown in **Figure 5.2** A.

Modelled on natural cellular systems, e.g. bacterial biofilms, we used the enzyme urease as an encapsulated double emulsion template to produce hydrogel films. The enzyme urease was added to the inner core of the double emulsions contained in a 96 plate filled with urea/ETTMP/PEGDA. Once the urea penetrates the double emulsions, a reaction is triggered to produce ammonia, which then enters the outer solution containing ETTMP and PEGDA as a precursor solution, causing an increase in pH that promotes thiol-acrylate gelation (**Figure 5.2**). We discuss below how the urea-urea reaction can be used to design functional materials, such as double emulsion (µ-reactors) loaded biofilm-inspired gel films for delivery of therapeutics or detection.

The approach is inspired by natural settings such as the immobilisation of bacterial cells in an extracellular matrix, where bacteria form a gluey film of extracellular polymeric substance (EPS) which assist them to bind to surfaces in colonies referred to as biofilms. The bacteria use an autocatalytic autoinducer signalling molecule to initiate biofilm formation above a certain threshold of group size, a phenomenon known as quorum sensing. Quorum sensing can be defined as the response of changes to cell number or cell density which in turn is responsible for the changes in overall behaviour[354,297]. In industry, biofilms are harmful in many cases and useful in many others, for example, in bacterial flow reactors, the biofilm protects the organisms from perturbations such as flows or aggressive chemicals and guarantees persistent bioactivity for continued chemical processing[355]. Here, ammonia acts as a signal molecule in the gel films loaded with double emulsions, triggering communication between neighbouring double emulsions and eventually leading to an increase in pH and thus gelation of thiol acrylate.

Thiol acrylate gel films loaded with double emulsions are materials that replicate the basic structure of bacterial biofilms and may be employed to deliver medicinal products by providing enhanced therapeutic drug protection within the trapped double emulsions. When the thiol acrylate gel film is subjected to an outside stimulus such as pH, light or heat, it can liberate the double emulsion droplets, which will then discharge their cargo (i.e. the drugs) in a well-controlled manner and hence provides improved spatiotemporal properties. A similar approach was discussed by Yikun Ju and co-workers in the field of regenerative medicine, where they explored embedding extracellular vesicles (EVs), which are nano-sized vesicles formed by paracellular secretion, into the hydrogel matrix, thereby prolonging the retention in certain areas and slowing down the release of EVs to induce self-healing properties[390,391,392,393]. In addition, cell-loaded hydrogels have attracted increasing attention as "bio-inks" for 3D bioprinting. The combination of cells (or synthetic cell models) and biomaterials precursors, frequently described as "bioinks", are printed to produce tissue-like patterns that replicate natural tissues, employing vesicles (or cell models, as in this case, double emulsions) as functional material delivery vehicles (drug carriers)[394,395]. In this regards, the thiol-acrylate hydrogels, with the combination of a dynamic pH switch of the urea urease reaction as the trigger for gelation, enable precise temporal and spatial control, providing the hydrogel with precise processing and cross-linking properties in situ. The double emulsion-loaded thiol-acrylate gel films can be customised for specific drug delivery applications.

Moreover, as it has recently been increasingly recognised that the production of microparticles is essential for biomedical applications, various materials and production methods for microfluidically produced emulsions with sophisticated structures are being researched[332,333]. We further used the double emulsion platform to produce urease-immobilised thiol-acrylate gel microparticles. The given double emulsion platform allows morphological synthesis of microparticles with adjustable size and morphology and different biological functionalities. A similar approach as before was used, namely the use of the UU reaction (autocatalytic production of base) to catalyse the gelation of ETTMP and PEGDA. This time, however, the hydrogel precursors (ETTMP and PEGDA) were encapsulated in the core of the double emulsions together with the enzyme urease during their preparation. The double emulsions encapsulated with urease and ETTMP/PEGDA were collected in a urea-

containing eppendorf, and the permeation of urea through the shell layer initiated the reaction that finally triggered gelation of the gel monomers, resulting in gel microparticles (shell-core particles and aqueous solid core particles), as shown in **Figure 5.3**. The centrifugation of the mixture of different microparticles resulted in the separation of shell-core particles floating at the top and aqueous (solid) core particles settling at the bottom of the tube (**Figure 5.3** B).

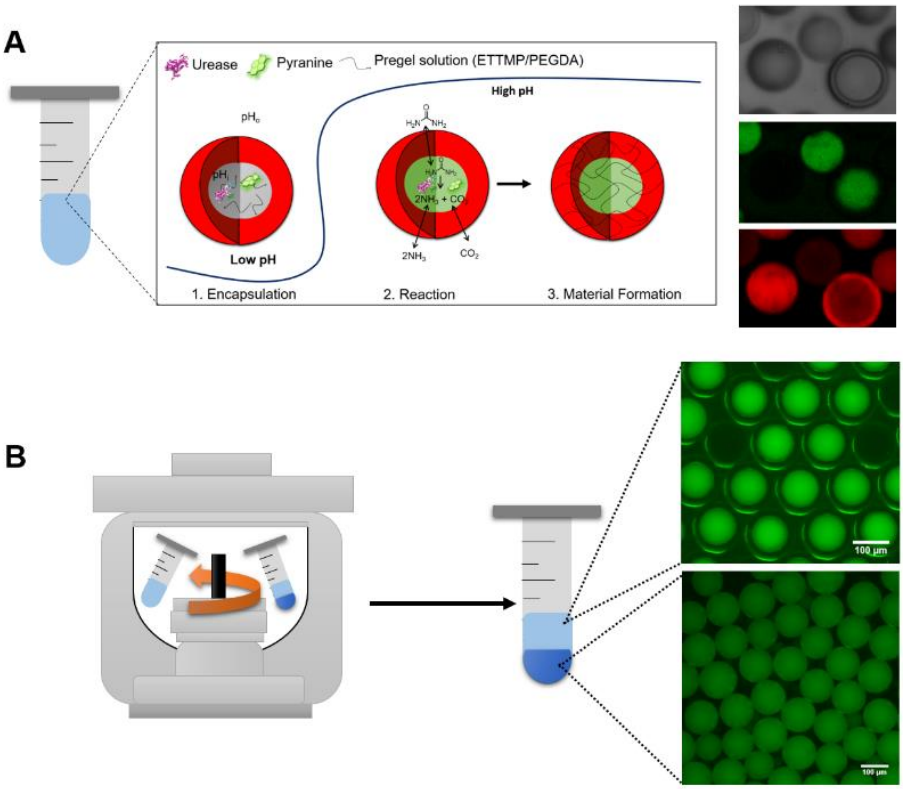


***Figure 5.3 Microfluidics-assisted preparation of thiol-acrylate microcapsules (shell-core particles) and microspheres (core particles)*** *(A) Scheme for the in situ synthesis of microparticles triggered by a UU reaction. The microfluidic W/O/W-based µ-reactors containing urease, pyranine, PEGDA and ETTMP were mixed with an external urea solution in an Eppendorf tube. The urea penetrates the core of the µ-reactor and hydrolyses to ammonia (catalysed by urease), the increase in pH ≥7 triggers base-catalysed gelation of thiol acrylate. The reaction concentrations were: [urea] = 0.07 M, [pyranine] = 50 µm, [urease] = 150 units/mL, [ETTMP] = 0.1 M and [PEGDA] = 0.15 M. The column of images on the right shows a combination of particles (shell core, aqueous core, and oil) with bright field image at the top, green fluorescent encapsulated pyranine in the middle, and labelled DilC12 at the bottom. (B) Illustration of the separation step using a centrifuge at 1000xg for 2 minutes separating the shell-core and aqueous particles, with shell-core and oil particles remaining at the top of the tube and the aqueous microspheres sinking to the bottom.*

Microparticles have been investigated for controlled release drug formulations and have shown great promise. The combination of feedback control (biocompatible urea-urea reaction) with the Michael addition reaction of thiol-acrylate microgels provides the basis for on-demand microparticle formation with improved controllability of gelation time. In addition, thiol-acrylate gels have demonstrated improved sustained release of the loaded drug, e.g. Langer and co-workers have demonstrated the sustained release profile of the drug methylprednisolone sodium succinate (MPSS) by a PEG-based hydrogel[389]. Another advantage of micro- and nano-systems platforms for drug delivery is the possibility of adaptable and tailored delivery of the drug to the target site of the disease due to the improved spatial control of the drugs in the body[396,397], avoiding premature degradation on the way to the target site[398,399].

The shell-core microparticles (microcapsules) are small-sized particles of a core (solid, liquid or gaseous) enclosed in a shielding outer shell. This distinctive feature enables the effective containment and preservation of sensitive or valuable cargo (for example active pharmaceutical ingredients, APIs) from the surrounding environment. The material utilised for the outer shell can be chosen according to unique requirements and offers flexibility and practicality, such as regulated release, responsive behaviour and enhanced retainment of drugs[204,333,332,400].The double emulsion strategy offers advantages due to the double layer structure of the double emulsion droplets and the adjustable features of every layer. For example, Hennequin et al. used a microfluidic technology based on lithography to produce monodisperse mononuclear microcapsules with controlled geometric and mechanical properties[401]. Jaimes-Lizcano et al. used a two-step emulsification process to prepare volatile W1/O/W2 double emulsions with different compositions, using cyclomethicone oils and silicone-based emulsifiers for the oil layer and the second water layer (W2), respectively[402]. However, the use of volatile ingredients such as cyclomethicone oils can lead to difficulties in the stability and storability of the double emulsions, as these ingredients can gradually evaporate. This may compromise the durability of the product and possibly affect the delivery of the inner medicinal compound over time.

The shell and core microcapsules, taken from the top of the tube, were further examined to evaluate the retention efficiency in terms of fluorescence of pyranine over time (several days). As expected, the shell and core microparticles showed greater efficiency in retaining pyranine over several days than the aqueous core particles as

well as increased stability of shell-core gelled microcapsules which is otherwise not possible with aqueous gel particles formed from W/O/W double emulsions (see **Figure 5.4** A), which lose pyranine quite rapidly within three days. However, to confirm the trapping of urease in the aqueous core particles, they were washed and reused to study the urease induction reaction by resetting with acetic acid (1 mM) and then added to urea solution (**Figure 5.4** B). A series of different experiments were also performed over several days to check for urease trapping and degradation over time, by adding the particles to urea solution with pyranine, showing a gradual slowing of the reaction and finally no reaction on day 13 (**Figure 5.4** C). Another important feature was the observation of controllable pH fronts with the urease-encapsulated microspheres, which can be adjusted with different urea concentrations, thereby adjusting the speed of the front. With a higher urea concentration (0.08 M) there was a faster induction time($T_{ind}$) and thus a faster pH front, while a lower urea concentration (0.04 M) results in a slower $T_{ind}$ and thus a slower transport of the pH front (**Figure 5.4** D).

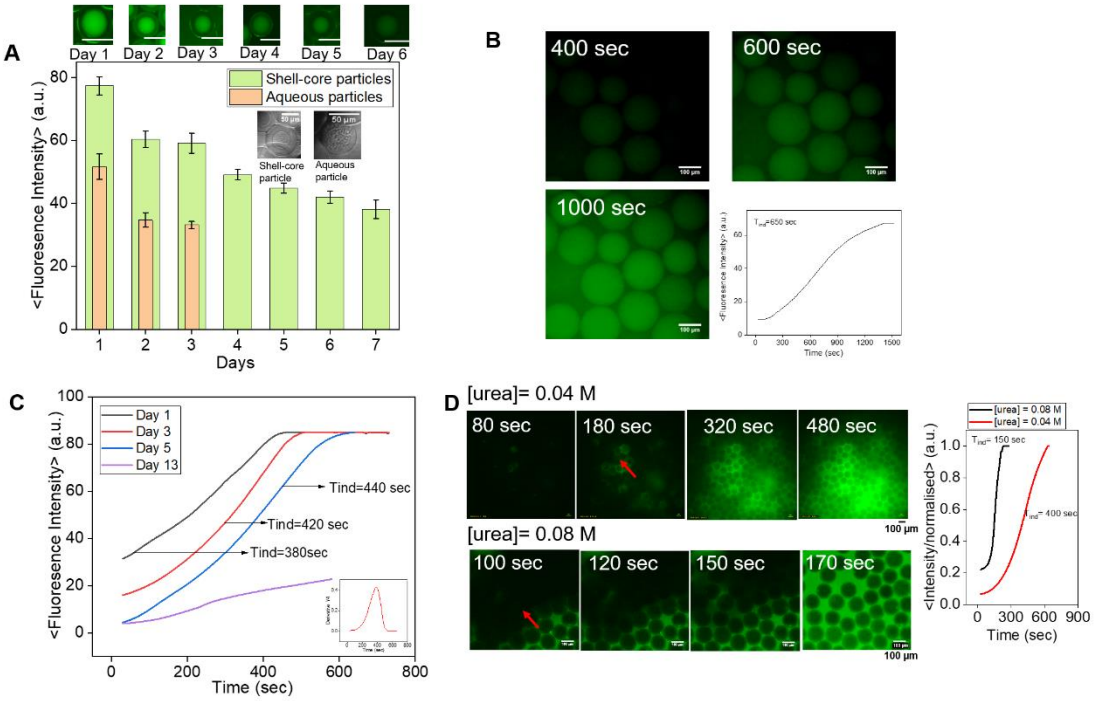


***Figure 5.4 The retention performance of shell-core microparticles and aqueous core microparticles in trapping pyranine, a green fluorescent dye, and urease enzyme*** *(loading of 150 U/ mL) (A) A bar graph was used to display the pyranine intensity trapped by both types of microparticles over time. On Day 1, the shell-core microparticles were noted to have retained 50.1% higher pyranine intensity relative to the aqueous core microparticles. On Day 7, the shell-core microparticles' fluorescence dropped by 51 % compared to Day 1. On contrary, the aqueous core microparticles exhibited reduced pyranine retention, with fluorescence being nearly negligible (undetectable) on day 4 (B) The washed urease-trapped core microspheres were reused to investigate the urea-urease (UU) induction reaction by resetting with acetic acid (1 mM), then adding to solution with the reaction concentrations: [urea] = 0.07 M, [pyranine] = 50 µm, and acid = 1 mM (C) Average intensity-time plot to investigate the UU reaction and $T_{ind}$ in core microparticles to study urease deactivation over days; the figure shows an increasing $T_{ind}$ (indicating a gradual decrease in urease activity) with an almost negligible reaction at day 13, the inset in the figure represents the first derivative of the average intensity with respect to time to obtain the maximum rate change, which is considered the induction period ($T_{ind}$). Scale bar = 100 µm (D) Spatial propagation of ammonia through a solution of core microparticles in urea/pyranine solution.*

Furthermore, the presented formulation of microfluidic double emulsions highlighted another important feature where the addition surfactants controls the dewetting process (separation of the inner core from the outer shell) of shell-core microcapsules. There is an initial stability window and then emulsions undergo the dewetting process[51,403,404] leading to the separation of the outer oil shell from the inner solid aqueous core with the membrane composed of POPC lipids and may resemble that

of lipid vesicles[332]. Here, the outer oil layer acts as a sacrificial payload holder, assisting in avoiding premature degradation or release to non-target sites and can be exploited to program the release time of the inner solid core particle and hence the release rate of encapsulated ingredients.

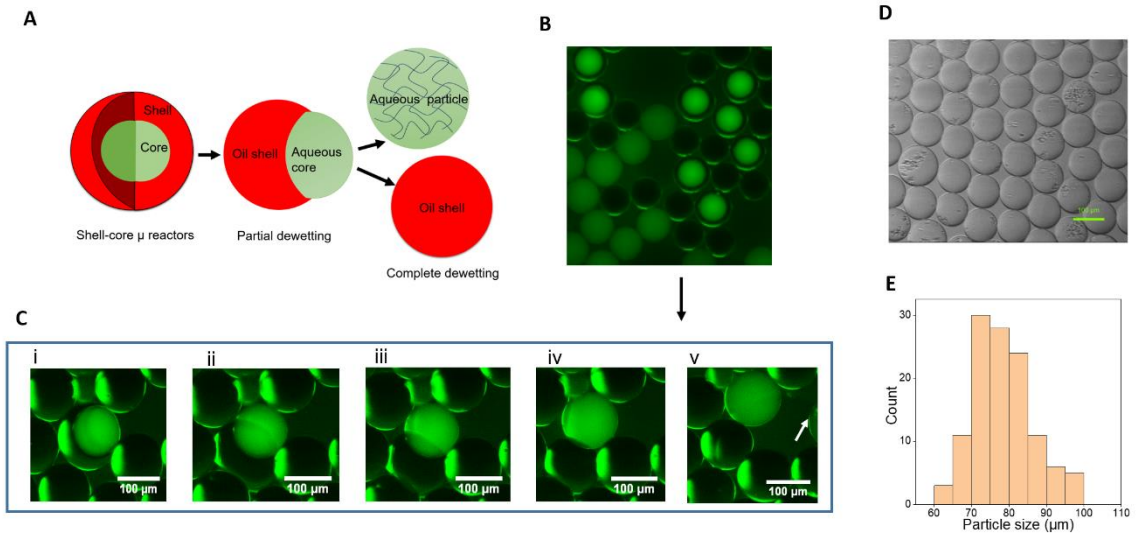


***Figure 5.5 Dewetting of core microspheres from the oil shell*** *(A) Schematic representation of the dewetting process in which the inner core particle separates completely from the outer shell after the partial dewetting step (B) Microscope image of a combination of core-shell, oil and aqueous core particles (C) Green fluorescent microscope images of thiol-acrylate gel microparticles, undergoing dewetting transition (D) Bright-field microscope image of thiol-acrylate microparticles separated from the urea reacted solution by washing in 1 mM acetic acid solution in a spin column (micro-centrifuge tube) (E) Particle size distribution of the separated dewetted particles (mean diameter= 75 μm and coefficient of variance, CV= 8), scale = 100 μm.*

**Figure 5.5** shows the dewetting mechanism of the proposed shell-core microparticles, where the shell-core-configured particles show enhanced green fluorescence compared to the dewetting aqueous core particles, indicating the protective shielding effect of the outer oil layer (**Figure 5.5** B). **Figure 5.5** C illustrates the release of the inner core particle. **Figure 5.5** D shows the bright field image of the separated (centrifuged) solid core microparticles and the size distribution (**Figure 5.5** E) obtained through the Matlab script as given in the section 7.5.2 of the Appendix 7.5.

### 5.3.2 Exploitation of Double Emulsions Template for Urease Inhibition

The most frequently studied bacterial ureases is that of H. pylori, a causative agent of gastric cancer, gastritis, and peptic ulcers[374]. Therefore, another approach taken here is to utilise the urease-encapsulated double emulsion platform to study the inhibition of the urease activity by molecular inhibitors and hence stop the reaction as one of the most important strategies for the treatment of H. pylori infections[174,373,408,409,374–376,405,405–407,407].

Urease inhibitors can be potent therapies for the effective treatment of pathogenic diseases caused by urease-dependent microorganisms. Commercially distributed urease inhibitors such as phosphorodiamidates, hydroxamic acid derivatives and imidazoles are, however, both toxic and of low stability, which hinders their clinical application[410,411]. Most anti-ureolytic agents, e.g. phosphodiamidates, quinones, metal ion chelators and metal ions, can be divided into three broad groups according to their mode of action, depending on where they attack the urease structure to its stop activity[409,408,407].

In this context, particular emphasis has been placed on $Ag^+$ ions, with urease (specifically that from jack bean) being strongly inhibited by $Ag^+$ ions, with 7 molecules inhibiting one urease molecule[405]. More recently, it has been investigated that Ag(I) inhibits urease by forming a binuclear pattern of two Ag(I) ions bound to the substantially retained metal triad αCys322-αHis323-αMet367, resulting in obstruction of the movement of a structural motif (mobile flap) integral to urease activity and hence inhibition of catalytic function[409].

However, there is limited knowledge about the permeability of $Ag^+$ ions through the bilayer and oil shell of the double emulsions, so silver nitrate (as a source of $Ag^+$ ions) was chosen here as a potential inhibitor of urease. In the present work, 0.1 mM silver nitrate ($AgNO_3$)[408] was added to the external solution to be permeable through the POPC lipids and surfactant-stabilised mineral oil shell to suppress the reaction. The $Ag^+$ was found to penetrate through the oil shell after a small delay when the reaction started to run (indicated by the red arrow in **Figure 5.6** B), but soon after sufficient $Ag^+$ accumulation, the reaction was stopped, which was compared to the control experiment where no $AgNO_3$ was added and the reaction proceeded as usual, as shown in **Figure 5.6** B and C. The process may involve formation of reverse micelles

with surfactant Span 80, but further investigation is required. The droplets were also made with HCl-based inner, outer, and external solutions to introduce a stronger acid into the system, and as predicted, the sample with $AgNO_3$ drastically lowered the activity of urease (as shown in the Appendix section 7.5.1 and **Figure 7.16**).

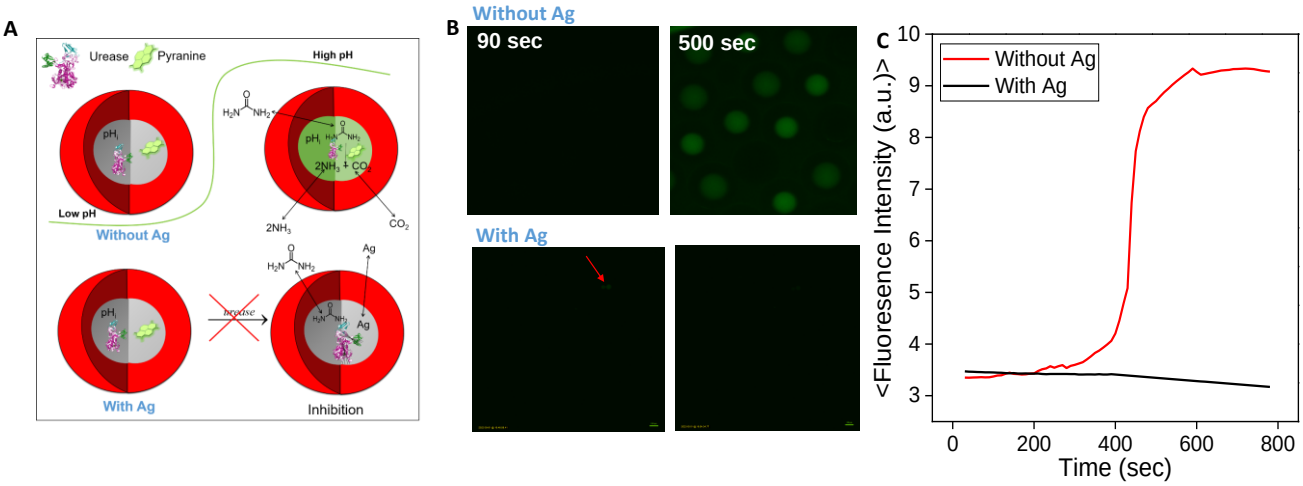


***Figure 5.6 Effect of the urease inhibitor on the urease-catalysed hydrolysis of urea (UU).*** *(A) Schematic representation of the UU reaction in W/O/W-μ reactors and the influence of the urease inhibitor ($AgNO_3$) on the UU reaction, the addition of which quenches the reaction (B) Two sets of microscopic fluorescence images of the emulsion sample mixed with external solution (ES) containing urea and acetic acid in the upper panel, in the lower panel, the ES additionally contains AgNO3 (enzyme inhibitor), which inhibits the reaction, and no fluorescence was detected (C) Fluorescence intensity of the emulsions over time when added to ES with and without $AgNO_3$. When mixed with ES without AgNO3, the typical induction reaction was observed, but when $AgNO_3$ was added to ES, an initial dampened fluorescence was observed that eventually subsided. The reaction concentrations were: [urea] = 0.07 M, [pyranine] = 50 μM, [AA] = 1 mM, [urease] = 50 Units/mL, [$AgNO_3$] = 0.1 mM epifluorescent microscope (LS560 Microscope, green fluorescence, and brightfield, green filter: excitation 457-493 nm; emission 508-552 nm, etaluma), and scale bar = 100 μm.*

## 5.4 Conclusions

The aim of this research was to use the microfluidic enzyme immobilisation technique and platform for encapsulated urease emulsions to enable their use in medical implants, biosensors and drug delivery devices. In addition, the reaction-diffusion of the urea-urease reaction was utilised to introduce dynamical increase in pH as a means of creating a tuneable platform (pH dependency of reaction rate) for enhancing control over gelling of thiol-acrylate, where the rate of the reaction and accompanied

change in pH can be altered by changing the reaction compositions (urea, urease, and acid content) as well as by changing the double emulsions configuration (shell to core ratio). Despite the fact that the discovery of this reaction dates back a century[178], the use of this method in synthetic cell models (double emulsions) has only gained prominence in the field of supramolecular gels and potential therapeutic platforms in the last ten years.

In this work, we have taken inspiration from nature (e.g. bacterial quorum sensing) to combine the urea-urea reaction with pH triggers of supramolecular pH-dependent gelation. The autocatalytic urea-urea reaction, in which the urease catalyses the formation of ammonia from urea, was encapsulated in the inner core solution and coupled with the polymerisation of a water-soluble thiol (ETTMP) and polyethylene glycol diacrylate (PEGDA) to form hydrogels, such as. e.g. biofilm inspired double emulsions loaded gel films and monodisperse spherical gel microparticles. Interestingly, fluorescence was maintained much longer in the core-shell particles compared to the aqueous core particles. These soft materials could serve as biomaterials for drug delivery. On the other hand, we also used the double emulsion platform as a means to study urease inhibition. We used the double emulsion template to study the transport of silver ions (Ag+) through the oil shell of μ-reactors stabilised with lipids and surfactants to explore controlled urease inhibition, which could be useful for developing a platform of antimicrobial agents against pathogenic bacteria. Our overall intention was to exploit the double emulsion template with the autocatalytic urease reaction for potential applications in biomedicine and therapeutics.

# 6 Conclusion of Thesis and Future Work

The basis of this doctoral thesis and our initial goal was to bring together two scientifically highly regarded fields, microreactor technology (microfluidics) and nonlinear enzyme kinetics (urea-urea reaction), into a dynamic framework for bioinspired materials applications. Within the second chapter, we took advantage from pressure driven droplet microfluidics and developed a system of enzyme-encapsulated double emulsion (W/O/W) droplets to obtain a localised pH pulse, with a controllable induction time and steady state in pH. Urease-encapsulated droplets of ~ 100 – 200 µm with a mineral oil shell thickness (POPC and surfactant stabilised) of 10 – 40 µm were prepared using a flow focussing device and the reaction was initiated off-chip by addition of droplets to a solution of urea. The pH increased uniformly and rapidly across the droplets after a time lag controlled by the diffusion of urea and then decreased to a steady state value either above or below pH 7, regulated by the rate of transport of ammonia out of the droplet. A distribution of induction times was obtained in the droplets thus demonstrating their potential to act as individual (µ)micro-reactors, whereas in other encapsulated urease systems the fast diffusion of ammonia resulted in increase in the pH in the surrounding solution.

In chapter three, to compare our understandings of experimental trends and the unique trends associated with the features of W/O/W double emulsions droplets, we have simulated the kinetics of the urea-urea reaction by considering a diffusion-controlled bilayer (concentric) sphere with a core encapsulating the urease enzyme and a layer consisting of a lipid-oil shell immersed in a finite external substrate medium (urea). The simulation results are not necessarily a quantitative comparison with the experimental results; instead, the focus is on a clear qualitative comparison of the influence of the various factors that contribute to shift in $T_{ind}$, such as the urea transport controlled by the shell, s/c, and core size. Using the core-shell model, we have confirmed the influence of the µ-reactor configuration on the reaction kinetics in addition to the influence associated with the reaction concentrations, and

demonstrated relatively simple control of the $T_{ind}$ of the microfluidics-based µ-reactor platform. Our results show that the induction time ($T_{ind}$) increased with increasing core radius (or decreasing shell thickness), with a smaller core (or thinner shell) resulting in a pH pulse profile and a larger core (or thicker shell) resulting in a sigmoidal pH time profile.

Nevertheless, by assembling a platform that enables a comprehensive investigation of the parameter space (chapter 2) in combined with theoretical modelling (chapter 3), we have acquired not only control over the kinetic results, but also gained a more holisticview of the behaviour of the system in its complete form. This better understanding has allowed us to broaden our scope and extend the practicality of our microfluidic system, e.g. in terms of chemical communication. Therefore, in chapter 4, inspired from natural cellular systems, bacterial cells and dictyostelium discoideum as an example, which exhibit synchronised chemical oscillations that are density-dependent, we show that in contrast to other systems, the release of ammonia (in the urease confined W/O/W droplets) can accelerate the reaction in all the droplets but there is no evident synchronisation of activity characterized by a wide distribution of induction times across the population of micro-reactors. This discrete behaviour, highlighted the tune-on-demand potential of this double emulsion template using microfluidic techniques. However, the investigation of behaviour of population/group of µ-reactors as a function of substrate urea concentration and the density of µ-reactors highlights that increasing the urea concentration and the number of µ-reactor triggers transitions to a more collective behaviour. This is attributed to increased transport rate of urea across the oil shell and the resulting increase overall production and diffusion of ammonia in the neighbouring µ-reactors. These experiments demonstrate the importance of diffusion vs reaction control (enzyme loading) in the investigation of collective effects driven by chemical communication in compartmentalised enzyme systems. This unique behaviour highlights the differences between the microfluidic reactors and the GUV host system used in previous studies and demonstrates the advantages of using microfluidic reactors for the study of complex biological systems and improved control over reaction dynamics. For instance, the understanding of density-dependent behaviour in synthetic µ-reactors and local communication can be utilized to design new materials for drug delivery systems with the ability to spatially tune the system.

Lastly, building upon our understandings, in the chapter 5, we exploit the double emulsion template with the autocatalytic urease reaction for potential applications in biomedicine and therapeutics. Here, we have taken inspiration from nature (e.g. bacterial quorum sensing) to combine the urea-urea reaction with pH triggers of supramolecular pH-dependent gelation. The encapsulated urea-urea reaction coupled with the polymerisation of a water-soluble thiol (ETTMP) and polyethylene glycol diacrylate (PEGDA) to form hydrogels throughout the sample, such as. e.g. biofilm inspired double emulsions loaded gel films and monodisperse spherical gel microparticles. In another approach to utilise this platform, we used the double emulsion platform as a means to study urease inhibition. We investigated the transport of silver ions (Ag+) through the oil shell of µ-reactors stabilised with lipids and surfactants to explore controlled urease inhibition, which could be useful for developing a platform of antimicrobial agents against pathogenic bacteria.

There are large parts of this dissertation that can be expanded upon. The most obvious way is to develop it further towards applications of this technology in materials science. Compartmentalisation of the urea-urease reaction in double emulsions generates new potential in the development of biocompatible feedback for pH-triggered processes and bioinspired applications in materials science. In the future, the microfluidic-based double emulsion platform could be used for fine tuning material properties, such as pH-triggered chitosan-inorganic particles, for medical applications. In this direction, one of the possible investigation route was to combine calcite precipitation in hydrogel matrices (chitosan). Here, the combination of microfluidics W/O/W loaded urease droplets will provide fine-tuned pH properties to generate novel calcite-chitosan hybrid materials which will have potential applications in biomedical applications, drug delivery, and waste water treatment. In another approach towards compartmentalisation, we intend to encapsulate giant unilamellar vesicles as drug carriers (synthesised by droplet transfer technique as described in section 1.3.2) in the double emulsions. The GUVs localise the drug to avoid contamination with other components of the reaction mixture in the double emulsions and protect the drug from degradation, improve stability, and control release kinetics. The onset of the urea-urea reaction and the associated (with the microfluidic double emulsions) programmed pH profiles will provide time-programmed release patterns of the drug (e.g. doxorubicin) loaded with the GUVs.

# 7 Appendices

## 7.1 **Appendix 1** – Chapter 1: Introduction

### 7.1.1 pH Dependence of the Urea Urease Reaction

The activity of Urease is highly pH dependant and exhibits a bell-shaped rate-pH curve, typical of enzymatic reactions. This can be explained by the presence of two acid equilibria giving inactive forms of enzyme and enzyme-substrate complex[170,183], with low activity in the protonated and deprotonated states[184]. Urease from jack bean, soybean, and most microorganism sources has an optimum pH around 7[170].

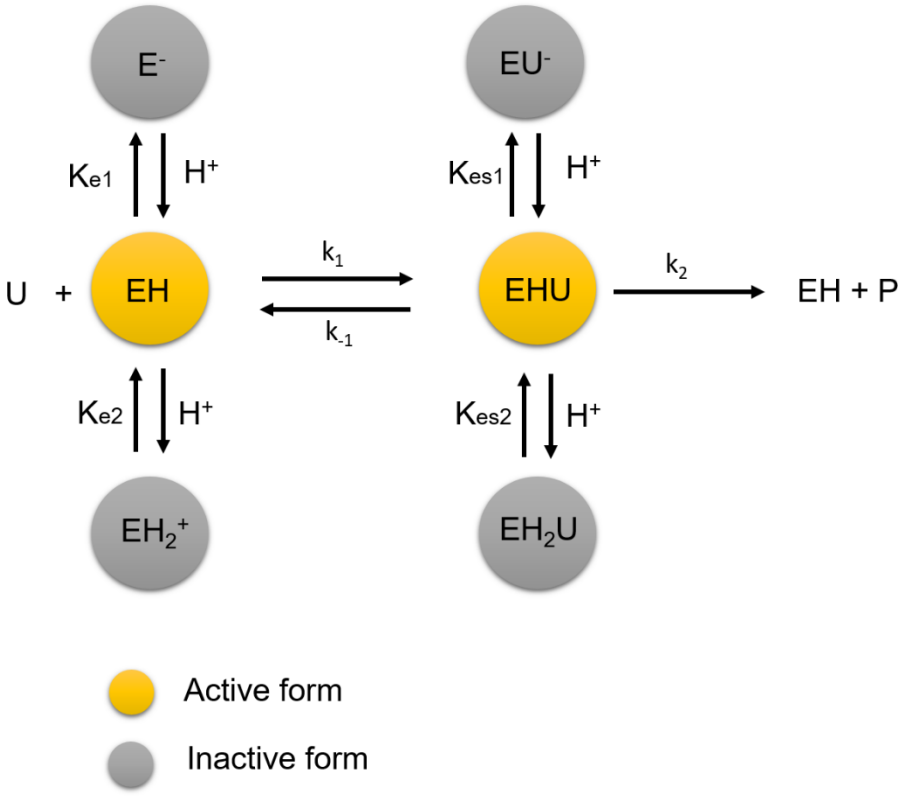


***Equation 7.1*** *Acid equilibria for active and inactive forms of enzyme and enzyme-substrate complex.*

As discussed in section 1.6.1.1, $K_M$ varies only slightly with acid concentration, which means that $K_{e1} = K_{es1}$ and $K_{e2} = K_{es2}$, i.e. the protonation equilibria are not altered in the presence of the substrate. Considering this, the expression for the rate is as follows[170,183]:

$$V = \frac{V_{max} U}{\left(K_M + U\right)\left(1 + \frac{K_{es2}}{H^+} + \frac{H^+}{K_{es1}}\right)}$$

***Equation 7.2*** *Modified form of Michaelis-Menten rate equation for urease activity, considering acid equilibria.*

### 7.1.2 Product Inhibition

The ammonium ion is found to inhibit the reaction by non-competive mechanism[170,183]

$$EH + P + U \rightleftharpoons EHPU \qquad Kp$$

This equilibrium can be incorporated into the expression for the Michaelis rate and yields:

$$V = \frac{V_{max} U}{(K_M + U)\left(1 + \frac{P}{K_p}\right)}$$

***Equation 7.3*** *Modified form of Michaelis-Menten rate equation for urease, considering product inhibition.*

### 7.1.3 Substrate Inhibition

The urea inhibits the reaction by an uncompetitive mechanism[170,183]:

$$EHU + U \rightleftharpoons EHU_2 \qquad Ks$$

This equilibrium can be incorporated into the expression for the Michaelis rate and yields:

$$V = \frac{V_{max} U}{\left(K_M + U\left(1 + \frac{U}{K_s}\right)\right)}$$

***Equation 7.4*** *Modified form of Michaelis-Menten rate equation for urease, considering susbtrate inhibition.*

## 7.2 **Appendix 2** – Chapter 2: A Microfluidic Double Emulsion Platform for Spatiotemporal Control of pH and Particle Synthesis

### 7.2.1 Fabrication of the Microfluidic Device

A thin layer of SU-8 3010 photoresists (MicroChem, Newton, MA) was spin-coated onto a Si wafer and then patterned using ultraviolet exposure through a chrome mask. In the fabrication process, PDMS and the curing agent (SYLGARD 184 Silicone Elastomer) were mixed carefully with ratio 10:1 and decanted onto the patterned SU-8 mold then degassing was performed in a desiccator using vacuum pressure to remove bubbles from the PDMS. Afterward, the PDMS on Si substrate was baked at 75 °C for 45-50 min. Following the baking, the PDMS was carefully pulled off from the Si substrate, and the microchannels were sliced to suitable sizes. The ports (inlet and outlet) of the PDMS device were punched (0.75 mm rapid core sampling tool, lot No. 161213) and then the microchannel was oxygen plasma-bonded (PDC 002, Harrick Plasma, Ithaca, USA) to the glass slide (24 mm × 60 mm, Menzel Glaser, Germany) for 30 s at 200 W and 200 mTorr. The device was heated in an oven at 75 °C for at least 4 min to anneal the bonding. The widths of the first and second junction were 100 µm and 150 µm, respectively.

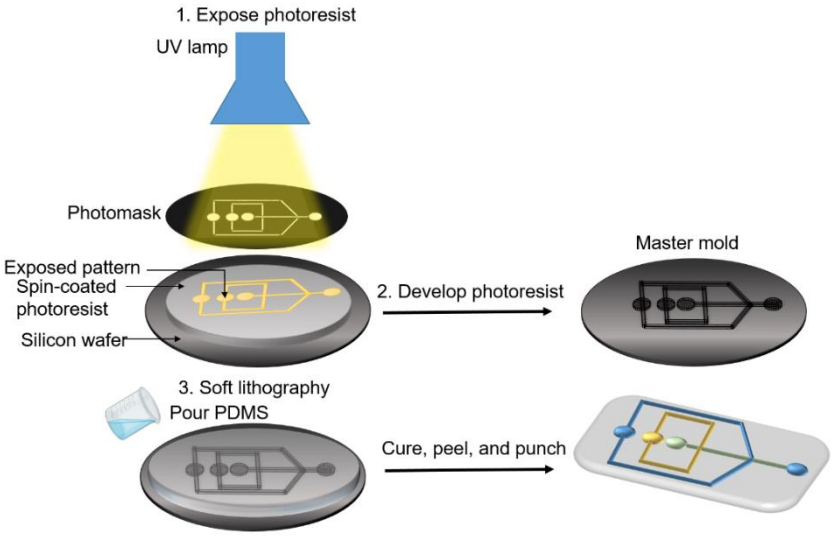


***Figure 7.1 A schematic illustration of the photolithography of the microfluidic device****. A photomask was exposed to UV light which patterns the design on Si-wafer (photoresist coated) to obtain*

*the master mould which then acts as a mould for PDMS curing. The PDMS is then peeled off the Si wafer and sealed to glass slide using plasma bonding after punching the inlet/outlet ports.*

### 7.2.2 Surface Treatment with PVA

A quick and easy approach to attain hydrophilicity is to treat the PDMS surface with polyvinyl alcohol (PVA) which is a hydrophilic polymer[251]. As PDMS is intrinsically hydrophobic and the continuous phase needed for the double emulsion droplet formation is water, a hydrophilic surface treatment guarantees thorough wetting of the walls when using the aqueous solution. A 1% PVA solution was used to create the OS (second junction) surface hydrophilic[412,413,252]. First the PVA powder was stirred in distilled water for 40 min at room temperature. Then we gradually increased the temperature on a hot plate (magnetic hotplate stirrer, ADS-HP-S-NT, with precision temperature controller ADS-TC-NT, Asynt) to 100 °C and stirred for another 40 minutes. Then we reduced the temperature to 65 °C and continue stirring for another 2 hours, adding water to compensate for the losses. Immediately after the plasma bonding and annealing of the device, PVA solution was drawn through the OS inlet reservoir using a 1 mL syringe while maintaining the vacuum at the outlet (using a 20 mL syringe), as illustrated in Figure S1. The chip was set aside for 10 min at room temperature and then heated on a hot plate (magnetic hotplate stirrer, ADS-HP-S-NT, with precision temperature controller ADS-TC-NT, Asynt) at 110 °C for 15 min. The chip was then cooled down to room temperature for 15 min. Three repetitive cycles of the above procedure were performed to create multilayer coating for improved surface treatment. The device is then set to use for the synthesis of W/O/W double emulsions and also can be kept for storage at room temperature as the hydrophilic coating persists for longer periods (several months).

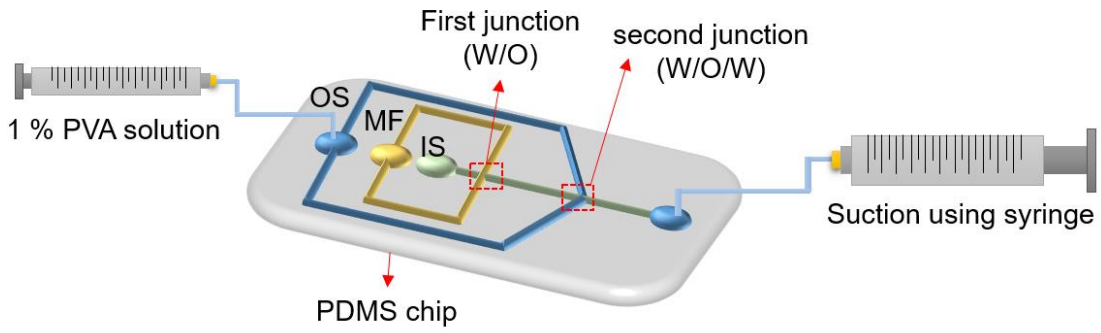


***Figure 7.2 Surface treatment of microfluidic chip**. To make the OF (second) junction hydrophilic, following the plasma bonding, 1 % PVA solution (~50 $\mu L$) was pushed through OF inlet reservoir (using a 1 mL syringe connected via microfluidic-tubing) while applying the negative pressure at the outlet of the device manually using a 20 mL syringe connected through microfluidic-tubing.*

### 7.2.3 Set-up for Synthesis of the Double Emulsions

The experimental set-up for the production of the double emulsions is shown in **Figure 7.3**. The inner, outer and middle fluids (IS, OS, MF) were driven from the reservoir holding rack connected with the pressure-driven pump (OB1 MkIII+, Elveflow, Paris, France) through microfluidic-tubing (microfluidic fittings 1/32" to 1/16" OD size adapter kit, Darwin microfluidics) to the microchannel. The flow rates were tuned using a custom-built Elveflow Smart Interface (ESI). A 2 mL Eppendorf tube was used as a collection vial for the double emulsions. The process was observed using a phase contrast/epiflouresent microscope connected to a computer.

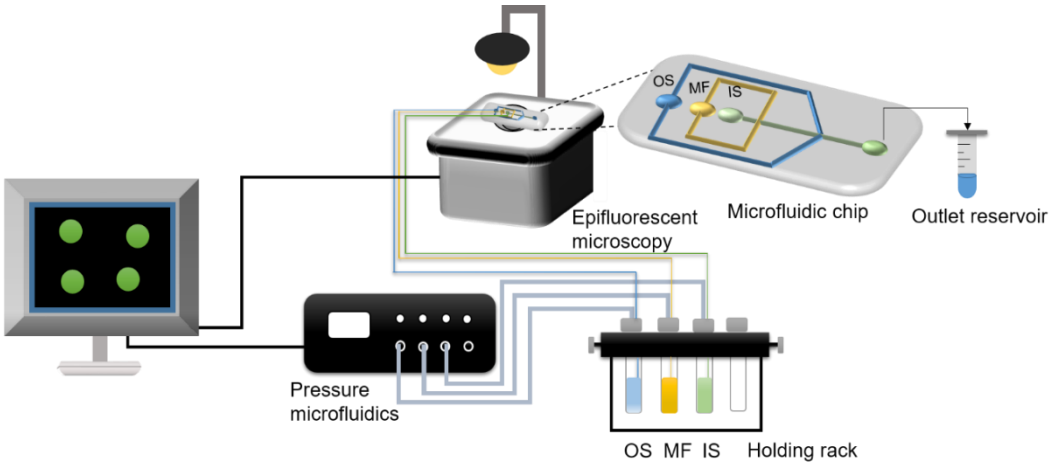


***Figure 7.3 Schematic representation of the experimental procedure for the production of double emulsions**. The microfluidic chip was connected to a pressure pump, OB1, and a reservoir holding rack through microfluidic tubing and the process was monitored using optical microscopy.*

### 7.2.4 Reaction Observation Off-chip

The reaction chamber consisted of either CoverWell™ perfusion chambers (8 – 9 mm diameter and 1.2 mm depth) or a chamber constructed in- house (**Figure 7.4**). The latter consisted of two pieces of double-sided tape of thickness 100 µm, with a circular hole (1000 µm diameter) produced in each piece of tape using a metal hole punch. The reaction chamber was attached to a microscope slide which was coated to reduce droplet instability and motion. After injection with solution, the chamber was sealed with a glass coverslip and the urea in the external solution diffused into the double emulsion initiating the urease reaction.

For determination of pH, the reaction was monitored in the CoverWell™ perfusion chambers using a Leica TCS SP8 confocal microscope (lens HC PL APO CS2 20x/0.75 DRY or 10x) with 405 nm (intensity: 4 - 8%) and 458 nm laser (intensity: 15 - 30%) consecutively for excitation and the emission wavelength range of 485 – 555 nm (Gain = 600).

The reaction was also monitored in the in-house reaction chambers using an inverted fluorescence microscope to follow the deprotonoted form of pyranine (Etaluma LS560 Microscope, green fluorescence, and brightfield, green filter: excitation 457-493 nm; emission 508-552 nm) with the fixed settings of gain = 3.750, illumination = 7.8 %, and exposure = 15.9 using either 4x, 10x, or 20x magnification.

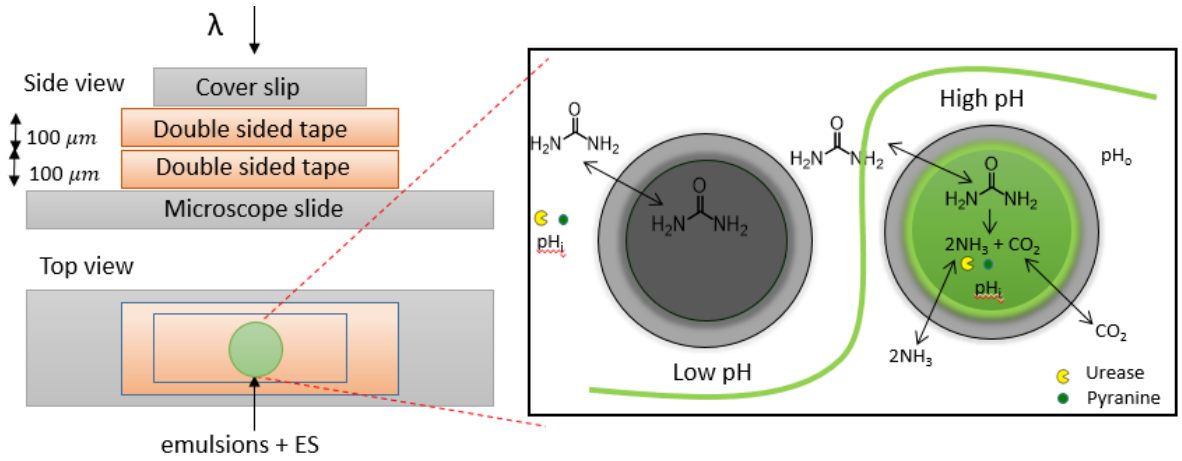


***Figure 7.4 Reaction chamber fabricated in-house*** *from double-sided tape and schematic of process occurring in the emulsion droplets.*

### 7.2.5 Calibration of the pH Fluoroprobe, Pyranine

For determination of the pH, the ratio of fluorescence, R = $F_{458}/F_{405}$, of pyranine at the two wavelengths is related to the pH through[414,415]:

$$\mathrm{pH} = \mathrm{pKa}' - \log\left(\frac{R - R_{max}}{R_{min-R}}\right)$$

***Equation 7.5*** *Relation of pyranine fluorescence with the pH.*

where $R_{min}$ is the ratio of absorbance of the protonated species ($PyOH^{3-}$), $R_{max}$ is the ratio of absorbance of the deprotonated form ($PyO^{4-}$) and $K_a$' is the apparent dissociation constant of pyranine. A solution of a certain pH containing pyranine (50 μM) was prepared using ammonia/ammonium reacted solution with pH adjusted using acetic acid and measured using a pH microelectrode. The solution was injected into a CoverWell™ perfusion chamber and the average intensity of several images was obtained at the two different excitation wavelengths using the confocal microscope. Calibration plots were performed regularly. The standard deviation in intensity was determined to be of order 10%. A fit to the data was obtained in OriginPro using the equation: $y = a + (b - a)/(1 + 10^{d*(c - x)})$ (**Figure 7.5**). The (apparent) pH was determined from SE3: $pH_{app} = c - (1/d)*\log((y - b)/(a - y))$ and, using the formula for the propagation of errors, the error in the pH, $s_{pH}$, was related to the error in $R$ ($s_y$): $s_{pH} = (s_y^2((y - b)/(y - a)^2 - 1/(y - a))^2(y - a)^2)/(d^2(y - b)^2))^{1/2}/\ln(10)$.

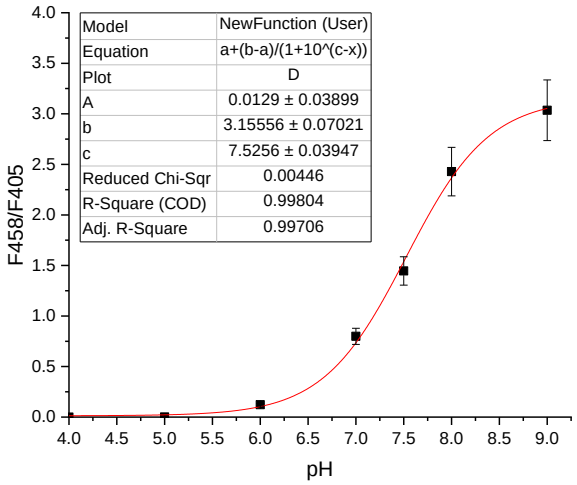


***Figure 7.5 Representative calibration curve for pyranine fluorescence as a function of pH****. Average ratio of fluorescence from multiple images obtained using confocal microscopy at lex = 450 and lex = 405 nm vs pH of solution and fitted equation (line): y = a + (b - a)/(1 + 10^d(c-x)) where a =*

*0.013 ± 0.04, b = 3.16 ± 0.07, c = 7.53 ± 0.04, d = 0. Error bars show 10% standard deviation determined from multiple measurements.*

### 7.2.6 Determination of Droplet Intensity, Shell and Core Sizes

Fluorescent images with $\lambda_{ex}$ = 405 and 450 nm and the corresponding brightfield images were obtained at regular time intervals with a typical pixel/µm ratio of 111/250. The images were processed using code developed in-house with MATLAB R2020a. The droplets were identified using the $\lambda_{405}$ image, green channel, (**Figure 7.6** A) and a circle constructed around the core using "imfindcircles". The average intensity in the droplets was obtained as the sum of the pixel intensities over the total number of pixels from the images at both $\lambda_{405}$ and $\lambda_{450}$. The ratio of intensities (F450/F405) was then determined and used to find pH (**Figure 7.5**). The shell and core size of the droplet was obtained using the brightfield image (**Figure 7.6** B and C). The MATLAB code was used to track droplets that were moving and the droplet number was recorded on each image to identify any erroneous measurements.

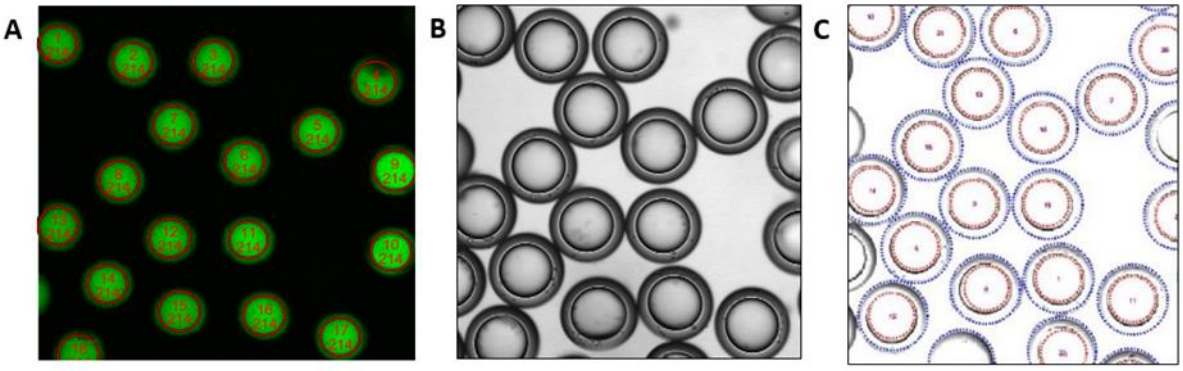


***Figure 7.6 Images obtained of the double emulsion droplets using the Leica confocal microscope and analysis in MATLAB*** *(A) fluorescence image at $\lambda_{ex}$ = 405 with droplets identified and numbered. The image number (214) is also shown. (B) corresponding brightfield image, (C) core, C, and outer shell, S, identified and used to determine droplet diameter and S/C.*

### 7.2.7 Fluorescent Labelling of Enzyme and Determination of Concentration

The enzyme was fluorescently labelled following the manufacturers instructions with some minor modifications (AnaTag™ HiLyte™ Fluor 488 Microscale Protein Labeling Kit). Briefly, a stock solution of 350 U/ml urease (type III) in 1 mM acetic acid was prepared. The urease solution was mixed with the dye solution and then purified. The absorbances at 280 nm and 499 nm were determined using a GENESYS 150 UV-vis

spectrophotometer. The absorbance at 280 nm was determined as 0.303 ± 0.006 and at 499 nm as 0.483 ± 0.006 from the average of three independent measurements. The protein concentration was determined from: [protein] = (($A_{280}$ – 0.19 x $A_{499}$)) x dilution factor/$\varepsilon_{protein}$ where ε = 203000 $cm^{-1}$ $M^{-1}$, the dilution factor was 1 and hence for a 350 U/ml stock solution, [protein] = 1.04 ± 0.02 µM.

### 7.2.8 Urease Reaction in Bulk Solution

The batch reaction of urease with urea was performed in a 3 mL quartz cuvette with a cross-shaped magnetic stirrer bar. Two stock solutions were prepared; solution A contained urease type III (100 U/mL) in 1 mM acetic acid and solution B contained urea (0.14 M) in 1 mM acetic acid solution. Then 1.4 mL of solution A was added to 1.4 mL of solution B and pH was monitored using a pH microelectrode and DrDAQ pH logger (**Figure 7.7** A). The rate of reaction is given by a modified Michaelis-Menten expression:

$$v_0 = \frac{k_1[E]_T[U]}{(K_M + [U])\left(1 + \frac{K_{es2}}{[H^+]} + \frac{[H^+]}{K_{es1}}\right)}$$

***Equation 7.6*** *Michaelis-Menten expression for the rate of reaction.*

where $k_1$ is the rate constant for decomposition of the enzyme-substrate complex, $[E]_T$ is the concentration of enzyme, $[U]$ is the concentration of urea, $K_M$ is the Michaelis constant, $[H^+]$ is the concentration of acid, and $K_{es2}$ and $K_{es1}$ are the protonation equilibria of the substrate-enzyme complex that give rise to the bell-shaped rate-pH curve. The pH-dependent relationship: rate = $1/(1 + H^+/K_{es1} + K_{es2}/H^+)$ is plotted in **Figure 7.7** B with the experimentally determined values of $K_{es1}$ = 3 x $10^{-7}$ and $K_{es2}$ = 1 x $10^{-10}$. [246]

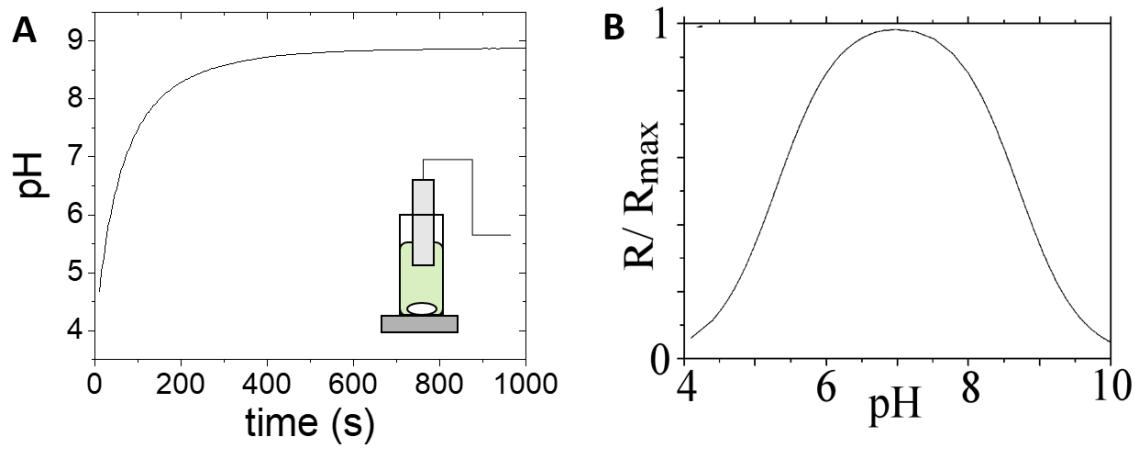


***Figure 7.7 Urease bulk reaction*** *(A) pH time profile in well stirred batch reactor concentrations [urea] = 0.07 M, [acetic acid] = 2 mM; [urease] = 50 Units/mL, [pyranine] = 50 µM, [phosphate]$_T$ = 80 mM and (B) bell-shaped rate-pH curve produced from theoretical relationship with experimentally determined values of $K_{es1}$ and $K_{es2}$.*

### 7.2.9 Fluorescence in the External Solution

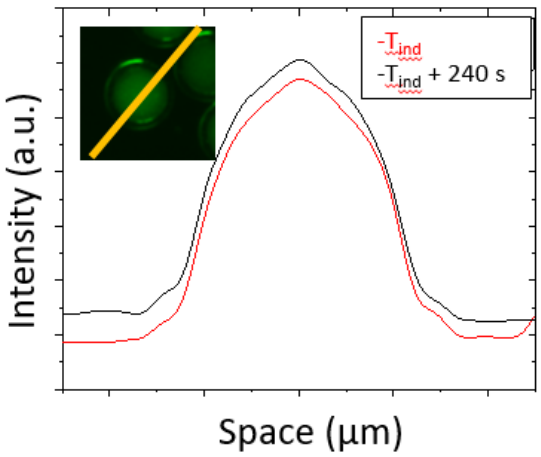


***Figure 7.8 Fluorescence profile across a droplet in chamber*** *with layer depth 200 µM along the indicated line at the induction time, $T_{ind}$, and at $T_{ind}$ + 240 s showing increase in fluorescence in solution with pyranine included in the external solution. Concentrations were [urea] = 0.07 M, [acetic acid] = 1 mM; [urease] = 50 Units/mL, [pyranine] = 50 µM, [phosphate]$_T$ = 80 mM. + 50 µM pyranine in external solution.*

### 7.2.10 Droplet Stability

A concentration of 0.28% (w/v) PF-127 was used to stabilize the inner droplet, which is below the critical micelle concentration (CMC) of PF-127 (0.35% (w/v)). With no surfactant we obtained complete dewetting of the inner droplet from the oil (**Figure 7.9** (Ai)) and reduced concentration of this surfactant led to partial dewetting (**Figure 7.9** Aii). In the absence of reaction, droplets were stable over the course of 48 hours (provided they were not stored in outer solution containing glycerol). In **Figure 7.9** B, the % of encapsulated inner droplets is shown at different time points relative to the initial % of double emulsions produced. The inner solution was composed of PF-127 0.28%, and sucrose (0.2 M), with added components: 1 mM acetic acid (orange), 1 mM acetic acid and urea (0.15 M), and 1 mM ammonia solution; the external solution was the same as the inner solution. There was a small loss of the double emulsions over time (determined by the fraction of intact double emulsions compared to total droplets), but there was little difference between the three cases, within experimental error. The S/C was 0.21 – 0.24 in these examples. We also compared stability of droplets with different shell thicknesses; with S/C of 0.17 the droplets were less stable, and dewetting was observed (**Figure 7.9** C). The indicated standard deviations were calculated from images of 2 – 4 separate samples. In the double emulsions with reaction, some of the droplets were found to be unstable and this was more prevalent in emulsions with thinner shells (**Figure 7.10** A and **Figure 7.10** B). Droplets that underwent partial dewetting were observed to react faster than ones that remained stable (**Figure 7.10** D and **Figure 7.10** E).

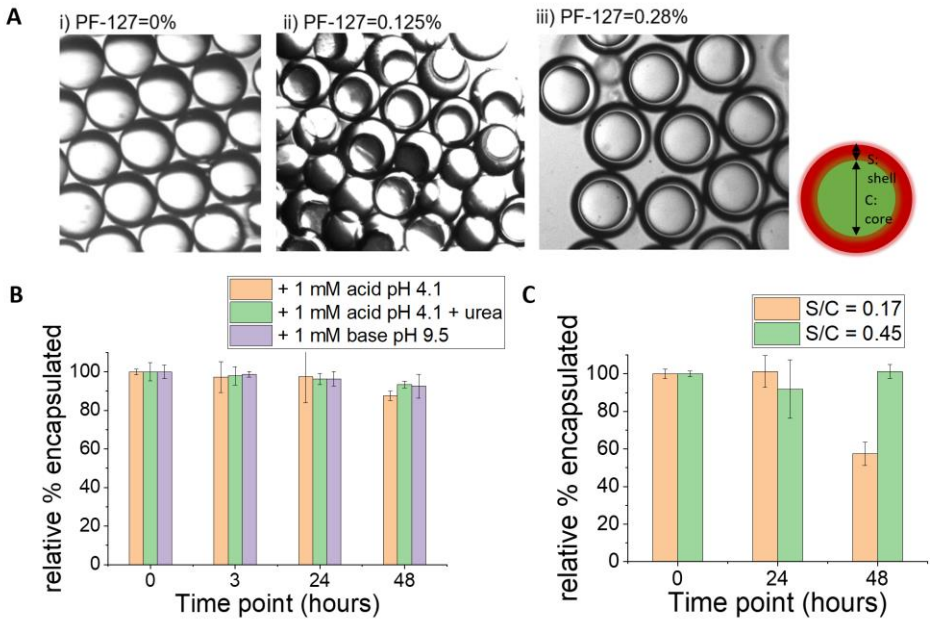


***Figure 7.9 Droplet stability without reaction.*** *(A) Role of PF-127 surfactant concentration in droplet stability (i) complete dewetting with no PF-127; (ii) partial dewetting (iii) stable droplet. (B) Droplet stability (fraction of cores encapsulated compared to initial fraction of intact droplets, S/C = 0.22) over 48 hours with different inner solution (IS) compositions (IS: PF-127 0.28%, sucrose (0.2 M), and added ingredients indicated; the middle fluid was mineral oil, 2% span and 6.5 mM POPC and ES: same as IS). (C) Droplet stability for two different shell:core ratios.*

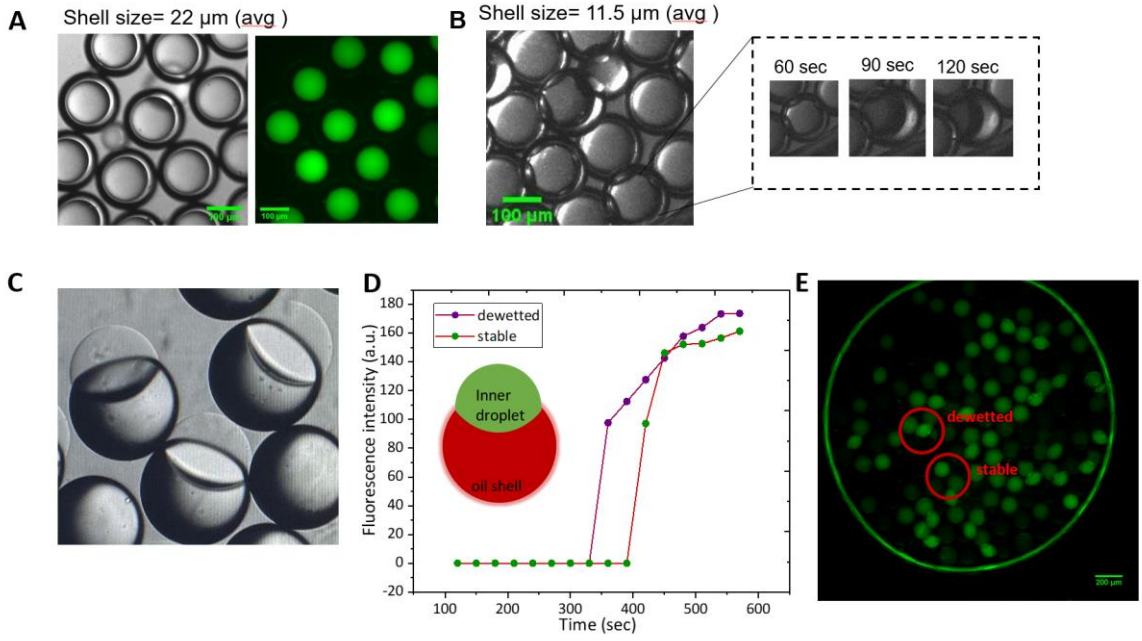


***Figure 7.10 Droplet stability with reaction.*** *(A) Reaction in intact droplets with thick shells (b) Dewetting of droplets with thinner shells during reaction. (C) Image of partially dewetted droplets with core protruding from oil shell. (D) Intensity in time and image of reaction showing that partially dewetted*

*(eye shape) droplets reacted more quickly than intact droplets (spherical shape). Concentrations were: [urea] = 0.04 M, [pyranine] = 50 µM, [AA] = 2 mM, [phosphate]T = 80 mM and [urease] = 20 Units/mL.*

### 7.2.11 Urease-Driven Calcium Phosphate and Calcium Carbonate Precipitation in Bulk Solution

The batch reaction of urease with urea was performed in a 3 ml quartz cuvette with a cross-shaped magnetic stirrer bar. Two stock solutions were prepared; solution A contained urease type III (100 U/mL), Phosphate = 0.8 M in 1 mM acetic acid and solution B contained urea (0.14 M) in 1 mM acetic acid solution with 340 mM calcium chloride added. 1.4 mL of solution A was added to 1.4 ml of solution B and pH was monitored using a pH microelectrode and DrDAQ pH logger.

### 7.2.12 Raman Spectra

Calcium phosphate and calcium carbonate crystals were characterized using a Senterra II Raman confocal microscope (Bruker) with an excitation wavelength of 532 nm, and power of 25 mW. The 100x objective was used to obtain images of 1594 x 1192 pixels and resolution of 0.04 µm/pixel. The spectral resolution was 1.5 $cm^{-1}$. The sample of solution from experiments with bulk solution was air dried on a microscope slide and an image was obtained of the particles with the microscope (**Figure 7.11** A). In agreement with earlier work, samples contained a mixture of amorphous calcium phosphate or weakly crystalline hydroxyapatite particles with characteristic Raman peaks at 950 $cm^{-1}$ and larger dumbbell shaped crystals of calcite, with characteristic Raman peaks at 711 $cm^{-1}$ and 1085 $cm^{-1}$ (**Figure 7.11** B)[246].

For samples obtained from experiments with the double emulsions, the solution was placed on a microscope slide and spherical particles or microplatelets from burst emulsions were observed. The size of the particles was estimated from the confocal images using MATLAB to be of the order of ~ 500 nm (530 ± 50 nm, **Figure 7.12** A). The Raman spectra of the platelets (**Figure 7.12** B) contained characteristic peaks at 986 $cm^{-1}$, 880 $cm^{-1}$ and 585 $cm^{-1}$ of dicalcium phosphate dehydrate, $CaHPO_4 \cdot 2H_2O$, brushite (**Figure 7.12** C)[416].

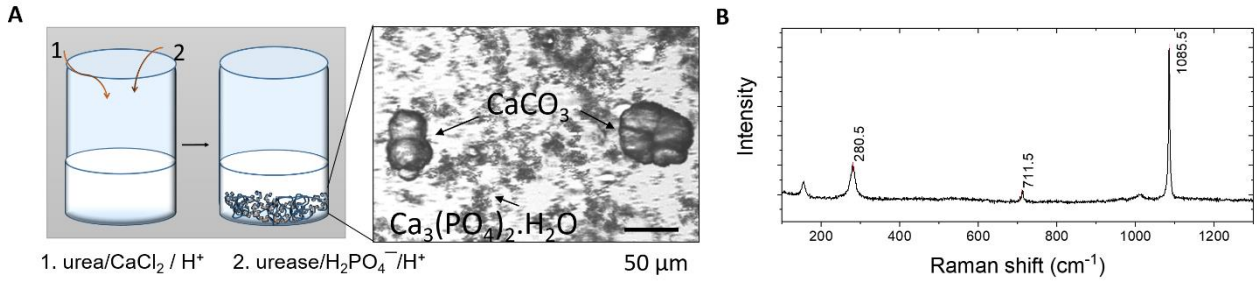


***Figure 7.11. Raman spectrum for bulk solution experiment*** *(A) Illustration of batch experiment with production of a mixture of calcium carbonate and calcium phosphate and microscope image of sample. (B) Raman spectra from confocal image of calcium carbonate obtained showing peaks for calcite at 711 and 1086 cm$^{-1}$.*

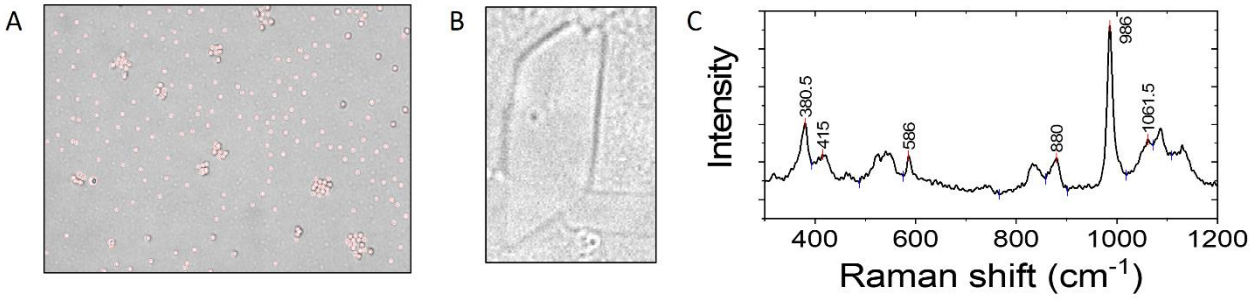


***Figure 7.12 Raman spectrum for double emulsion-based particles*** *(A) Confocal image (63 x 43 µm) of sample of particles from double emulsion sample and circles obtained using MATLAB for estimating particle size. (B) Confocal image (22 x 32 µm) of sample of platelet from double emulsions. (C) Raman spectrum of platelet obtained from sample showing characteristic peaks for brushite at 986 cm$^{-1}$, 880 cm$^{-1}$ and 585 cm$^{-1}$.*

### 7.2.13 Determination of Apparent Area or Length of Calcium Phosphate Precipitate

A comparison of the approximate growth rate of the calcium phosphate structures was determined using ImageJ. The green channel of the RGB images obtained using optical microscopy (with resolution 0.75 pixels/µm) was used to find “apparent” area and length since information regarding the 3D structure could not be obtained. The area containing the precipitate was selected. A threshold filter (percentile) was applied giving a binary image with precipitate and the pen tool was used to fill any pixels containing precipitate that were not highlighted (**Figure 7.13** A). The area occupied by the precipitate was then extracted. The apparent length of the platelet crystals was obtained from the longest axis and plotted in time from a series of images (**Figure 7.13**

B). The average growth rate was calculated from the slope of the plot between 600 and 800 s was 0.12 + 0.02 µm $s^{-1}$.

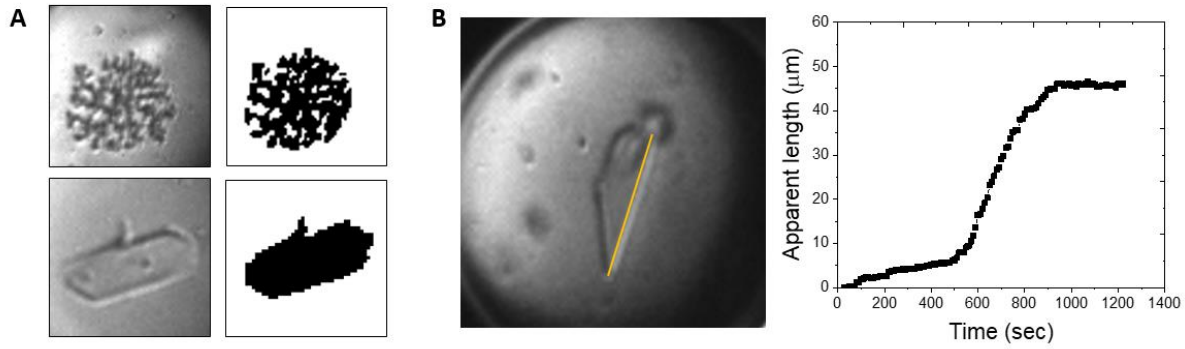


***Figure 7.13 Apparent area or length of calcium phosphate precipitates,*** *(A) Microscope images of calcium phosphate precipitates (35 x 35 µm) and processed binary images used for determination of apparent area occupied by precipitate. (B) Image of platelet (100 x 100 µm) with longest axis identified (yellow line) and apparent length of the crystal in time.*

## 7.2.14 Population Level Crystals

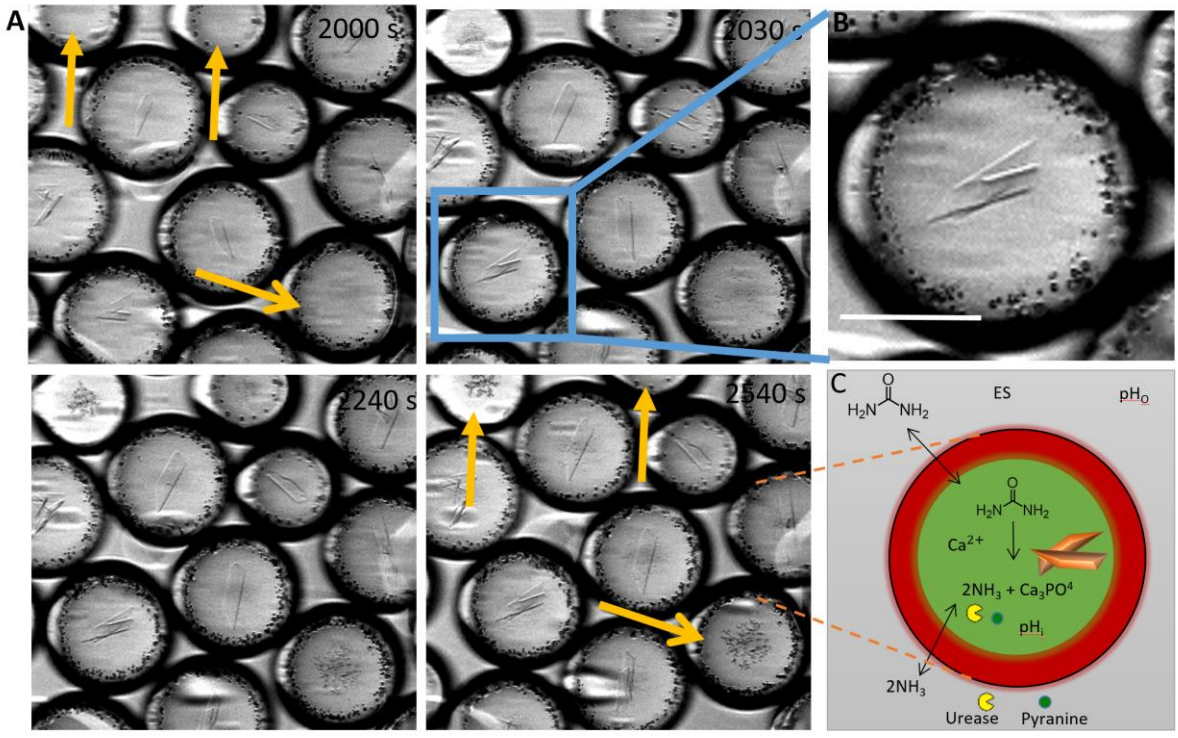


***Figure 7.14 Population level crystals*** *Calcium phosphate formation in a population of droplets with average S/C = 0.09 (the small black circles at the inner oil-water interface are bubbles). The reaction concentrations were: [urea] = 0.15 M, [AA] = 1 mM, [urease] = 50 U/ mL, [phosphate]$_T$ = 80 mM, and [$CaCl_2$] = 0.15 M (A) Time-lapse imaging of urea-urease triggered precipitate formation. Yellow arrows*

*indicate droplets in which nanoparticles formed. (B) multiple crystals formed in some droplets, brightfield microscope (etaluma, 10x magnification), and scale bar = 50 µm (C) A schematic image of the mechanism of crystal growth triggered by the base production in urea hydrolysis reaction.*

## 7.3 **Appendix 3** – Chapter 3: A Modelling Approach to Predict the Influence of Shell-core Reactor Configuration on the Induction Time of Urea-urease Reaction

The Matlab script was written in two parts, one of which contains the reaction-diffusion equations (at the interfaces and edges of the layered core-shell sphere) according to Section 3.4 and is named "oil_urease_eq.m", while the second part contains the initial conditions and constants used in the first part and was termed as 'run_oil_urease_eq.m'. This was done to simplify the code.

### 7.3.1 Matlab Script for 'oil_urease_eq.m'

```
% Urease-loaded drop in contact with solution via oil layer
% variables - 1 U, 2 N, 3 NH, 4 H, 5 OH, 6 CO2, 7 HCO3, 8 CO3, 9 HA,
10 A,
function F = oil_urease_eq(t,c)
global kE Km KES1 KES2 E KS Kp
global DU Dn Dnh DH DOH Dco2 Dhco3 Dco3 DHa Da
global L BL L2 T N h ho2 r ir hs
global DUo Dno Dco2o DHao Dao Dnho
global U0 H0 OH0
global Pu Pn Pco2 Pha
global ku kn kco2 kha
global k2 k2r k3 k3r k4 k4r k5 k5r k6 k6r


a=2.0/hs;
%left boundary - no flux
R1 = kE*E*c(1)/(1+KES2/c(4)+c(4)/ KES1)/(Km+c(1));
%R1 = kE*E*c(1)/(1+KES2/c(4)+c(4)/
KES1)/(Km+c(1)*(1+c(1)/KS))/(1+c(3)/Kp);
F(1) =  a*DU*(c(11)-c(1))  - R1;
%Urea  at wall (No-Flux boundary)
F(2) =  a*Dn*(c(12)-c(2)) + 2*R1 - k2*c(2)*c(4) + k2r*c(3);
%N  at wall (No-Flux boundary)
F(3) =  a*Dnh*(c(13)-c(3)) + k2*c(2)*c(4) - k2r*c(3);
%NH at wall (No-Flux boundary)
F(4) = a*DH*(c(14)-c(4)) + k5r - k5*c(4)*c(5) + k2r*c(3)-
k2*c(2)*c(4)+k3r*c(6)-k3*c(4)*c(7)+k4r*c(7)-k4*c(8)*c(4)+k6r*c(9)-
k6*c(10)*c(4); %H at wall (No-Flux boundary)
F(5) = a*DOH*(c(15)-c(5)) + k5r - k5*c(4)*c(5);
%OH at wall (No-Flux boundary)
F(6) =  a*Dco2*(c(16)-c(6)) + R1-k3r*c(6)+k3*c(4)*c(7);
F(7) =  a*Dhco3*(c(17)-c(7)) + k3r*c(6)-k3*c(4)*c(7)-
k4r*c(7)+k4*c(8)*c(4);
```

```
F(8) =  a*Dco3*(c(18)-c(8)) + k4r*c(7)-k4*c(8)*c(4);
F(9) = a*DHa*(c(19)-c(9)) - k6r*c(9)+k6*c(10)*c(4);
F(10) = a*Da*(c(20)-c(10)) + k6r*c(9)-k6*c(10)*c(4);

%droplet core
for m=N+1:N:N*L-10
    R = kE*E*c(m)/(1+KES2/c(m+3)+c(m+3)/KES1)/(Km+c(m));
    %R = kE*E*c(1)/(1+KES2/c(4)+c(4)/
KES1)/(Km+c(1)*(1+c(1)/KS))/(1+c(3)/Kp);
    F(m)    = ir(m)/hs*DU*((c(m+N)-c(m))*(r(m)+ho2)-(c(m)-c(m-
N))*(r(m)-ho2)) - R;                    %urea in drop
    F(m+1) = ir(m+1)/hs*Dn*((c(m+1+N)-c(m+1))*(r(m+1)+ho2)-(c(m+1)-
c(m+1-N))*(r(m+1)-ho2)) + 2*R + k2r*c(m+2) - k2*c(m+1)*c(m+3);
%N in drop
    F(m+2) = ir(m+2)/hs*Dnh*((c(m+2+N)-c(m+2))*(r(m+2)+ho2)-(c(m+2)-
c(m+2-N))*(r(m+2)-ho2)) + k2*c(m+1)*c(m+3) - k2r*c(m+2);
%NH in drop
    F(m+3) = ir(m+3)/hs*DH*((c(m+3+N)-c(m+3))*(r(m+3)+ho2)-(c(m+3)-
c(m+3-N))*(r(m+3)-ho2)) + k5r - k5*c(m+3)*c(m+4) + k2r*c(m+2) -
k2*c(m+1)*c(m+3)+k3r*c(m+5)-k3*c(m+3)*c(m+6)+k4r*c(m+6)-
k4*c(m+7)*c(m+3)+ k6r*c(m+8)-k6*c(m+9)*c(m+3);
    F(m+4) = ir(m+4)/hs*DOH*((c(m+4+N)-c(m+4))*(r(m+4)+ho2)-(c(m+4)-
c(m+4-N))*(r(m+4)-ho2)) + k5r - k5*c(m+3)*c(m+4);
    F(m+5) = ir(m+5)/hs*Dco2*((c(m+5+N)-c(m+5))*(r(m+5)+ho2)-
(c(m+5)-c(m+5-N))*(r(m+5)-ho2)) +R - k3r*c(m+5)+k3*c(m+3)*c(m+6);
    F(m+6) = ir(m+6)/hs*Dhco3*((c(m+6+N)-c(m+6))*(r(m+6)+ho2)-
(c(m+6)-c(m+6-N))*(r(m+6)-ho2)) +k3r*c(m+5)-k3*c(m+3)*c(m+6)-
k4r*c(m+6)+k4*c(m+7)*c(m+3);
    F(m+7) = ir(m+7)/hs*Dco3*((c(m+7+N)-c(m+7))*(r(m+7)+ho2)-
(c(m+7)-c(m+7-N))*(r(m+7)-ho2)) + k4r*c(m+6)-k4*c(m+7)*c(m+3);
    F(m+8) = ir(m+8)/hs*DHa*((c(m+8+N)-c(m+8))*(r(m+8)+ho2)-(c(m+8)-
c(m+8-N))*(r(m+8)-ho2)) - k6r*c(m+8)+k6*c(m+9)*c(m+3);
    F(m+9) = ir(m+9)/hs*Da*((c(m+9+N)-c(m+9))*(r(m+9)+ho2)-(c(m+9)-
c(m+9-N))*(r(m+9)-ho2)) + k6r*c(m+8)-k6*c(m+9)*c(m+3);
end
%aq interface
R2 = kE*E*c(N*L-9)/(1+KES2/c(N*L-9+3)+c(N*L-9+3)/ KES1)/(Km+c(N*L-
9));
F(N*L-9) =  ir(N*L-9)/hs*DU*(-(c(N*L-9)-c(N*L-9-N))*(r(N*L-9)-
ho2))+ir(N*L-9)*Pu*(c(N*L+1)/ku-c(N*L-9))-R2 ;
%Urea at interface
F(N*L-8) = ir(N*L-8)/hs*Dn*(-(c(N*L-8)-c(N*L-8-N))*(r(N*L-8)-ho2))+
ir(N*L-8)*Pn*(c(N*L+2)/kn-c(N*L-8))+ 2*R2 + k2r*c(N*L-9+2) -
k2*c(N*L-9+1)*c(N*L-9+3) ;
F(N*L-7) = a*Dnh*(c(N*L-7-N)-c(N*L-7))+ k2*c(N*L-9+1)*c(N*L-9+3) -
k2r*c(N*L-9+2) ;
F(N*L-6) = a*DH*(c(N*L-6-N)-c(N*L-6))+ k5r - k5*c(N*L-9+3)*c(N*L-
9+4) + k2r*c(N*L-9+2) - k2*c(N*L-9+1)*c(N*L-9+3)+k3r*c(N*L-9+5)-
k3*c(N*L-9+3)*c(N*L-9+6)+k4r*c(N*L-9+6)-k4*c(N*L-9+7)*c(N*L-
9+3)+k6r*c(N*L-9+8)-k6*c(N*L-9+9)*c(N*L-9+3) ;
F(N*L-5) = a*DOH*(c(N*L-5-N)-c(N*L-5))+ k5r - k5*c(N*L-9+3)*c(N*L-
9+4) ;
F(N*L-4) = ir(N*L-4)/hs*Dco2*(-(c(N*L-4)-c(N*L-4-N))*(r(N*L-4)-
ho2))+ ir(N*L-4)*Pco2*(c(N*L+6)/kco2-c(N*L-4))+R2 - k3r*c(N*L-
9+5)+k3*c(N*L-9+3)*c(N*L-9+6) ;
```

```
F(N*L-3) =  a*Dhco3*(c(N*L-3-N)-c(N*L-3))+k3r*c(N*L-9+5)-k3*c(N*L-
9+3)*c(N*L-9+6)-k4r*c(N*L-9+6)+k4*c(N*L-9+7)*c(N*L-9+3) ;
F(N*L-2) =  a*Dco3*(c(N*L-2-N)-c(N*L-2))+ k4r*c(N*L-9+6)-k4*c(N*L-
9+7)*c(N*L-9+3);
F(N*L-1) = ir(N*L-1)/hs*DHa*(-(c(N*L-1)-c(N*L-1-N))*(r(N*L-1)-
ho2))+ir(N*L-1)*Pha*(c(N*L+9)/kha-c(N*L-1))- k6r*c(N*L-
9+8)+k6*c(N*L-9+9)*c(N*L-9+3);
F(N*L) = a*Da*(c(N*L-N)-c(N*L))+ k6r*c(N*L-9+8)-k6*c(N*L-9+9)*c(N*L-
9+3);

%oil interface
F(N*L+1) = ir(N*L+1)/hs*DUo*((c(N*L+1+N)-c(N*L+1))*(r(N*L+1)+ho2))-
ir(N*L+1)*Pu*(c(N*L+1)/ku-c(N*L-9));     %U  at wall (No-Flux
boundary)
F(N*L+2) =  ir(N*L+2)/hs*Dno*((c(N*L+2+N)-
c(N*L+2))*(r(N*L+2+1)+ho2))-ir(N*L+2)*Pn*(c(N*L+2)/kn-c(N*L-8)) ;
%N  at wall (No-Flux boundary)
F(N*L+3) =  0 ;                          %NH at wall (No-Flux
boundary)a*Dnho*(c(N*L+3+N)-c(N*L+3))
F(N*L+4) = 0;    %H  at wall (No-Flux boundary)
F(N*L+5) = 0 ;                             %OH at wall (No-Flux
boundary)
F(N*L+6) =  ir(N*L+6)/hs*Dco2o*((c(N*L+6+N)-
c(N*L+6))*(r(N*L+6)+ho2))-ir(N*L+6)*Pco2*(c(N*L+6)/kco2-c(N*L-4)) ;
F(N*L+7) =  0 ;
F(N*L+8) = 0;
F(N*L+9) = ir(N*L+9)/hs*DHao*((c(N*L+9+N)-c(N*L+9))*(r(N*L+9)+ho2))-
ir(N*L+9)*Pha*(c(N*L+9)/kha-c(N*L-1));
F(N*L+10) = 0;

%oil layer
for b=N*L+11:N:N*L+BL*N-10
    F(b)    =  ir(b)/hs*DUo*((c(b+N)-c(b))*(r(b)+ho2)-(c(b)-c(b-
N))*(r(b)-ho2)); %S in oil layer
    F(b+1) =  ir(b+1)/hs*Dno*((c(b+1+N)-c(b+1))*(r(b+1)+ho2)-
(c(b+1)-c(b+1-N))*(r(b+1)-ho2)); %P in oil layer
    F(b+2) =  0 ; %PH in oil layerir(b+2)/hs*Dnho*((c(b+2+N)-
c(b+2))*(r(b+2)+ho2)-(c(b+2)-c(b+2-N))*(r(b+2)-ho2))
    F(b+3) =  0 ;  %H in boundary layer
    F(b+4) = 0;  %OH in boundary layer
    F(b+5) = ir(b+5)/hs*Dco2o*((c(b+5+N)-c(b+5))*(r(b+5)+ho2)-
(c(b+5)-c(b+5-N))*(r(b+5)-ho2)) ;
    F(b+6) = 0 ;
    F(b+7) = 0;
    F(b+8) = ir(b+8)/hs*DHao*((c(b+8+N)-c(b+8))*(r(b+8)+ho2)-
(c(b+8)-c(b+8-N))*(r(b+8)-ho2)) ;
    F(b+9) = 0 ;
end

%oil interface

F(L*N+BL*N-9) = ir(L*N+BL*N-9)/hs*DUo*(-(c(L*N+BL*N-9)-c(L*N+BL*N-9-
N))*(r(L*N+BL*N-9)-ho2))+ir(L*N+BL*N-9)*Pu*(-c(L*N+BL*N-
9)/ku+c(L*N+BL*N+1)); %S right boundary
```

```
F(L*N+BL*N-8) = ir(L*N+BL*N-8)/hs*Dno*(-(c(L*N+BL*N-8)-c(L*N+BL*N-8-
N))*(r(L*N+BL*N-8)-ho2))+ir(L*N+BL*N-8)*Pn*(-c(L*N+BL*N-
8)/kn+c(L*N+BL*N+2)) ; %P right boundary
F(L*N+BL*N-7) = 0; %PH right boundarya*Dnho*(-c(L*N+BL*N-
7)+c(L*N+BL*N-7-N))
F(L*N+BL*N-6) = 0 ; %H right boundary
F(L*N+BL*N-5) = 0 ; %OH right boundary
F(L*N+BL*N-4) = ir(L*N+BL*N-4)/hs*Dco2o*(-(c(L*N+BL*N-4)-c(L*N+BL*N-
4-N))*(r(L*N+BL*N-4)-ho2))+ir(L*N+BL*N-4)*Pco2*(-c(L*N+BL*N-
4)/kco2+c(L*N+BL*N+6)) ;
F(L*N+BL*N-3) = 0 ;
F(L*N+BL*N-2) = 0 ;
F(L*N+BL*N-1) = ir(L*N+BL*N-1)/hs*DHao*(-(c(L*N+BL*N-1)-c(L*N+BL*N-
1-N))*(r(L*N+BL*N-1)-ho2))+ir(L*N+BL*N-1)*Pha*(-c(L*N+BL*N-
1)/kha+c(L*N+BL*N+9));
F(L*N+BL*N) = 0;

%layer3 - external solution
%aqueous interface
F(L*N+BL*N+1) = ir(L*N+BL*N+1)/hs*DU*((c(L*N+BL*N+1+N)-
c(L*N+BL*N+1))*(r(L*N+BL*N+1)+ho2))-ir(L*N+BL*N+1)*Pu*(-c(L*N+BL*N-
9)/ku+c(L*N+BL*N+1)); %S right boundary
F(L*N+BL*N+2) = ir(L*N+BL*N+2)/hs*Dn*((c(L*N+BL*N+2+N)-
c(L*N+BL*N+2))*(r(L*N+BL*N+2)+ho2))-ir(L*N+BL*N+2)*Pn*(-c(L*N+BL*N-
8)/kn+c(L*N+BL*N+2)) + k2r*c(L*N+BL*N+1+2) -
k2*c(L*N+BL*N+1+1)*c(L*N+BL*N+1+3); %P right boundary
F(L*N+BL*N+3) = a*Dnh*(-c(L*N+BL*N+3)+c(L*N+BL*N+3+N)) +
k2*c(L*N+BL*N+1+1)*c(L*N+BL*N+1+3) - k2r*c(L*N+BL*N+1+2) ; %PH right
boundary
F(L*N+BL*N+4) = a*DH*(-c(L*N+BL*N+4)+c(L*N+BL*N+4+N)) + k5r -
k5*c(L*N+BL*N+1+3)*c(L*N+BL*N+1+4) + k2r*c(L*N+BL*N+1+2) -
k2*c(L*N+BL*N+1+1)*c(L*N+BL*N+1+3)+k3r*c(L*N+BL*N+1+5)-
k3*c(L*N+BL*N+1+3)*c(L*N+BL*N+1+6)+k4r*c(L*N+BL*N+1+6)-
k4*c(L*N+BL*N+1+7)*c(L*N+BL*N+1+3)+k6r*c(L*N+BL*N+1+8)-
k6*c(L*N+BL*N+1+9)*c(L*N+BL*N+1+3) ;    %H  at wall (No-Flux
boundary); %H right boundary
F(L*N+BL*N+5) = a*DOH*(-c(L*N+BL*N+5)+c(L*N+BL*N+5+N))  + k5r -
k5*c(L*N+BL*N+1+3)*c(L*N+BL*N+1+4); %OH right boundary
F(L*N+BL*N+6) = ir(L*N+BL*N+6)/hs*Dco2*((c(L*N+BL*N+6+N)-
c(L*N+BL*N+6))*(r(L*N+BL*N+6)+ho2)) -ir(L*N+BL*N+6)*Pco2*(-
c(L*N+BL*N-4)/kco2+c(L*N+BL*N+6)) -
k3r*c(L*N+BL*N+1+5)+k3*c(L*N+BL*N+1+3)*c(L*N+BL*N+1+6) ;
F(L*N+BL*N+7) = a*Dhco3*(-c(L*N+BL*N+7)+c(L*N+BL*N+7+N))
+k3r*c(L*N+BL*N+1+5)-k3*c(L*N+BL*N+1+3)*c(L*N+BL*N+1+6)-
k4r*c(L*N+BL*N+1+6)+k4*c(L*N+BL*N+1+7)*c(L*N+BL*N+1+3);
F(L*N+BL*N+8) = a*Dco3*(-c(L*N+BL*N+8)+c(L*N+BL*N+8+N)) +
k4r*c(L*N+BL*N+1+6)-k4*c(L*N+BL*N+1+7)*c(L*N+BL*N+1+3) ;
F(L*N+BL*N+9) = ir(L*N+BL*N+9)/hs*DHa*((c(L*N+BL*N+9+N)-
c(L*N+BL*N+9))*(r(L*N+BL*N+9)+ho2))-ir(L*N+BL*N+9)*Pha*(-c(L*N+BL*N-
1)/kha+c(L*N+BL*N+9))-
k6r*c(L*N+BL*N+1+8)+k6*c(L*N+BL*N+1+9)*c(L*N+BL*N+1+3);
F(L*N+BL*N+10) = a*Da*(-c(L*N+BL*N+10)+c(L*N+BL*N+10+N))+
k6r*c(L*N+BL*N+1+8)-k6*c(L*N+BL*N+1+9)*c(L*N+BL*N+1+3);

%aqeuous layer
for q=L*N+BL*N+11:N:T-10
```

```
    F(q)    = ir(q)/hs*DU*((c(q+N)-c(q))*(r(q)+ho2)-(c(q)-c(q-
N))*(r(q)-ho2)) ;                          %S in
    F(q+1) = ir(q+1)/hs*Dn*((c(q+1+N)-c(q+1))*(r(q+1)+ho2)-(c(q+1)-
c(q+1-N))*(r(q+1)-ho2)) + k2r*c(q+2) - k2*c(q+1)*c(q+3);
%P in seed
    F(q+2) = ir(q+2)/hs*Dnh*((c(q+2+N)-c(q+2))*(r(q+2)+ho2)-(c(q+2)-
c(q+2-N))*(r(q+2)-ho2)) + k2*c(q+1)*c(q+3) - k2r*c(q+2);
%PH in seed
    F(q+3) = ir(q+3)/hs*DH*((c(q+3+N)-c(q+3))*(r(q+3)+ho2)-(c(q+3)-
c(q+3-N))*(r(q+3)-ho2)) + k5r - k5*c(q+3)*c(q+4) + k2r*c(q+2) -
k2*c(q+1)*c(q+3)+k3r*c(q+5)-k3*c(q+3)*c(q+6)+k4r*c(q+6)-
k4*c(q+7)*c(q+3)+ k6r*c(q+8)-k6*c(q+9)*c(q+3);  %H in bead
    F(q+4) = ir(q+4)/hs*DOH*((c(q+4+N)-c(q+4))*(r(q+4)+ho2)-(c(q+4)-
c(q+4-N))*(r(q+4)-ho2)) + k5r - k5*c(q+3)*c(q+4);   %OH in bead
    F(q+5) = ir(q+5)/hs*Dco2*((c(q+5+N)-c(q+5))*(r(q+5)+ho2)-
(c(q+5)-c(q+5-N))*(r(q+5)-ho2)) - k3r*c(q+5)+k3*c(q+3)*c(q+6);
    F(q+6) = ir(q+6)/hs*Dhco3*((c(q+6+N)-c(q+6))*(r(q+6)+ho2)-
(c(q+6)-c(q+6-N))*(r(q+6)-ho2)) +k3r*c(q+5)-k3*c(q+3)*c(q+6)-
k4r*c(q+6)+k4*c(q+7)*c(q+3);
    F(q+7) = ir(q+7)/hs*Dco3*((c(q+7+N)-c(q+7))*(r(q+7)+ho2)-
(c(q+7)-c(q+7-N))*(r(q+7)-ho2)) + k4r*c(q+6)-k4*c(q+7)*c(q+3);
    F(q+8) = ir(q+8)/hs*DHa*((c(q+8+N)-c(q+8))*(r(q+8)+ho2)-(c(q+8)-
c(q+8-N))*(r(q+8)-ho2)) - k6r*c(q+8)+k6*c(q+9)*c(q+3);
    F(q+9) = ir(q+9)/hs*Da*((c(q+9+N)-c(q+9))*(r(q+9)+ho2)-(c(q+9)-
c(q+9-N))*(r(q+9)-ho2)) + k6r*c(q+8)-k6*c(q+9)*c(q+3);
end

%right boundary - no flux
F(T-9) = 2.0/hs*DU*(-c(T-9)+c(T-9-N)); %U right boundary
F(T-8) = 2.0/hs*Dn*(-c(T-8)+c(T-8-N))+ k2r*c(T-7) - k2*c(T-8)*c(T-6)
; %P right boundary
F(T-7) = 2.0/hs*Dnh*(-c(T-7)+c(T-7-N))+k2*c(T-8)*c(T-6) - k2r*c(T-7)
; %PH right boundary
F(T-6) =  2.0/hs*DH*(-c(T-6)+c(T-6-N))+ k5r - k5*c(T-6)*c(T-5) +
k2r*c(T-7) - k2*c(T-8)*c(T-6)+k3r*c(T-4)-k3*c(T-6)*c(T-3)+k4r*c(T-
3)-k4*c(T-2)*c(T-6) + k6r*c(T-1)-k6*c(T)*c(T-6); %H right boundary
F(T-5) =  2.0/hs*DOH*(-c(T-5)+c(T-5-N))+ k5r - k5*c(T-6)*c(T-5) ;
%OH right boundary
F(T-4) = 2.0/hs*Dco2*(-c(T-4)+c(T-4-N))- k3r*c(T-4)+k3*c(T-6)*c(T-3)
;
F(T-3) = 2.0/hs*Dhco3*(-c(T-3)+c(T-3-N))+k3r*c(T-4)-k3*c(T-6)*c(T-
3)-k4r*c(T-3)+k4*c(T-2)*c(T-6) ;
F(T-2) = 2.0/hs*Dco3*(-c(T-2)+c(T-2-N))+ k4r*c(T-3)-k4*c(T-2)*c(T-6)
;
F(T-1) = 2.0/hs*DHa*(-c(T-1)+c(T-1-N)) - k6r*c(T-1)+k6*c(T)*c(T-6);
F(T) = 2.0/hs*Da*(-c(T)+c(T-N)) + k6r*c(T-1)-k6*c(T)*c(T-6);

F=F';

%       at the wall                                          boundary layer              surrounding soultion
%       |                                                    |                           |
%       cell_1  cell_2  cell_3  cell_4  ... cell_m   ...    cell_L      cell_L+1  cell_L+b   ...   fixed
concentrations
% U     c(1)    c(9)    c(17)    c(25)  ... c(m)     ...    c(L*N-4)    c(L*N+1)  c(L*N+b)   ...   S0
% P     c(2)    c(10)    c(18)    c(26)  ... c(m+1)   ...   c(L*N-3)    c(L*N+2)  c(L*N+b+1) ...   N0
% PH    c(3)    c(11)    c(19)    c(27)  ... c(m+2)   ...   c(L*N-2)    c(L*N+3)  c(L*N+b+2) ...   NH0
% H     c(4)    c(12)    c(20)    c(28)  ... c(m+3)   ...   c(L*N-1)    c(L*N+4)  c(L*N+b+3) ...   H0
% OH    c(5)    c(13)   c(21)    c(29)  ... c(m+4)   ...   c(L*N)      c(L*N+5)  c(L*N+b+4) ...   OH0
```

### 7.3.2 Matlab Script for 'run_oil_urease_eq.m'

```
% Urease-loaded drop in contact with solution via oil layer
% variables - 1 U, 2 N, 3 NH, 4 H, 5 OH, 6 CO2, 7 HCO3, 8 CO3, 9 HA,
10 A,
tic
clear all
close all
global kE Km KES1 KES2   Kp    %enzyme constants
global DU Dn Dnh Dn DH DOH Dco2 Dhco3 Dco3 DHa Da   %aqueous
diffusion coefficients
global L BL L2 T N  h ho2 r ir hs  %domain size parameters
global DUo Dno Dco2o DHao    %diffusion coefficients in oil
global E U0 H0 OH0 HA A      %initial values
global Pu Pn Pco2 Pha        %permeability coefficients
global ku kn kco2 kha        %partition coefficients
global k2 k2r k3 k3r k4 k4r k5 k5r k6 k6r KW Kac  %rate and
equilibrium constants

%constants
kE=3.5e-6; Km=0.003; KES1=5e-6; KES2=2e-9; KS=3;Kp=0.002;
k2=4.3e10; k2r=24; k3=7.9e4; k3r=0.037; k4=5e10; k4r=2.8;k5=1e11;
k5r=1e-3; k6r=7.8e5;k6=4.5e10;  KW=1e-14;Kac=k6r/k6;  % forwards
reactionL H+ + NH3 = NH4+
DU=1e-3; DH=2e-3; DOH=1e-3; Dn=1e-3; Dnh=1e-3; Dco2=1e-3; Dhco3=1e-
3; Dco3=1e-3; DHa=1e-3; Da=1e-3;% unit of D: mm^2/sec
DUo=1e-3/20; Dno=1e-3/20; Dco2o=1e-3/20; DHao=1e-3/20; % unit of D:
mm^2/sec
Pu=5e-5; Pn=0.1; Pco2=0.1; Pha=0.0001; % unit of P: mm/sec
ku=0.001; kn=1; kco2=1; kha=0.1;


% ****initial conditions****
E=50.0; %drop
HA=0;  %drop
U0=0.04;   % in bulk solution
H0=0.0001;    % in bulk solution
%H0=sqrt(HA*Kac);
OH0 = KW/H0; % in bulk solution
A=0;


% ************************************************
N=10;       % number of variables U, N, NH, H, OH, CO2, HCO3, CO3,
HA, A
L=56;         %number of cells in drop  L*h = radius of drop
BL=15;       % number of cells in oil
L2=100;       % number of cells in external solution
T=L*N+BL*N+N*L2;  %total length
t_final = 500;         % final time in sec
t_op = 1;              % output period in s; For example, 60
corresponds to 1 min
t_fg = 20;    % plotting  period: n * t_op; For example, t_fg = 30
means plot every 30th output i.e. every 30 minutes
```

```
h=0.001; % spatial resolution in mm (domain length in reality = T *
h)
hs=h*h;
ho2 = h/2;
R = h:h:h*(L+BL+L2); % radial coordinates of cells
iR = 1./R;           % 1/radial coordinate
r = repelem(R,N);
ir = repelem(iR,N);
ti = 0:t_op:t_final;    % output times
st = size(ti);

% initial conditions in drop
for iv=1:N:N*L
    c0(iv)=0.0; %S
    c0(iv+1)=0.0; %N
    c0(iv+2)=0.0; %NH
    c0(iv+3)=H0; %H
    c0(iv+4)=OH0; %OH
    c0(iv+5)=0.0;   %CO2
    c0(iv+6)=0.0;  %HCO3
    c0(iv+7)=0.0;  %CO3
    c0(iv+8)=HA;  %Ha
    c0(iv+9)=A;  %a
end
% initial conditions in oil
for ivb=N*L+1:N:N*L+BL*N
    c0(ivb)=0; %S
    c0(ivb+1)=0.0; %N
    c0(ivb+2)=0.0; %NH
    c0(ivb+3)=0; %H
    c0(ivb+4)=0; %OH
    c0(ivb+5)=0.0;   %CO2
    c0(ivb+6)=0.0;  %HCO3
    c0(ivb+7)=0.0;  %CO3
    c0(ivb+8)=0.0;  %Ha
    c0(ivb+9)=0.0;  %a
end
%initial conditions in external solution
for ivc=N*L+BL*N+1:N:T
    c0(ivc)=U0; %S
    c0(ivc+1)=0.0; %N
    c0(ivc+2)=0.0; %NH
    c0(ivc+3)=H0; %H
    c0(ivc+4)=OH0; %OH
    c0(ivc+5)=0.0;   %CO2
    c0(ivc+6)=0.0;  %HCO3
    c0(ivc+7)=0.0;  %CO3
    c0(ivc+8)=HA;  %Ha
    c0(ivc+9)=A;  %a
end
% ode solver
options = odeset('AbsTol',1e-11);
[ti,C] = ode15s('oil_urease_eq',ti,c0,options);

% figures
```

```
sp = linspace(0,L*h+BL*h+L2*h,L+BL+L2);    %spatial coordinate
time=linspace(0,t_final,t_final/(t_fg*t_op)+1);

figure
c=0;
for i=1:t_fg:st(2);
    c=c+1;
    pHs(c,:)=-log10(C(i,4:N:T));        %pH    file
    plot(sp,-log10(C(i,4:N:T)),'-')%plot ph in space at different
time points
    hold on
end
xlabel('space / mm')
ylabel('pH')

figure
for i=1:2:T/N;
    plot(time,pHs(:,i),'-') %plot pH in time at different spatial
points
    hold on
end
xlabel('time / s')
ylabel('pH')

c=0;
figure
for i=1:t_fg:st(2);
    c=c+1;
    Hp(c,:)=(C(i,4:N:T));        %H+    file
    plot(sp,C(i,4:N:T),'-') %plot acid in space at different times
    hold on
end
xlabel('space / mm')
ylabel('[H+]')
hold on

c=0;
figure
for i=1:t_fg:st(2);
    c=c+1;
    U(c,:)=C(i,1:N:T);                          %urea file
    plot(sp,log10(C(i,1:N:T)),'-')           %plot urea
    hold on
end
xlabel('space / mm')
ylabel('log([urea] / M')
%ylim([0 log(S0)])

c=0;
figure
for i=1:t_fg:st(2);
    c=c+1;
    nh3(c,:)=C(i,2:N:T);
    plot(sp,log10(C(i,2:N:T)),'-')
    hold on
end
```

```
xlabel('space / mm')
%ylim([0 0.1])
ylabel('log[NH_3] / M')

figure
cm=flip(parula);
spl = surf(pHs);
spl.EdgeColor = [0 0 0];
spl.EdgeAlpha = [0];
colormap(cm)
ylabel('time /  s')
xlabel('space / mm')
zlabel('pH')
set(gcf,'color','w')
xlim([0 T/N])
ylim([0 t_final/(t_fg*t_op)+1])
zlim([2 11])
%set(gca,'XTick',0:20:200,'XTickLabel',0:2:21,'YTick',0:10:100,'YTic
kLabel',0:5:100,'ZTick',[3 5 7 10])
box on
save('particle.mat')

toc

csvwrite('matlab2.csv',pHs);
```

## 7.4 **Appendix 4** – Chapter 4: Chemical Communication and Collective Effects in Urease Double Emulsion Systems

### 7.4.1 Matlab Code for Image Tracking

```
% Backward tracking without calculating intensity ratios
clear all
close all
dir = 'C:\Users\CBE-User\Documents\lab\Experiments\Double emulsion
reaction\stack2aft\1\';
dir1='C:\Users\CBE-User\Documents\lab\Experiments\Double emulsion
reaction\stack2aft\1\';
fnr = 'MyExperiment_F2_0000'; % file mane root
fi = 1;         % first image
li = 11;         % last image
sens=0.95;
fmt = 'tif';     % image format
thd = 30;        % displacement threshold for vesicles movement
between frames
tr = '0';
patch1 = [51 743 274 34]; % to cover time stamp on image
patch2 = [596 703 76 55]; % to cover space bar on
imageMyExperiment_WHITE_000025
%patch3 = [1 236 34 92];
Pixel2MicroMeterRatio = 15/50;
if li < 10
    st = [tr,num2str(li)];
```

```
else
    st = num2str(li);
end
i_final = imread([dir,fnr,st,'.',fmt]);
i_final(patch1(2):patch1(2)+patch1(4),patch1(1):patch1(1)+patch1(3),
1:3) = 0;
i_final(patch2(2):patch2(2)+patch2(4),patch2(1):patch2(1)+patch2(3),
1:3) = 0;
%i_final(patch3(2):patch3(2)+patch3(4),patch3(1):patch3(1)+patch3(3)
,1:3) = 0;
%i_final(:,:,2) = medfilt2(i_final(:,:,2),[10 10]);
i_final_adj = imadjust(i_final(:,:,2));
[CircCenter0, CircRadii0] = imfindcircles(i_final_adj,[10
15],'ObjectPolarity','bright','sensitivity',sens);
nov = length(CircRadii0);
imshow(i_final_adj);
hold on
viscircles(CircCenter0, CircRadii0,'EdgeColor','r','linewidth',0.5);
for n = 1:nov
  hold on

text(CircCenter0(n,1),CircCenter0(n,2)+2,num2str(n),'fontsize',8,'ho
rizontalalignment','center','verticalalignment','bottom','color','r'
);
end
print([dir1,fnr,'_t',st,'_eval'],'-dpng','-r100')
p(:,1) = CircCenter0(:,1);
p(:,2) = CircCenter0(:,2);
intensity = zeros(li-fi,nov);
RealCircDiameter = zeros(1,nov);
for q = li:-1:fi
    if q < 10
        st = ['0',num2str(q)];
    else
        st = num2str(q);
    end
    i1 = imread([dir,fnr,st,'.',fmt]);

i1(patch1(2):patch1(2)+patch1(4),patch1(1):patch1(1)+patch1(3),1:3)
= 0;

i1(patch2(2):patch2(2)+patch2(4),patch2(1):patch2(1)+patch2(3),1:3)
= 0;
    imshow(i1);
    %i12 = rgb2gray(i1);
    %i22 = rgb2gray(i2);
    i12 = i1(:,:,2); % green channel
    %i12 = medfilt2(i12,[10 10]);
    i12a = imadjust(i12);
    [CircCenter, CircRadii] = imfindcircles(i12a,[10
15],'ObjectPolarity','bright','sensitivity',sens);
    if exist("CircRadii")
        NumOfCells = length(CircRadii);
        for v = 1:NumOfCells
            for vt = 1:nov
```

```
                if sqrt((p(vt,1)-CircCenter(v,1))^2+(p(vt,2)-
CircCenter(v,2))^2) < thd
                    hold on
                    viscircles(CircCenter(v,:),
CircRadii(v,1),'EdgeColor','r','linewidth',0.5);
                    hold on

text(CircCenter(v,1),CircCenter(v,2)+2,num2str(vt),'fontsize',8,'hor
izontalalignment','center','verticalalignment','bottom','color','red
');
                    hold on
                    text(CircCenter(v,1),CircCenter(v,2)-
2,num2str(q),'fontsize',8,'horizontalalignment','center','verticalal
ignment','top','color','red');
                    r2 = CircRadii(v,1)^2;
                    inty = 0.0;
                    pix_count = 0;
                    for hc = CircCenter(v,1)-
CircRadii(v,1):CircCenter(v,1)+CircRadii(v,1)
                        for vc = CircCenter(v,2)-
CircRadii(v,1):CircCenter(v,2)+CircRadii(v,1)
                            if (((hc-CircCenter(v,1))^2 + (vc-
CircCenter(v,2))^2) < r2 && round(vc) < 700 && round(hc)<700&&
round(vc) > 0 && round(hc)>0)
                                %[round(vc) round(hc)]
                                inty = inty +
double(i12(round(vc),round(hc)));
                                pix_count = pix_count + 1;
                            end
                        end
                    end
                    intensity(q-fi+1,vt) = inty/pix_count;
                    p(vt,:) = CircCenter(v,:);

RealCircDiameter(vt)=2*CircRadii(v)/Pixel2MicroMeterRatio;
                end
            end
            drawnow
        end
        vesicles_tracked=[1:1:nov]';
        clear CircCenter CircRadii
    else
        disp("No cells found")
    end
end
d=diff(intensity);
[l v]=max(d);
ctime=v*30+60;
xlswrite([[dir1,fnr,'_t',st,'_ch_data2'],'_'],RealCircDiameter,'Real
CircDiameter');
xlswrite([[dir1,fnr,'_t',st,'_ch_data2'],'_'],intensity,'intensity';


close
```

### 7.4.2 Chemical Communication as a Function of Number of µ-reactors

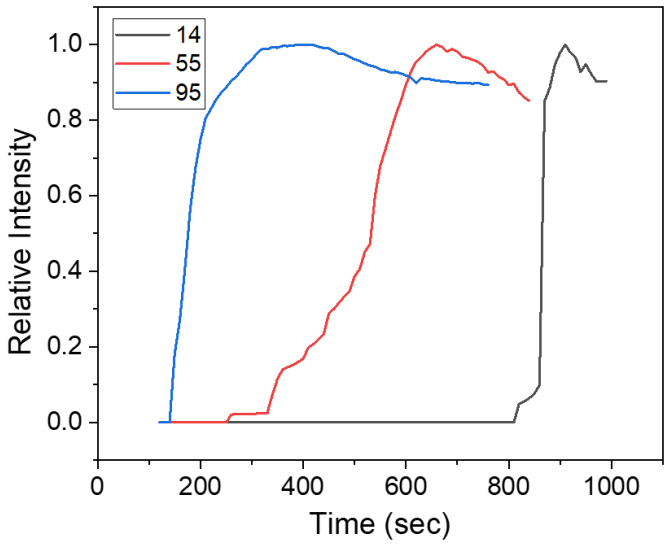


***Figure 7.15 Effect of the number of µ-reactors on the average intensity-time profile.*** *Time vs relative intensity profile for comparing the avg. induction time for three sets of different number of emulsions (14, 55, and 95). The reaction concentrations were: [urea] = 0.07 M, [pyranine] = 60 µM, [AA] = 1 mM, and [urease] = 50 Units/mL. Here, the size of the emulsion droplets are smaller (avg. s/c=0.08) compared to the one estimated in* ***Figure 4.6*** *B.*

## 7.5 **Appendix 5** – Chapter 5: Exploitation of the Urease Double Emulsion Platform in Applications

### 7.5.1 Urease Inhibition

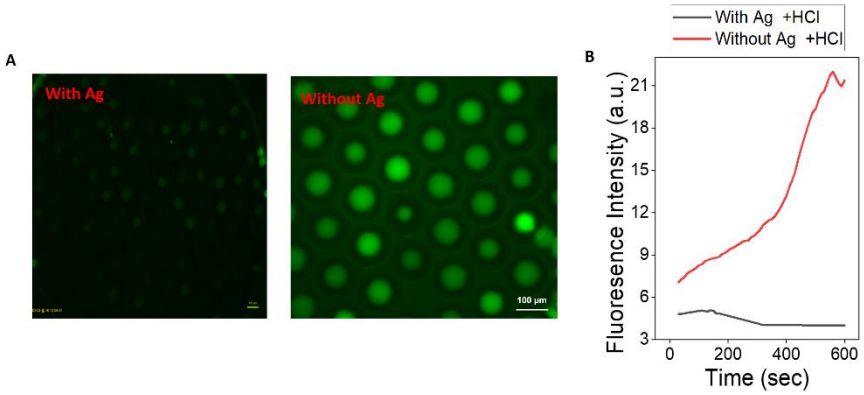


***Figure 7.16 Effect of the urease inhibitor on the activity of urease (UU)****. (B) Microscopic fluorescence images for reaction observation within the emulsion sample mixed with two different external solutions (ES) containing urea and HCl in the right image, and $AgNO_3$, urea, and HCl in the left image, the addition of $AgNO_3$ (enzyme inhibitor) stops the reaction, and no fluorescence was detected*

*(C) Fluorescence intensity of the emulsions over time when added to the ES with and without $AgNO_3$, when mixed with the ES without $AgNO_3$ the typical induction reaction was observed, however, with the addition of AgNO3 in ES an initial dimmed fluorescence was detected which eventually fades away. . The reaction concentrations were: [urea] = 0.07 M, [pyranine] = 50 µM, [HCl] = 0.01 mM, [urease] = 50 Units/mL, [$AgNO_3$]= 0.1 mM epifluorescent microscope (LS560 Microscope, green fluorescence, and brightfield, green filter: excitation 457-493 nm; emission 508-552 nm, etaluma), and scale bar = 100 µm.*

### 7.5.2 MATLAB Code for Size Distribution of Particles:

```
clear all
close all

dir = 'C:\Users\CBE-User\Documents\lab\Experiments\Double emulsion
reaction\Paper\applications_last chapter\Madeleine\';
filename = '2nd day aq.tif';
fullpath = fullfile(dir, filename);

sens=0.97;

i_final = imread(fullpath);

i_final_adj = imadjust(i_final(:,:,2));
[CircCenter0, CircRadii0] = imfindcircles(i_final_adj,[30
130],'ObjectPolarity','bright','sensitivity',sens);
nov = length(CircRadii0);
imshow(i_final_adj);
hold on
viscircles(CircCenter0, CircRadii0,'EdgeColor','r','linewidth',0.5);

RealCircDiameter = zeros(1,nov);
for v = 1:nov
    hold on
    viscircles(CircCenter0(v,:),
CircRadii0(v,1),'EdgeColor','r','linewidth',0.5);
    RealCircDiameter(v) = 2 * CircRadii0(v);
    hold on

text(CircCenter0(v,1),CircCenter0(v,2)+2,num2str(RealCircDiameter(v)
),'fontsize',8,'horizontalalignment','center','verticalalignment','b
ottom','color','red');
end
```

# List of Equations

# List of Tables

# List of Figures

## Chapter 1:

## Chapter 2:

## Chapter 3:

## Chapter 4:

## Chapter 5:

## Chapter 7:

# References


1 M. Chappell and S. Payne, in *Physiology for Engineers: Applying Engineering Methods to Physiological Systems*, Springer International Publishing, Cham, 2020, pp. 1–19.

2 W. D. STEIN, in *Transport and Diffusion Across Cell Membranes*, ed. W. D. STEIN, Academic Press, 1986, pp. 231–361.

3 W. Shinoda, *Biochim. Biophys. Acta - Biomembr.*, 2016, **1858**, 2254–2265.

4 B. Yetkin-Arik, I. M. C. Vogels, P. Nowak-Sliwinska, A. Weiss, R. H. Houtkooper, C. J. F. Van Noorden, I. Klaassen and R. O. Schlingemann, *Sci. Rep.*, 2019, **9**, 1–14.

5 Y. Zhai and G. Zhai, *J. Control. Release*, 2014, **193**, 90–99.

6 N. S. Chandel, *Cold Spring Harb. Perspect. Biol.*, 2021, **13**, 1–12.

7 G. M. Cooper, *The cell : a molecular approach / Geoffrey M. Cooper.*, ASM Press, Washington, D.C, Second edi., 2000.

8 V. L. Michaelis and M. L. Maud Menten, *J. Chem. Soc*, 1913, 333–369.

9 A. Cornish-Bowden, *Perspect. Sci.*, 2015, **4**, 3–9.

10 H. Li, Y. Yang, W. Hong, M. Huang, M. Wu and X. Zhao, *Signal Transduct. Target. Ther.*, 2020, 5.

11 J. C. Blain and J. W. Szostak, *Annu. Rev. Biochem.*, 2014, **83**, 615–640.

12 L. Schoonen and J. C. M. Van Hest, *Adv. Mater.*, 2016, **28**, 1109–1128.

13 A. Pohorille and D. Deamer, *Trends Biotechnol.*, 2002, **20**, 123–128.

14 B. De Kruijff, *Nature*, 1997, **386**, 129–130.

15 J. N. Israelachvili, *BBA - Biomembr.*, 1977, **469**, 221–225.

16 B. de Kruijff, *Curr. Opin. Chem. Biol.*, 1997, **1**, 564–569.

17 A. Cheng and M. Caffrey, *J. Phys. Chem.*, 1996, **100**, 5608–5610.

18 B. Martinac, P. R. Rohde, A. R. Battle, E. Petrov, P. Pal, A. F. Foo, V. Vásquez, T. Huynh and A. Kloda, *Studying mechanosensitive ion channels using liposomes.*, 2010, vol. 606.

19 Y. H. M. Chan and S. G. Boxer, *Curr. Opin. Chem. Biol.*, 2007, **11**, 581–587.

20 G. Tresset, *PMC Biophys.*, 2009, **2**, 1–25.

21 V. P. Torchilin, *Nat. Rev. Drug Discov.*, 2005, **4**, 145–160.

22 D. Stamou, C. Duschl, E. Delamarche and H. Vogel, *Angew. Chemie - Int. Ed.*, 2003, **42**, 5580–5583.

23 A. D. Bangham and R. W. Horne, *J. Mol. Biol.*, 1964, **8**, 660–668, IN2–IN10.

24 M. Antonietti and S. Förster, *Adv. Mater.*, 2003, **15**, 1323–1333.

25 A. Jesorka and O. Orwar, *Annu. Rev. Anal. Chem.*, 2008, **1**, 801–832.

26 D. L. Perrier, L. Rems, M. T. Kreutzer and P. E. Boukany, *Sci. Rep.*, 2018, **8**, 1–10.

27 Y. Lu, G. Allegri and J. Huskens, *Mater. horizons*, 2022, **9**, 892–907.

28 A. D. Bangham, M. M. Standish and J. C. Watkins, *J. Mol. Biol.*, 1965, **13**, 238–252.

29 H. Hauser, *Proc. Natl. Acad. Sci. U. S. A.*, 1989, **86**, 5351–5355.

30 D. Deamer and A. D. Bangham, *BBA - Biomembr.*, 1976, **443**, 629–634.

31 F. Szoka and D. Papahadjopoulos, *Proc. Natl. Acad. Sci. U. S. A.*, 1978, **75**, 4194–4198.

32 R. Cortesi, E. Esposito, S. Gambarin, P. Telloli, E. Menegatti and C. Nastruzzi, *J. Microencapsul.*, 1999, **16**, 251–256.

33 M. Ollivon, S. Lesieur, C. Grabielle-Madelmont and M. Paternostre, *Biochim. Biophys. Acta - Biomembr.*, 2000, **1508**, 34–50.

34 D. T. Murray, J. Griffin and T. A. Cross, *Biochemistry*, 2014, **53**, 2454–2463.

35 U. Kragh-Hansen, M. Le Maire and J. V. Møller, *Biophys. J.*, 1998, **75**, 2932–2946.

36 R. Peschka, T. Purmann and R. Schubert, *Int. J. Pharm.*, 1998, **162**, 177–183.

37 A. L. Bernard, M. A. Guedeau-Boudeville, V. Marchi-Artzner, T. Gulik-Krzywicki, J. M. Di Meglio and L. Jullien, *J. Colloid Interface Sci.*, 2005, **287**, 298–306.

38 S. L. Regen and Y. Nagawa, *J. Am. Chem. Soc.*, 1992, **114**, 1668–1672.

39 E. F. Marques, *Langmuir*, 2000, **16**, 4798–4807.

40 H. Hoffmann, C. Thunig, P. Schmiedel and U. Munkert, *Langmuir*, 1994, **10**, 3972–3981.

41 H. Poincare, *Langmuir*, 2000, 9099–9102.

42 M. J. Hope, M. B. Bally, G. Webb and P. R. Cullis, *BBA - Biomembr.*, 1985, **812**, 55–65.

43 S. Šegota and D. urd ica Težak, *Adv. Colloid Interface Sci.*, 2006, **121**, 51–75.

44 J. P. Reeves and R. M. Dowben, *J. Cell. Physiol.*, 1969, **73**, 49–60.

45 K. Tsumoto, H. Matsuo, M. Tomita and T. Yoshimura, *Colloids Surfaces B Biointerfaces*, 2009, **68**, 98–105.

46 D. S. Dimitrov, 1986, 303–311.

47 M. Angelova and D. S. Dimitrov, *Trends Colloid Interface Sci. II*, 2007, **67**, 59–67.

48 T. Shimanouchi, H. Umakoshi and R. Kuboi, *Langmuir*, 2009, **25**, 4835–4840.

49 S. Pautot, B. J. Frisken and D. A. Weitz, *Langmuir*, 2003, **19**, 2870–2879.

50 A. Yamada, T. Yamanaka, T. Hamada, M. Hase, K. Yoshikawa and D. Baigl, *Langmuir*, 2006, **22**, 9824–9828.

51 C. S. Ho, J. W. Kim and D. A. Weitz, *J. Am. Chem. Soc.*, 2008, **130**, 9543–9549.

52 H. C. Shum, D. Lee, I. Yoon, T. Kodger and D. A. Weitz, *Langmuir*, 2008, **24**, 7651–7653.

53 E. Lorenceau, A. S. Utada, D. R. Link, G. Cristobal, M. Joanicot and D. A. Weitz, *Langmuir*, 2005, **21**, 9183–9186.

54 A. L. Bailey and P. R. Cullis, *Biochemistry*, 1997, **36**, 1628–1634.

55 J. Wilschut, N. Düzgüneş, R. Fraley and D. Papahadjopoulos, *Biochemistry*, 1980, **19**, 6011–6021.

56 S. Kulin, R. Kishore, K. Helmerson and L. Locascio, *Langmuir*, 2003, **19**, 8206–8210.

57 A. Moscho, O. Orwar, D. T. Chiu, B. P. Modi and R. N. Zare, *Proc. Natl. Acad. Sci. U. S. A.*, 1996, **93**, 11443–11447.

58 N. Oku and R. C. Macdonald, *BBA - Biomembr.*, 1983, **734**, 54–61.

59 K. J. Gao, G. Li, X. Lu, Y. G. Wu, B. Q. Xu and J. H. Fuhrhop, *Chem. Commun.*, 2008, 1449–1451.

60 E. Touitou, N. Dayan, L. Bergelson, B. Godin and M. Eliaz, *J. Control. Release*, 2000, **65**, 403–418.

61 S. Ota, S. Yoshizawa and S. Takeuchi, *Angew. Chemie*, 2009, **121**, 6655–6659.

62 K. Funakoshi, H. Suzuki and S. Takeuchi, *J. Am. Chem. Soc.*, 2007, **129**, 12608–12609.

63 H. Suzuki, K. V. Tabata, H. Noji and S. Takeuchi, *Langmuir*, 2006, **22**, 1937–1942.

64 P. Walde, K. Cosentino, H. Engel and P. Stano, *ChemBioChem*, 2010, **11**,

848–865.

65 P. Carrara, P. Stano and P. L. Luisi, *ChemBioChem*, 2012, **13**, 1497–1502.

66 D. S. Dimitrov and M. I. Angelova, *Bioelectrochemistry Bioenerg.*, 1988, **19**, 323–336.

67 M. I. Angelova and D. S. Dimitrov, *Faraday Discuss. Chem. Soc.*, 1986, **81**, 303.

68 S. Pautot, B. J. Frisken and D. A. Weitz, , DOI:10.1073/pnas.1931005100.

69 A. Moga, N. Yandrapalli, R. Dimova and T. Robinson, *ChemBioChem*, 2019, **20**, 2674–2682.

70 N. Deng, M. Yelleswarapu and W. T. S. Huck, , DOI:10.1021/jacs.6b02107.

71 N. Deng, M. Yelleswarapu, L. Zheng and W. T. S. Huck, 2017, 587–590.

72 C. Martino and A. J. DeMello, *Interface Focus*, 2016, **6**, 20160011.

73 K. Kamiya, R. Kawano, T. Osaki, K. Akiyoshi and S. Takeuchi, *Nat. Chem.*, 2016, **8**, 881–889.

74 I. Clemente, K. Torbensen, E. Di Cola, F. Rossi, S. Ristori and A. Abou-Hassan, *RSC Adv.*, 2019, **9**, 33429–33435.

75 G. M. Whitesides, *Nature*, 2006, **442**, 368–373.

76 P. N. Nge, C. I. Rogers and A. T. Woolley, .

77 A. Manz, N. Graber and H. M. Widmer, *Sensors Actuators B Chem.*, 1990, **1**, 244–248.

78 D. Mark, S. Haeberle, G. Roth, F. Von Stetten and R. Zengerle, *Chem. Soc. Rev.*, 2010, **39**, 1153–1182.

79 E. K. Sackmann, A. L. Fulton and D. J. Beebe, *Nature*, 2014, **507**, 181–189.

80 D. R. Reyes, D. Iossifidis, P. Auroux and A. Manz, *Anal. Chem.*, 2002, **74**, 2623–2636.

81 D. Janasek, J. Franzke and A. Manz, *Nature*, 2006, **442**, 374–380.

82 A. J. DeMello, *Nature*, 2006, **442**, 394–402.

83 P. Yager, T. Edwards, E. Fu, K. Helton, K. Nelson, M. R. Tam and B. H. Weigl, *Nature*, 2006, **442**, 412–418.

84 J. El-Ali, P. K. Sorger and K. F. Jensen, *Nature*, 2006, **442**, 403–411.

85 H. Craighead, *Nature*, 2006, **442**, 387–393.

86 D. Psaltis, S. R. Quake and C. Yang, *Nature*, 2006, **442**, 381–386.

87 K. Ren, J. Zhou and H. Wu, .

88 Y. Xia and G. M. Whitesides, *Angew. Chemie Int. Ed.*, 1998, **37**, 550–575.

89 R. S. Lima, P. A. G. C. Leão, M. H. O. Piazzetta, A. M. Monteiro, L. Y. Shiroma, A. L. Gobbi and E. Carrilho, *Nat. Publ. Gr.*, 1–15.

90 S. A. Peyman, R. H. Abou-saleh, J. R. Mclaughlan, N. Ingram, B. R. G. Johnson, K. Critchley, S. Freear, J. A. Evans, A. F. Markham, P. Louise and S. D. Evans, 2012, 4544–4552.

91 P. Watts, C. Wiles and P. Watts, 2007, 727–732.

92 J. C. Mcdonald, D. C. Duffy, J. R. Anderson, D. T. Chiu and G. M. Whitesides, .

93 D. C. Duffy, J. C. McDonald, O. J. A. Schueller and G. M. Whitesides, *Anal. Chem.*, 1998, **70**, 4974–4984.

94 S. K. Sia and G. M. Whitesides, *Electrophoresis*, 2003, **24**, 3563–3576.

95 K. Ren, J. Zhou and H. Wu, *Acc. Chem. Res.*, 2013, **46**, 2396–2406.

96 S.-E. Ong, *Front. Biosci.*, 2008, **13**, 2757.

97 J. K. Nunes, S. S. H. Tsai, J. Wan and H. A. Stone, *J. Phys. D. Appl. Phys.*, , DOI:10.1088/0022-3727/46/11/114002.

98 Y. Wang and P. Dimitrakopoulos, *Theor. Comput. Fluid Dyn.*, 2012, **26**, 361–379.

99 T. M. Squires and S. R. Quake, *Rev. Mod. Phys.*, 2005, **77**, 977–1026.

100 J. Atencia and D. J. Beebe, *Nature*, 2005, **437**, 648–655.

101 S. Y. Teh, R. Lin, L. H. Hung and A. P. Lee, *Lab Chip*, 2008, **8**, 198–220.

102 J. U. Shim, R. T. Ranasinghe, C. A. Smith, S. M. Ibrahim, F. Hollfelder, W. T. S. Huck, D. Klenerman and C. Abell, *ACS Nano*, 2013, **7**, 5955–5964.

103 I. Kobayashi, S. Mukataka and M. Nakajima, *Ind. Eng. Chem. Res.*, 2005, **44**, 5852–5856.

104 M. Leman, F. Abouakil, A. D. Griffiths and P. Tabeling, *Lab Chip*, 2015, **15**, 753–765.

105 C. N. Baroud, F. Gallaire and R. Dangla, *Lab Chip*, 2010, **10**, 2032–2045.

106 S. K. Y. Tang and G. M. Whitesides, *Optofluidics Fundam. Devices, Appl.*, 2010, 7–32.

107 D. C. Duffy, J. C. McDonald, O. J. A. Schueller and G. M. Whitesides, *Anal. Chem.*, 1998, **70**, 4974–4984.

108 J. C. McDonald and G. M. Whitesides, *Acc. Chem. Res.*, 2002, **35**, 491–499.

109 A. S. Utada, A. Fernandez-Nieves, H. A. Stone and D. A. Weitz, *Phys. Rev. Lett.*, 2007, **99**, 1–4.

110 P. Guillot, A. Colin, A. S. Utada and A. Ajdari, *Phys. Rev. Lett.*, 2007, **99**, 1–4.

111 A. S. Utada, A. Fernandez-Nieves, J. M. Gordillo and D. A. Weitz, *Phys. Rev. Lett.*, 2008, **100**, 1–4.

112 E. Kang, S. J. Shin, K. H. Lee and S. H. Lee, *Lab Chip*, 2010, **10**, 1856–1861.

113 J. H. Xu, S. W. Li, J. Tan, Y. J. Wang and G. S. Luo, *AIChE J.*, 2006, **52**, 3005–3010.

114 T. Thorsen, R. W. Roberts, F. H. Arnold and S. R. Quake, *Phys. Rev. Lett.*, 2001, **86**, 4163–4166.

115 T. Nisisako, T. Torii and T. Higuchi, *Lab Chip*, 2002, **2**, 24–26.

116 C. Priest, S. Herminghaus and R. Seemann, *Appl. Phys. Lett.*, 2006, **88**, 1–3.

117 S. L. Anna, N. Bontoux and H. A. Stone, *Appl. Phys. Lett.*, 2003, **82**, 364–366.

118 G. F. Christopher and S. L. Anna, *J. Phys. D. Appl. Phys.*, , DOI:10.1088/0022-3727/40/19/R01.

119 Y. C. Tan, V. Cristini and A. P. Lee, *Sensors Actuators, B Chem.*, 2006, **114**, 350–356.

120 A. Woodward, T. Cosgrove, J. Espidel, P. Jenkins and N. Shaw, *Soft Matter*, 2007, **3**, 627–633.

121 L. Yobas, S. Martens, W. L. Ong and N. Ranganathan, *Lab Chip*, 2006, **6**, 1073–1079.

122 H. Gu, M. H. G. Duits and F. Mugele, *Int. J. Mol. Sci.*, 2011, **12**, 2572–2597.

123 T. Nisisako, T. Torii and T. Higuchi, 2004, **101**, 23–29.

124 Z. Nie, S. Xu, M. Seo, P. C. Lewis and E. Kumacheva, 2005, 8058–8063.

125 S. Takeuchi, P. Garstecki, D. B. Weibel and G. M. Whitesides, *Adv. Mater.*, 2005, **17**, 1067–1072.

126 L. Shang, Y. Cheng and Y. Zhao, *Chem. Rev.*, 2017, **117**, 7964–8040.

127 S. Okushima, T. Nisisako, T. Torii and T. Higuchi, *Langmuir*, 2004, **20**, 9905–9908.

128 A. S. Utada, E. Lorenceau, D. R. Link, P. D. Kaplan, H. A. Stone and D. A. Weitz, *Science (80-. ).*, 2005, **308**, 537–541.

129 N. N. Deng, M. Yelleswarapu, L. Zheng and W. T. S. Huck, *J. Am. Chem. Soc.*, 2017, **139**, 587–590.

130 Y. Ai, R. Xie, J. Xiong and Q. Liang, *Small*, 2020, **16**, 1–24.

131 C. Martino and A. J. deMello, *Interface Focus*, , DOI:10.1098/rsfs.2016.0011.

132 N. N. Deng, M. Yelleswarapu and W. T. S. Huck, *J. Am. Chem. Soc.*, 2016,

**138**, 7584–7591.

133 B. Yu, R. J. Lee and L. J. Lee, *Methods Enzymol.*, 2009, **465**, 129–141.

134 D. Van Swaay and A. Demello, *Lab Chip*, 2013, **13**, 752–767.

135 A. Huebner, S. Sharma, M. Srisa-Art, F. Hollfelder, J. B. Edel and A. J. DeMello, *Lab Chip*, 2008, **8**, 1244–1254.

136 S. Gulati, V. Rouilly, X. Niu, J. Chappell, R. I. Kitney, J. B. Edel, P. S. Freemont and A. J. DeMello, *J. R. Soc. Interface*, , DOI:10.1098/rsif.2009.0083.focus.

137 B. Zheng, C. J. Gerdts and R. F. Ismagilov, *Curr. Opin. Struct. Biol.*, 2005, **15**, 548–555.

138 Y. Schaerli, R. C. Wootton, T. Robinson, V. Stein, C. Dunsby, M. A. A. Neil, P. M. W. French, A. J. DeMello, C. Abell and F. Hollfelder, *Anal. Chem.*, 2009, **81**, 302–306.

139 A. B. Theberge, F. Courtois, Y. Schaerli, M. Fischlechner, C. Abell, F. Hollfelder and W. T. S. Huck, *Angew. Chemie - Int. Ed.*, 2010, **49**, 5846–5868.

140 C. Martino, M. Zagnoni, M. E. Sandison, M. Chanasakulniyom, A. R. Pitt and J. M. Cooper, *Anal. Chem.*, 2011, **83**, 5361–5368.

141 S. Xu, Z. Nie, M. Seo, P. Lewis, E. Kumacheva, H. A. Stone, P. Garstecki, D. B. Weibel, I. Gitlin and G. M. Whitesides, *Angew. Chemie - Int. Ed.*, 2005, **44**, 724–728.

142 F. C. Chang and Y. C. Su, *J. Micromechanics Microengineering*, , DOI:10.1088/0960-1317/18/6/065018.

143 W. A. C. Bauer, M. Fischlechner, C. Abell and W. T. S. Huck, *Lab Chip*, 2010, **10**, 1814–1819.

144 L. Y. Chu, A. S. Utada, R. K. Shah, J. W. Kim and D. A. Weitz, *Angew. Chemie - Int. Ed.*, 2007, **46**, 8970–8974.

145 C. Martino, L. Horsfall, Y. Chen, M. Chanasakulniyom, D. Paterson, A. Brunet, S. Rosser, Y. J. Yuan and J. M. Cooper, *ChemBioChem*, 2012, **13**, 792–795.

146 M. He, J. S. Edgar, G. D. M. Jeffries, R. M. Lorenz, J. P. Shelby and D. T. Chiu, *Anal. Chem.*, 2005, **77**, 1539–1544.

147 H. N. Joensson, M. L. Samuels, E. R. Brouzes, M. Medkova, M. Uhlén, D. R. Link and H. Andersson-Svahn, *Angew. Chemie Int. Ed.*, 2009, **48**, 2518–2521.

148 G. Ashkenasy, T. M. Hermans, S. Otto and A. F. Taylor, *Chem. Soc. Rev.*, 2017, **46**, 2543–2554.

149 J. W. Szostak, D. P. Bartel and P. L. Luisi, 387–390.

150 A. Küchler, M. Yoshimoto, S. Luginbühl, F. Mavelli and P. Walde, *Nat. Nanotechnol.*, 2016, **11**, 409–420.

151 I. Petrikovics, K. Hong, G. Omburo, Q. Z. Hu, L. Pei, W. D. McGuinn, D. Sylvester, C. Tamulinas, D. Papahadjopoulos, J. C. Jaszberenyi and J. L. Way, *Toxicol. Appl. Pharmacol.*, 1999, **156**, 56–63.

152 M. Yoshimoto, S. Wang, K. Fukunaga, D. Fournier, P. Walde, R. Kuboi and K. Nakao, *Biotechnol. Bioeng.*, 2005, **90**, 231–238.

153 R. P. Washington, W. W. West, G. P. Misra and J. A. Pojman, *J. Am. Chem. Soc.*, 1999, **121**, 7373–7380.

154 S. Aubert, M. Bezagu, A. C. Spivey and S. Arseniyadis, *Nat. Rev. Chem.*, , DOI:10.1038/s41570-019-0139-6.

155 A. K. Horváth and I. Nagypál, *ChemPhysChem*, 2015, **16**, 588–594.

156 G. Csekö, Q. Gao, A. Takács and A. K. Horváth, *J. Phys. Chem. A*, 2019, **123**, 3959–3968.

157 H. Landolt, *Ber. Dtsch. Chem. Ges.*, 1886, **19**, 1317–1365.

158 K. Kovacs, R. E. McIlwaine, S. K. Scott and A. F. Taylor, *Phys. Chem. Chem. Phys.*, 2007, **9**, 3711–3716.

159 G. Hu, C. Bounds, J. A. Pojman and A. F. Taylor, *J. Polym. Sci. Part A Polym. Chem.*, 2010, 48, 2955–2959.

160 V. Voorsluijs, I. G. Kevrekidis and Y. De Decker, *Phys. Chem. Chem. Phys.*, 2017, **19**, 22528–22537.

161 I. Lagzi, B. Kowalczyk, D. Wang and B. A. Grzybowski, *Angew. Chemie - Int. Ed.*, 2010, **49**, 8616–8619.

162 A. M. Turing, *Bull. Math. Biol.*, 1990, **52**, 153–197.

163 Z. Tan, S. Chen, X. Peng, L. Zhang and C. Gao, *Science (80-. ).*, 2018, **360**, 518–521.

164 E. L. Wittbecker and P. W. Morgan, *J. Polym. Sci. Part A Polym. Chem.*, 1996, **34**, 521–529.

165 P. W. Morgan and S. L. Kwolek, *J. Polym. Sci.*, 1959, **40**, 299–327.

166 P. Goodyer and L. Goodyer, *Exped. Med. Revis. Ed.*, 2014, **521**, 105–110.

167 V. K. Vanag, D. G. Míguez and I. R. Epstein, *J. Chem. Phys.*, , DOI:10.1063/1.2378833.

168 M. J. B. Hauser and L. F. Olsen, *J. Chem. Soc. - Faraday Trans.*, 1996, **92**,

2857–2863.

169 S. Bagyan, T. Mair, E. Dulos, J. Boissonade, P. De Kepper and S. C. Müller, *Biophys. Chem.*, 2005, **116**, 67–76.

170 B. Krajewska, *J. Mol. Catal. B Enzym.*, 2009, **59**, 9–21.

171 M. J. Maroney and S. Ciurli, *Chem. Rev.*, 2014, **114**, 4206–4228.

172 P. A. Karplus, M. A. Pearson and R. P. Hausinger, *Acc. Chem. Res.*, 1997, **30**, 330–337.

173 S. Benini, W. R. Rypniewski, K. S. Wilson, S. Miletti, S. Ciurli and S. Mangani, *Structure*, 1999, **7**, 205–216.

174 L. Mazzei, F. Musiani and S. Ciurli, *J. Biol. Inorg. Chem.*, 2020, **25**, 829–845.

175 S. Benini, P. Kosikowska, M. Cianci, L. Mazzei, A. G. Vara, Ł. Berlicki and S. Ciurli, *J. Biol. Inorg. Chem.*, 2013, **18**, 391–399.

176 B. Krajewska, R. Van Eldik and M. Brindell, *J. Biol. Inorg. Chem.*, 2012, **17**, 1123–1134.

177 B. Krajewska, *J. Mol. Catal. B Enzym.*, 2016, **124**, 70–76.

178 K. Kappaun, A. R. Piovesan, C. R. Carlini and R. Ligabue-Braun, *J. Adv. Res.*, 2018, **13**, 3–17.

179 B. Krajewska and S. Ciurli, *Plant Physiol. Biochem.*, 2005, **43**, 651–658.

180 S. J. Jones, A. F. Taylor and P. A. Beales, *Exp. Biol. Med.*, 2019, **244**, 283–293.

181 B. P. Callahan, Y. Yuan and R. Wolfenden, *J. Am. Chem. Soc.*, 2005, **127**, 10828–10829.

182 B. Krajewska and W. Zaborska, *J. Mol. Catal. - B Enzym.*, 1999, **6**, 75–81.

183 M. M. Wrobel, T. Bánsági, S. K. Scott, A. F. Taylor, C. O. Bounds, A. Carranzo and J. A. Pojman, *Biophys. J.*, 2012, **103**, 610–615.

184 A. V. Straube, S. Winkelmann, C. Schütte and F. Höfling, *J. Phys. Chem. Lett.*, 2021, 12, 9888–9893.

185 F. Rossi, F. Mavelli, P. Stano and D. Caivano, *Commun. Comput. Inf. Sci.*, , DOI:10.1007/978-3-319-32695-5.

186 T. Bánsági and A. F. Taylor, *J. Phys. Chem. B*, 2014, **118**, 6092–6097.

187 G. Hu, J. A. Pojman, S. K. Scott, M. M. Wrobel and A. F. Taylor, *J. Phys. Chem. B*, 2010, **114**, 14059–14063.

188 F. Muzika, T. Bánsági, I. Schreiber, L. Schreiberová and A. F. Taylor, *Chem. Commun.*, 2014, **50**, 11107–11109.

189 I. N. Bubanja, T. Bánsági and A. F. Taylor, *React. Kinet. Mech. Catal.*, 2018, **123**, 177–185.

190 T. Bánsági and A. F. Taylor, *Isr. J. Chem.*, 2018, **58**, 706–713.

191 M. M. Wrobel, *Sch. Chem. 2012, Univ. Leeds.*

192 C. M. Chang, G. R. D. Prabhu, C. M. Tseng and P. L. Urban, *Anal. Chem.*, 2019, **91**, 8814–8819.

193 Y. Qin and J. M. S. Cabral, *Biocatal. Biotransformation*, 2002, **20**, 1–14.

194 D. M. Escala, A. P. Muñuzuri, A. De Wit and J. Carballido-Landeira, *Phys. Chem. Chem. Phys.*, 2017, **19**, 11914–11919.

195 E. Tóth-Szeles, J. Horváth, G. Holló, R. Szcs, H. Nakanishi and I. Lagzi, *Mol. Syst. Des. Eng.*, 2017, **2**, 274–282.

196 R. W. Jaggers and S. A. F. Bon, *Mater. Horizons*, 2017, **4**, 402–407.

197 R. W. Jaggers and S. A. F. Bon, *J. Mater. Chem. B*, 2017, **5**, 7491–7495.

198 E. Jee, T. Bánsági, A. F. Taylor and J. A. Pojman, *Angew. Chemie - Int. Ed.*, 2016, **55**, 2127–2131.

199 Y. Miele, S. J. Jones, F. Rossi, P. A. Beales and A. F. Taylor, *J. Phys. Chem. Lett.*, 2022, 13, 1979–1984.

200 H. Che, S. Cao and J. C. M. Van Hest, *J. Am. Chem. Soc.*, 2018, **140**, 5356–5359.

201 R. Tomasi, J.-M. Noël, A. Zenati, S. Ristori, F. Rossi, V. Cabuil, F. Kanoufi and A. Abou-Hassan, *Chem. Sci.*, 2014, **5**, 1854–1859.

202 L. Li and R. F. Ismagilov, *Annu. Rev. Biophys.*, 2010, **39**, 139–158.

203 S. Marre and K. F. Jensen, *Chem. Soc. Rev.*, 2010, **39**, 1183–1202.

204 F. M. Galogahi, Y. Zhu, H. An and N. T. Nguyen, *J. Sci. Adv. Mater. Devices*, 2020, **5**, 417–435.

205 O. J. Dressler, X. Casadevall i Solvas and A. J. deMello, *Annu. Rev. Anal. Chem.*, 2017, **10**, 1–24.

206 J. Wang, S. Hahn, E. Amstad and N. Vogel, *Adv. Mater.*, 2022, **34**, 2107338.

207 K. Torbensen, F. Rossi, S. Ristori and A. Abou-Hassan, *Lab Chip*, 2017, **17**, 1179–1189.

208 B. C. Buddingh' and J. C. M. Van Hest, *Acc. Chem. Res.*, 2017, **50**, 769–777.

209 K. K. Dey, X. Zhao, B. M. Tansi, W. J. Méndez-Ortiz, U. M. Córdova-Figueroa, R. Golestanian and A. Sen, *Nano Lett.*, 2015, **15**, 8311–8315.

210 O. Rifaie-Graham, J. Yeow, A. Najer, R. Wang, R. Sun, K. Zhou, T. N. Dell, C.

Adrianus, C. Thanapongpibul, M. Chami, S. Mann, J. R. de Alaniz and M. M. Stevens, *Nat. Chem.*, 2023, **15**, 110–118.

211 J. Guzowski, K. Gizynski, J. Gorecki and P. Garstecki, *Lab Chip*, 2016, **16**, 764–772.

212 S. Maiti, I. Fortunati, C. Ferrante, P. Scrimin and L. J. Prins, *Nat. Chem.*, 2016, **8**, 725–731.

213 Y. Miele, Z. Medveczky, abor Holí, B. Tegze, I. DerényiDer, ef ZoltánZolt, E. Altamura, I. Lagzi and F. Rossi, , DOI:10.1039/c9sc05195c.

214 T. Litschel, B. Ramm, R. Maas, M. Heymann and P. Schwille, *Angew. Chemie - Int. Ed.*, 2018, **57**, 16286–16290.

215 J. R. Casey, S. Grinstein and J. Orlowski, *Nat. Rev. Mol. Cell Biol.*, 2010, **11**, 50–61.

216 D. Del Giudice, F. Frateloreto, C. Sappino and S. Di Stefano, *European J. Org. Chem.*, 2022, **2022**, e202200407.

217 H. C. Shum, A. Bandyopadhyay, S. Bose and D. A. Weitz, *Chem. Mater.*, 2009, **21**, 5548–5555.

218 S. Liang, J. Li, X. Li, J. Man, J. K. Nunes and H. Chen, *J. Am. Ceram. Soc.*, 2018, **101**, 3787–3796.

219 H. Che, S. Cao and J. C. M. Van Hest, *J. Am. Chem. Soc.*, 2018, **140**, 5356–5359.

220 Y. Miele, T. Bánsági Jr., A. F. Taylor, P. Stano and F. Rossi, *Commun. Comput. Inf. Sci.*, 2016, **587**, 197–208.

221 D. Welch and J. B. Christen, *Lab Chip*, 2014, **14**, 1191–1197.

222 N. Fomina, C. A. Johnson, A. Maruniak, S. Bahrampour, C. Lang, R. W. Davis, S. Kavusi and H. Ahmad, *Lab Chip*, 2016, **16**, 2236–2244.

223 B. Krajewska, *J. Mol. Catal. B Enzym.*, 2009, **59**, 9–21.

224 R. W. Jaggers and S. A. F. Bon, *Mater. Horizons*, 2017, **4**, 402–407.

225 S. Panja and D. J. Adams, *Chem. – A Eur. J.*, 2021, **27**, 8928–8939.

226 I. Maity, C. Sharma, F. Lossada and A. Walther, *Angew Chem Int Ed Engl*, 2021, **60**, 22537–22546.

227 W. P. van den Akker, H. Wu, P. L. W. Welzen, H. Friedrich, L. K. E. A. Abdelmohsen, R. A. T. M. van Benthem, I. K. Voets and J. C. M. van Hest, *J. Am. Chem. Soc.*, 2023, **145**, 8600–8608.

228 X. Wang, S. Moreno, S. Boye, P. Wen, K. Zhang, P. Formanek, A. Lederer, B.

Voit and D. Appelhans, *Chem. Mater.*, 2021, **33**, 6692–6700.

229 R. R. Mahato, Priyanka, E. Shandilya and S. Maiti, *Chem. Sci.*, 2022, **13**, 8557–8566.

230 T. Zhao, Y. E, J. Cui, J. Hao and X. Wang, *J. Colloid Interface Sci.*, 2022, **623**, 674–684.

231 S. Panja, A. M. Fuentes-Caparrós, E. R. Cross, L. Cavalcanti and D. J. Adams, *Chem. Mater.*, 2020, **32**, 5264–5271.

232 L. R. Arriaga, S. S. Datta, S. H. Kim, E. Amstad, T. E. Kodger, F. Monroy and D. A. Weitz, *Small*, 2014, 10, 950–956.

233 S. Teh, R. Khnouf, H. Fan and A. P. Lee, *Biomicrofluidics*, 2011, **044113**, 1–12.

234 K. Torbensen and A. Abou-Hassan, *J. Flow Chem.*, 2015, **5**, 234–240.

235 S. Okushima, T. Nisisako, T. Torii and T. Higuchi, *Langmuir*, 2004, **20**, 9905–9908.

236 S. Ding, C. A. Serra, T. F. Vandamme, W. Yu and N. Anton, *J. Control. Release*, 2019, **295**, 31–49.

237 W. Li, L. Zhang, X. Ge, B. Xu, W. Zhang, L. Qu, C.-H. Choi, J. Xu, A. Zhang, H. Lee and D. A. Weitz, *Chem. Soc. Rev.*, 2018, **47**, 5646–5683.

238 A. Yashina, F. Meldrum and A. deMello, *Biomicrofluidics*, 2012, **6**, 22001.

239 M. Michel, M. Winterhalter, L. Darbois, J. Hemmerle, J. C. Voegel, P. Schaaf and V. Ball, *Langmuir*, 2004, **20**, 6127–6133.

240 B. Krajewska, *J. Adv. Res.*, 2018, **13**, 59–67.

241 D. N. Cacace, A. T. Rowland, J. J. Stapleton, D. C. Dewey and C. D. Keating, *Langmuir*, 2015, **31**, 11329–11338.

242 A. T. Rowland, D. N. Cacace, N. Pulati, M. L. Gulley and C. D. Keating, *Chem. Mater.*, 2019, **31**, 10243–10255.

243 A. Clarà Saracho, L. Lucherini, M. Hirsch, H. M. Peter, D. Terzis, E. Amstad and L. Laloui, *J. Mater. Chem. A*, 2021, **9**, 24438–24451.

244 V. P. Galván-Chacón, L. Costa, D. Barata and P. Habibovic, *Acta Biomater.*, 2021, **128**, 486–501.

245 J. Enax, F. Meyer, E. Schulze Zur Wiesche and M. Epple, *Nanomater.*, , DOI:10.3390/nano12224075.

246 B. Bohner, T. Bánsági Jr, Á. Tóth, D. Horváth and A. F. Taylor, *Angew. Chemie Int. Ed.*, 2020, **59**, 2823–2828.

247 I. Clemente, K. Torbensen, E. Di Cola, F. Rossi, S. Ristori and A. Abou-Hassan, *RSC Adv.*, 2019, **9**, 33429–33435.

248 H. Kim, S. M. Jo, F. Meng, Y. Guo, H. Thérien-Aubin, R. Golestanian, K. Landfester and E. Bodenschatz, *Adv. Funct. Mater.*, , DOI:10.1002/adfm.202006019.

249 J. C. Mcdonald, D. C. Duffy, J. R. Anderson and D. T. Chiu, *Electrophoresis*, 2000, **21**, 27–40.

250 Y. Xia and G. M. Whitesides, *Angew. Chemie - Int. Ed.*, 1998, **37**, 550–575.

251 T. Trantidou, Y. Elani, E. Parsons and O. Ces, *Microsystems Nanoeng.*, , DOI:10.1038/micronano.2016.91.

252 D. Wu, Y. Luo, X. Zhou, Z. Dai and B. Lin, *Electrophoresis*, 2005, **26**, 211–218.

253 I. V Kopanichuk, E. A. Vedenchuk, A. S. Koneva and A. A. Vanin, *J. Phys. Chem. B*, 2018, **122**, 8047–8055.

254 E. Altamura, F. Milano, R. R. Tangorra, M. Trotta, O. H. Omar, P. Stano and F. Mavelli, *Proc Natl Acad Sci U S A*, 2017, **114**, 3837–3842.

255 S. Stocks-Fischer, J. K. Galinat and S. S. Bang, *Soil Biol. Biochem.*, 1999, **31**, 1563–1571.

256 T. Barkay and J. Schaefer, *Curr. Opin. Microbiol.*, 2001, **4**, 318–323.

257 N. K. Dhami, M. S. Reddy and M. S. Mukherjee, *Front. Microbiol.*, 2013, 4, 314.

258 W. Habraken, P. Habibovic, M. Epple and M. Bohner, *Mater. Today*, 2016, **19**, 69–87.

259 V. Sokolova and M. Epple, *Chem. – A Eur. J.*, 2021, **27**, 7471–7488.

260 B. Han and M. Louhi-Kultanen, *Cryst. Growth Des.*, 2018, **18**, 1622–1628.

261 J. A. Stammeier, B. Purgstaller, D. Hippler, V. Mavromatis and M. Dietzel, *MethodsX*, 2018, **5**, 1241–1250.

262 G. Montes-Hernandez and F. Renard, *J. Phys. Chem. C*, 2020, **124**, 15302–15311.

263 K. Ishikawa, E. Garskaite and A. Kareiva, *J. Sol-Gel Sci. Technol.*, 2020, **94**, 551–572.

264 G. B. Ramírez-Rodríguez, J. M. Delgado-López and J. Gómez-Morales, *CrystEngComm*, 2013, **15**, 2206–2212.

265 Y. S. Cho, M. Moon, G. Holló, I. Lagzi and S. H. Yang, *Langmuir*, 2022, **38**, 2515–2524.

266 A. Larrañaga, M. Lomora, J. R. Sarasua, C. G. Palivan and A. Pandit, *Prog. Mater. Sci.*, 2017, **90**, 325–357.

267 M. J. Booth, V. Restrepo Schild, F. G. Downs and H. Bayley, *Mol. Biosyst.*, 2017, **13**, 1658–1691.

268 S. Maiti, I. Fortunati, C. Ferrante, P. Scrimin and L. J. Prins, *Nat. Chem.*, 2016, 8, 725–731.

269 U. Bulbake, S. Doppalapudi, N. Kommineni and W. Khan, *Pharmaceutics*, 2017, **9**, 1–33.

270 J. M. Smith, R. Chowdhry and M. J. Booth, *Front. Mol. Biosci.*, 2022, **8**, 1–9.

271 Y. Miele, T. Bánsági, A. F. Taylor and F. Rossi, *Lect. Notes Bioeng.*, 2018, 63–74.

272 V. Noireaux and A. Libchaber, *Proc. Natl. Acad. Sci.*, 2004, **101**, 17669–17674.

273 M. Michel, M. Winterhalter, L. Darbois, J. Hemmerle, J. C. Voegel, P. Schaaf and V. Ball, *Langmuir*, 2004, **20**, 6127–6133.

274 M. A. Budroni, K. Torbensen, O. L. Pantani, S. Ristori, F. Rossi and A. Abou-Hassan, *Chem. Commun.*, 2020, **56**, 11771–11774.

275 Y. Elani, *Biochem. Soc. Trans.*, 2016, **44**, 723–730.

276 H. N. Joensson and H. Andersson Svahn, *Angew. Chemie - Int. Ed.*, 2012, **51**, 12176–12192.

277 R. Lentini, N. Y. Martín, M. Forlin, L. Belmonte, J. Fontana, M. Cornella, L. Martini, S. Tamburini, W. E. Bentley, O. Jousson and S. S. Mansy, *ACS Cent. Sci.*, 2017, **3**, 117–123.

278 E. A. Wolfe and T. M. Chang, *Int. J. Artif. Organs*, 1987, **10**, 269–274.

279 S. A. Giannos, S. M. Dinh and B. Berner, *J. Pharm. Sci.*, 1995, **84**, 539–543.

280 G. Sachs, D. Scott, D. Weeks, K. Melchers, K. Stingl, K. Altendorf and E. P. Bakker, *Trends Microbiol.*, 2002, **10**, 217–218.

281 W. W. Chen, M. Niepel and P. K. Sorger, *Genes Dev.*, 2010, **24**, 1861–1875.

282 T. Bánsági and A. F. Taylor, *Life*, 2019, **9**, 1–11.

283 T. Bánsági and A. F. Taylor, *J. R. Soc. Interface*, , DOI:10.1098/rsif.2017.0945.

284 F. Rossi, F. Mavelli, P. Stano and D. Caivano, *Commun. Comput. Inf. Sci.*, , DOI:10.1007/978-3-319-32695-5.

285 N. R. Clement and J. M. Gould, *pyrenetrisulfonate) as a Probe of Internal Aqueous Hydrogen Ion Concentration in Phospholipid Vesicles1"*, .

286 E. J. Carr and G. Pontrelli, *Math. Biosci.*, 2018, **303**, 1–9.

287 Y. Xia and G. M. Whitesides, *Angew. Chemie - Int. Ed.*, 1998, **37**, 550–575.

288 F. Sa, *Eng. Geol.*, 2016, 2019–2020.

289 B. Krajewska and S. Ciurli, *Plant Physiol. Biochem.*, 2005, **43**, 651–658.

290 V. Russo, T. Salmi, F. Mammitzsch, O. Jogunola, R. Lange, J. Wärnå and J. P. Mikkola, *Chem. Eng. Sci.*, 2017, **172**, 453–462.

291 E. J. Carr and I. W. Turner, *Appl. Math. Model.*, 2016, **40**, 7034–7050.

292 E. J. Carr and N. G. March, *Appl. Math. Comput.*, 2018, **333**, 286–303.

293 A. N. Ford Versypt and R. D. Braatz, *Comput. Chem. Eng.*, 2014, **71**, 241–252.

294 E. A. Celaya, J. J. A. Aguirrezabala and P. Chatzipantelidis, *Procedia Comput. Sci.*, 2014, **29**, 1014–1026.

295 S. A. M. Yatim, Z. B. Ibrahim, K. I. Othman and M. B. Suleiman, *Math. Probl. Eng.*, , DOI:10.1155/2013/989381.

296 D. Van Der Spoel, S. Manzetti, H. Zhang and A. Klamt, *ACS Omega*, 2019, **4**, 13772–13781.

297 C. M. Waters and B. L. Bassler, *Annu. Rev. Cell Dev. Biol.*, 2005, **21**, 319–346.

298 S. De Monte, F. D'Ovidio, S. Danø and P. G. Sørensen, *Proc. Natl. Acad. Sci. U. S. A.*, 2007, **104**, 18377–18381.

299 S. Bianco, S. Panja and D. J. Adams, *Gels*, , DOI:10.3390/gels8020132.

300 E. Jee, T. Bánsági, A. F. Taylor and J. A. Pojman, *Angew. Chemie - Int. Ed.*, 2016, **55**, 2127–2131.

301 X. Fan and A. Walther, *Angew. Chemie - Int. Ed.*, 2021, **60**, 3619–3624.

302 T. Danino, O. Mondragón-Palomino, L. Tsimring and J. Hasty, *Nature*, 2010, **463**, 326–330.

303 A. W. F. Edwards, *Math. Intell.*, 2005, 27, 89.

304 M. Weitz, A. Mückl, K. Kapsner, R. Berg, A. Meyer and F. C. Simmel, *J. Am. Chem. Soc.*, 2014, **136**, 72–75.

305 F. Szoka and D. Papahadjopoulos, *Annu. Rev. Biophys. Bioeng.*, 1980, 9, 467–508.

306 T. Chakraborty, S. M. Bartelt, J. Steinkühler, R. Dimova and S. V. Wegner, *Chem. Commun.*, 2019, 55, 9448–9451.

307 S. M. Bartelt, J. Steinkühler, R. Dimova and S. V. Wegner, *Nano Lett.*, 2018,

18, 7268–7274.

308 M. J. Hope, M. B. Bally, G. Webb and P. R. Cullis, *Biochim. Biophys. Acta - Biomembr.*, 1985, **812**, 55–65.

309 S. Matosevic, *BioEssays*, 2012, 34, 992–1001.

310 R. Tivony, M. Fletcher, K. Al Nahas and U. F. Keyser, *ACS Synth. Biol.*, 2021, 10, 3105–3116.

311 M. J. Hope, M. B. Bally, G. Webb and P. R. Cullis, *Biochim. Biophys. Acta - Biomembr.*, 1985, **812**, 55–65.

312 A. Darszon, C. A. Vandenberg, M. Schönfeld, M. H. Ellisman, N. C. Spitzer and M. Montal, *Proc. Natl. Acad. Sci. U. S. A.*, 1980, **77**, 239–243.

313 K. Torbensen and A. Abou-Hassan, *J. Flow Chem.*, 2015, **5**, 234–240.

314 S. Teh, R. Khnouf, H. Fan and A. P. Lee, 2011, **044113**, 1–12.

315 D. G. Davies, M. R. Parsek, J. P. Pearson, B. H. Iglewski, J. W. Costerton and E. P. Greenberg, *Science (80-. ).*, 1998, **280**, 295–298.

316 W. K. Surewicz, *Chem. Phys. Lipids*, 1984, **34**, 363–372.

317 H. Kim, S. M. Jo, F. Meng, Y. Guo, H. Thérien-Aubin, R. Golestanian, K. Landfester and E. Bodenschatz, *Adv. Funct. Mater.*, 2020, 30.

318 J. F. Totz, J. Rode, M. R. Tinsley, K. Showalter and H. Engel, *Nat. Phys.*, 2018, **14**, 282–285.

319 M. A. Budroni, K. Torbensen, S. Ristori, A. Abou-Hassan and F. Rossi, *J. Phys. Chem. Lett.*, 2020, **11**, 2014–2020.

320 K. Yoshikawa, R. Aihara and K. Agladze, *J. Phys. Chem. A*, 1998, **102**, 7649–7652.

321 H. S. Lawson, G. Holló, R. Horvath, H. Kitahata and I. Lagzi, *J. Phys. Chem. Lett.*, 2020, **11**, 3014–3019.

322 R. Toth, A. F. Taylor and M. R. Tinsley, *J. Phys. Chem. B*, 2006, **110**, 10170–10176.

323 A. T. Winfree, 2002, **298**, 2336–2337.

324 J. Garcia-Ojalvo, M. B. Elowitz and S. H. Strogatz, *Proc. Natl. Acad. Sci. U. S. A.*, 2004, **101**, 10955–10960.

325 G. Gerisch and B. Hess, *Proc. Natl. Acad. Sci. U. S. A.*, 1974, **71**, 2118–2122.

326 S. De Monte, F. D'Ovidio, S. Danø and P. G. Sørensen, *Proc. Natl. Acad. Sci. U. S. A.*, 2007, **104**, 18377–18381.

327 M. Weitz, J. Kim, K. Kapsner, E. Winfree, E. Franco and F. C. Simmel, *Nat.*

*Chem.*, 2014, **6**, 295–302.

328 T. Litschel, B. Ramm, R. Maas, M. Heymann and P. Schwille, *Angew. Chemie - Int. Ed.*, 2018, **57**, 16286–16290.

329 P. Stano, T. P. De Souza, P. Carrara, E. Altamura, E. D'Aguanno, M. Caputo, P. L. Luisi and F. Mavelli, *Mech. Adv. Mater. Struct.*, 2015, **22**, 748–759.

330 H. Saito, Y. Kato, M. Le Berre, A. Yamada, T. Inoue, K. Yosikawa and D. Baigl, *ChemBioChem*, 2009, **10**, 1640–1643.

331 V. Nanjundiah, *Biophys. Chem.*, 1998, **72**, 1–8.

332 W. Li, L. Zhang, X. Ge, B. Xu, W. Zhang, L. Qu, C. H. Choi, J. Xu, A. Zhang, H. Lee and D. A. Weitz, *Chem. Soc. Rev.*, 2018, **47**, 5646–5683.

333 D. T. Chong, X. S. Liu, H. J. Ma, G. Y. Huang, Y. L. Han, X. Y. Cui, J. J. Yan and F. Xu, *Microfluid. Nanofluidics*, 2015, **19**, 1071–1090.

334 I. L. H. Ong and E. Amstad, *Small*, 2019, **15**, 1–12.

335 F. Gao, Z. G. Su, P. Wang and G. H. Ma, *Langmuir*, 2009, **25**, 3832–3838.

336 K. Schroën, J. de Ruiter and C. C. Berton-Carabin, *Food Eng. Rev.*, 2020, **12**, 101–120.

337 N. P. Aditya, S. Aditya, H. Yang, H. W. Kim, S. O. Park and S. Ko, *Food Chem.*, 2015, **173**, 7–13.

338 B. Tal-Figiel, *Chem. Eng. Res. Des.*, 2007, **85**, 730–734.

339 C. A. Fraker, A. J. Mendez, L. Inverardi, C. Ricordi and C. L. Stabler, *Colloids Surfaces B Biointerfaces*, 2012, **98**, 26–35.

340 A. H. Khan, S. P. Zhou, M. Moe, B. A. Ortega Quesada, K. R. Bajgiran, H. R. Lassiter, J. A. Dorman, E. C. Martin, J. A. Pojman and A. T. Melvin, *ACS Biomater. Sci. Eng.*, 2022, **8**, 3977–3985.

341 F. Islands and D. Survey, *Nature*, 1960, **185**, 63–64.

342 Y. Li, J. Rodrigues and H. Tomás, *Chem. Soc. Rev.*, 2012, **41**, 2193–2221.

343 A. Khademhosseini, R. Langer, J. Borenstein and J. P. Vacanti, *Proc. Natl. Acad. Sci. U. S. A.*, 2006, **103**, 2480–2487.

344 A. Khademhosseini and R. Langer, *Biomaterials*, 2007, **28**, 5087–5092.

345 D. Seliktar, 2012, **336**, 1124–1129.

346 N. Annabi, A. Tamayol, J. A. Uquillas, M. Akbari, L. E. Bertassoni, C. Cha, G. Camci-Unal, M. R. Dokmeci, N. A. Peppas and A. Khademhosseini, *Adv. Mater.*, 2014, **26**, 85–124.

347 R. A. Pérez, J. E. Won, J. C. Knowles and H. W. Kim, *Adv. Drug Deliv. Rev.*,

2013, **65**, 471–496.

348 C. Garcia-Galan, Á. Berenguer-Murcia, R. Fernandez-Lafuente and R. C. Rodrigues, *Adv. Synth. Catal.*, 2011, **353**, 2885–2904.

349 U. Hanefeld, L. Gardossi and E. Magner, *Chem. Soc. Rev.*, 2009, **38**, 453–468.

350 D. N. Tran and K. J. Balkus, *ACS Catal.*, 2011, **1**, 956–968.

351 R. A. Sheldon, *Adv. Synth. Catal.*, 2007, **349**, 1289–1307.

352 R. A. Sheldon and J. M. Woodley, *Chem. Rev.*, 2018, **118**, 801–838.

353 V. Nele, J. P. Wojciechowski, J. P. K. Armstrong and M. M. Stevens, *Adv. Funct. Mater.*, 2020, **30**, 1–22.

354 B. A. Hense, C. Kuttler, J. Müller, M. Rothballer, A. Hartmann and J. U. Kreft, *Nat. Rev. Microbiol.*, 2007, **5**, 230–239.

355 N. Qureshi, B. A. Annous, T. C. Ezeji, P. Karcher and I. S. Maddox, *Microb. Cell Fact.*, 2005, **4**, 1–21.

356 S. Sevim, A. Sorrenti, C. Franco, S. Furukawa, S. Pané, A. J. Demello and J. Puigmartí-Luis, *Chem. Soc. Rev.*, 2018, **47**, 3788–3803.

357 P. R. A. Chivers and D. K. Smith, *Nat. Rev. Mater.*, 2019, **4**, 463–478.

358 M. D. Bootman, H. L. Roderick, W. J. Lederer, D. A. Nicoll, S. Longoni, K. D. Philipson, C. C. Hale, J. M. Russell, M. P. Blaustein, A. Noma, H. Irisawa, D. W. Hilgemann, Y. Koide, J. Kimura, M. Ottolia, L. Xu, Z. Qu, R. F. Reilly, S. Benzer, J. Lytton, L. V Hryshko, S. Matsuoka, J. S. Frank, P. P. Schnetkamp, V. Cherezov, L. Baars, S. K. Singh, T. Kawate, Y. Jin, E. Gouaux, J. P. Glusker, S. A. Beebe, C. W. Bock, G. R. Moore, S. Iwata, A. D. Cameron and D. Drew, *Science (80-. ).*

359 S. G. Lee, H. Lee, A. Gupta, S. Chang and P. S. Doyle, *Adv. Funct. Mater.*, 2016, **26**, 4896–4905.

360 C. Vigier-Carrière, F. Boulmedais, P. Schaaf and L. Jierry, *Angew. Chemie Int. Ed.*, 2018, **57**, 1448–1456.

361 B. Yang, D. J. Adams, M. Marlow and M. Zelzer, *Langmuir*, 2018, **34**, 15109–15125.

362 M. Lovrak, W. E. J. Hendriksen, C. Maity, S. Mytnyk, V. Van Steijn, R. Eelkema and J. H. Van Esch, *Nat. Commun.*, 2017, **8**, 1–9.

363 A. Hayer, L. Shao, M. Chung, L. M. Joubert, H. W. Yang, F. C. Tsai, A. Bisaria, E. Betzig and T. Meyer, *Nat. Cell Biol.*, 2016, **18**, 1311–1323.

364 B. C. Zarket and S. R. Raghavan, *Nat. Commun.*, , DOI:10.1038/s41467-017-00077-7.

365 M. Rizwan, R. Yahya, A. Hassan, M. Yar, A. D. Azzahari, V. Selvanathan, F. Sonsudin and C. N. Abouloula, *Polymers (Basel).*, , DOI:10.3390/polym9040137.

366 D. Spitzer, V. Marichez, G. J. M. Formon, P. Besenius and T. M. Hermans, *Angew. Chemie Int. Ed.*, 2018, **57**, 11349–11353.

367 J. Raeburn, B. Alston, J. Kroeger, T. O. McDonald, J. R. Howse, P. J. Cameron and D. J. Adams, *Mater. Horizons*, 2014, **1**, 241–246.

368 L. Thomson, R. Schweins, E. R. Draper and D. J. Adams, *Macromol. Rapid Commun.*, , DOI:10.1002/marc.202000093.

369 L. Schlichter, C. C. Piras and D. K. Smith, *Chem. Sci.*, 2021, **12**, 4162–4172.

370 J. Leira-Iglesias, A. Tassoni, T. Adachi, M. Stich and T. M. Hermans, *Nat. Nanotechnol.*, 2018, **13**, 1021–1027.

371 S. N. Semenov, A. J. Markvoort, T. F. A. De Greef and W. T. S. Huck, *Angew. Chemie - Int. Ed.*, 2014, **53**, 8066–8069.

372 G. Panzarasa, T. Sai, A. L. Torzynski, K. Smith-Mannschott and E. R. Dufresne, *Mol. Syst. Des. Eng.*, 2020, **5**, 445–448.

373 I. Konieczna, M. Kwinkowski, B. Kolesi, Z. Kami and W. Kaca, 2012, 789–806.

374 S. T. S. Hassan, , DOI:10.3390/children4010002.

375 K. Macegoniuk, *Folia Biol. Oecologica*, 2013, **9**, 9–16.

376 L. V Modolo, A. X. De Souza and P. Horta, 2015, 35–44.

377 H. Kotturi, A. Abuabed, H. Zafar, E. Sawyer, B. Pallipparambil, H. Jamadagni and M. Khandaker, *J. Funct. Biomater.*, 2017, **8**, 39.

378 M. K. Schesny, M. Monaghan, A. H. Bindermann, D. Freund, M. Seifert, J. A. Eble, S. Vogel, M. P. Gawaz, S. Hinderer and K. Schenke-Layland, *Biomaterials*, 2014, **35**, 7180–7187.

379 B. Xia, Z. Jiang, D. Debroy, D. Li and J. Oakey, *Biomicrofluidics*, , DOI:10.1063/1.4993122.

380 A. Sabnis, M. Rahimi, C. Chapman and K. T. Nguyen, *J. Biomed. Mater. Res. - Part A*, 2009, **91**, 52–59.

381 A. S. Sawhney, C. P. Pathak and J. A. Hubbell, *Macromolecules*, 1993, **26**, 581–587.

382 C. A. Deforest, B. D. Polizzotti and K. S. Anseth, *Nat. Mater.*, 2009, **8**, 659–

664.

383 H. Li, T. Ma, M. Zhang, J. Zhu, J. Liu and F. Tan, *J. Mater. Sci. Mater. Med.*, , DOI:10.1007/s10856-018-6199-1.

384 J. L. Drury and D. J. Mooney, *Biomaterials*, 2003, **24**, 4337–4351.

385 E. M. Ahmed, *J. Adv. Res.*, 2015, **6**, 105–121.

386 U. S. K. Madduma-Bandarage and S. V. Madihally, *J. Appl. Polym. Sci.*, 2021, **138**, 1–23.

387 J. W. Chan, C. E. Hoyle, A. B. Lowe and M. Bowman, *Macromolecules*, 2010, **43**, 6381–6388.

388 A. H. Khan, J. K. Cook, W. J. Wortmann Iii, N. D. Kersker, A. Rao, J. A. Pojman and A. T. Melvin, , DOI:10.1002/jbm.b.34565.

389 C. D. Pritchard, T. M. O'Shea, D. J. Siegwart, E. Calo, D. G. Anderson, F. M. Reynolds, J. A. Thomas, J. R. Slotkin, E. J. Woodard and R. Langer, *Biomaterials*, 2011, **32**, 587–597.

390 Y. Ju, Y. Hu, P. Yang, X. Xie and B. Fang, *Mater. Today Bio*, 2023, **18**, 100522.

391 B. Safari, M. Aghazadeh, S. Davaran and L. Roshangar, *Eur. J. Pharm. Biopharm.*, 2022, **171**, 50–59.

392 Y. Zhou, S. Liu, M. Zhao, C. Wang, L. Li, Y. Yuan, L. Li, G. Liao, W. Bresette, J. Zhang, Y. Chen, J. Cheng, Y. Lu and J. Liu, *J. Control. Release*, 2019, **316**, 93–104.

393 G. Fuhrmann, , DOI:10.1038/s41565-019-0625-5.

394 G. Tan, J. Xu, Q. Yu, J. Zhang, X. Hu, C. Sun and H. Zhang, .

395 C. Antich, J. de Vicente, G. Jiménez, C. Chocarro, E. Carrillo, E. Montañez, P. Gálvez-Martín and J. A. Marchal, *Acta Biomater.*, 2020, **106**, 114–123.

396 W. Liu, M. Griffith and F. Li, *J. Mater. Sci. Mater. Med.*, 2008, **19**, 3365–3371.

397 A. K. Dash and G. C. Cudworth, *J. Pharmacol. Toxicol. Methods*, 1998, **40**, 1–12.

398 J. Bourquin, A. Milosevic, D. Hauser, R. Lehner, F. Blank, A. Petri-Fink and B. Rothen-Rutishauser, *Adv. Mater.*, 2018, **30**, 1704307.

399 J. Li and D. J. Mooney, *Nat. Rev. Mater.*, , DOI:10.1038/natrevmats.2016.71.

400 D. Lensen, D. M. Vriezema and J. C. M. van Hest, *Macromol. Biosci.*, 2008, **8**, 991–1005.

401 Y. Hennequin, N. Pannacci, C. P. De Torres, G. Tetradis-Meris, S. Chapuliot,

E. Bouchaud and P. Tabeling, *Langmuir*, 2009, **25**, 7857–7861.

402 Y. A. Jaimes-Lizcano, Q. Wang, E. C. Rojas and K. D. Papadopoulos, *Colloids Surfaces A Physicochem. Eng. Asp.*, 2013, **423**, 81–88.

403 D. Lee and D. A. Weitz, *Adv. Mater.*, 2008, **20**, 3498–3503.

404 C. J. Martinez, J. W. Kim, C. Ye, I. Ortiz, A. C. Rowat, M. Marquez and D. Weitz, *Macromol. Biosci.*, 2012, 12, 946–951.

405 J. F. Ambrose, G. B. Kistiakowsky, A. G. Kridl and A. G. Kridl, *J. Am. Chem. Soc.*, 1951, **73**, 1232–1236.

406 P. Kafarski and M. Talma, *J. Adv. Res.*, 2018, **13**, 101–112.

407 L. Mazzei, M. Cianci, A. Gonzalez Vara and S. Ciurli, *Dalt. Trans.*, 2018, **47**, 8240–8247.

408 S. Svane, J. J. Sigurdarson, F. Finkenwirth, T. Eitinger and H. Karring, *Sci. Rep.*, 2020, **10**, 1–14.

409 L. Mazzei, M. N. Wenzel, M. Cianci, M. Palombo, A. Casini and S. Ciurli, *ACS Med. Chem. Lett.*, 2019, **10**, 564–570.

410 H. Azizian, F. Nabati, A. Sharifi, F. Siavoshi, M. Mahdavi and M. Amanlou, *J. Mol. Model.*, 2012, **18**, 2917–2927.

411 A. Ibrar, I. Khan and N. Abbas, *Arch. Pharm. (Weinheim).*, 2013, **346**, 423–446.

412 N. N. Deng, M. Yelleswarapu and W. T. S. Huck, *J. Am. Chem. Soc.*, 2016, **138**, 7584–7591.

413 S. Deshpande, Y. Caspi, A. E. C. Meijering and C. Dekker, *Nat. Commun.*, 2016, **7**, 1–9.

414 R. Bizzarri, C. Arcangeli, D. Arosio, F. Ricci, P. Faraci, F. Cardarelli and F. Beltram, *Biophys. J.*, 2006, **90**, 3300–3314.

415 K. Kano and J. H. Fendler, *Biochim. Biophys. Acta - Biomembr.*, 1978, **509**, 289–299.

416 I. A. Karampas and C. G. Kontoyannis, *Vib. Spectrosc.*, 2013, **64**, 126–133.